ABSTRACT

Title of dissertation: NUMERICAL SIMULATION OF BOUNDARY LAYER TRANSITION DUE TO EXTERNAL DISTURBANCES

Victor Ovchinnikov, Doctor of Philosophy, 2006

Dissertation directed by: Professor Ugo Piomelli
Department of Mechanical Engineering

Bypass transition in flat-plate boundary layers due to a highly disturbed free stream is investigated via numerical simulation. The first part of the study presents DNS & LES of the interaction between a laminar boundary layer and a von Kármán vortex street behind a circular cylinder. Rapid, bypass-like transition to turbulence is observed for higher Reynolds number cases. An investigation of the underlying transition mechanism is performed. The second part of the study focuses on transition due to the effects of isotropic free-stream turbulence (FST). First, the effects of different inflow parameters on the location of transition onset are examined. The length scale of the FST and the extent of its penetration into the boundary layer are among the parameters that affect srongly the transition onset location. In subsequent simulations, we include the leading edge of the flat plate inside the computational domain. The results reveal the presence of small-amplitude laminar streaks at the streamwise location corresponding to the inflow boundary of the

truncated-domain simulations. We conclude that such simulations should not be expected to provide quantitative predictions of bypass transition. However, with suitable calibration, they represent a useful tool for investigating bypass transition physics. Finally, DNS of bypass transition in the flat-plate boundary layer induced by high-amplitude FST are carried out. In one simulation, the boundary conditions are chosen to match the 6% FST ERCOFTAC experiment T3B. The mean velocity and Reynolds stress profiles are in good agreement with the experimental dataset. In the other simulations, the length scale and intensity of the oncoming FST are varied to determine the effects on the onset and mechanism of transition. Our results indicate that the physics of FST-induced boundary-layer transition are dependent on the choice of the FST length scale.A description of statistical quantities is followed by a study of the transition mechanism. Qualitative similarities between bypass transition due to FST and wake-induced transition are underlined and the challenges of predicting boundary-layer transition in this complex environment are discussed.

NUMERICAL SIMULATION OF BOUNDARY LAYER TRANSITION DUE TO EXTERNAL DISTURBANCES

by

Victor Ovchinnikov

Dissertation submitted to the Faculty of the Graduate School of the
University of Maryland, College Park in partial fulfillment
of the requirements for the degree of
Doctor of Philosophy
2006

Advisory Commmittee:

Professor Ugo Piomelli, Chair/Advisor
Professor James Baeder
Professor Elias Balaras
Professor Peter Bernard
Dr. Meelan M. Choudhari
Professor James Wallace

PREFACE

Transition to turbulence in wall-bounded flows is one of the most studied problems in fluid dynamics. Notorious for its mathematical complexity, it is also of significant engineering interest. It is well known, for example, that a turbulent boundary-layer flow results in an higher viscous drag, increased heat transfer between the wall and the fluid and enhanced mixing; it may also be less prone to separation compared to laminar flow. For these reasons, the ability to control, or at least predict, the onset of laminar-turbulent transition is crucial to the design of aerodynamic components with a significant extent of laminar flow. Despite the relative simplicity of the laminar channel and boundary-layer flows, the various disturbances ultimately leading to transition induce a myriad of complex phenomena that have challenged some of the most talented minds. Consequently, compared to other areas in fluid dynamics, the understanding of transition to turbulence has been slow to come. Despite outstanding progress in the area of natural transition, bypass transition in boundary-layers caused by moderate to high amplitude turbulence in the free stream is still not well understood. In the past decade, advances in computing power and the development of efficient numerical algorithms have made many transitional flows amenable to Direct Numerical and Large Eddy Simulation (DNS/LES). Many results from DNS of laminar-turbulent transition have been validated experimen-

tally, and earned this tool a permanent place in transition research. The current dissertation is a numerical study of boundary-layer transition in a highly-disturbed free-stream environment. Our primary focus is on transition caused by coherent disturbances (wakes) generated by obstacles upstream of the boudary layer, but the germane topic of transition due to high-amplitude free-stream turbulence (FST), is also studied. Our research aims at investigating the physical mechanisms reponsible for the transition process in both types of free-stream disturbance environments.

This dissertation includes previously published work in the form of one journal article and two conference papers co-authored by V.O., U.P. and Dr. Meelan M. Choudhari of the NASA Langley Research Center. The papers are being included with the permission of the Dissertation Advisor and the Graduate Director. The examining committee has determined that the student has made substantial contributions to these papers and agrees that this work should be included in the dissertation.

DEDICATION

To my friends and mentors Ugo Piomelli, Alex Iosevich and Paul D. Roepe, for their belief and encouragement.

ACKNOWLEDGMENTS

My special thanks to Ugo Piomelli and Meelan M. Choudhari for their guidance, to Elias Balaras and Peter Bernard for their helpful discussions, and to Elyse Beaulieu-Lucey, Senthil Radhakrishnan, Giuseppe De Prisco, Nikolaos Beratlis and Reza Keimasi for their friendship.

Financial support of the NASA Langley Research Center and the use of their computational resources are gratefully acknowledged.

Contents

List of Tables

List of Figures

Nomenclature

Abbreviations

3D	Three-dimensional
APG	Adverse pressure gradient
AR	Aspect ratio
DFFT	Discrete fast Fourier transform
DNS	Direct numerical simulation
FD	Finite difference
IB	Immersed boundary
FST	Free-stream turbulence
LE	Leading edge
LES	Large eddy simulation
NS	Navier-Stokes
NSE	Navier-Stokes Equations
TKE	Turbulent kinetic energy
ZPG	Zero pressure gradient
f.s.t.	Free-stream turbulence

Roman symbols

$E(k)$ ..... 3D Energy spectrum
C_f ..... $= \frac{\tau_w}{\rho U_\infty^2/2}$, skin friction coefficient
C_p ..... $= \frac{2(p_\infty - p)}{\rho U_\infty^2}$, pressure coefficient
L ..... A length scale
L_{11} ..... $= \int_0^\infty \frac{\overline{u'(x)u'(x+r)}}{\overline{u'(x)u'(x)}} dr$, integral length scale
L_k ..... $= \left(k^{3/2}\right) / \left(U_\infty dk/dx\right)$, dissipation length scale
H ..... $= \theta/\delta^*$, boundary-layer shape factor
D ..... Cylinder diameter
F ..... $= 10^6 \omega\nu/U_\infty^2$, nondimensional frequency
K ..... $= -\left(\nu/U_\infty^2\right)\left(dU_\infty/dx\right)$, the acceleration parameter
L_x ..... Domain size in the x-direction
L_y ..... Domain size in the y-direction
L_z ..... Domain size in the z-direction
R ..... Radius of superellipse in §6
Re_D ..... Reynolds number based on the cylinder diameter

Re_L ..... Reynolds number based on the FST length scale, L_{11}
Re_x ..... Reynolds number based on distance from the plate leading edge
Re_θ ..... Reynolds number based on the boundary-layer momentum thickness, θ
Re_τ ..... Reynolds number based on the friction velocity, u_τ
R_{uu} ..... Spanwise correlation function of the u-velocity
R_{vv} ..... Spanwise correlation function of the v-velocity
R_{ww} ..... Spanwise correlation function of the w-velocity
Tu ..... $= (\sqrt{\langle u'u' \rangle} + \sqrt{\langle v'v' \rangle} + \sqrt{\langle w'w' \rangle})/3$, turbulence intensity
U_0 ..... Free-stream velocity
U_{cyl} ..... Cylinder vertical velocity
U_∞ ..... Free-stream velocity
f ..... Disturbance attenuation profile in §5
f_i ..... i_{th} component of immersed boundary force
k ..... $= \frac{1}{2}(\langle u'u' \rangle + \langle v'v' \rangle + \langle w'w' \rangle)$, turbulent kinetic energy
k_x (k_1) ... Streamwise wavenumber in §4
k_y (k_2).... Spanmwise wavenumber in §4
k_z (k_3).... Wall-normal wavenumber in §4
nx ..... Number of grid points in the x-direction
ny ..... Number of grid points in the y-direction
nz ..... Number of grid points in the z-direction
p ..... Pressure
s ..... Arclength coordinate in §6
t ..... Nondimensional time
u ..... Streamwise velocity component
u^+ ..... Streamwise velocity normalized by the friction velocity, u_τ
u_τ ..... $= \sqrt{\frac{\tau_w}{\rho}}$, friction velocity
u_{rms} ..... Streamwise turbulent intensity
v ..... Spanwise velocity in §4 and §5; wall-normal velocity in §2, §3 and §6
v_{rms} ..... Turbulent intensity in the y-direction
w ..... Wall-normal velocity in §4 and §5; spanwise velocity in §2, §3 and §6
w_{rms} ..... Turbulent intensity in the z-direction
x (x_1) .... Streamwise coordinate
y (x_2) .... Spanwise coordinate in §4 and §5; wall-normal coordinate in §2, §3 and §6
y^+ ..... Wall-normal distance normalized by the viscous length scale, δ_v
z (x_3) .... Wall-normal coordinate in §4 and §5; spanwise coordinate in §2, §3 and §6

Greek symbols

Δ_x ..... Grid spacing in the x-direction
Δ_y ..... Grid spacing in the y-direction

Δ_z ..... Grid spacing in the z-direction
Γ ..... Circulation
α ..... Exponent in FST decay law, see §4
β ..... Spanwise wavenumber
δ_{98} ..... 98% boundary-layer thickness
δ_{99} ..... 99% boundary-layer thickness
δ_{99}^0 ..... 99% boundary-layer thickness at the inflow of the simulations in §4
δ^* ..... $= \int_0^{y_{\text{edge}}} \left(1 - \frac{\langle U \rangle}{U_{\text{edge}}}\right) dy$, Boundary-layer displacement thickness
δ_v ..... Viscous length scale, ν/u_τ
η ..... $= \frac{z}{\sqrt{\nu U_\infty / x}}$, Blasius similarity variable in §5
ν ..... Molecular kinematic viscosity
ν_T ..... Turbulent viscosity
ω ..... Frequency
ω_0 ..... Fundamental frequency
τ_{ij} ..... $= \overline{u_i u_j} - \overline{u}_i \overline{u}_j$, the subgrid-scale (SGS) stress
τ_w ..... $= \mu \frac{\partial \langle U \rangle}{\partial y}$ at the solid wall, wall stress
θ ..... $= \int_0^{y_{\text{edge}}} \frac{\langle U \rangle}{U_{\text{edge}}} \left(1 - \frac{\langle U \rangle}{U_{\text{edge}}}\right) dy$, boundary-layer momentum thickness

Superscripts and subscripts

$(\,^+)$ ..... Nondimensional quantity normalized using the viscous length scale δ_v and the friction velocity u_τ
$\overline{(\,)}$ ..... The operation of Reynolds-averaging, or grid-filtering, depending on context
$\langle\,\rangle$ ..... The operation of Reynolds-averaging
$(\,')$ ..... Denotes a fluctuation from the mean
$\widehat{(\,)}$ ..... The operation of test-filtering
$(\,)_{rms}$ ..... Root-mean-square of a variable

Chapter 1

Introduction

This chapter presents a brief background for the present investigation and a review of the pertinent literature on boundary-layer transition. Keeping with tradition, we start with natural transition, move on to discuss bypass transition, and finish with wake/boundary-layer interactions. The last two topics are directly relevant to the present research. The chapter concludes with a statement of the technical objectives and an outline of the organization of the results.

1.1 Motivation

In many wall-bounded flows of engineering interest, it is often desirable to delay the onset of laminar-turbulent transition in order to reduce the skin friction drag on the surface. In aeronautical applications, drag reduction via laminar flow control is primarily relevant to the cruise configuration. Typical high-lift configurations used during the take-off and landing stages of commercial subsonic transports involve multi-element airfoils consisting of a leading edge slat and a trailing edge flap in addition to the wing. Flight tests suggest that the high-lift flow fields may involve large regions of laminar flow. Due to the intricate coupling between transition and flow separation in such flows, accurate predictions of transition inset is crucial to the

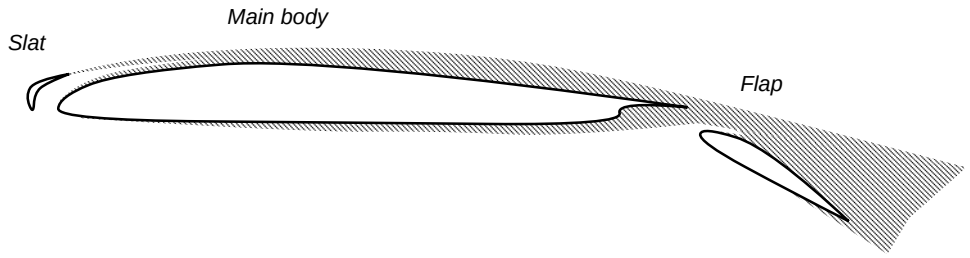

Figure 1.1: Multi-element airfoil.

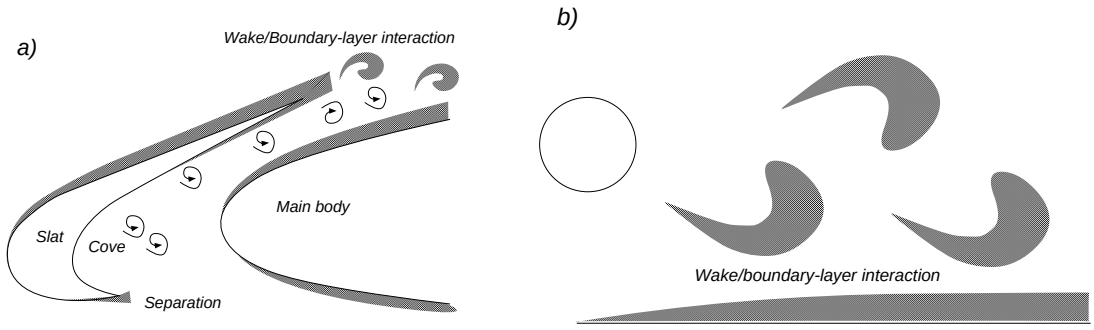

Figure 1.2: a) Slat/main body junction of an airfoil b) Interaction in a simplified geometry

design of high-lift devices. While transition scenarios on a single airfoil have been studied in great detail, *e.g.* natural or bypass transition in isolated boundary layers, boundary-layer transition due to disturbances generated by upstream geometry, as in the multi-element airfoil, has received less scrutiny, and is investigated in the current work.

A model multi-element airfoil is illustrated in figure 1.1. The shaded areas represent the boundary layers and wakes forming on the three elements, the upstream slat, the main element in the middle, and the downstream flap. Figure 1.2*(a)* shows a close-up of the slat/body region. In the figure, the slat is in the extended position

to delay the onset of stall on the main element at higher angles of attack. The gap and the overlap settings between the slat and the main body are calculated to optimize the overall performance of the high-lift system. The evolution of the boundary layer on the suction surface of the main element is significantly influenced by the wake of the slat. The wake turbulence may include vortex shedding from the trailing edge and may be further augmented by the vortical structures emanating from the separated flow in the slat cove region.

In the current research, we perform Direct Numerical Simulations (DNS) to study the interaction between the unsteady trailing-edge wake of an upstream element and the laminar boundary layer over a downstream element. To study such flows in a simpler setting, we consider a model problem, illustrated in figure 1.2*(b)*, which consists of a circular cylinder positioned above a flat plate. This configuration removes the effects of surface curvature and pressure gradients on the boundary-layer development, yet retains the essential aspects of wake/boundary-layer interaction. Our aim is to elucidate the physical mechanism underlying this interaction and draw comparisons to the well-known phenomenon of bypass transition due to free-stream turbulence.

In a realistic flow environment, the boundary layer over the main airfoil element depicted in figure 1.1 will be subjected to both, vortical disturbances from the trailing edge of the slat and turbulence in the free steam. Thus, it is interesting to see whether the two mechanisms of interaction involve the same fundamental boundary-layer physics, and which mechanism is likely to dominate the transition in

the boundary layer. The answers to these questions are essential to develop realiable predictive models for transition in high-lift flow fields.

Although FST-induced bypass transition has been studied extensively through experiments, complementary high-accuracy numerical simulations are few and not quite complete. In particular, neither the effect of the FST integral length scale nor the role of the leading edge during the transition process has been systematically addressed. Moreover, even at low values of FST length scale, the finer details of the transition mechanism are still debated. Finally, the issue of generating the appropriate inflow boundary conditions for bypass transition simulations beginning downstream of the leading edge is not fully settled. Therefore, a substantial part of this investigation is devoted to simulations of FST-induced bypass transition using different inflow-generation methods and at different values of the FST length scale. We carry out a grid refinement study and obtain agreement with a benchmark experiment. We conclude with an investigation of the physics of FST-induced transition and a discussion of the different transition scenarios.

1.2 Natural transition

In 1880, Lord Rayleigh presented a linear stability theory for inviscid parallel shear flows. This theory described a "roll-up" instability of inflectional velocity profiles in unbounded shear flows, but failed in wall-bounded flows, such as the Blasius boundary layer, in which viscosity is actually necessary for the initial in-

stability. Orr (1907) and Sommerfeld (1908) included the effects of viscosity within Rayleigh's linear theory. For a given basic flow, the goal is to solve for the disturbance phase speed (eigenvalue) and the disturbance profile (eigenfunction), as a function of the Reynolds number and streamwise wavenumber. Tollmien (1929) and Schlichting (1933) independently obtained solutions of Orr-Sommerfeld equation for the Blasius boundary layer (Tollmien-Schlichting waves). Disturbance profiles corresponding to these solutions were measured by Schubauer & Skramstad (1947) in carefully controlled experiments involving artificial excitation, although the agreement with theory was not perfect due to nonparallel effects (nonparallel theories predict higher TS wave growth and yield a better agreement with experiments [Gaster 1974]). Bennett (1953) also observed TS waves in naturally-occuring flow. A review of linear stability mechanisms is given by Bayly, Orszag, and Herbert (1988). For certain values of the streamwise wavenumber, TS waves amplify in a narrow band of Reynolds numbers, or between the lower and upper branches of the linear stability curve. At sufficiently low amplitudes, TS waves grow downstream of Branch I on a slow viscous scale and decay harmlessly past Branch II. At higher initial amplitudes, *i.e.* greater than approximately 1% of U_0, rapidly-evolving three-dimensional instabilities are known to appear. Klebanoff, Tidstrom & Sargent (1962) generated boundary-layer disturbances using a vibrating ribbon and observed regions of enhanced and diminished perturbation velocity alternating in the spanwise direction, which they labeled peaks and valleys. Because the spanwise scale of the pattern was the same as the TS wavelength, this mode of transition has become known

as the fundamental (or K-type, for Klebanoff) breakdown. This (nonlinear) stage was characterized by rows of Λ-shaped vortices that are aligned in the streamwise direction. These vortices lead to the formation of localized layers of high shear, followed by a sudden appearance of spikes during each cycle of the oscilloscope traces. These spikes multiplied, doubling and tripling in number, and leading, finally, to a turbulent spot.

The experiments of Klebanoff *et al.* (1962) were reproduced by Kachanov *et al.* (1985) and Kachanov *et al.* (1990). It was found that the disturbances remained deterministic up until the late stages of breakdown. The spectra had clear signals of the fundamental and harmonic frequencies right before the appearance of spikes, at which stage the total disturbance intensity increased rapidly near the high-shear layers. Spike formation was not attributed to a jump in amplitude, but to phase synchronization in disturbance harmonics in a definite region of space. Kachanov (1987, 1990) developed a wave-resonant theory of K-type breakdown as an extension of the resonant triad theory of Craik (1971) and the subsequent work of Nayfeh & Bozatli (1979). The wave-resonant concept explained the experimentally observed 3D amplification and spike generation.

Rist (1990), Rist & Fasel (1991) and Rist & Fasel (1995) performed spatial DNS of controlled transition in a flat-plate boundary layer, aiming to reproduce the experiments of Kachanov *et al.* (1985). These authors obtained good agreement with experiments up to the stage of spike formation. The initial disturbance was a 2D wave with very small spanwise periodic variation. Nonlinear effects soon gener-

ated other modes, with spanwise high-frequency modes generated more quickly than 2D streamwise counterparts. The growth of spanwise modes saturated before the onset of breakdown. These authors confirmed that spike development is a predictable event, caused by the synchronization of wave components in a narrow frequency range. Iso-surfaces of the spanwise vorticity perturbation developed tongue-like structures, which became more elongated with the streamwise distance. While being stretched in the streamwise direction, these structures developed streamwise waviness. Iso-surfaces of the streamwise vorticity were Λ-shaped. The legs of the vortices are near and parallel to the wall, but the tip is displaced vertically into the outer boundary layer.

In visualisation studies of boundary-layer transition, Knapp & Roach (1968) observed Λ-vortices in a staggered, instead of aligned, arrangement. Kachanov *et al.* (1977) also noticed this pattern while performing controlled transition experiments. These authors realized that the staggered Λ-vortex arrangement leads to a qualitatively different mode of breakdown from the K-type. This scenario was later denoted N-type, or subharmonic breakdown, after the fact that the dominant streamwise wavelength of the disturbance is twice that of the fundamental TS wave. In this case, no spikes are present. The amplitude of the fundamental wave grows until the signal becomes random, accompanied by a weak growth of higher harmonics. Usually, the initial amplitude of the fundamental wave is small compared to the K-breakdown. The onset of three-dimensionality starts with the formation and rapid development of a broad packet of low-frequency disturbances. They are

quasi-subharmonic fluctuations with half the frequency of the fundamental, but with random amplitude and constant phase. Geometrically, the amplified subharmonic consists of a pair of 3D instability waves inclined at $\theta = \pm 63$ to the flow direction. Laminar breakdown begins with the appearance of quasi-random disturbances near the frequencies $\omega/\omega_0 = 3/2,\ 5/2$, where ω_0 is the frequency of the fundamental wave.

Craik (1971) developed a theory of resonant three-wave interaction for the boundary layer based on a weakly-nonlinear approach. The triad consists of one 2D instability wave and two oblique subharmonic waves, propagating at angles of same magnitude but opposite sign. Craik's model did not generate widespread interest until the first observations of amplified subharmonic modes in the boundary layer (Kachanov *et al.* 1977). Craik-type resonances were observed experimentally by Saric *et al.* (1981), Thomas & Saric (1981) and Kachanov & Levchenko (1984). The resonant triad model was valid, but ultimately incomplete. Craik's idea was extended by Nayfeh & Bozatli (1979). These authors studied the resonant interaction of four waves, $(\omega_0, 0)$,$(2\omega_0, 0)$,$(\omega_0, \pm\beta)$, which could result in the amplification of 3D waves with the fundamental frequency ω_0. Orszag & Patera (1983) carried out numerical studies of 3D secondary instability of TS waves. They found that different types of disturbances can arise. Primary resonance with the TS wave produces peak-valley splitting as the TS wave amplitude exceeds a threshold, while subharmonic resonance can occur at smaller TS wave amplitudes. Their calculated disturbance velocities and growth rates were consistent with experiments. The authors concluded that secondary instability originates from the redistribution of spanwise

vorticity into streamwise-periodic lumps near the critical layer. The growth of 3D modes arises from the combined effects of vortex tilting and stretching.

Herbert (1984, 1986, 1987) carried out Floquet analysis of secondary instability in the presence of a finite amplitude TS wave and obtained good overall agreement with experiments on both fundamental (K-type, peak-valley splitting) and subharmonic (N-type) breakdown. He concluded that peak-valley splitting is likely to occur at lower frequencies and higher TS wave amplitude. The subharmonic instability modes were found to be more unstable than the fundamental. Spalart & Yang (1987) carried out DNS of transition in a temporally-growing boundary layer and also observed that subharmonic modes were more unstable. DNS of N-type breakdown were also performed by Fasel (1990) and Kleiser & Zang (1991) and showed good overall agreement with experiments.

The combined efforts of experimentalists and theoriticians essentially clarified the physics of N-type transition in the flat-plate boundary layer. The main mechanism is due to a rapid resonant amplification of 3D quasi-subharmonic modes through their interaction with a quasi-2D initial TS wave, amplified by the primary flow instability. For thorough reviews of the mechanisms of secondary instability and subsequent disturbance evolution, the reader is referred to the articles by Herbert (1988) and Kachanov (1994).

1.3 TS-wave receptivity

In the above discussion, we have focused on the evolution of a small disturbance present in the boundary layer as an initial condition. In reality, the process of receptivity, *i.e.* the generation of this initial disturbance through the interaction of the mean 2D flow with acoustic, vortical, or geometric (*e.g.* surface roughness) disturbances, is of equal importance. Mathematically, receptivity is an initial-boundary-value, rather than an eigenvalue problem, *i.e.* it should admit solutions for all values of wavenumbers and frequencies, and thus has to be treated differently. Selected receptivity studies are sumarized below. For a recent comprehensive review, the reader is referred to Saric *et al.* (2002).

In a seminal paper, Goldstein (1983) used high-Reynolds number asymptotics to investigate the receptivity of the flat plate boundary layer to acoustic waves. His analysis explains how the O(1) nonparallel flow effect in the leading-edge region can transfer energy from a long wavelength to the short TS wave. In a subsequent paper, Goldstein (1985) showed that short-scale variations in surface geometry can lead to a direct transfer of energy from the free stream acoustic disturbance to a TS wave. Golstein & Hultgren (1987) studied the influence of leading-edge curvature on the receptivity process.

Lin *et al.* (1992) studied via DNS the boundary-layer receptivity to acoustic disturbances in the presence of an elliptic leading-edge. The discontinuity in curvature at the ellipse/flat-plate junction was found to be a source of TS-wave re-

ceptivity. The receptivity decreased with increasing leading-edge sharpness (higher aspect ratio). Lin *et al.* (1992) also found that the resultant TS wave amplitude halved when a superellipse was used, eliminating the curvature discontinuity. Buter & Reed (1994) studied boundary-layer receptivity to free-stream vorticity for the same geometry as Lin *et al.* (1992). As the disturbance convected past the body, it was ingested into the upper part of the boundary layer. Signals at the TS wavelength were prevalent near the wall, while near the boundary-layer edge disturbances of the free-stream wavelength were observed. The receptivity to vorticity was smaller than the receptivity to sound by a factor of three. TS-wave response was linear up to free-stream disturbance amplitudes of 4.2% and 2.1% of the free-stream velocity, for symmetric and antisymmetric disturbances, respectively.

1.4 Bypass transition

The studies of boundary-layer transition summarized above were motivated by early theoretical results from linear stability theory (LST). The neglect of the non-linear term, which rendered the problem tractable, required that the amplitudes of the initial perturbation be sufficiently small. This condition may be met in a number of external aerodynamic flows, particularly in aeronautical applications because of the benign nature of the disturbance environment. Certain flows of engineering interest, *e.g.* in turbomachinery, involve high-amplitude disturbances that invalidate a straightforward application of LST. In fact, with free-stream vortical disturbances

in excess of 1% of the free-stream velocity (low/moderate-amplitude free-stream turbulence), the TS-wave scenario appears to be absent. The boundary layer undergoes a more rapid transition, at flat-plate Reynolds numbers up to an order of magnitude lower than those predicted via the linear theory. The disturbance growth rate is also higher and occurs on a convective, rather than a slow viscous time scale associated with TS waves. Morkovin (1969) referred to this transition phenomenon as "bypass transition," after the fact that the classical TS mechanism is bypassed. In the following, we summarize the most important experimental, theoretical, and numerical research on bypass transition. This discussion is repeated in chapter 6 of this dissertation, where we also present the bulk of our DNS results on FST-induced boundary-layer transition.

1.4.1 Experimental work on transition due to FST

Klebanoff (1971) observed that the Blasius boundary layer develops unsteady undulations of the streamwise velocity with a frequency content that is significantly lower than that of the unstable TS waves. The amplitude of the peak response increased in proportion to the FST amplitude, and grew larger in proportion with the boundary-layer thickness. Arnal & Juillen (1978) found no evidence of TS waves in the transition process, and observed that the peak of the low-frequency disturbance energy is located in the middle of the boundary layer. Kendall (1985) observed long streamwise streaks with small spanwise scales, which he called Klebanoff modes.

He also confirmed the finding of Klebanoff (1971) that the disturbance $u_{\rm rms}$ grows in proportion to the boundary-layer thickness. Westin *et al.* (1994) reported that the mean velocity profile is only slightly modified, despite boundary-layer $u_{\rm rms}$ levels of 10% of the free-stream velocity. They also confirmed a linear dependence of the boundary-layer $u_{\rm rms}$ on the layer thickness. Comparing with other experiments, they noted that the constant of proportionality may be variable. Matsubara & Alfredsson (2001) reviewed several experiments performed at the Royal Institute of Technology (KTH). They found that the spanwise spacing of streaks (of opposite sign of the u'-velocity perturbation, *i.e.* high- and low-speed) increases with the FST level, and also slightly increases with the streamwise distance. Towards the end of the transition zone, it is approximately equal to the boundary-layer thickness. These authors suggested that the spanwise scale selection occurs within the boundary layer. In a later publication, however, Fransson & Alfredsson (2003) concluded that the selection process is more complex and is influenced by the FST scale, among other effects. Matsubara & Alfredsson (2001) confirmed that the transitional boundary-layer $u_{\rm rms}$ peak is located approximately in the middle of the layer and show that the length of streaks increases in proportion to the layer thickness. From their flow visualization studies, the authors concluded that the appearance of "turbulent spots" (Emmons, 1951) – patches of irregular fluid motion surrounded by quasi-laminar flow that appear in the last stages of transition – may be due to secondary instabilies of the streaks. Recently, Fransson, Matsubara & Alfredsson (2005) performed additional experiments using a wide range of FST intensities and

length scales and made several important contributions. First, there is an initial region near the leading edge where the disturbance grows more slowly than farther downstream, *i.e.* the receptivity process requires a certain distance. Second, the disturbance energy increases in proportion to the FST energy and the flat-plate Reynolds number (Re_x). Third, the transition Reynolds number is inversely proportional to the FST energy. Finally, the extent of the transition zone increases in proportion to the flat-plate Reynolds number. These findings should be confirmed in future experiments and numerical simulations. Although Fransson *et al.* (2005) vary the FST length scale in a controlled manner, they do not sort their data based on the length scale. Thus, the effect of the FST length scale is not addressed in their work. Jonáš, Mazur & Uruba (2001) study the effect of the FST dissipation length scale on the onset of transition at the FST intensity of 3%. Based on their measurements of the intermittency function, they find that the onset of transition is moved upstream with increasing length scale, and that the transition region becomes longer. Further, quantitative studies of the effect of the FST length scale are needed, especially because, together with other factors, such as leading-edge geometry, they may explain some of the discrepancies in the experiments performed to date.

1.4.2 Theoretical work

Several approaches have been taken to understand the physics of bypass transition from a theoretical point of view. Ellingsen & Palm (1975) proposed a linear mechanism for the inviscid evolution of an initial disturbance in the presence of a mean shear. Due to the non-orthogonality of the linearized incompressible Navier-Stokes (NS) operator, an initial disturbance may undergo an initial "transient" growth before exponential decay. In particular, the streamwise disturbance component may grow linearly in time, evolving into a streak. A similar mechanism due to Moffat was also referenced by Philips (1969). Landahl (1980) produced a physical explanation for this phenomenon, known as the "lift-up" effect. Pairs of counterrotating vortices are able to lift low-momentum fluid into the upper boundary-layer, producing a streak of negative velocity fluctuation. Transient growth theory has been used with some success in several wall-bounded flows. Butler & Farrel (1992) found optimal perturbations for plane channel, Couette, and parallel boundary-layer flow. Andersson, Breggen & Henningson (1999) and Luchini (2000) used optimization techniques to find optimal disturbances for a Blasius boundary layer. The optimal disturbance was found to be a pair of counterrotating vortices and the downstream perturbation was a streaky structure with a spanwise scale of 1.4 times the boundary-layer thickness. Good agreement was found between the disturbance cross-stream profile and u_{rms} data of Westin et al. (1994). Since transient growth theory is linear, it can only describe the initial transition stages, and not its later de-

velopment. A theoretical study of streak breakdown as part of a self-sustaining cycle can be found, for example, in Waleffe (1997). Andersson *et al.* (2001) used Floquet theory to investigate secondary instabilities of the optimal final disturbance from Andersson *et al.* (1999). These authors found critical streak amplitudes for the sinuous and varicose instabilities to be 26% and 37%, respectively. A different approach was used by Bertolotti (1997), who used the parabolic stability equations (PSE) to study the response of the boundary layer away from the leading edge to vortical modes in the free stream. He found that low frequency stationary modes produce disturbance profiles that are in good agreement with experiments. Leib, Wundrow & Goldstein (1999) solved the linear boundary-region equations, accounting for the FST interaction with a solid surface. The results indicate the importance of the cross-stream velocity components in triggering streamwise streaks. Their predictions provide encouraging agreement with measured boundary-layer data for lower levels of FST.

1.4.3 Computational work

Large-Eddy Simulations (LES) and Direct Numerical Simulations (DNS) of transition in boundary layers have been slow to come due to the high costs of computation. Not only must the boundary layer resolution be sufficiently fine to ensure accurate disturbance evolution, but the streamwise domain size must be large enough to capture all stages of the boundary-layer development. The first DNS of

boundary-layer transition due to FST in a spatial formulation was performed by Rai & Moin (1993), who used a finite-difference, fractional-step, compressible NS solver to model the experiments of Blair (1983). The disturbance was generated to match the von Kármán energy spectrum with a prescribed intensity and length scale. The location of transition onset agreed with the experiments adequately, but the skin friction development farther downstream was compromised due to under-resolution. Their work indicates that the resolution needed to simulate a transitional flow is as high as that for a turbulent boundary layer. Voke & Yang (1995) used a finite volume conservative method to perform LES of boundary-layer transition, in an attempt to reproduce the experiments of Roach & Brierlay (1992). Although their simulations were severely under-resolved and the FST properties were not matched to the experiment, they were able to provide qualitative insights into the transition mechanism. The wall-normal FST component acts with the mean shear of the flow to produce the Reynolds shear stress, which, together with the mean shear, drives the production of the streamwise Reynolds stress. A proper DNS of FST-induced transition was performed by Jacobs & Durbin (2001). Following Grosch & Salwen (1978), these authors expanded the FST in the eigenfunctions of the linear Orr-Sommerfeld operator to provide a realistic inflow condition without simulating flow around the leading edge. With fine, turbulent-like resolution in the entire boundary layer, they obtained very good agreement with the T3A experiment of Roach & Brierlay (1992) at 3% FST intensity. Klebanoff modes were found to be a prominent feature of their simulations, and were generated nonlinearly by the penetration of

the FST into the boundary layer. The spanwise streak spacing was in agreement with the optimal results of Andersson *et al.* (1999). No evidence of streak instability was reported in their work. Instead, low-speed streaks provide a receptivity path between the FST and the boundary layer, but are otherwise irrelevant to transition.

Brandt, Schlatter & Henningson (2004) performed DNS of boundary-layer transition due to FST with variable length scale and intensity. They used the disturbance generation method in Jacobs & Durbin (2001) but also with the Squire modes for the wall-normal vorticity. They found that for a given FST intensity, increasing the FST length scale moves the onset of transition upstream. The spanwise scale of the streaks did not vary appreciably with the FST length scale. Many aspects of their simulations are in qualitative agreement with Alfredsson & Matsubara (2001). Using flow visualizations, Brandt *et al.* (2004) conclude that streak breakdown and turbulent spot formation is caused by one of two instability modes of low speed streaks. The sinuous mode, characterized by streak oscillations in the spanwise direction was observed more frequently than the varicose mode, which was due to streak oscillation in the wall-normal direction. The authors noted that the transition mechanism due to streak instability may resemble the behaviour of streaks in turbulent boundary layers. Ovchinnikov, Piomelli & Choudhari (2004) use DNS to study the effect of inflow parameters on the onset of transition. They confirm the finding of Brandt *et al.* (2004) on the effect of the FST length scale and also show that by manipulating the FST spectrum one can significantly change the location of transition onset. They also suggest that including the leading edge

of the plate may be necessary for accurate transition prediction.

1.5 Wake/boundary-layer interaction

An additional class of transition scenarios arises in flow situations in which the boundary layer over a submerged body is impacted by unsteadiness generated by an upstream body. A boundary layer interacting with a wake of sufficient strengh may undergo a rapid and premature transition due to the ingestion of wake turbulence. In some instances, transition occurs in a boundary layer that would otherwise remain laminar for all time. Quintessential examples of such flows are wake/boundary layer interactions in turbomachinery and wake/boundary layer interactions in multi-element airfoils. These two examples differ from each other due to the large unsteady effects in the first case, and thus are discussed separately.

1.5.1 Unsteady interaction

In a turbine, stator vanes will be continuously affected by a velocity field contaminated by wakes from the blades on the upstream rotor. Since the rotor and the stator are in relative motion, a typical stator vane will be impacted by wakes at different chord locations on the suction side, in a manner dependent on the velocity of the rotor and on the number of rotor blades. Furthermore, during the periods when the vane is not in the path of an upstream wake, its external flow will be quiescent. Boundary layers on the moving rotor blades undergo a similar

interaction with the wakes from the stator vanes. Since the wakes impact the vanes intermittently (albeit periodically), this mode of wake/boundary-layer interaction is labeled unsteady. The axes of the wakes passing through the cascade channels are inclined to the blade walls, so that at different distances from the wall, the free-stream oscillates at a different phase.

Because transition to turbulence affects important design parameters such as drag, mixing, and heat transfer, the case of unsteady interactions in turbomachinery applications has received extensive study by experimentalists and theoreticians in the 1980's. Many results are summarized by Mayle (1991). We quote a few examples especially relevant to the current work. The geometry of a turbine and the physics involved lead to a very complex flow regime. A simplified geometry was studied by Herbst (1980) and Pfeil, Herbst & Schroder (1983). In these experiments, a 2D laminar boundary-layer was impacted by wakes generated by an array of cylinders mounted on a rotating squirrel cage. The velocity of the cylinders was approximately perpendicular to the plate at all times (directed towards the plate). In this manner, the effects of surface curvature and pressure gradient were separated from the effects of the wake. Pfeil *et al.* (1983) devised a conceptual model from their experiments as the number of mounted cylinders was varied. This model is summarized below.

Undisturbed flow undergoes natural transition according to the linear stability theory. When a turbulent spot arises, it is followed by a "becalmed" region of flow in which no additional turbulent spot can arise. When wakes are present, the laminar boundary layer is intensely disturbed. Turbulent spots form farther

upstream than in the undisturbed case, and are followed by similar becalmed regions. If the wake frequency is low enough, spots due to natural transition can also occur, but with a small enough cylinder spacing, natural transition can be prevented completely. Completion of transition in the disturbed case is actually farther downstream, because of the becalmed flow regions. When the cylinder spacing is reduced below a critical value, the wakes merge in the afflux, thus approximating a high-amplitude FST environment. In this case, the length of the transition region decreases markedly. The average velocity of the leading edge of the spots is higher than that of the trailing edge, leading to spot spreading and merger. While the start of the transition zone is the same for any number of cylinders, the end moves upstream with increasing passing freqency. At the highest frequency, transition was complete upstream of the start of the natural transition zone.

Basing their setup on that of Pfeil *et al.*(1983), Liu & Rodi (1991) conducted a similar experiment with the aim to study the detailed physics and provide reliable data on 2D wake-induced boundary-layer transition. Four separate experiments were conducted with 4, 8, 12 and 24 cylinders, respectively. Properties of the individual wakes were significantly altered by the arrangement of the cylinders and did not exhibit the spreading and decay of single wakes in unconfined surroundings. Contrary to the findings of Pfeil *et al.*, when the flow was undisturbed, natural transition was not observed. This discrepancy is probably due to differences in the background free-stream enviroment. The authors also report that the onset of turbulence moves upstream with increasing wake frequency, but stops moving when the

frequency is so high that the wakes merge near the plate leading edge. In this case, the rotating cage generates an approximation to FST. The intermittent passage of turbulent spots was accompanied by an increase in the boundary-layer u_{rms}, the displacement thickness and the ensemble-averaged velocity deficit, and a decrease in the shape factor. Even in those cases in which the u_{rms} and the mean free-stream velocity remained fairly uniform over a cycle, the displacement thickness and the shape factor varied significantly. There was also a slight phase lag between the regions of velocity deficit and high u_{rms}.

The unsteadiness was also studied in a Lagrangian frame of reference, *i.e.* with the measurements taken following laminar and turbulent patches of the flow. The boundary-layer regions underneath passing wakes were fully turbulent with the u_{rms} almost constant in space and a shape factor close to 1.5. Similarly, u_{rms} and the shape factor underneath laminar free-stream regions indicated a laminar boundary-layer; these laminar "stripes" became turbulent at the end of the test section for 8, 12, and 24 mounted cylinders, but not for 4. Velocity profiles were also measured and had a logarithmic profile for turbulent patches and a "shallow" profile for laminar ones. It was also concluded that upstream movement of transition onset was caused by wake disturbances and not by a local adverse pressure gradient associated with the wakes.

A detailed Direct Numerical Simulation (DNS) of transition due to passing wakes was recently performed by Wu, Jacobs, Hunt, and Durbin (1999). The flow configuration was very similar to the one used by Liu & Rodi (1991), except that

the velocity of the virtual cylinders was always normal to the plane of the plate (the flow around the cylinders was not computed, and the effect of their wakes was incorporated into the inflow boundary condition, hence the qualifier "virtual"). The inlet into the simulation domain was located downstream of the plate leading edge at $Re_\theta = 80$, and the inflow velocity consisted of a Blasius profile upon which a time-varying velocity field was superimposed to approximate the wakes. The wake-velocity field was obtained from a previous DNS of a plane wake, multiplied by the Blasius profile to bring the disturbance to zero at the wall. With 54 million grid cells inside the domain, Wu *et al.* (1999) were able to get a detailed view of the flow physics. The picture of transition agrees qualitatively with the experimental data of Liu & Rodi (1991). The transition scenario was characterized by the appearance of streaky disturbances in the u-velocity fluctuation, similar to the ones observed by Matsubara & Alfredsson (1996). When acted on by a free-stream eddy of a certain type, some streaks gave rise to turbulent spots. The authors indicated that the forcing by a free-stream eddy is crucial in the breakdown process *i.e.* the breakdown does not occur due to a streak instability *per se*. A typical turbulent spot looked similar to smoke visualization results of Zhong *et al.* (1998). Growing as it propagates downstream, the spot had an approximate reverse arrowhead shape. The authors proposed that the reason for a reversed and not a forward arrowhead shape is that in this case transition is top-down, *i.e.* starting at the top of the boundary layer, and not bottom-up (as in roughness-induced spots).

The onset of transition was defined as the region of sharp skin friction increase

(C_f). Amplitude of root-mean-square (rms) fluctuations in C_f was highest in the regions of high flow intermittency due to the passage of turbulent spots. In the fully- turbulent boundary-layer region, the flow statistics were in agreement with DNS data of Spalart (1988). The authors performed additional simulations (i) with the cylinder velocity reversed (*i.e.* the cylinders moving away from the plate) and (ii) with the mean wake deficit artificially set to zero (so that only the turbulent fluctuations were present). From these calculations, the authors concluded that the wake deficit of mean velocity profile has a strong influence on the phase-averaged C_f in the transition region. Removing the mean wake velocity profile and retaining only the fluctuations eliminated the difference in C_f between $U_{cyl} < 0$ and $U_{cyl} > 0$ cases (cylinders moving towards and away from the plate, respectively).

1.5.2 Steady interaction

The flow over a multi-element airfoil represents another type of wake/boundary layer interaction important for aerospace applications. Multi-element airfoils are used in situations where high lift is required, such as during aircraft landing and takeoff, so that the involved boundary layers are subject to adverse pressure gradients (APG) and are often on the verge of separation. With a wake passing near to and merging with the boundary layer, the modification of boundary-layer dynamics is important in airfoil design. The separation characteristics can be strongly influenced by the state of the boundary layer flow.

The reason for significant interaction between an airfoil slat wake and the boundary layer over the main body (wing) is tied to the optimal overall design of the multi-element configuration. The slat wake is initially away from the wing surface and does not merge with the boundary-layer until near mid-chord. This separation distance is due to the optimum gap between the slat and the leading edge of main wing. If this gap is reduced, there is earlier merging, which thickens the viscous layer, increasing the likelihood of separation upstream of the flap. If the gap is too large, the suction peak at the leading edge of the main element is increased, and an adverse pressure gradient leads to leading-edge separation.

The turbulence in the slat wake may be amplified by the presence of a "cove" on the pressure side of the slat, which is required for a snug fit in cruise conditions. The flow separates in the cove (although usually reattaches on the lower surface of the slat near the trailing edge), producing additional turbulence. While this example bears many similarities with wake/boundary-layer interactions in turbomachinery, there is no relative motion of airfoil components. This implies that the upstream wake will merge with the downstream boundary layer at a fixed chord location (in an ensemble averaged sense). Thus, the only unsteadiness present is in the dynamics of the wake itself. Consequently, such cases of wake/boundary-layer interaction are labeled steady (*i.e.* statistically stationary). Due to the absence of large unsteady effects, experiments and numerical simulations are typically easier to perform. A review of experimental and theoretical work prior to 1990 can be found in Squire (1989). Since this topic is directly relevant to the present research, several important

experiments (in simplified geometries) are reviewed below.

Zhou & Squire (1985) studied experimentally the interaction between an airfoil wake and a flat-plate boundary layer. They found that near the wall, the evolution of the wake is strongly modified by the boundary layer. The boundary layer shows a large momentum deficit in the outer core, but has the statistics of a turbulent boundary layer near the wall. The streamwise region of interaction could be divided into three parts. In the first, the wake and the boundary layer are separated by a potential core. In the second, the wake and the boundary layer begin to merge. Physically, this region is the most important and complicated. The flow in the overlap region (*i.e.* in the outer boundary layer and the outer wake) is completely different from that in an undisturbed boundary-layer flow. In the third, the merging is complete. The resulting boundary layer is thicker than that in undisturbed flow. This last stage may not be reached by the end of the airfoil.

In the initial part of the merging region, the region of negative shear stress ($-\overline{uv} < 0$) in the inner part of the wake was not completely eliminated (by the influence of the boundary layer, which has $-\overline{uv} > 0$). The location of zero shear stress did not coincide with the location of $d\overline{U}/dy = 0$, indicating questionable the validity of simple eddy viscosity models for turbulent simulations of the merging region. The speed of merging increased with increasing levels of turbulence in the wake. In an adverse pressure gradient (APG), the rate of lateral wake-spreading was faster, speeding up the interaction.

Savill & Zhou (1983) performed smoke visualization studies of wake/boundary-

layer interactions using cylinders, plates, and airfoils, mounted at different locations relative to a flat plate. The authors emphasize the differences between strong and weak types of interaction. If a wake retains its initial (vortical) coherence during its merger with the boundary layer, strong interaction is taking place. In this case, the boundary layer is likely to inherit some of the characteristics of the wake, *e.g.*, the wake-shedding frequency. This would be the mode of interaction if the wake-generating body were placed close to the boundary layer of interest. If, by the time the interaction takes place, the wake is incoherent, (that is, it approximates a free-stream turbulence [FST] environment), the a weak interaction is said to occur. An example of weak interaction would be a cylinder wake developing sufficiently far away from a boundary layer that the von Kármán vortex street has lost its dominant frequencies and turned into essentially chaotic flow.

The authors found that in the case of strong interaction between a cylinder wake and the boundary layer, an interchange of mushroom-shaped vortices between the wake and the boundary layer takes place. The cylinder wake was different from FST and had clearly organized structures and non-zero shear stress. Overall, the interaction region was dominated by the movement of large scale structures into the boundary layer, which transported shear stress of "opposite" sign (in turbulent boundary-layers $\overline{uv} < 0$, whereas in the the wake $\overline{uv} > 0$).

This phenomenon has been noticed in several previous works, for example by Bario, Charnay, and Papailliou (1982), who studied the wake created by a symmetrical airfoil interacting with the boundary layer of a longitudinally displaced airfoil

in an adverse pressure gradient. These authors found regions of "negative production," *i.e.* those in which $d\overline{U}/dy$ and $-\overline{uv}$ are of opposite sign. The authors provide the explanation that if an eddy that is formed from a boundary-layer ejection event travels from a region of positive mean velocity gradient (outer boundary-layer and outer half-wake) into a region of negative mean velocity gradient, the eddy transports with itself the turbulent properties generated in the outer boundary layer (such as $\overline{uv} < 0$). Thus, in a limited region of the inner half wake, in spite of the negative velocity gradient, $\overline{uv}$ remains negative. As mentioned before, this counter-gradient transport phenomenon invalidates those eddy viscosity models, in which the shear stress $-\overline{uv}$ is proportional to the mean velocity gradient.

Kyriakides, Kastrinakis, Nychas, and Goulas (1996) conducted an experimental investigation of boundary-layer transition due to a von Kármán vortex street behind a circular cylinder at Reynolds numbers in the range $385 \leq Re_D \leq 10,500$, based on the cylinder diameter. Various positions of the cylinder relative to the flat-plate leading edge were invesigated (spanning weak-to-strong regimes of interaction). In the absence of cylinder wakes, the boundary layer remained laminar, and with the wakes present, rapid transition was observed in nearly all cases. The onset of transition was identified from signals of the streamwise velocity inside the boundary layer. The amplitude of the initially sinusoidal signal (due to the coherence of the von Kármán street coherence) increased linearly as a function of the streamwise distance up to $x/D = 6.8$. The location at which the sinusoidal behavior disappeared was taken as the location of transition. This criterion gave some surprising results,

such as that for $Re_D = 385$, the onset of transition was observed at $Re_x = 2,625$. Typical plate Reynolds numbers (Re_x) of transition onset for bypass transition are O(10^5). Also, with this criterion, the values of the maximum boundary-layer u_{rms} achieved at position of transition onset, were smaller than 5%. The values of u_{rms} typical of boundary-layer bypass transition are above 10% (*e.g.* Matsubara & Alfredsson, 2001). The end of the transitional regime was defined as the location at which the wake has completely merged with the boundary layer. Similar to Zhou & Squire (1985), three distinct flow regions were observed: (i) the wake and the boundary-layer separated by a potential core, (ii) the region of merging, and (iii) the (thicker) confluent turbulent boundary layer region. The frequency of cylinder wake-shedding (Strouhal frequency) was present in the boundary-layer velocity signal at all experimental locations and its strength decayed with the streamwise distance. The secondary harmonic was also observed. This was a clear indication that the boundary layer is affected by the coherent dynamics of the wake.

By varying experimental parameters, Kyriakides *et al.* (1996) reported the following general trends: Increasing the frequency of shedding, the cylinder distance upstream of the leading edge and its vertical proximity to the plate, produces a decrease in the transition Reynolds number (upstream transition). Increasing the vertical distance from the plate has the opposite effect.

The work of Kyriakides *et al.* (1996) was continued in Kyriakides, Kastrinakis, Nychas, and Goulas (1999a,b). These publications provide additional details of case 12 ($Re_D = 3,500$) of the former paper, which corresponds to a cylinder location

of $(x/D, y/D) = (-1, 2.5)$, relative to the plate leading edge. Strong interaction of the cylinder wake with the boundary layer produced transition at $x/D = 3.3$ ($Re_x = 11,550$). Transition was complete by $x/D = 12$ ($Re_x = 42,000$). A spectral peak coresponding to the Strouhal frequency of the wake could be identified up to location $x/D = 17$.

The time averaged velocity profiles were used to compute contours of the streamfunction. The transitional region was characterized by a secondary vortical structure forming near the wall, directly beneath a passing Kármán vortex with negative vorticity (clockwise rotation). This secondary structure (with positive vorticity) was convected away from the wall with the streamwise distance. Based on $\overline{uv}$-, $\overline{u^2v}$-, and $\overline{v^3}$-contours, the authors concluded that during the passage of a primary votex with negative vorticity, turbulent energy is transferred to the boundary layer ($\overline{u^2v}$ and $\overline{v^3}$ are both negative) and during the passage of a vortex with positive vorticity, energy is transferred to the wake from the boundary layer (both $\overline{u^2v}$ and $\overline{v^3}$ are maximum and positive). The authors remark that the elongated streamwise structures reported in the studies of bypass transition due to FST, *e.g.* Westin *et al.* (1994), were not observed in their experiments.

From the examination of shear stress and mean velocity profiles inside the transtional region, the authors conclude that a region of negative energy production, similar to the one reported by Bario *et al.* (1982), exists in the region of overlap between the lower reaches of the wake and the upper region of the boundary layer. In this region, turbulence energy is transferred from the wake toward the wall.

Following Wallace, Eckelman, & Brodkey (1972), Kyriakides *et al.* (1999b) performed a quadrant splitting analysis of the negative production region and concluded that it is dominated by "interactions wallward," *i.e.* $u' < 0, v' < 0$, in contrast to ejections and sweeps ($u' < 0$, $v' > 0$ and $u' > 0$, $v' < 0$) found in turbulent boundary layers.

Doligalski, Smith, and Walker (1994) have reviewed the problem of vortex/wall interactions on a more fundamental level. When a spanwise vortex is convected parallel to (and sufficiently close to) a solid surface, a viscous response is generated in the near-wall flow. A vortex Reynolds number may be defined as $Re = \Gamma/2\pi\nu$, where Γ is the circulation. At a sufficiently high Reynolds number, a sequence of events initiates in the boundary layer that ends in an abrupt eruption of surface fluid and usually leads to the formation of a new upstream vortex structure. Such eruptions develop because any vortex in proximity to a wall induces an adverse pressure gradient on the boundary layer, in a frame of reference that moves with the vortex. Theoretical results (Elliott, Cowley, and Smith 1993, Cowley, Van Dommelen, Lam 1991) imply that steady motion at high Reynolds numbers is not possible under such circumstances and an abrupt erution is likely. It is initiated by a local concentration of the vorticity field within the boundary layer, which stimulates a rising "spire" of fluid that interacts strongly with the external flow. These spires contain vorticity and "roll up" into vortices. On the boundary-layer scale, eruptions appear as explosively growing spikes in the displacement thickness. These spikes have a thickness that approaches zero as $Re \to \infty$. On the scale of the external flow, the

event appears as a sharply focused concentration of vorticity near the surface about to eject into free stream.

Luton, Ragab & Telionis (1995) performed 2D numerical simulations of the early stages of interaction between a spanwise vortex and a boundary layer and confirmed the appearance of boundary-layer eruptions for primary vortices with large negative vorticity (*i.e.* clockwise rotation). The clockwise vortex induces upstream vorticity that erupts from the boundary layer and interacts inviscidly with the primary vortex. The experimental data of Kyriakides *et al.* is insufficient to decide whether the above mechanism plays a significant role in their work.

1.6 Aim of current study

In the previous section we reviewed selected works that show several paths to boundary-layer transition due to a disturbed free-stream environment. These paths are, no doubt, related: the case of transition due to wakes of moving compressor blades resembles FST-induced transition, in the limiting case of narrow wake spacing such that the wakes merge prior to reaching the affected stator vane. On the other hand, in the limit of zero velocity of the blades relative to the vanes, a case of steady (statistically stationary) interaction, analogous to the one encountered in multi-element airfoils, results. It is therefore natural to view the three broad categories of transition due to a highly disturbed free-stream (FST, unsteady and steady interaction) as complementary and overlapping. In particular, many observations

and findings regarding one scenario may also be valid for the other two.

In the past two decades, advances in numerical algorithms and computing hardware have made computer simulations of flows a powerful research tool. Direct Numerical Simulations (DNS), in particular, continue to provide data that are difficult or impossible to measure in an experiment, and enrich our understanding of fluid dynamics on a continual basis. Because of its current restriction to low Reynolds number flows, DNS is not a stand-alone prediction tool for high-Reynolds number flows of practical interest. Rather, DNS is an ideal tool for the discovery of new low-Reynolds-number physics. Careful generalization to high-Reynolds number flows promises improved predictions.

As shown in the works of Wu *et al.* (1999), Jacobs & Durbin (2001), and Brandt *et al.* (2004), DNS has done much to further our understanding of unsteady wake-induced and FST-induced transition. Good agreement with experiment in the second reference is especially encouraging. Our aim in this reasearch is to elucidate by DNS the physical mechanisms underlying steady wake/boundary-layer interaction (wake-induced transition) and to present our findings in the broader context of boundary-layer transition due to a disturbed free stream. The availability of a full 3D velocity field allows a high level of detail, similar to that found in the above references.

Our work may be naturally divided into two broad categories:

- Simulations of steady cylinder-wake-induced boundary-layer transition

- Simulations of FST-induced boundary-layer transition.

The first topic has not been previously studied by high-fidelity numerical simulations and therefore directly complements the works of Wu *et al.* (1999), Jacobs & Durbin (2001), and Brandt *et al.* (2004).

Investigations of the second topic were necessary to provide additional results on FST-induced transition and to answer some of the questions left open in previous studies. During the course of this research, high-accuracy DNS of FST-induced transition were performed, which for the first time computed the interaction of the turbulence with the leading edge of the flat plate.

Examination of the two transition scenarios was related to other experimental and numerical investigations, and represents a step towards a general understanding of boundary-layer transition.

Specifically, the accomplishments of this research are the following:

- the mechanism of boundary layer transition due to a steady interaction with cylinder wakes have been elucidated in a simplified geometry using statistical analysis and flow visualization

- the transition mechanism identified have been related to other studies of bypass transition

- a study on the applicability of widely-used inflow conditions for simulations of bypass transition due to FST has been performed. A strong sensitivity of transition location to *ad hoc* inflow parameters has been demonstrated

- well resolved DNS of FST-induced boundary-layer transition that include the effects of the leading edge region have peen performed with good agreement with experimental data

- the influence of the FST intensity and length scale on the location of transition onset has been investigated

- an alternative mechanism of boundary-layer transition due to FST of large length scale is discovered and studied in detail

Our investigations have provided answers to some questions, partial answers to others, and raised several more that should be addressed in future studies. The most important unanswered questions are:

- does the mechanism of steady wake-induced boundary-layer transition change fundamentally if the flow geometry is changed (minimally, if the location of the cylinder axis is shifted)?

- is this mechanism still dominant if free-stream turbulence is superimposed on the wake flow, as is the case in many aerodynamic flows?

- quantitatively, what is the effect of the leading edge geometry on the location of FST-induced transition onset? How sensitive is this dependence on the FST length scale and intensity?

- quantitatively, what is the effect of the FST length scale on the location of

transition onset? How sensitive is this dependence on the leading edge geometry and FST intensity?

- how do the answers to the above questions change with streamwise curvature and pressure gradient?

It is our belief that with time, answers to these complex and open-ended questions will lead to the long-awaited understanding of bypass transition in wall-bounded flows.

1.7 Organization

A summary of the numerical method used in the current simulations is presented in Chapter 2. The main body of this dissertation is comprised of four self-contained articles, two of which have been published in conference proceedings, the third is awaiting publication in the Journal of Fluid Mechanics, and the fourth is under review by the same journal. These articles are reproduced in chapters 3 through 6, each preceded by a foreword that explains the article's significance in the context of the entire thesis. When necessary, an article is followed by additional data and discussion. Each article contains its own complete list of references, and the entire bibliography is compiled at the end of the thesis. The articles that form the basis for this dissertation are, respectively,

1. Ovchinnikov, V. O., Piomelli, U., & Choudhari, M. M. Numerical

simulations of boundary-layer transition induced by a cylinder wake. *J. Fluid Mech. Accepted for publication.*

2. Ovchinnikov, V. O., Piomelli, U., & Choudhari, M. M. 2004 Inflow conditions for numerical simulations of bypass transition *AIAA Paper*, **2004-0591**.

3. Ovchinnikov, V. O., Piomelli, U., & Choudhari, M. M. Numerical simulations of boundary layer bypass transition with leading edge effects. In *Proc. 4th Int. Symp. Turbulence and Shear Flow Phenomena*, Williamsburg, Virginia, June 25-27, 2005, 425–430.

4. Ovchinnikov, V. O., Piomelli, U., & Choudhari, M. M. Numerical simulations of boundary-layer bypass transition due to high-amplitude free-stream turbulence. *J Fluid Mech. Submitted for publication.*

Chapter 7 summarizes key results and contributions and underscores several features of boundary-layer transition that appear common to the class of problems studied herein.

1.8 References

[1] Alfredsson, P. H. & Matsubara, M. 1996 Streaky structures in transition. In *Transitional Boundary Layers in Aeroacoustics* Henkes, R. A. W. M & Ingen, J. L. eds., 374–386

[2] Bayly, B.J., Orszag, S. A. & Herbert, T. 1988 Instability mechanisms in shear-flow transition. *Annu. Rev. Fluid Mech* **20** 359–392.

[3] Bennet, H. W. 1953 An experimental study of boundary layer transition. *Kimberley Clark Corp. Tech. Rep.*(prepared for Off. Nav. Res.), NEENAH, Wis.

[4] Blair, M. F. 1983 Influence of free-stream turbulence on turbulent boundary-layer heat transfer and mean profile development. Part I – Experimental data. *ASME J. Heat Transf.* **105** 33–40.

[5] Brandt, L., Schlatter, P. & Henningson, D. S. 2004 Transition in boundary layers subject to free-stream turbulence. *J. Fluid Mech.* **517**, 167–198.

[6] Buter, T. A.& Reed, H. L. 1994 Boundary layer receptivity to free-stream vorticity. *Phys. Fluids* **6** 3368–3379.

[7] Cowley, S. J., Van Dommelen, L. L., Lam, S. T. 1991 On the use of Lagrangian variables in descriptions of unsteady boundary-layer separation. *Phil. Trans. R. Soc. London Ser. A* **333** 343–78.

[8] Craik, A. D. D. 1971 Nonlinear resonant instability in boundary layers. *J. Fluid Mech.* **50** 393–413.

[9] Dietz, A. J. 1987 Boundary layer receptivity to transient convected disturbances. *AIAA Paper* **97-1962**.

[10] Doligalski, T. L., Smith C. R. & Walker, J. D. A. 1994 Vortex interactions with walls *Annu. Rev. Fluid Mech* **26** 573–616.

[11] Elliott, J. W., Cowley, S. J., Smith, F. T. 1983 Breakdown of boundary layers: (i) on moving surfaces; (ii) in self-similar unsteady flows; (iii) in a fully unsteady flow. *Geophys. Astrophys. Fluid Dyn.* **25** 77–138.

[12] Fasel, H. 1990 Numerical simulation of instability and transition in boundary layer flows. In *Laminar-Turbulent Transition* Arnal, D. & Michel, R., eds., Springer-Verlag, 578–598.

[13] Fransson, J. H. M., Matsubara, M. & Alfredsson, P. H. 2005 Transition induced by free-stream turbulence. *J. Fluid Mech.* **527** 1–25.

[14] Fransson, J. H. M. & Alfredsson, P. H. 2003 On the disturbance growth in an asymptotic suction boundary layer. *J. Fluid Mech.* **482** 51–90.

[15] Gaster, M. 1974 On the effects of boundary-layer growth on flow stability. *J. FLuid Mech.* **66** 465–80.

[16] Goldstein, M. E. 1983 The evolution of Tollmien-Schlichting waves near a leading edge. *J. Fluid Mech.* **127** 59–81.

[17] Goldstein, M. E. 1985 Scattering of acoustic waves into Tollmien-Schlichting waves by small streamwise variations in surface geometry. *J. Fluid Mech.* **154** 509–529.

[18] Goldstein, M. E. & Hultgren, L. S. 1987 A note on the generation of Tollmien-Schlichting waves by sudden surface-curvature change. *J. Fluid Mech.* **181** 519–525.

[19] Herbert, T. 1984 Analysis of the subharmonic route to transition in boundary layers. *AIAA Paper* **84-0009**.

[20] Herbert, T. 1985 Three-dimensional phenomena in the transitional flat-plate boundary layer. *AIAA Paper* **85-0489**.

[21] Herbert, T. 1987 On the mechanism of transition in boundary layers. *AIAA Paper* **87-1201**.

[22] Herbert, T. 1988 Secondary instability of boundary layers. *Annu. Rev. Fluid Mech* **20** 487–526.

[23] Herbst, R. 1980 Entwicklung von Grenzschichten bei instation arer Zustr omung. PhD Thesis, Technical University Darmstadt.

[24] Jacobs, G. J. & Durbin, P. A. 2001 Simulations of bypass transition. *J. Fluid Mech.* **428**, 185–212.

[25] Kachanov, Y. S. 1984 On the resonant nature of the breakdown of a laminar boundary layer. *J. Fluid Mech.* **184** 43–74.

[26] Kachanov, Y. S. 1990 Secondary and cascade resonant instabilities of boundary layers. Wave-resonant concept of a breakdown and its substantiation. In

Laminar-Turbulent Transition Arnal, D. & Michel, R., eds., Springer-Verlag, 65–80.

[27] Kachanov, Y. 1994 Physical mechanisms of laminar-boundary-layer transition. *Annu. Rev. Fluid Mech* **26** 411–482.

[28] Kachanov, Y. S., Kozlov, V. V., Levchenko, V. Y. 1977 Nonlinear development of a wave in a boundary layer. Transl. *Fluid Dyn.* 1978 **12** 383–90.

[29] Kachanov, Y. S., Kozlov, V. V., Levchenko, V. Y., Ramazanov, M. P. 1985 Experimental study of K-regime breakdown of laminar boundary layer. In *Laminar-Turbulent Transition* Kozlov, V. V. ed., Springer-Verlag, 61–73.

[30] Kachanov, Y. S., Kozlov, V. V., Levchenko, V. Y., Ramazanov, M. P. 1990 Transl. *Sov. J. Appl. Phys.* 1990 **4**.

[31] Kachanov Y. S. & Levchenko, V. Y. 1984 The resonant interaction of disturbances at laminar-turbulent transition in a boundary layer. *J. Fluid Mech* **138** 209–247.

[32] Kendall, J. M. 1985 Experimental study of disturbances porduced in a pretransitional laminar boundary layer by weak free stream turbulence. *AIAA Paper* **85-1695**.

[33] Kendall, J. M. 1990 Boundary-layer receptivity to freestream turbulence. *AIAA Paper* **90-1504**.

[34] Kendall, J. M. 1991 Studies on laminar boundary-layer receptivity to freestream turbulence near a leading edge. *Boundary Layer Stability and Transition to Turbulence*, Technical Report FED **114**, ASME.

[35] Klebanoff, P. S. 1971 Effect of freestream turbulence on the laminar boundary layer. *Bull. Amer. Phys. Soc.* **10**, 1323.

[36] Klebanoff, P. S., Tidstrom, K. D. & Sargent, L. M. 1962 The three-dimensional nature of boundary-layer instability. *J. Fluid Mech.* **12** 1–34.

[37] Kleiser, L. & Zang, T. A. 1991 Numerical simulation of transition in wall-bounded shear flows. *Annu. Rev. Fluid Mech.* **23** 495–537.

[38] Knapp C. F. & Roache, P. J. 1968 A combined visual and hot-wire anemometer investigation of boundary-layer transition. *AIAA J.* **6** 29–36.

[39] Kyriakides N. K., Kastrinakis, E. G., Nychas, S. G. & Goulas, A. 1996 Boundary layer transition induced by a von Karman vortex street wake. *Proc. Inst. Mech. Eng.* **210**, 167–179.

[40] Kyriakides N.K., Kastrinakis, E.G., Nychas, S.G., & Goulas, A. 1999a Aspects of flow structure during a cylinder-wake induced laminar/turbulent transition. *AIAA J* **37**, 1197–1205.

[41] Kyriakides N. K., Kastrinakis, E. G., Nychas, S. G., & Goulas, A. 1999 A bypass wakeinduced laminar turbulent transition. *Eur J. Mech. B-Fluid* **18**, 1049–1065.

[42] Lin, N., Reed, H. L., Saric, W.C. 1992 Effect of leading-edge geometry on boundary layer receptivity to free-stream sound. In *Instability, Receptivity, and Turbulence* Hussaini, M., Kumar, A., Streett, C., eds. Springer-Verlag, 421–440.

[43] Liu, X. & Rodi, W. 1991 Experiments on transitional boundary layers with wake-induced unsteadiness *J. Fluid Mech.* **231**, 229–256.

[44] Luton, A., Ragab, S. & Telionis, D. 1995 Interactions of spanwise vortices with a boundary layer. *Phys. Fluids* **7** 2757–2765.

[45] Matsubara, M. & Alfredsson, H. 2001 Disturbance growth in boundary layers subjected to free-stream turbulence. *J. Fluid. Mech.* **430**, 149–168.

[46] Mayle, R. E. The role of laminar-turbulent transition in gas turbine engines. *Trans. ASME: J. Turbomachinery* **113** 509–537.

[47] Morkovin, M. V. 1969 On the many faces of transition. In *Viscous Drag Reduction*, C.S. Wells, ed. Plenum, 1-31.

[48] Nayfeh, A. H. & Bozatli, A. N. 1979 Nonlinear wave interactions in boundary layers *AIAA Paper* **79-1456**

[49] Orr W. M. F. 1907 The stability or instability of the steady motions of a perfect liquid and a viscous liquid. *Proc. R. Ir. Acad. A* **27** 9–27, 69–138.

[50] Orszag S. A. & Patera, A. T. 1983 Secondary instability of wall-bounded shear flows. *J. Fluid Mech.* **128** 347–85.

[51] Pfeil, H., Herbst, R. & Schr oder, T. 1983 Investigation of laminar-turbulent transition of boundary layers disturbed by wakes. *Trans. ASME A: Engng for Power* **105** 130–137.

[52] Rai, M. M. & Moin, P. 1993 Direct numerical simulation of transition and turbulence in a spatially evolving boundary layer. *J. Comput. Phys.* **109**, 169–192.

[53] Rayleigh, Lord 1880 On the stability, or instability, of certain fluid motions. In *Scientific Papers of Lord Rayleigh*, Dover **1** 474–487.

[54] Rist, U. 1990 Numerische Untersuchtung der r aumlichen, dreidimensionalen St orungsentwicklung beim Grenzschlichtumschlag. PhD thesis. Inst. A Mech. Univ. Stuttgart

[55] Rist U. & Fasel, H. 1991 Spatial three-dimensional numerical simulation of laminar-turbulent transition in a flat-plate boundary layer. *Boundary Layer Trasition & Control Conf.* Cambridge, UK, R. Aeronaut Soc., 25.1–25.9.

[56] Rist, U. & Fasel, H. 1995 Direct numerical simulation of controlled transition in a flat-plate boundary layer. *J. Fluid Mech.* **298** 211–248.

[57] Roach, P. E., & Brierley, D. H. 1992 The influence of a turbulent free-stream on zero pressure gradient transitional boundary layer development part

I: test cases T3A and T3B. In *Numerical Simulation of unsteady flows and transition to turbulence*, O. Pironneau, W. Rodi, I. L. Rhyming, A. M. Savill and T. V. Truong, eds. Cambridge, 319–347.

[58] Saric, W. S., Carter, J. D. & Reynolds, G. A. Computation and visualization of unstable-wave streaklines in a boundary layer. *Bull. Am. Phys. Soc.* **26** 1252.

[59] Saric, W.S., Reed, H. L., & Kerschen, E. J. 2002 Boundary-layer receptivity to freestream disturbances. *Annu. Rev. Fluid Mech.* **34** 291–319.

[60] Savill, A. M. & Zhou Ming De 1983 Wake/boundary layer and wake/wake interactions – smoke flow visualisation and modelling. In *Proc. Second Asian Congress of Fluid Mechanics* 743–754.

[61] Schlichting, H. 1933 Zur Entstehung der Turbulenz bei der Plattenstromung. *Nachr. Ges. Wiss. G ottingen Math.-Phys. Kl.* **1933** 181–208.

[62] Schubauer, G. B. & Skramstad, H. K. 1947 Laminar boundary-layer oscillations on a flat plate *NACA Report 909*

[63] Sommerfeld, A. 1908 Ein Beitrag zur hydrodynamischen Erklarung der turbulenten Flussigkeitsbewegung. *Atti. Congr. Int. Math., 4th, Rome* 116–124.

[64] Spalart, P. R. & Yang, K. S. 1987 Numerical study of ribbon-induced transition in Blasius flow. *J. Fluid Mech.* **178** 345–65.

[65] Squire L. C. 1989 Interactions between wakes and boundary-layers. *Prog. Aerospace Sci.* **26**, 261–288.

[66] Thomas, A. S. & Saric, W. S. 1981 Harmonic and subharmonic waves during boundary-layer transition. *Bull. Am. Phys. Soc.* **26** 1252.

[67] Tollmien, W. 1929 Uber die Entstehung der Turbulenz. *Nachr. Ges. Wiss. G ottingen Math.-Phys. Kl.* **1929** 21–44

[68] Wallace, J. M., Elckelman, H. & Brodkey, R. S. 1972 The wall region in turbulent shear flow. *J. Fluid Mech.* **54** 39–48.

[69] Westin, K. J. A., Boiko, B. G. B., Klingmann, G. B., Kozlov, V. V., Alfredsson, P. H. 1994 Experiments in a boundary layer subjected to free stream turbulence. Part I. Boundary layer structure and receptivity. *J. Fluid. Mech.* **281**, 193–218.

[70] Wu, X., Jacobs, R. G., Hunt, J. C. R. & Durbin, P. A. 1999 Simulation of boundary layer transition induced by periodically passing wakes *J. Fluid Mech.* **398**, 109–153.

[71] Zhong, S., Kittichaikarn, C., Hodson, H. P. & Ireland, P. T. 1998 Visualization of turbulent spots under the unfluence of adverse pressure gradients. In *Proc. 8th Intl. Conf. on Flow Visualization, Italy.*

[72] Zhou, M. D. & Squire, L. C. 1985 The interaction of a wake with a turbulent boundary-layer. *J. Aeronaut.* **89**, 72–81.

Chapter 2

Numerical method

2.1 Governing equations

In the current investigation, we perform Direct and Large-Eddy Simulations (DNS and LES) of boundary-layer transition. The governing equations for DNS are the Navier-Stokes (NS) equations

$$\frac{\partial u_j}{\partial x_j} = 0, \tag{2.1}$$

$$\frac{\partial u_i}{\partial t} + \frac{\partial}{\partial x_j}\left(u_j u_i\right) = -\frac{\partial p}{\partial x_i} + \frac{1}{Re}\nabla^2 u_i + f_i, \tag{2.2}$$

written in a nondimensional form using the free-stream velocity U_∞ and an appropriate length scale L. In the wake/boundary-layer simulations, L was the cylinder diameter (D), and for simulations of FST-induced transition, either the half-thickness of the plate, or the boundary-layer thickness at a reference location. The resulting Reynolds number is defined as $Re_L = U_\infty L/\nu$. The presence of the body forces f_i ($\overline{f}_i$ in the case of LES) is due to the immersed boundary forcing, which models the effect of a submerged body (cylinder, or flat-plate leading edge) on the ambient fluid, as described in the last section of this chapter.

2.2 Numerical algorithm

Despite low convergence rates as the number of grid cells is increased, second-order central finite-difference (FD) formulations on staggered meshes ensure conservation of mass, momentum and kinetic energy in the discrete sense[1], reflecting the basic conservation properties of the Navier-Stokes equations. For this reason, 2^{nd}-order central schemes have been very popular in DNS and LES of incompressible flows, which require accurate representation of the smallest resolved scales of the flow. Additionally, the staggered arrangement is preferred to the collocated because it produces a physical pressure field by avoiding the even-odd decoupling problem inherent in collocated FD formulations (Ferziger & Peric 1998). Moreover, when the FD formulas that are 2^{nd}-order accurate for equispaced meshes are used on stretched meshes, the conservation properties remain unaffected, even though the order of accuracy may drop to somewhat below 2.0, depending on the degree of stretching. Consequently, such numerical schemes are well-suited for our problems, and a popular variant, implemented in our code, is described in detail below.

2.2.1 Spatial and temporal discretization

The formulation is based on the fractional-step method of Chorin (1968) and Kim & Moin (1985). The spatial derivatives are represented by second-order-accurate central finite-differencing (FD) on a staggered mesh. The arrangement

[1] In the limit of zero divergence, see Morinishi, Lund, Vasilyev & Moin (1998)

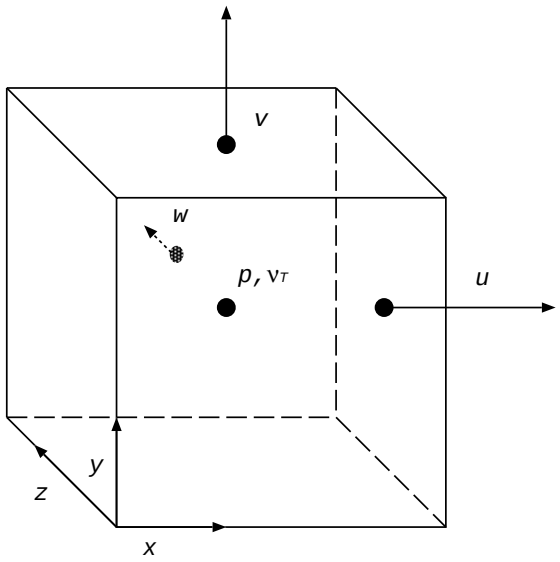

Figure 2.1: Staggered variable arrangement.

of the primitive variables is illustrated in figure 2.1. The three velocities u, v and w are defined on the cell face normal to the respective direction, and the pressure p and the turbulent viscosity (in the case of LES) ν_T, at the cell center.

The momentum equation for each velocity component u_i is advanced at the corresponding velocity node using the 2^{nd}-order (in time) Adams-Bashforth explicit method for both convective and viscous terms. The pressure at the last iteration (n) is also included:

$$\frac{u_i^* - u_i^n}{\Delta t} = \frac{3}{2}H_i^n - \frac{1}{2}H_i^{n-1} - \frac{\delta_2 p^n}{\delta_2 x_i}, \tag{2.3}$$

where

$$H_i^n = -\frac{\delta_2\left(u_i^n u_j^n\right)}{\delta_2 x_j} + \frac{1}{Re}\frac{\delta_2^2 u_i^n}{\delta_2 x_j \delta_2 x_j}, \tag{2.4}$$

$\frac{\delta_2}{\delta_2 x_i}()$ represents the second-order finite-difference approximation to the corresponding derivative, Δt is the time step, and the superscript n indicates the current in-

teration. The above equation yields a provisional "predicted" velocity u_i^*, which is not divergence-free. Mass conservation is applied indirectly in the "corrector" step:

$$\frac{u_i^{n+1} - u_i^*}{\Delta t} = -\frac{\delta_2 \left(\delta p^{n+1}\right)}{\delta_2 x_i} \tag{2.5}$$

Requiring the corrected velocity u_i^{n+1} to be divergence-free, *i.e.* $\delta_2 u_i^{n+1}/\delta_2 x_i = 0$, a relation for the pressure correction δp^{n+1} may be obtained:

$$\frac{\delta_2}{\delta_2 x_i}\left[\frac{u_i^{n+1} - u_i^*}{\Delta t}\right] = \frac{\delta_2}{\delta_2 x_i}\left[-\frac{\delta_2 \left(\delta p^{n+1}\right)}{\delta_2 x_i}\right] \Rightarrow \frac{\delta_2 u_i^*}{\delta_2 x_i} = \Delta t \frac{\delta_2^2 \left(\delta p^{n+1}\right)}{\delta_2 x_i \delta_2 x_i}. \tag{2.6}$$

Thus, the above correction step requires the solution of a Poisson difference equation for the pressure correction δp^{n+1}. This procedure is illustrated below. Expanding the discrete Laplacian produces

$$\frac{\delta_2 u_i^*}{\delta_2 x_i} = \Delta t \frac{\delta_2^2 \left(\delta p^{n+1}\right)}{\delta_2 x_i \delta_2 x_i} \qquad = \Delta t \left[\frac{\delta_2^2 \left(\delta p^{n+1}\right)}{\delta_2 x \delta_2 x} + \frac{\delta_2^2 \left(\delta p^{n+1}\right)}{\delta_2 y \delta_2 y} + \frac{\delta_2^2 \left(\delta p^{n+1}\right)}{\delta_2 z \delta_2 z}\right] \tag{2.7}$$

Since in our simulations the boundary conditions are periodic in the spanwise (z) direction, applying the discrete fast Fourier transform (DFFT) yields N_z uncoupled equations of the form:

$$\frac{\widehat{\delta_2 u_i^*}}{\delta_2 x_i} = \Delta t \left[\frac{\delta_2^2 \left(\widehat{\delta p}^{\,n+1}\right)}{\delta_2 x \delta_2 x} + \frac{\delta_2^2 \left(\widehat{\delta p}^{\,n+1}\right)}{\delta_2 y \delta_2 y} - \kappa_k^2 \widehat{\delta p}^{\,n+1}\right], \tag{2.8}$$

where N_z is the number of grid cells in the spanwise direction, $k \in [-N_z/2, N_z/2 - 1]$, $\kappa_k = 2\left(cos\left[2\pi k/N_z\right] - 1\right)/\Delta z$ is the modified wavenumber, $\widehat{(\,)}$ represents a Fourier amplitude coefficient for a given wavenumber, and the dependence on x, y, and κ_k is implied for all terms. Each Helmholz equation in the above system is solved by a cyclic reduction algorithm (Swarztrauber, 1974).

Once the pressure correction is calculated, the predicted velocity is updated using equation 2.5, and the pressure at timestep $n+1$ is obtained by

$$p^{n+1} = p^n + \delta p^{n+1}. \tag{2.9}$$

The timestep Δt is obtained in accordance with the CFL and viscous conditions, which require, respectively,

$$\Delta t \; max_i \left(\frac{|u_i|}{\Delta x_i} \right) \leq CFL, \quad \text{and} \tag{2.10}$$

$$max_i \left(\frac{\nu \Delta t}{\Delta x_i^2} \right) \leq \sigma. \tag{2.11}$$

To ensure numerical stability, CFL and σ were set to 0.3, and 0.25, respectively (Ferziger & Peric 2001).

2.2.2 Boundary conditions

The outflow condition for each simulation was based on the idea by Orlanski (1976). In this formulation, the following wave equation is solved at the most downstream grid node:

$$\frac{\phi^{n+1} - \phi^n}{\Delta t} = -U_{\text{conv}} \frac{\delta_1 \phi}{\delta_1 x}, \tag{2.12}$$

where ϕ is any of the three velocity components, U_{conv} is the average velocity across the most downstream plane, and $\frac{\delta_1}{\delta_1 x}()$ represents first-order accurate FD[2]. This convective treatment minimizes the reflection of pressure waves into the computational

[2]The overall second-order accuracy of the code is maintained even if the boundary treatment is first order.

domain, but its approximate nature does lead to modification of the flow field in a finite region near the outflow plane. For this reason, the results in the downstream 10%–15% of the computational domains were discarded in all of the simulations described herein.

The pressure boundary condition was periodic in the spanwise direction and homogeneous Neumann on all other boundaries.

The other boundary conditions were dependent on the specific problem. Chapters 3–6 are each preceeded by a section that explains the corresponding geometry and boundary conditions in detail.

2.3 Large eddy simulation

In large-eddy simulation, the flow field is separated into large (resolved) scales and small (subgrid) scales. Given a flow variable ϕ, the large-scale component is obtained using the filtering operation:

$$\overline{\phi}(x) = \int_{-\infty}^{\infty}\int_{-\infty}^{\infty}\int_{-\infty}^{\infty} \phi(x')\, G(x, x'; \Delta)\, dx', \tag{2.13}$$

where $G(x, x'; \Delta)$ is the filter kernel with filter width Δ, and x is a spatial coordinate.

Applying the filtering operation to the Navier-Stokes equations (2.1 and 2.2) and assuming that the filtering operation commutes with temporal and spatial dif-

ferentiation[3], one obtains the filtered NS equations:

$$\frac{\partial \overline{u}_j}{\partial x_j} = 0, \tag{2.14}$$

$$\frac{\partial \overline{u}_i}{\partial t} + \frac{\partial}{\partial x_j}\left(\overline{u}_j \overline{u}_i\right) = -\frac{1}{\rho}\frac{\partial \overline{p}}{\partial x_i} + \frac{1}{Re}\nabla^2 \overline{u}_i - \frac{\partial \tau_{ij}}{\partial x_j} + \overline{f_i}, \tag{2.15}$$

The term $\tau_{ij} = \overline{u_i u_j} - \overline{u}_i \overline{u}_j$ denotes the subgrid-scale (SGS) stress, which represents the effect of small (subgrid) scales on the resolved velocity field. In the present calculations, τ_{ij} was modeled using the dynamic eddy-viscosity model (DEVM) with Lagrangian averaging (Meneveau, Lund & Cabot 1996), which is an extension of the original DEVM with planar averaging (Germano, Piomelli, Cabot & Moin 1991). The essential idea behind DEVM with Lagrangian averaging is described below.

The anisotropic part of the SGS stress τ_{ij} is represented by an eddy-viscosity assumption:

$$\tau_{ij} - \frac{\delta_{ij}}{3}\tau_{kk} = -2\nu_T \overline{S}_{ij} = -2c_S^2 \Delta^2 \left|\overline{S}\right| \overline{S}_{ij}, \tag{2.16}$$

where δ_{ij} is the Kronecker delta tensor, $\left|\overline{S}\right| = \left(2\overline{S}_{ij}\overline{S}_{ij}\right)^{1/2}$, $\overline{S}_{ij}$ is the filtered rate-of-strain tensor, and c_S is a dynamic coefficient. The application of a second filter $G\left(\hat{x}, \hat{x}'; 2\Delta\right)$ (with twice the filter width) to the filtered NS equations, produces a subtest-scale stress defined as

$$T_{ij} = \widehat{\overline{u_i u_j}} - \widehat{\overline{u}}_i \widehat{\overline{u}}_j, \tag{2.17}$$

[3]True to second order accuracy. See Vasilyev, Lund & Moin (1998) for a discussion of commutation errors.

where $\widehat{()}$ stands for filtering at the 2Δ scale. The Germano (1992) identity states:

$$L_{ij} = T_{i,j} - \widehat{\tau}_{ij}, \tag{2.18}$$

where $L_{ij} = \widehat{\overline{u}_i \overline{u}_j} - \widehat{\overline{u}}_i \widehat{\overline{u}}_j$ is the stress due to flow scales intermediate between Δ and 2Δ, and can be computed directly from an LES flow field. Using the same eddy viscosity assumption to parameterize the subtest-scale stress (with twice the filter width), one obtains

$$T_{i,j} - \frac{\delta_{i,j}}{3} T_{kk} = -2\nu_T \overline{S}_{ij} = -2c_S^2 \left(2\Delta\right)^2 \left|\widehat{\overline{S}}\right| \widehat{\overline{S}}_{ij}. \tag{2.19}$$

The Germano identity requires

$$L_{ij} = 2\Delta^2 \left[c_S^2 \left|\overline{S}\right| \overline{S}_{ij} - 4c_S^2 \left|\widehat{\overline{S}}\right| \widehat{\overline{S}}_{ij}\right], \quad \text{or} \tag{2.20}$$

$$e_{ij} = L_{ij} - 2\Delta^2 \left[c_S^2 \left|\overline{S}\right| \overline{S}_{ij} - 4c_S^2 \left|\widehat{\overline{S}}\right| \widehat{\overline{S}}_{ij}\right] = 0. \tag{2.21}$$

The idea fundamental to the dynamic eddy-viscosity model, is to choose the value c_S in such a way that the error e_{ij} in the above identity is minimized in an appropriate average sense. The DEVM with Lagrangian averaging is based on error minimization along particle path lines. This choice is particularly well-suited to complex-geometry flows, in which planar averaging is precluded by the lack of homogeneous directions. The choice of error accumulation function used by Meneveau *et al.* (1996)[4] gives

[4]The total error is weighted towards recent events using a weight function that decays exponentially in time.

the following simple rules for the dynamic determination of c_S:

$$c_S^2 = \frac{\Upsilon_{LM}}{\Upsilon_{MM}}, \tag{2.22}$$

$$\frac{D\Upsilon_{LM}}{Dt} = \frac{1}{T}\left(L_{ij}M_{ij} - \Upsilon_{LM}\right), \tag{2.23}$$

$$\frac{D\Upsilon_{MM}}{Dt} = \frac{1}{T}\left(M_{ij}M_{ij} - \Upsilon_{MM}\right), \quad \text{and} \tag{2.24}$$

$$T = 1.5\Delta\left(\Upsilon_{MM}\Upsilon_{MM}\right)^{-1/8}. \tag{2.25}$$

The DEVM with Lagrangian averaging yields results that are slightly superior to the DEVM with planar averaging (for flows in which both averaging methods are applicable), but requires nearly twice the computational cost of an LES with no model (both in memory and in CPU time), because of explicit filtering at the test filter width. Furthermore, since the derivation of the dynamic model requires that both the grid filter and the test filter length scales correspond to the inertial range of the flow energy spectrum, for the transtitional and low Reynolds-number turbulent flows studied in this dissertation, the dynamic model does not significantly alleviate the resolution requirement of DNS.

Consequently, for many of our simulations, it proved more memory-efficient to increase the number of grid nodes and perform DNS instead of LES.

2.4 The immersed boundary method

Second-order finite-difference codes based on Cartesian geometries are appreciated for their speed, memory efficiency, and ease of use. These benefits come at a price: by virtue of their simple design, Cartesian codes are unable to han-

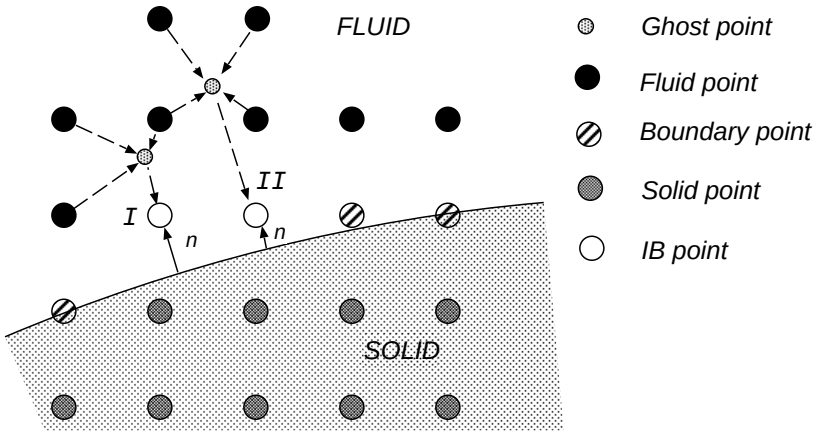

Figure 2.2: The immersed boundary method

dle complex geometries directly. Fortunately, an alternative, indirect treatment of complex boundaries has been developed, beginning with the pioneering work of Peskin (1972), who computed flow around heart valves using an "immersed boundary" method with a Cartesian-based code. Since that time, a large amount of literature has been published, investigating many variations of the original idea. A recent review is given by Mittal & Iaccarino (2005). In the following, we describe one particular formulation that has been validated in various flows, in conjunction with a second-order FD method, and was successfully used in our simulations. Our implementation follows Balaras (2004), who extended the work of Fadlun, Verzicco, Orlandi & Mohd-Yusof (2000).

In this method, the effect of a submerged object on the fluid is modelled by a set of discrete forces, imposed at the appropriate velocity locations. Conceptually, this procedure is illustrated in figure 2.2. The flow field is interrupted by a contour that represents the solid-fluid interface. Taking the (stationary) solid to be below the

line, the grid nodes are naturally divided into three categories: (i) nodes in the fluid region (unfilled and solid dots), (ii) nodes inside the body (shaded dots), and (iii) nodes located on the boundary to within a prescribed tolerance ϵ (striped dots). The immersed boundary procedure consists of imposing a force field at the fluid nodes adjacent to the solid boundary (unfilled nodes) or directly on the boundary (striped nodes) in such a way that the modified velocities are consistent with the proximity of the body.

In the context of our second-order code, the procedure is as follows: Let u^n denote the streamwise component of the velocity at node I in figure 2.2 at timestep n. To account for the force field, we have a modified equation for the predicted velocity, u^*:

$$\frac{u^* - u^n}{\Delta t} = \frac{3}{2}H_i^n - \frac{1}{2}H_i^{n-1} - \frac{\delta_2 p^n}{\delta_2 x} + f_i^n, \tag{2.26}$$

where H^n represents the discretized convective and viscous terms at timestep n, as before. Note that the force f^n is evaluated using information at timestep n, *i.e.* explicitly. If the desired fluid velocity at node I were known, *i.e.* $u^{n+1} = V$, the force could be approximated by setting $u^* = V$ in equation 2.26 as

$$f_i^n = -\frac{3}{2}H_i^n + \frac{1}{2}H_i^{n-1} + \frac{\delta_2 p^n}{\delta_2 x} + \frac{V - u^n}{\Delta t} \tag{2.27}$$

Upon substituting this equation into 2.26, it becomes obvious that the above application of forces is equivalent to modifying the predicted velocity u^* directly, *i.e.* setting $u^* = V$. For this reason, the above approach is called "direct forcing."

The modified predicted velocity field, which we denote by u^{**}, is made solenoidal

using a correction step identical to the one in equation 2.5 (for the streamwise component):

$$u^{n+1} = u^{**} - \Delta t \frac{\delta_2 \left(\delta p^{n+1}\right)}{\delta_2 x}, \tag{2.28}$$

with δp^{n+1} obtained by inverting the Poisson equation

$$\frac{\delta_2^2 \left(\delta p^{n+1}\right)}{\delta_2 x_i \delta_2 x_j} = \frac{1}{\Delta t} \frac{\delta_2 u_i^{**}}{\delta_2 x_i}. \tag{2.29}$$

Note that the formulation of the Poisson equation is unaffected by the presence of the forces, which implies that the correction step is allowed to modify the forced velocity field at the immersed boundary. Consequently, the corrected velocity u^{n+1} will be different from V. Fadlun *et al.* (2000), however, found that the modification of the immersed boundary velocities is negligibly small ($O\left(10^{-3} - 10^{-4}\right)$) relative to the velocity values themselves. More importantly, the many validations presented in their paper, along with those in Balaras (2004), demonstrate that the direct forcing treatment preserves the overall 2^{nd}-order accuracy of the code.

The remaining question concerns the determination of V. This process is illustrated in figure 2.2 in 2D for immersed boundary (IB) points I and II. In the direct forcing approach, V is obtained from bilinear interpolation using the prescribed velocity on the boundary and the predicted velocities at the fluid nodes adjacent to the IB nodes. First, the usual velocity prediction step is performed (2.3). For each IB point, a surface normal n passing through the point is then computed (for a stationary body, this step is performed once at the beginning of the calculation). The normal is repeatedly extended farther out into the flow field

by small increments Δh, until its end (the ghost point in figure 2.2) is inside a grid cell with three or four nodes in the fluid region. The velocity value at the ghost point is obtained using bilinear interpolation from the surrounding fluid nodes, and the velocity at the IB node, using linear interpolation from the ghost point and the point on the body that lies on the surface normal. This procedure applies only to nodes adjacent to the boundary on the fluid side of the interface. Inside the solid, the velocity and pressure are allowed to adjust freely. Their behavior in this region is unphysical and has no apparent influence on the fluid side.

Because we use a staggered spatial discretization (figure 2.1), the v and w velocity nodes are at different locations in space. Thus, the IB points of the v and w velocity components each use a different interpolation stencil. Other than this, the forcing procedure is the same as for the u component.

Finally, the IB forcing was also applied to Υ_{LM} in the case of LES, (in the numerator on the right-hand-side of equation 2.22) to ensure that the eddy viscosity ν_T approached zero at the solid boundary.

The direct forcing approach as described above is second-order-accurate, memory-efficient, and incurs negligible overhead, compared to the overall cost of computation. As such, it a valuable alternative to complex-geometry formulations. We remark that all of the simulations presented in this dissertation are fully explicit in time. However, when the viscous terms are computed implicitly, *e.g.* using Crank-Nicolson time advancement, the above forcing procedure should also be implicit. This involves a straightforward modification of the matrix that results from CN

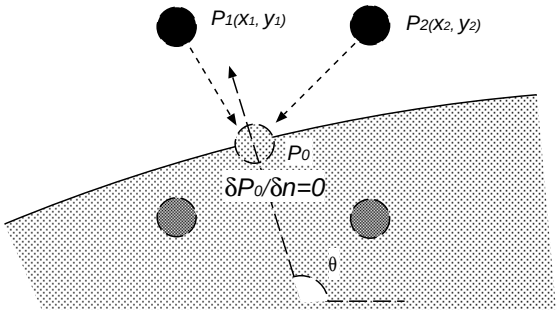

Figure 2.3: Pressure recovery

discretization and is described in Fadlun *at al.* (2000).

2.4.1 Pressure recovery

The pressure field on the submerged body was recovered using the linear reconstruction method described in Tseng & Ferziger (2003), illustrated in figure 2.3. This method requires pressure values at two fluid nodes and the normal pressure gradient at a surface point, which is assumed to be zero.

The pressure at the surface point $P_0\,(x,\ y)$ is given by

$$P_0 = a_0 + a_1 x + a_2 y, \tag{2.30}$$

where

$$\vec{a} = B^{-1}\phi, \quad \vec{a} = \begin{bmatrix} a_0 \\ a_1 \\ a_2 \end{bmatrix}, \quad B = \begin{bmatrix} 0 & \text{-sin}\,(\theta) & \cos\,(\theta) \\ 1 & x_1 & y_1 \\ 1 & x_2 & y_2 \end{bmatrix}, \quad \phi = \begin{bmatrix} \frac{\partial P_0}{\partial n} \\ P_1 \\ P_2 \end{bmatrix} \tag{2.31}$$

In the above, $(x_1,\ y_1)$ and $(x_2,\ y_2)$ are the coordinates of the two nodes in the fluid region, P_1 and P_2 represent the pressure at those nodes, and $\tan\,(\theta)$ is the

slope of the surface normal.

2.5 Code parallelization

The above algorithm was parallelized using the Message-passing interface (MPI). The computation is distributed between n processors (n was varied between 1 and 16 for the simulations described in this dissertation) in the following way. The flow domain is subdivided into n regions along the flow direction, with each region containing the same number of cells. Before the predictor step (equation 2.3), each processor receives velocity values from the two adjacent planes upstream and downstream as local "boundary conditions." Additional velocity values are transmitted if for some immersed-boundary nodes the interpolation stencil is outside the local domain. The Poisson equation 2.6 is solved efficiently by distributing the uncoupled Helmholtz problems equally among the n processors. This is the most communication-intensive step, as it requires that each processor receive a complete set of complex coefficients for a given spanwise wavenumber κ_k, which is initially scattered between the n processors. The subsequent inverse DFFT requires the reverse of this process. The above parallelization resulted in a nearly linear reduction in computational time as the number of processors n was increased from 1 to 16.

2.6 References

[1] Balaras, E. 2004 Modeling complex boundaries using an external force field on Cartesian grids in large-eddy simulations. *Comput. Fluids* **33**, 375–404

[2] Chorin, A. J. 1968 Numerical solution of the Navier-Stokes equations. *Math. Comput.* **22**, 742–762.

[3] Fadlun, E. A., Verzicco, R., Orlandi, P. & Mohd-Yusof, J. 2000 Combined immersed-boundary finite-fifference methods for three-dimensional complex flow simulations. *J. Comput. Phys.* **161**, 35–60.

[4] Ferziger, J. H. & Peric, M. 1998 *Computational methods for fluid dynamic* (Springer Verlag, Berlin Heidelberg).

[5] Germano, M. 1992 Turbulence: the filtering approach. *J. Fluid Mech.* **238** 325–336

[6] Germano, M., Piomelli, U., Moin, P. & Cabot, W. H. 1991 A dynamic subgrid-scale eddy viscosity model. *Phys. Fluids A* **3** 1760–1765

[7] Kim, J. & Moin, P. 1985 Application of a fractional step method to incompressible Navier-Stokes equations. *J. Comput. Phys.* **59**, 308–323.

[8] Meneveau, C., Lund, T. S. & Cabot, W. H. 1996. A Lagrangian dynamic subgrid-scale model of turbulence. *J. Fluid Mech.* **319**, 353–385.

[9] Mittal R., Iaccarino, G. 2005 Immersed Boundary Methods *Annu. Rev. Fluid Mech.* **37** 239–261

[10] Swarztrauber,P. N. 1974 A direct method for the discrete solution of separable elliptic equations. *SIAM J. Numer. Anal.* **11** 1136–1150

[11] Tseng, Y., Ferziger, J. H. 2003 A ghost-cell immersed boundary method for flow in complex geometry. *J. Comput. Phys.* **192** 593–623

[12] Vasilyev O. V, Lund, T .S, Moin, P. 1998 A general class of commutative filters for LES in complex geometries. *J. Comput. Phys.* **146** 82–104

Preface to Chapter 3

In the following article, "Numerical simulations of boundary-layer transition induced by a cylinder wake," we investigate the problem of statistically stationary wake/boundary-layer interactions in a simplified geometry. The wake-generating element is a circular cylinder, and the affected boundary-layer develops along a flat plate in a zero-pressure-gradient (ZPG) environment. The slat/main-body gap in a multi-element airfoil configuration is represented by the vertical distance from the cylinder axis to the leading edge (LE) of the plate. For the cases currently studied, this gap was kept fixed by setting the location of the cylinder axis at $(x, y) = (0, 3.5D)$ relative to the leading edge. Since the ultimate objective of this research is to improve transition prediction capabilities, we vary the flow Reynolds number over one order of magnitude (but still in the low Reynolds-number regime) for a fixed geometry, hoping that the physics that these simulations have in common will also be dominant at higher Reynolds numbers.

The cylinder-plate geometry was chosen for two basic reasons. First, the absence of curvature and streamwise pressure gradients along the plate isolates the effects of interaction with the vortical disturbances in the free stream. Second, both the ZPG boundary-layer flow and the flow past a circular cylinder have been extensively investigated in the past. This permits simultaneous code validation and comparison of interacting *vs.* noninteracting flow (*e.g.* boundary-layer disturbed by

wakes *vs.* buffeted or turbulent boundary layer in an undisturbed free stream).

In the current configuration, the boundary layer undergoes the three stages of evolution discussed in the introduction: (i) the wake and the boundary layer separated by a potential core, (ii) the merging/interaction region, and (iii) the fully-turbulent boundary-layer region. It is shown that the cylinder wake induces a rapid boundary-layer transition at sufficiently high Reynolds numbers, with many similarities to bypass transition due to FST.

The effect of the separation between the cylinder axis and the leading edge is not explicitly addressed, and should be the subject of a future study.

Chapter 3

Numerical simulations of boundary-layer transition induced by a cylinder wake[1]

3.1 Abstract

Direct and large-eddy simulations of the interaction between a laminar boundary layer and a von Kármán vortex street behind a circular cylinder are carried out for three values of the Reynolds number based on the cylinder diameter and free-stream velocity: $Re_D = 385$, 1155 and 3900. Rapid, bypass-like transition to turbulence is observed in the two higher Reynolds number cases. Flow statistics in the transitional and turbulent regions are examined, followed by an investigation of the underlying transition mechanism. Qualitative similarities between wake-induced transition and bypass transition due to free-stream turbulence are discussed and the challenges of predicting boundary-layer transition in this complex environment are pointed out.

[1]To be published as

Ovchinnikov, V. O., Piomelli, U. & Choudhari, M. M., 2005 Numerical simulations of boundary-layer transition induced by a cylinder wake. *J. Fluid Mech. Accepted for publication*

3.2 Introduction

High-lift systems have a significant impact on the overall cost and safety of aircraft. According to Meredith (1993), a 1% improvement in the maximum lift coefficient (or lift-to-drag ratio) could translate into an increased payload of 14 to 22 passengers on a large twin-engine transport airplane. An optimal aerodynamic design of a multi-airfoil high-lift configuration requires careful consideration of both inviscid and viscous flow phenomena. In particular, laminar-to-turbulent transition is a crucial issue for ground-to-flight scaling of high-lift flow fields.

The familiar transition mechanisms over a single isolated airfoil are also relevant to transition over the multi-element airfoil configurations encountered in high-lift applications. These include, respectively, transition due to one or more types of hydrodynamic instabilities (attachment line instabilities, streamwise instabilities in the form of Tollmien-Schlichting waves or Rayleigh modes, and crossflow vortex instabilities) or leading-edge contamination—a form of subcritical (*i.e.*, bypass) transition. An additional transition mechanism that is unique to multi-element airfoils involves boundary-layer contamination due to unsteady wakes of upstream elements or additional types of vortical disturbances originating from the separated cove flow beneath an upstream element. While the "single-element" class of transition mechanisms has been widely studied in the literature (see, for example, Kusunose & Cao 1994), the wake-contamination issue has received little scrutiny thus far and is the focus of this paper. Transition due to wake/boundary layer interaction is also known

to occur in turbine flows, where the interaction involves the wake of an upstream blade and the boundary layer of a downstream one. The transition process in this case is inherently unsteady. As the wake impinges on the downstream airfoil, a turbulent region analogous to a turbulent spot is formed locally, which travels in the boundary layer of the downstream blade and perturbs it. Wake/boundary-layer interaction over multi-element airfoils involves the wake of an upstream element that develops nearly parallel to the boundary layer on a downstream one. Wake induced transition in this case is due to a steady interaction in which the position of the wake and the resulting onset of transition remain fixed with respect to the boundary layer.

Most of the prior investigations of the interactions between turbulent wakes and boundary layers have concentrated on the unsteady case. The unsteady character of the impingement zone (which travels downstream in time) plays an important role in the dynamics of the flow, as shown by a number of investigators (see, for example, Liu & Rodi (1991), Wu, Jacobs, Hunt & Durbin (1999), and references therein). In contrast, the number of studies devoted to steady wake/boundary-layer interactions is much smaller. Squire (1989) summarizes many of the investigations conducted prior to 1989. Particularly important is the work by Zhou & Squire (1985), who examined the interaction between the wake of an airfoil and a flat plate. They found that a region in which the wake and boundary layer are separated by a potential core is followed by a merging zone. Across this zone the velocity profile in the outer part of the boundary layer is substantially different from that

in a regular flat-plate boundary layer. Zhou & Squire also observed that the positions of zero Reynolds shear stress and zero mean velocity gradient do not coincide, indicating that the Boussinesq approximation inherent in the scalar eddy viscosity models becomes suspect in such flows.

Kyriakides *et al.* (1996) performed experiments on boundary-layer transition induced by a von Kármán vortex street behind a circular cylinder. The cylinder was mounted above the plate, and the Reynolds number based on cylinder diameter was varied between 385 and 10,500. These authors reported transition for all Reynolds numbers and noted several interesting trends as the diameter of the cylinder and its location relative to the plate were varied. Unfortunately, their paper did not report turbulent statistics besides profiles of mean streamwise velocity and disturbance spectra at their lowest Reynolds number. More importantly from our standpoint, the transitional aspects of the boundary-layer flow were not investigated in detail.

In most wake/boundary-layer interaction scenarios, the wake is initially separated from the boundary layer and merges with it some distance downstream. The merging distance depends, of course, on the spreading rate of the wake and on the boundary-layer growth (*i.e.*, on the Reynolds number), as well as on the initial distance between the wake and the solid body. The shape of the body that forms the wake is also important: bluff body wakes are characterized by a von Kàrmàn vortex street that involves strong, coherent eddies (the spanwise "rollers"), along with "braid vortices" between the rollers. Wakes of airfoils or flat plates may or may not contain such coherent motions, depending, among other factors, on the sharpness of

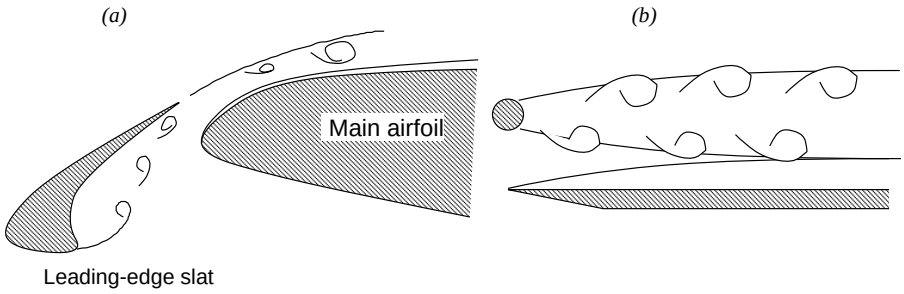

Figure 3.1: Sketch of *(a)* the multi-airfoil configuration and *(b)* the model problem.

the trailing edge, on whether the flow is attached or separated, etc. In the case of bluff body wakes, two types of interaction can be identified (Zhou & Squire 1985): a "strong interaction" case that occurs when the wake still contains coherent eddies in the interaction region, and a "weak interaction" one, in which the interaction takes place sufficiently far downstream of the cylinder that the spanwise rollers have decayed.

The present paper will focus on a numerical simulation of two element transition scenario in the simplified case of a cylinder placed above the leading edge of a flat plate; boundary layer-transition is induced by the wake generated by the cylinder. Because of the extensive prior studies pertaining to flat-plate and cylinder flows in isolation, the cylinder-plate combination is convenient yet retains the essential physics of realistic complex geometry cases. Furthermore, the experimental data of Kyriakides *et al.* (1996) can be used to validate the computational results to a limited extent. Two of the cases simulated here, $Re_D = 385$ and $Re_D = 1155$, were discussed by Kyriakides *et al.* (cases 1 and 2 in their paper). They also reported a case at $Re_D = 3,500$, close to the $Re_D = 3,900$ case studied herein.

The streamwise location of the cylinder axis is taken to be right above the leading edge of the flat plate. Our simulations begin upstream of the cylinder and the flat plate leading edge and extend into the fully turbulent region, thus including the entire domain of interest.

The present paper is organized as follows: First we present the numerical formulation, details of the configuration geometry, and the initial and boundary conditions. We then discuss flow validation and resolution studies. Next, we show and discuss the results, with an emphasis on the transition mechanism and transition prediction. We end with possible directions for future investigations.

3.3 Problem Formulation

In the present study we perform both direct- and large-eddy simulations of incompressible flow. In the case of direct numerical simulations (DNS), we solve the incompressible equations of conservation of mass and momentum:

$$\frac{\partial u_j}{\partial x_j} = 0, \tag{3.1}$$

$$\frac{\partial u_i}{\partial t} + \frac{\partial}{\partial x_j}\left(u_j u_i\right) = -\frac{\partial p}{\partial x_i} + \frac{1}{Re_D}\nabla^2 u_i + f_i, \tag{3.2}$$

while in the case of large-eddy simulation (LES), we use the filtered equations of motion:

$$\frac{\partial \overline{u}_j}{\partial x_j} = 0, \tag{3.3}$$

$$\frac{\partial \overline{u}_i}{\partial t} + \frac{\partial}{\partial x_j}\left(\overline{u}_j \overline{u}_i\right) = -\frac{\partial \overline{p}}{\partial x_i} + \frac{1}{Re_D}\nabla^2 \overline{u}_i - \frac{\partial \tau_{ij}}{\partial x_j} + \overline{f_i}, \tag{3.4}$$

where the overbar represents the filtered variables, and $\tau_{ij} = \overline{u_i u_j} - \overline{u}_i \overline{u}_j$ is the subgrid-scale stress (SGS), which in the present calculations was modeled using the dynamic eddy-viscosity model with Lagrangian averaging (Meneveau, Lund & Cabot 1996). The equations above have been made dimensionless using the free-stream velocity U_∞ and the cylinder diameter D. The resulting Reynolds number is defined as $Re_D = U_\infty D/\nu$. The presence of the body forces f_i is due to the immersed boundary method, described below.

The equations of motion are solved using a fractional step method (Chorin 1968, Kim & Moin 1985). We use a staggered-grid arrangement, with central approximations for all the derivatives and explicit Adams-Bashforth time advancement for the convective and diffusive terms. The method is second-order accurate in both time and space. Following the time advancement step, the predicted velocity field is made solenoidal by solving the Poisson equation for the pseudo-pressure[2] and correcting the predicted velocities with the pseudo-pressure gradient. The method fully conserves mass, momentum, and energy in the discrete sense (see Morinishi, Lund, Vasilyev & Moin 1998). The coordinates x_1, x_2, and x_3 (or, interchangeably, x, y and z) refer, respectively, to the streamwise, wall-normal and spanwise velocity directions. The grid is uniform in the spanwise direction and stretched in the streamwise and wall-normal directions to ensure adequate resolution within the boundary layer (particularly in the transitional region) and the convecting cylinder wake. The code has been extensively validated for a variety of turbulent and relam-

[2]Equal to the actual pressure to second-order accuracy.

inarizing flows (Balaras, Benocci & Piomelli 1995; Piomelli, Balaras & Pascarelli 2000; Balaras, Piomelli & Wallace 2001).

The above algorithm was parallelized using the Message-Passing Interface (MPI). The computational box is divided into n equal subdomains in the flow direction and each of the n processors integrates the equations of motion in one of the subdomains. The pseudo-pressure field is obtained by applying a spanwise Fast Fourier Transform (FFT) to the discrete Poisson equation. This yields a pentadiagonal matrix for each Fourier mode, which is then inverted by a cyclic reduction algorithm. Each processor is assigned a subset of the Fourier modes resulting from the application of FFT.

The Cartesian computational grid does not conform to the cylinder body. To satisfy the no-slip boundary conditions at the cylinder surface, we employ the immersed boundary method of Fadlun, Verzicco, Orlandi & Mohd-Yusof (2000), following the implementation of Balaras (2004). In this procedure the body forces f_i or $\overline{f}_i$ are non-zero only in grid cells near the cylinder surface and are assigned in such a way that the velocity on the cylinder surface is zero to second-order. When the predicted velocity is projected onto a divergence-free field, the velocity perturbations that are introduced in the vicinity of the cylinder are small (Fadlun *et al.* 2000), so that the corrected velocity is also second-order accurate around the cylinder body. Finally, we note that in the case of explicit time advancement, calculating and including a force field in the momentum equations is equivalent to modifying the predicted velocities directly. The immersed boundary method, as

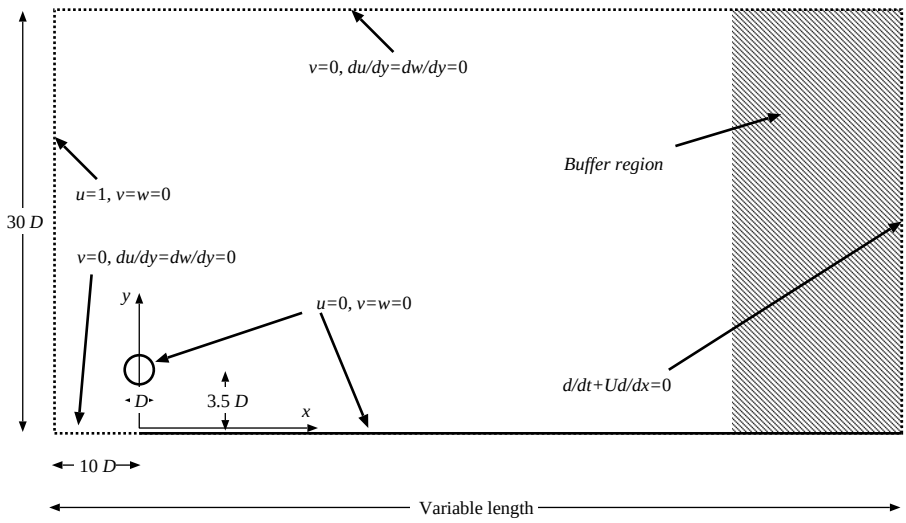

Figure 3.2: Computational configuration and boundary conditions.

described above, has been extensively validated in laminar and turbulent flows in the references mentioned above. For further validation in the specific context of interest, we also performed an LES of the flow past a circular cylinder at $Re_D = 3900$, which will be described in Section 3.

3.3.1 Initial and boundary conditions

Figure 3.2 shows a sketch of the computational configuration and boundary conditions. All our calculations start ten cylinder diameters upstream of the flat-plate leading edge. On the lower side of the domain, ahead of the leading edge of the plate, we apply free-slip conditions ($\partial u/\partial y = \partial w/\partial y = 0$, $v = 0$), whereas we apply no-slip conditions on the plate. In order to avoid the numerical difficulties associated with modeling a sharp leading edge (*i.e.*, the possibility of numerical instabilities due to the sudden change from the homogeneous Neumann to the Dirichlet conditions),

we merged the two conditions smoothly over a length $x \simeq 8$ using a hyperbolic tangent function. Since the flow around the leading edge is slowed down gradually rather than suddenly, the above merging approximates modeling a finite thickness leading edge. We verified that the mean velocity profiles sufficiently far downstream of the leading edge asymptote to the Blasius solution.

Along the free-stream boundary, we imposed free-slip conditions. This boundary condition does not allow outflow through the top side of the domain, causing the flow above the boundary layer to accelerate in order to compensate for the boundary-layer growth. In our simulations, the acceleration parameter due to this effect, $K \equiv -(\nu/U_\infty^2)(dU_\infty/dx)$, was of the order of 10^{-7}. The value of K at which a turbulent boundary layer is expected to relaminarize is around 3.0×10^{-6} (Spalart 1986). Since in our case, K is an order of magnitude lower, we do not expect the acceleration to affect transition significantly.

The inlet condition consisted of a uniform streamwise velocity profile. At the outflow we imposed non-reflecting boundary conditions (Orlanski 1976). Simulation results in the last 15% of the domain were discarded because of the proximity of the outflow boundary. Since the grid was stretched significantly in this region, however, only about 7% of the grid cells were wasted. In the spanwise direction, z, periodic boundary conditions were used.

The three calculations performed in this work required substantial computational resources, especially those at $Re_D = 1155$ and $Re_D = 3900$. The computational expense was necessary to resolve properly the boundary-layer leading edge,

the cylinder wake, and the transitional region of the boundary layer, which is known to be sensitive to the grid resolution (Jacobs & Durbin 2001; Ovchinnikov, Piomelli & Choudhari 2004). Therefore, two overlapping computational domains were used in the above two cases to minimize the computational resources required. The first box contained the cylinder and the flat-plate leading edge and had very fine resolution near the wall and near the cylinder surface (to allow accurate implementation of the immersed boundary method) as well as in the shear layers emanating from the cylinder separation. Some distance downstream of the cylinder, where the plate boundary layer is thicker and the smallest scales within the cylinder wake have grown in size, the wall-normal resolution requirement could be relaxed. At this location, a time sequence of planes of velocity was stored and used as the inflow condition for a second computational domain that had fewer points in the wall-normal direction, but maintained the fine streamwise resolution required to resolve the transition zone (Jacobs & Durbin 2001, Ovchinnikov *et al.* 2004). The multi domain aproach has been used by researchers in the past with good success (Rai & Moin 1993, Huai, Joslin & Piomelli 1997). However, strictly speaking, it violates the ellipticity of the incompressible Navier-Stokes (NS) equations. To estimate the magnitude of the errors, we performed two DNS of the flow past a circular cylinder at $Re_D = 3900$. In the first, the computational domain was inside a single box spanning $x = -10D$ — $8D$, and in the second, it was split between two boxes spanning $x = -10D$ — $4.7D$, and $x = 4.7D$ — $8D$, respectively. The cylinder axis was located at $(x, y) = (0D, 15D)$ and the wall-normal domain was $30D$. The

wall-normal domain had 352 cells in the first simulation and the first box of the second simulation, and 232 cells in the second box of the second simulation. Linear interpolation was used to transfer the velocity from the outflow plane of the first box to the inflow plane of the second box. The resolution was in accordance with the validation study presented in the next section. The simulations were started from the same initial field and advanced synchronously. This permitted comparisons of instantaneous as well as time-averaged fields. For the two simulations, contours of the instantaneous velocity were almost indistinguishable in the region $x = 4.7D$ — $8D$. The maximum deviation in the mean velocity in this region was 4%, and the streamwise Reynolds stress $\langle uu \rangle$ was underpredicted by at most 8% in the two-box simulation. This mild underprediction is expected since linear interpolation used to transfer the velocity field is dissipative. Overall, the error incurred by the multi domain approach seems justified by the 34% savings in computational time.

Despite the reduced cost of the split domain approach, the simulations required a total of 65 and 80 million points for the $Re_D = 1155$ and $Re_D = 3900$ cases, respectively. In order to obtain converged statistics, each case required a total CPU time of 300–400 hours per processor on an 8-processor Pentium 4 cluster.

The initial condition for the low Reynolds number calculation ($Re_D = 385$) was a uniform velocity profile throughout the entire domain. For the first box of the higher Reynolds number calculations, the initial condition was obtained by interpolating the converged velocity field from a lower Reynolds number calculation. For the second box, a Blasius boundary-layer solution with the appropriate boundary-layer

thickness at the inlet (obtained from the first box) was used as initial condition.

3.3.2 Simulation Parameters

The flat-plate leading edge was located at $x = 10$ on the bottom boundary, and the cylinder axis at $x = 10$, $y = 3.5$ for all simulations (as mentioned above, all lengths are made dimensionless by the cylinder diameter D), as shown in figure 3.2. Table 3.1 summarizes the simulation parameters. The computational domain for the $Re_D = 385$ case was a rectangular box of dimensions $L_x \times L_y \times L_z = 150 \times 20 \times 2\pi$. For the $Re_D = 1155$ case, the first box had dimensions $100 \times 20 \times 2\pi$; cross-stream planes were extracted at location $x = 60$, interpolated onto the wall-normal mesh of box 2, and fed into a second computational box of dimensions $115 \times 20 \times 2\pi$. With respect to the flat-plate leading edge, the useful region of the calculation, therefore, extended from $x = -10$ to $x = 150$ (the last 15 units of the second domain are discarded because the grid stretching results in excessive coarseness of the mesh in this region, and the effect of the outflow boundary conditions alters the flow physics). For the $Re_D = 3900$ case, the first box had dimensions $30 \times 20 \times 2\pi$; cross-stream planes were extracted at $x = 17.3$ and fed into a second box of dimensions $60 \times 20 \times 2\pi$. For the highest Reynolds number simulation, the computational domain could be shorter because transition takes place closer to the leading edge than in the other cases. As will be shown, in the $Re_D = 1155$ case transition begins in the first box and completes in the second box, while in the $Re_D = 3900$ case, the

Case	Re	Method	$L_x \times L_y \times L_z$	$nx \times ny \times nz$
1	385	DNS	$150 \times 20 \times 2\pi$	$1128 \times 192 \times 48$
			$100 \times 20 \times 2\pi$ (useful)	
2	1155	LES	$100 \times 20 \times 2\pi$ (box 1)	$1056 \times 384 \times 128$ (box 1)
			$115 \times 20 \times 2\pi$ (box 2)	$624 \times 200 \times 128$ (box 2)
			$160 \times 20 \times 2\pi$ (useful)	
3	3900	DNS	$30 \times 20 \times 2\pi$ (box 1)	$608 \times 448 \times 160$ (box 1)
			$60 \times 20 \times 2\pi$ (box 2)	$1168 \times 310 \times 160$ (box 2)
			$58 \times 20 \times 2\pi$ (useful)	

Table 3.1: Simulation parameters.

transition process is entirely confined to the second box.

The governing equations were advanced in time until a steady state was reached, statistics were then accumulated for a period of 130–150 dimensionless time units (25-30 wake shedding cycles). Convergence of the statistical sample was verified by comparing the statistics obtained using only half of the sample with those obtained using the entire sample. First-order quantities differed by less than 1%, second moments by less than 5%.

Method	Re	$\Delta x^+_{\max}$	$\Delta y^+_{\max}$	$\Delta z^+_{\max}$
DNS	385	7.0	0.25	3.0
LES	1155 (box 1)	10.0	0.21	2.8
LES	1155 (box 2)	12.0	1.0	3.1
DNS	3900 (box 1)	4.0	0.3	6.0
DNS	3900 (box 2)	10.5	0.9	7.0

Table 3.2: Largest grid size in viscous units ($\Delta^+(x) = \Delta(x) \cdot u_\tau(x)/\nu$) near the flat plate.

3.4 Grid requirements

In order to ensure the accuracy of our calculations, we needed to establish separate grid resolution requirements for the evolving boundary layer and the cylinder wake. The grid requirements for the simulation of turbulent boundary layers using 2nd-order accurate central difference schemes are well known ($\Delta x^+ \simeq 15$, $\Delta y^+_{\min} < 1$, $\Delta z^+ \simeq 6$ for DNS, $\Delta x^+ \simeq 50$, $\Delta y^+_{\min} < 1$, $\Delta z^+ \simeq 20$ for LES) and were easily achieved in the fully turbulent region. Table 3.2 shows the largest grid size in wall units for all the calculations.

For transitional flows, the grid requirements are less well established. However, the results presented in this paper will show that the phenomenon of wake induced transition is analogous to bypass transition due to free-stream turbulence (FST). Accordingly, the computational grids used in the present study were based on previ-

ous work related to FST-induced transition (see Jacobs & Durbin 2001; Ovchinnikov *et al.* 2004). As argued in these references, boundary-layer bypass transition is especially sensitive to streamwise resolution. Ovchinnikov *et al.* (2004) show that an excessively coarse streamwise grid compromises the evolution of the turbulence spots characteristic of boundary-layer bypass transition (Jacobs & Durbin 2001; Ovchinnikov *et al.* 2004; Brandt, Schlatter & Henningson 2004), and that under-resolved calculations predict a premature and abrupt transition. In all of our simulations, the streamwise grid spacing was under 12 viscous units throughout the transition region, which is sufficiently fine according to Jacobs & Durbin (2001).

To verify the grid resolution requirements in the vicinity of the cylinder, we first examined the two extreme cases, $Re_D = 385$ and 3900. For the low Reynolds number case, $Re_D = 385$, near cylinder resolution was the same as that used by Balaras (2004), who validated the immersed boundary method for the flow past a circular cylinder at $Re_D = 300$ against reference simulations based on boundary conforming grids. The two Reynolds numbers are sufficiently close that using the same resolution is justified.

For the high Reynolds number case, we performed DNS and LES of the flow past a circular cylinder at $Re_D = 3900$ and compared our results with the DNS data of Kravchenko & Moin (2000). For the LES we used a computational box of dimensions $L_x \times L_y \times L_z = 30 \times 30 \times \pi$ (with the same spanwise dimension of the domain used by Kravchenko & Moin 2000), which was discretized on a $496 \times 352 \times 80$ grid. The cylinder was located at $x = 10$, $y = 15$. A DNS simulation on the same

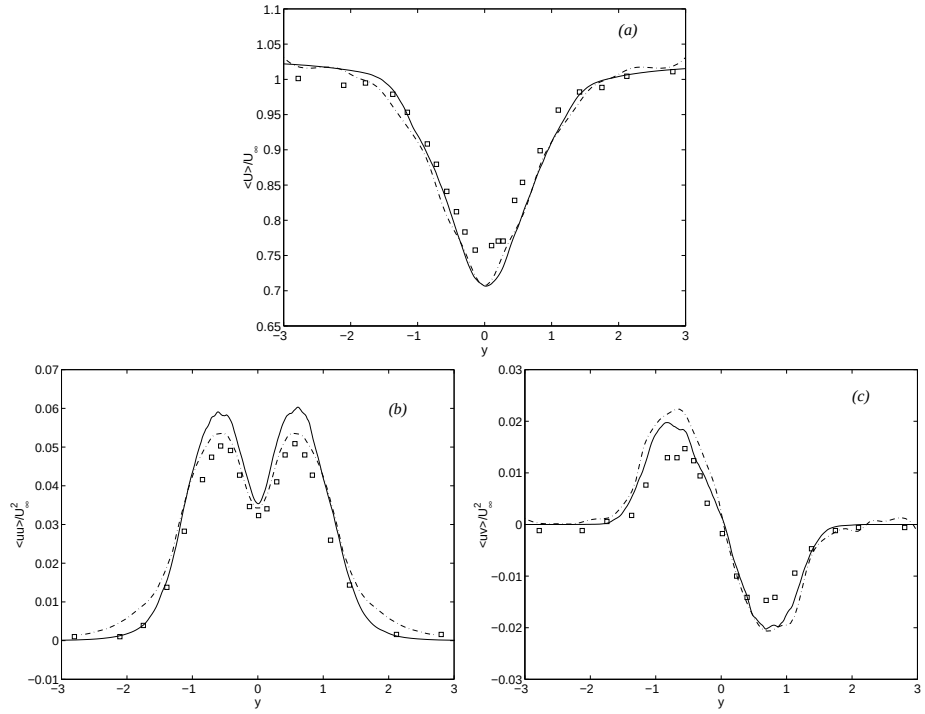

Figure 3.3: Profiles of *(a)* streamwise velocity, *(b)* streamwise Reynolds stress $\langle u'u' \rangle$, *(c)* Reynolds shear stress $\langle u'v' \rangle$ across the cylinder wake at $x = 4$; —— present LES; □ Experiment (Ong & Wallace 1996); -·-· DNS (Kravchenko & Moin 2000); $Re_D = 3900$

domain but using a $608 \times 352 \times 80$ grid (with slightly higher concentration of wall-normal points near the cylinder), produced nearly the same results as the LES. In both cases the average spacing between adjacent points near the cylinder was 0.015 and 0.011 in the LES and DNS cases, respectively. Free-slip conditions were applied on the top and bottom boundaries, the inlet condition was a uniform streamwise velocity profile, and at the outflow, a non-reflecting convective outflow condition was used (Orlanski 1976). While the simulations of Kravchenko & Moin (2000) are performed using boundary conforming cylindrical grids and a numerical method based on B-splines, our code is based on a rectangular Cartesian grid and uses the immersed boundary method to represent the cylinder; for this reason we cannot match our grid resolution directly to theirs. To ensure a comparable resolution, however, we required the number of immersed boundary points (the points just outside the cylinder surface at which forces are applied to mimic the presence of the body) to be no less than the number of points lying on the cylinder surface in the azimuthal direction in their final grid. In our validation case, we used 210 immersed boundary points along the cylinder countour compared with 185 surface points used by Kravchenko & Moin (2000). At this resolution we obtained very good agreement with their results. Figure 3.3 presents a comparison of the mean velocity and the streamwise and shear Reynolds stress profiles at $x/D = 4$ from our simulation with the DNS of Kravchenko & Moin (2000) as well as experiments of Ong & Wallace (1996)[3] Increasing further the number of immersed boundary points

[3]The pressure coefficient $C_p = 2\left(p - p_\infty\right)/U_\infty^2$ is shown in the addendum.

to 255 produced no change in the simulation statistics (not shown). With the $Re_D = 385$ and 3900 cases validated and the near cylinder resolution known for the two cases, we estimated the near cylinder resolution necessary to ensure accuracy in the $Re_D = 1155$ case. This was done by assuming that the thickness of the laminar boundary layer attached to the cylinder decreases with $\sqrt{Re_D}$, which implies that the $Re_D = 1155$ simulation requires approximately half the near cylinder resolution of the $Re_D = 3900$ case. For further confidence in the $Re_D = 1155$ results, we also performed the first box of the $Re_D = 1155$ simulation of wake/boundary-layer interaction on a coarser grid, which used only $816 \times 288 \times 96$ to discretize the first box and had 30% fewer points in each direction in the near cylinder region. The results of the two simulations were in good agreement, indicating that the fine grid is more than sufficient to resolve the important eddies in the transition region and in the wake.

For the actual $Re_D = 3900$ wake/boundary-layer simulation, we used the same near cylinder resolution as described above for the validation case. The validity of the laminar boundary-layer solution upstream of the transition region was confirmed by observing agreement with the Blasius solution sufficiently far from the leading edge (where the integral quantities such as displacement and momentum thickness and shape factor matched the analytical solution to within 1%). At the streamwise location of transition onset ($x = 20$), the boundary layer was resolved with 50 wall-normal grid cells. Throughout the transitional and turbulent regions, the first wall-normal point was always below $y^+ = 1$. For the $Re_D = 1155$, we ensured that

the near-wall region was similarly resolved.

Finally, we examined spanwise two-point correlations of velocity fluctuations to verify that the spanwise size of the computational domain was sufficient for the fuctuations to become decorrelated. Starting from the onset of transition, the correlation in the two velocity fluctuation components decays rapidly to zero, except near the wake centerline, where some spanwise coherence due to the von Kármán street is present throughout the domain. Upstream of the transitional region, the correlation plots remained oscillatory across the boundary layer, which was due to pronounced streamwise streaky structures existing prior to transition. Some of these observations are illustrated in figure 3.10, which is discussed in the section on the transition mechanism.

3.5 Results

3.5.1 Flow Development

This section presents an overview of our results for the three Reynolds number cases considered. Most of the emphasis is placed on the evolution of various flow metrics from the laminar into the turbulent regimes. An examination of the receptivity mechanism and laminar breakdown is deferred until the next section.

As stated previously, the simulations at $Re_D = 385$ and 3900 were treated by DNS, while in the intermediate Reynolds number simulation the SGS model was included. However, the eddy viscosity was significant only in the near wake

of the cylinder (where small scales are generated by the shear-layer instability) reaching maximum values of approximately 1.2 times the molecular viscosity. The grid resolution in the boundary layer was fine enough that the eddy viscosity in that region was negligible, and the transition calculation was effectively a DNS.

In the following, we define time-averaged quantities as

$$F = \langle f \rangle = \frac{1}{L_z}\frac{1}{T}\int_o^{L_z}\int_{t-T}^{t} f(x,y,z,\tau)d\tau dz. \tag{3.5}$$

The integration period, T, was equal to approximately 25 shedding periods and was sufficient to ensure statistical convergence of the data presented herein, as mentioned above.

In our discussion, we will emphasize several the streamwise evolution of statistical flow quantities across the region of laminar-turbulent transition. The skin friction coefficient

$$C_f = \frac{\tau_w}{\rho U_\infty^2/2} \tag{3.6}$$

(where τ_w is the time-averaged wall stress), is an indicator of transition onset since it increases markedly across the transition region. The shape factor $H \equiv \theta/\delta^*$, where the displacement thickness δ^* and momentum thickness θ are defined as

$$\delta^* = \int_0^{y_{\text{edge}}} \left(1 - \frac{\langle U \rangle}{U_{\text{edge}}}\right) dy; \qquad \theta = \int_0^{y_{\text{edge}}} \frac{\langle U \rangle}{U_{\text{edge}}}\left(1 - \frac{\langle U \rangle}{U_{\text{edge}}}\right) dy. \tag{3.7}$$

The shape factor is equal to 2.6 in Blasius flow and ranges from 1.3 to 1.4 in turbulent flow. It is an inverse measure of the boundary-layer momentum, which increases in the turbulent regime. The integration in (3.7) is performed up to the edge of the

boundary layer, y_{edge} (defined as the location of maximum mean velocity between the wake and the plate), and the "effective" free-stream velocity, U_{edge}, is the mean velocity at this location.

We also examine the near-wall behavior of the velocity and turbulent kinetic energy (TKE) profiles throughout the domain. In fully turbulent boundary layers, the velocity profile has a logarithmic region, and the TKE profile has a near-wall peak caused by low- and high-speed streaks of streamwise velocity. The log-law expression used in our comparisons is $u^+ = 2.44 \times log\,(y^+) + 5.5$. Finally, we will discuss the budget of the TKE across the transitional region $k = \langle u_i' u_i' \rangle / 2$. It is given by:

$$\frac{\partial k}{\partial t} = -\langle U_i \rangle \frac{\partial k}{\partial x_j} - \frac{\partial \langle U_i \rangle}{\partial x_j} \langle u_i' u_j' \rangle - \nu \left\langle \frac{\partial u_i'}{\partial x_j} \frac{\partial u_i'}{\partial x_j} \right\rangle - \frac{1}{\rho} \frac{\partial \langle p' u_i' \rangle}{\partial x_i} + \nu \nabla^2 k - \frac{1}{2} \frac{\partial \langle u_j' u_i' u_i' \rangle}{\partial x_j}. \tag{3.8}$$

The terms on the right side of (3.8), which is derived from the Reynolds-Averaged Navier Stokes (RANS) equations, are referred to, respectively, as advection, production, dissipation, pressure work, viscous diffusion, and turbulent transport. In the case of LES at $Re_D = 1155$, additional subgrid-scale (SGS) transport and dissipation terms are present on the right-hand side. They are defined, respectively, as

$$T_{SGS} = -\frac{\partial \left(u_i' \tau_{ij}' \right)}{\partial x_j} \tag{3.9}$$

$$D_{SGS} = \tau_{ij}' \frac{\partial u_i'}{\partial x_j}. \tag{3.10}$$

and are included in the RANS transport and dissipation. The sum of the computed

terms in the budgets was very small throughout the computational domain, indicating good convergence. For example, in the fully turbulent region, the maximum imbalance was 2% and 4% of the maximum production for the $Re_D = 1155$ and $Re_D = 3900$ cases, respectively.

Figure 3.4 shows instantaneous snapshots of the flow field for each Re_D case. Although the computational domains have different streamwise sizes, the axes limits for the three plots are the same to facilitate comparison. Pressure isosurfaces highlight the cylinder wake, and contours of the streamwise velocity fluctuation show the perturbations near the wall as well as in the wake. A more coherent von Kármán vortex street can be observed for the $Re_D = 385$ case than for the $Re_D = 1155$ and 3900 cases. In the higher Re_D cases, consistent with the Reynolds number increase, the cylinder wake contains eddies of a much finer scale. The spanwise rollers of the vortex street rapidly become three-dimensional. Concomitant with the deformations of the rollers, elongated streamwise streaks of high- and low-speed fluid appear inside the laminar boundary layer. In the $Re_D = 385$ case, although the laminar boundary layer is buffeted by the shed vortices, it remains stable and no transition to turbulence is observed within the computational domain. In contrast, in the $Re_D = 1155$ and $Re_D = 3900$ cases, the onset of laminar-turbulent transition is clearly visible at approximately $x = 30$ ($Re_x = 34,650$) and $x = 20$ ($Re_x = 78,000$), respectively, judging from the appearance of near-wall pertrubations. Transition is accompanied by significant changes in the mean flow statistics, as well as the generation of fine-scale streaky structures near the wall. The average spacing between the near-wall

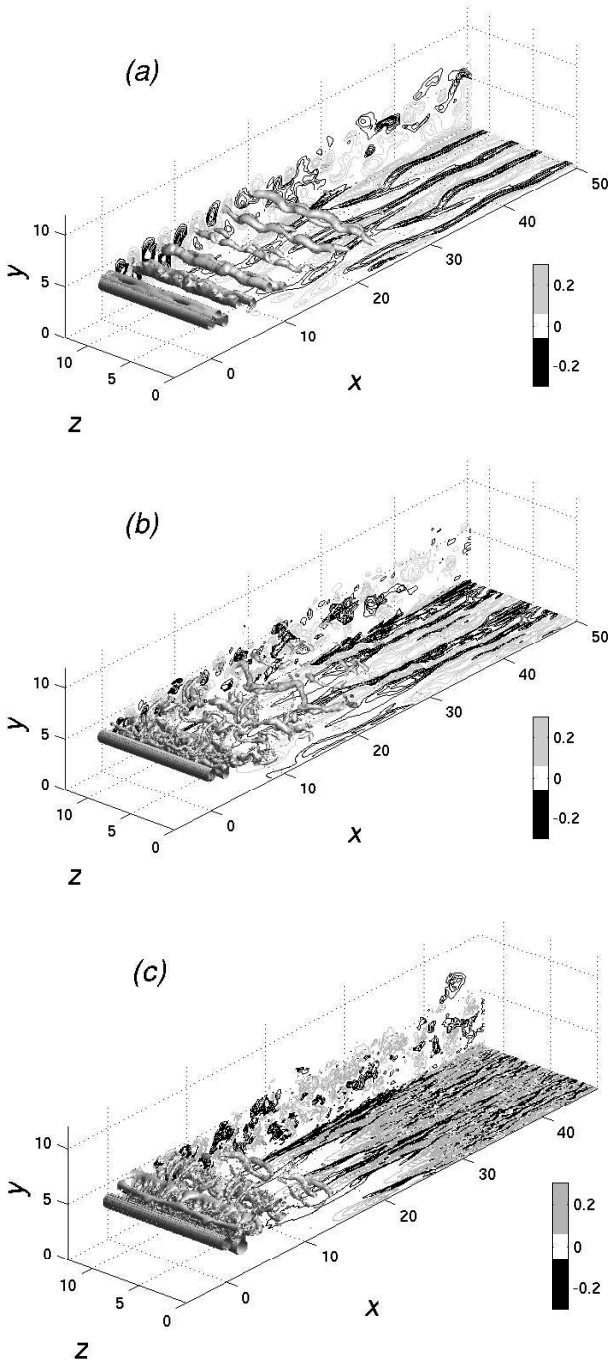

Figure 3.4: Isosurfaces of pressure ($p = -0.08$) and streamwise velocity fluctuation contours inside the boundary layer and in the wake; (a) $Re_D = 385$, (b) $Re_D = 1155$, (c) $Re_D = 3900$

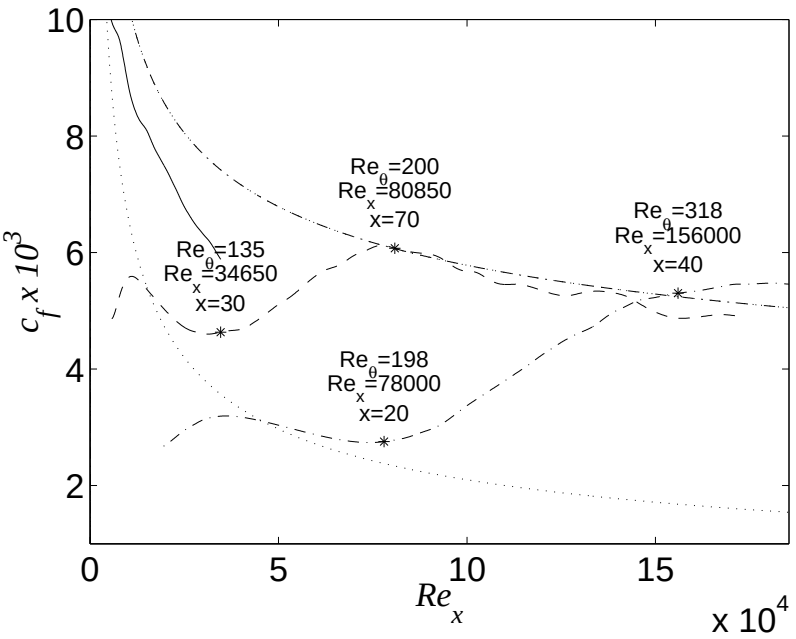

Figure 3.5: Skin friction coefficient; —— $Re_D = 385$, --- $Re_D = 1155$, —·— $Re_D = 3900$; ····· laminar C_f, —···— turbulent C_f; the asterisks indicate the locations of the onset and the end of transition.

streaks is about 100 wall units, consistent with typical turbulent wall-bounded flows. The streaks become visible downstream of $x \simeq 30$ in figure 3.4*(c)*, which extends into the fully turbulent region, but are less clear in figure 3.4*(b)*, which extends only through the middle of the transitional region.

In figure 3.5, we show the streamwise evolution of skin friction for the three cases. In each case the skin friction starts from a perturbed laminar value that does not coincide with the Blasius profile. This is due to the combination of the proximity to the leading edge (where Blasius similarity is invalid) and the free-stream acceleration due to the flow obstruction by the cylinder, which causes the

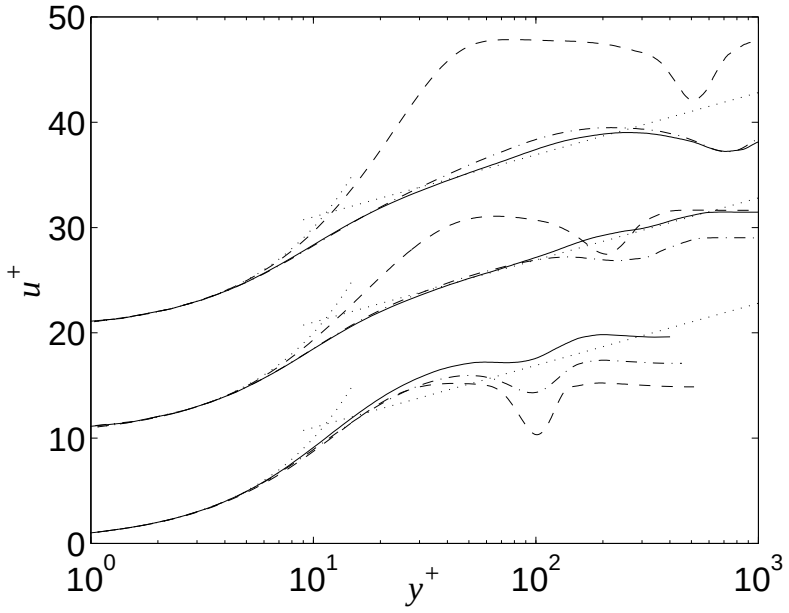

Figure 3.6: Mean streamwise velocity profiles in wall units; bottom: $Re_D = 385$; --- $x = 20$, $Re_x = 7,700$, —·— $x = 50$, $Re_x = 19,250$, —— $x = 90$, $Re_x = 34,650$ middle: $Re_D = 1155$; --- $x = 30$, $Re_x = 34,650$, —·— $x = 70$, $Re_x = 80,850$, —— $x = 150$, $Re_x = 173,250$ top: $Re_D = 3900$; --- $x = 20$, $Re_x = 78,000$, —·— $x = 40$, $Re_x = 156,000$, —— $x = 47$, $Re_x = 183,300$; The plots for the different Reynolds number cases are offset by 10 units in the vertical direction.

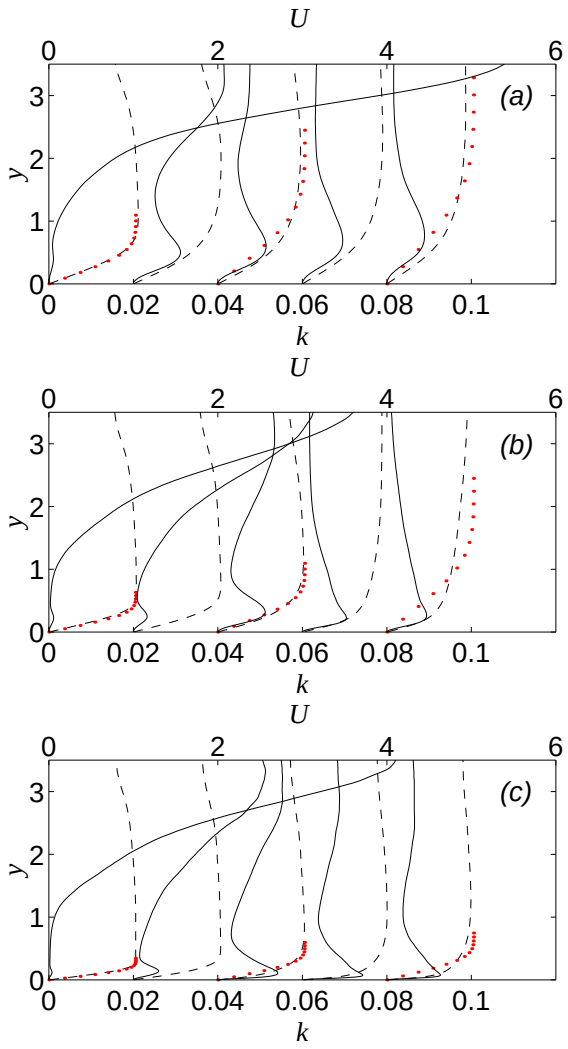

Figure 3.7: Profiles of mean velocity (---) and the turbulent kinetic energy (——); (a) $Re_D = 385$; from left to right, the plots correspond to $x = 10,\ 30,\ 50,\ 70,\ 90$, $Re_x = 3,850,\ 11,550,\ 19,250,\ 26,950,\ 34,650$; (b) $Re_D = 1155$; from left to right, the plots correspond to $x = 10,\ 15,\ 30,\ 90,\ 150$, $Re_x = 11,550,\ 17,325,\ 34,650,\ 103,950,\ 173,250$; (c) $Re_D = 3900$; from left to right, the plots correspond to $x = 10,\ 20,\ 30,\ 40,\ 47$, $Re_x = 39,000,\ 78,000,\ 117,000,\ 156,000,\ 183,300$. The dots correspond to Blasius profiles at the respective Re_x values. The U and k plots are offset by 1 and 0.02, respectively.

initial skin-friction undershoot. In the absence of the cylinder, the Blasius profile was matched by $x = 6$, for the $Re_D = 385$ case. Figures 3.5.1 and 3.7 show profiles of the streamwise velocity at various locations for the three Re_D cases. In figure 3.7, we have also included profiles of the turbulent kinetic energy at the respective stations.

We begin with a discussion of the statistics for the $Re_D = 385$ case. The skin-friction coefficient shows increasing deviation from the perturbed laminar level but does not rise more than halfway towards the turbulent value. This behavior is consistent with evolution of the mean velocity: the velocity profiles show a small progressive deviation from the laminar Blasius solution (figure 3.7 *(a)*), but there is no trend towards a logarithmic law (figure 3.5.1, bottom), and the fuller velocity profile is due to a perturbed laminar flow regime. The shape factor for this case has a minimum value of 2.25, which is below the Blasius value of 2.6 but far from the turbulent value of 1.5. Figure 3.7 also shows an initial increase in the boundary-layer TKE peak with streamwise distance, which is most likely due to the growth of the laminar boundary-layer streaks visible in figure 3.4, which will be discussed in the next section. The TKE peak remains near the middle of the boundary layer and not near the wall as in a turbulent wall-bounded flow. Finally, the Reynolds number based on the momentum thickness, Re_θ, only reaches 105 by the end of the domain ($x = 90$, $Re_x = 34,650$). To our knowledge, the lowest value of Re_θ at which a turbulent boundary layer can be generated experimentally is 285 (Bandyopadhyay 1987). In our $Re_D = 1155$ calculation, the boundary layer had fully turbulent

statistics at $Re_\theta \simeq 200$.

For the $Re_D = 1155$ case, the C_f curve begins to rise at $x = 30$ ($Re_x \simeq 35,000$), indicating the onset of transition. The skin-friction maximum (which may be viewed as the end of transition) is attained at $x \simeq 70$ ($Re_x \simeq 81,000$). We note in passing that this Reynolds number is far below the range characteristic of transition due to Tollmien-Schlichting (TS) waves ($Re_x \simeq 10^6$). The low transitional Re_x value is more consistent with bypass transition due to moderate-amplitude free-stream turbulence (*e.g.* Roach & Brierlay 1992).

The skin-friction development at $Re_D = 3900$ indicates that transition to turbulence begins at $x \simeq 20$ ($Re_x = 78,000$) and is complete by $x = 40$, or $Re_x = 156,000$. Also visible is a pronounced skin friction overshoot of the values predicted by the calculation in the turbulent region. As mentioned earlier, we met or exceeded the standard grid resolution requirements for a turbulent boundary layer, so the overshoot is probably not due to a lack of resolution. Unfortunately, our computational domain did not extend beyond location $x = 47$, so the behavior of the skin-friction farther downstream remains unknown for this case.

The velocity profiles for the $Re_D = 1155$ and 3900 cases (figures 3.7*(b), (c)*) indicate a greater deviation from the Blasius profile than observed for $Re_D = 385$, starting at locations $x \simeq 50$ and $x \simeq 30$ ($Re_x = 57,750$ and $Re_x = 117,000$), respectively. Figure 3.5.1 (middle and bottom profiles) shows that the mean near-wall streamwise velocity profiles at $Re_D = 1155$ and $Re_D = 3900$ develop a logarithmic layer, suggesting that a turbulent equilibrium is established. For the $Re_D = 3900$

case, one observes a momentum deficit in the cylinder wake region even where the boundary-layer velocity profile appears turbulent. This is due to the fact that the development of statistical quantities in the wake is x-dependent and not Re_x-dependent, as will be discussed later. For both Re_D cases, the shape factor reaches a value of approximately $\simeq 1.5$ consistent with turbulent flow. The TKE profiles in figure 3.7*(b)* and *(c)* show that by the locations $x = 50$ ($Re_D = 1155$) and $x = 30$ ($Re_D = 3900$) the boundary-layer peak is moving closer to the wall. At $x = 100$ ($Re_x = 115,500$) and $x = 41$ ($Re_x = 160,000$) for the lower and higher Re_D cases, respectively, the position of the peak was about 15 wall units, close to the accepted value of 12 for near-wall turbulent flows. The evolution of boundary-layer TKE will be discussed at greater length in the next section in the context of the mechanism of transition.

The budgets of the TKE were also computed for each case. Figure 3.8 shows the development of the TKE budget corresponding to the $Re_D = 1155$ simulation. We focus on this case, but the differences from the other cases will be noted. The data are normalized by the free-stream velocity and cylinder diameter. This choice was made in order to separate the effects of the mean flow evolution (which enters through the change in u_τ) from the evolution of the budget terms, which involve higher-order moments. The figure illustrates that the maximum of the boundary layer TKE production is initially near the middle of the laminar boundary layer. The location of the peak approximately coincides with the location of the maximum u_{rms}. As the perturbed laminar boundary grows in thickness, the peak in the production

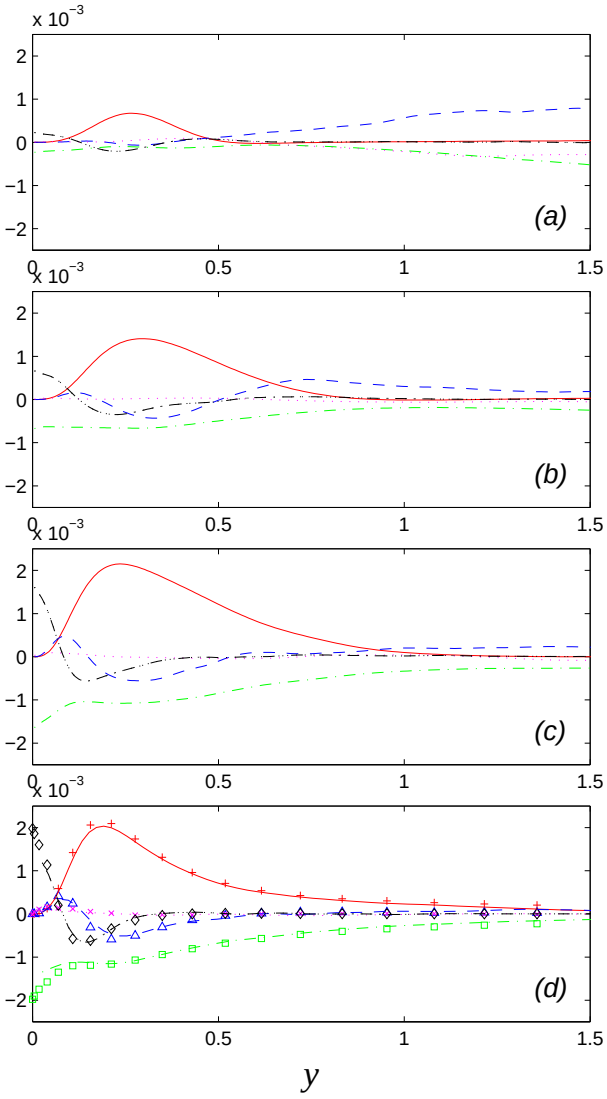

Figure 3.8: Budgets of k at various locations; $Re_D = 1155$. All terms are normalized by U_∞ and D. (a) $x = 15, Re_x = 17,325, \delta_{99} = 0.51$; (b) $x = 30, Re_x = 34,650, \delta_{99} = 0.92$; (c) $x = 47, Re_x = 54,285, \delta_{99} = 1.18$; (d) $x = 90, Re_x = 103,950, \delta_{99} = 2.1$. Symbols: channel flow DNS by Moser *et al.* (1999); lines: present simulation. +, —— : production; □ , —·— Dissipation; △ , --- Turbulent transport; × , ····· Pressure diffusion; ◇ , —···— Viscous diffusion.

slowly moves farther away from the wall, up to the onset of transition at $x = 30$; beyond this location it moves rapidly toward the wall. While the wake is strong, ($x < 30$), turbulent transport (the dashed line in figure 3.8) increases the boundary-layer turbulence by convecting wake turbulence into the outer part of the boundary layer. In this region the dissipation and the turbulent transport inside the boundary layer are small and the budgets are balanced by the advection term (unlike fully turbulent boundary layers, in a transitional boundary layer, due to a rapid growth of the TKE, the term $-\langle U \rangle \partial k/\partial x$ is significant). By $x = 30$, ($Re_x = 34,650$), (plot *b*) the magnitudes of the budget terms are about 2/3 of their turbulent values; and by $x = 47$, ($Re_x = 54,285$), the budget is nearly that of a turbulent near-wall flow. Interestingly, at this location the near-wall streamwise velocity profile does not yet have a logarithmic region; the laminar-turbulent shift in the mean velocity profile occurs after a near-wall turbulence cycle has been established. At the final location, $x = 90$, ($Re_x = 183,300$), we have also included the turbulent channel flow data of Moser, Kim & Mansour (1999) obtained at $Re_\tau = 395$ for comparison (the use of channel rather than boundary-layer data for comparison is justified because the near-wall behavior of the two flows is very similar). To convert the channel flow data to outer coordinates, we used the local u_τ and ν from our simulation. The comparison in figure 3.8*(d)* shows that a turbulent equilibrium is fully established. An examination of the TKE budgets for the $Re_D = 3900$ case revealed a similar development, except that between locations $x = 26$ and $x = 40$, the dissipation at the wall exceeds the peak energy production inside the boundary layer. The near-

wall peak in the turbulent transport is about 50% of the peak production, compared to 25% typical of near-wall turbulent flows. By location $x = 47$, ($Re_x = 183,300$), the TKE budget is again very close to data of Moser *et al.* (1999), indicating that a turbulent equilibrium has been reached. The development of the TKE budget corresponding to $Re_D = 385$ case was similar to that of the $Re_D = 1155$ case prior to the transition onset. The y-location of the turbulence production peak increases throughout the computational domain, and the magnitude of the peak increases initially, then decreases downstream of $x = 20$, ($Re_x = 6,700$), indicating that the perturbation is decaying.

3.5.2 Instability and laminar breakdown

The purpose of this section is to identify the important stages in flow evolution prior to the onset of fully developed turbulence. We focus our attention primarily on the $Re_D = 385$ and $Re_D = 3900$ cases; the intermediate $Re_D = 1155$ case combines elements from both. Much of our discussion will be inspired by the $Re_D = 385$ case data, since the low Reynolds number implies a narrower range of scales that makes the identification of coherent structures easier. Many of the observations regarding this case carry over to the higher Re_D cases, although important differences will be pointed out in the course of the discussion.

Visualizations of the three flow fields in figure 3.4 were discussed in the previous section. The prominent difference between the cases is in range of flow scales, which

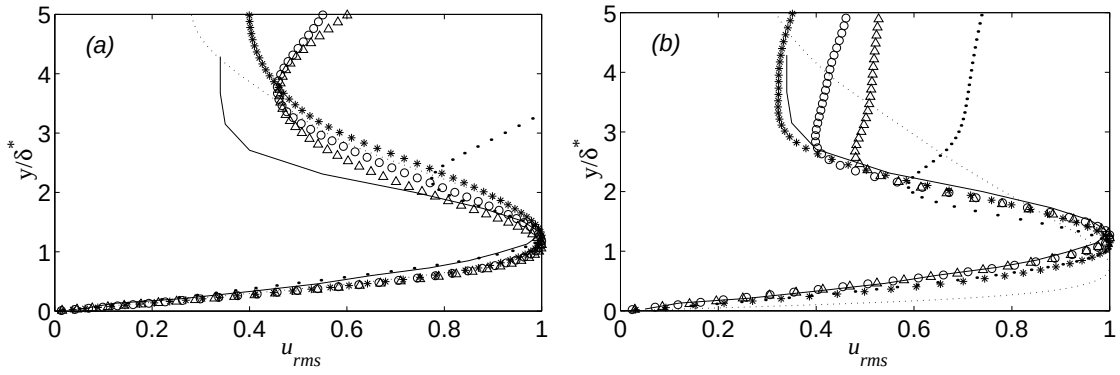

Figure 3.9: Profiles of u_{rms} across the boundary layer normalized by the maximum boundary-layer u_{rms}; δ^* is the displacement thickness; (a) $Re_D = 385$; • $x = 10$, △ $x = 30$, ◯ $x = 40$, ⋆ $x = 60$, ····· $x = 90$; (b) $Re_D = 3900$; • $x = 5$, △ $x = 10$, ◯ $x = 15$, ⋆ $x = 20$, ····· $x = 30$; —— from Matsubara & Alfredsson (2001)

increases with the Reynolds number. The higher the Reynolds number, the more rapidly the cylinder wake loses its coherence, and the more unstable the boundary layer is to perturbation. Despite the difference in the Reynolds number, we believe that the mechanism of interaction is the same in all three cases, as described below.

The visualizations in figure 3.4 show the generation of streamwise velocity streaks downstream of location $x \simeq 10$ for all cases. To characterize these streaks, we computed profiles of u_{rms} inside the perturbed boundary layer, shown in figure 3.9 for the $Re_D = 385$ and $Re_D = 3900$ cases. Since the streaks are the only disturbances present, the nonzero Reynolds stress is entirely caused by them. When the wall-normal coordinate is scaled with the local displacement thickness, and u_{rms} with its maximum inside the boundary layer, the profiles exhibit a region of approximate

self-similarity. For the $Re_D = 385$ case, the self-similar region is established at $x \simeq 20$ and persists downstream up to $x = 90$ ($Re_x = 34,650$), as the boundary layer remains laminar. For the $Re_D = 3900$ case, this region is limited to the range $x \in [10, 20]$. Farther downstream transition to turbulence occurs, and the location of the u_{rms} peak shifts towards the wall. In the figure we also show the experimental data of Matsubara and Alfredsson (2001), which was obtained from a transitional boundary layer subjected to moderate free-stream turbulence. The agreement with measured data is good, indicating that the streaks found in our simulations may be related to the Klebanoff modes (Klebanoff 1971) observed in the experiment. We note that the self-similarity is approximate: the peak in u_{rms} moves closer to the wall with increasing Reynolds number. This trend is also present in the experiments of Mastubara & Alfredsson (2001) and in the numerical simulations of boundary-layer transition due to FST by Brandt *et al.* (2004).

To determine the average spacing between the streaks, we computed spanwise correlation functions of streamwise and wall-normal velocity fluctuations. In figure 3.10 we plot these functions for the $Re_D = 385$ and $Re_D = 3900$ cases at various streamwise positions at $y = 0.2$. The first streamwise location for each Reynolds number was chosen to match the approximate onset of streak self-similarity. Both R_{uu} and R_{vv} correlations in figure 3.10 *(a)* and *(b)* predict an average streak spacing of $2.5D$ at $Re_D = 385$ (twice the distance to the first R_{uu} zero crossing, or four times the distance to the first R_{vv} zero crossing). For this case, the streak spacing remains approximately constant throughout the domain. The bottom curves in plots *(c)*

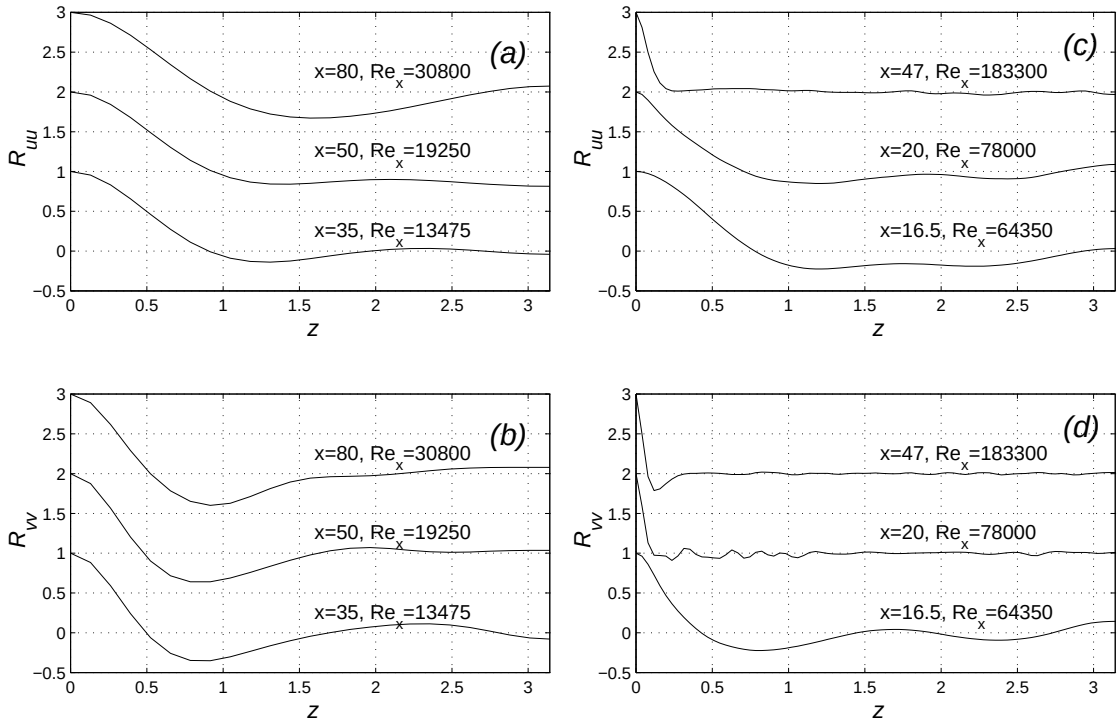

Figure 3.10: Spanwise correlation functions of the streamwise and wall-normal velocity fluctuations; (a) $Re_D = 385$, R_{uu}; (b) $Re_D = 385$, R_{vv}; (c) $Re_D = 3900$, R_{uu}; (d) $Re_D = 3900$, R_{vv}; the correlation functions are computed at $y = 0.2$. The curves at successive x-locations are offset by 1 in the vertical direction.

and *(d)*, corresponding to $Re_D = 3900$, are also consistent with streamwise streaks separated by $\simeq 2.5D$. For the intermediate case, $Re_D = 1155$, the streak spacing was estimated to be the same. This finding may seem surprising, since there is a factor of five difference in Re_x between the highest and the lowest Reynolds number. The boundary-layer thickness δ_{99} is 1.59 for the $Re_D = 385$ case at location $x = 35$ and 0.35 for the $Re_D = 3900$ case at location $x = 16.5$. Thus there is also a factor of 4.5 difference in δ_{99}. At the above locations, the streaks are $1.6\delta_{99}$ and $7.2\delta_{99}$ apart for the two cases, respectively. Experiments and simulations on boundary-layer transition due to moderate to strong levels of f.s.t (*e.g.* Matsubara & Alfredsson 2001, Jacobs & Durbin 2001), in contrast, report streamwise streaks with mean separation of the order of the boundary-layer thickness. An explanation of this discrepancy follows shortly below when we discuss the evolution of the cylinder wake.

Figure 3.10 *(c)* and *(d)* also shows spanwise correlations functions at location $x = 20$, at the onset of transition, and at $x = 47$ when the flow is fully turbulent. An abrupt decrease in streak spacing to $0.5D$ is evident; these streaks are different from those described above and characterize the near-wall region of turbulent wall-bounded flows. Interestingly, at location $x = 20$, the R_{vv} curve already shows small scale fluctuations whereas the R_{uu} curve is little different from the one at location 16.5, suggesting that the laminar breakdown first manifests itself through the wall-normal velocity component (the correlation function for the spanwise velocity fluctuation, R_{ww}, was very similar to R_{uu}).

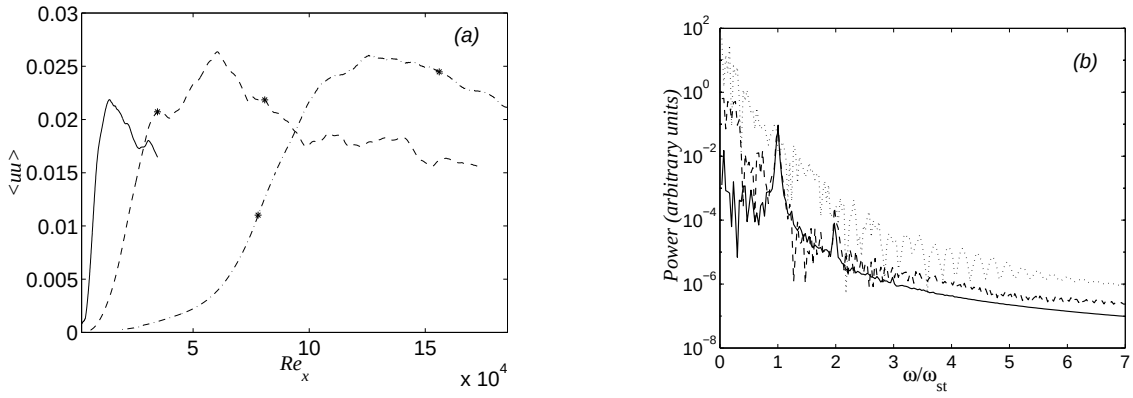

Figure 3.11: (a) Maximum streamwise Reynolds stress $\langle uu \rangle$ inside the boundary layer. —— $Re_D = 385$, --- $Re_1, 155$, —·— $Re_D = 3900$; (b) Spectra of streamwise velocity inside the boundary layer for the $Re_D = 385$ case; —— $x = 0$, --- $x = 10$ ····· $x = 30$

In figure 3.11*(a)* we show the maximum streamwise Reynolds stress $\langle uu \rangle$ inside the boundary layer for the three Re_D cases. The stars indicate the locations of the onset of transition and the C_f maximum. All three curves exhibit a region of rapid growth followed by a slow decrease. For the $Re_D = 1155$ and $Re_D = 3900$ cases, we note an overshoot of $\langle uu \rangle$ within the transitional region. A similar overshoot upstream of the onset of turbulence is also documented in the studies of bypass transition due to free-stram turbulence by Matsubara & Alfredsson (2001) and is probably a general feature of boundary-layer bypass transition.

To determine whether the initial growth of the streamwise Reynolds stress in our simulations is localized to a particular band of frequencies, we computed frequency spectra of streamwise velocity fluctuation at various locations in the domain.

Figure 3.11*(b)* shows frequency spectra for the $Re_D = 385$ case at the streamwise locations $x = 0$, $x = 10$, and $x = 30$, corresponding to $Re_x = 0$, $Re_x = 3,850$, and $Re_x = 11,550$. The higher two Re_x values are within the rapid growth region, which extends to $Re_x \simeq 14,000$. The wall-normal location was $y = 0.1$ for the three curves, which falls inside the bottom 15% of the boundary layer for the two downstream stations. The frequency axis is normalized with $\omega_{St} = 0.215$, corresponding to the Strouhal frequency of wake shedding. A peak corresponding to the shedding frequency of the cylinder can be seen at the first two locations. This peak is caused by the instant propagation of the unsteadiness of the cylinder wake shedding through the pressure. The peak becomes less prominent with downstream distance, and by location $x = 40$, it is completely obscured by the presence of the neighboring frequencies. We also note the initial presence of two higher-order harmonics of the Strouhal frequency. Only one harmonic was detected for the $Re_D = 3900$ case, perhaps because the signal was more noisy at this Reynolds number. The presence of harmonics was also noted by Kyriakides *et al.* (1996) during their experiment.

More significantly, figure 3.11*(b)* indicates that most of the growth in the $\langle uu \rangle$ Reynolds stress at $Re_D = 385$ occurs within the low frequency range, at or below 1/4 of the shedding frequency of the cylinder. This observation is consistent with the growth of the streamwise streaks inside the boundary layer with the downstream distance. A growth region similar to ours has been noted in experiments on bypass transition due to FST (*e.g.* Klebanoff 1971), which is caused by the growth of low frequency Klebanoff modes inside the perturbed boundary layer. Several experi-

ments showed that the streamwise Reynolds stress grows in proportion with the flat-plate Reynolds number Re_x, although the constant of proportionality is not agreed upon (see Westin, Boiko, Klingmann, Kozlov & Alfredsson (1994) for further discussion). In our simulations, we do not see a well defined linear growth region. This is most likely because the disturbance does not interact with the boundary layer starting from the leading edge, or that the disturbance environment associated with strong wake/boundary-layer interactions is different from FST Outside of the boundary layer in the wake region, we did not observe energy growth in the low frequencies; the amplitude of the Strouhal frequency remained dominant through the entire computational domain.

The spectra corresponding to the $Re_D = 3900$ case (not shown) had a similar behavior for the low frequency modes in the rapid growth region. Downstream of location $x = 20$, we observed rapid growth in high frequencies, characteristic of the breakdown to turbulence. No spectra were obtained for the $Re_D = 1155$ case.

The behavior of disturbance spectra is in partial agreement with the experiments of Kyriakides *et al.* (1999b). Although their configuration was slightly different, with the cylinder axis located one diameter upstream of the plate and the Reynolds number set to $3,500$, the important features of the flow should be comparable between the two cases. Kyriakides *et al.* (1999b) were able to detect velocity fluctuations at the Strouhal frequency inside the boundary layer within the Reynolds number range $Re_x = 24,500$ - $59,500$. They used the velocity signal to deduce the presence of a secondary vortical structure located within the boundary

layer, which was induced by a von Kármán vortex with negative spanwise vorticity. They did not, however, report any structures with large streamwise scales, which are prominent in our simulations. This may be because they did not place probes sufficiently far downstream of the leading edge. In our $Re_D = 3900$ simulation, streamwise streaks were clearly visible at $x \simeq 16$, corresponding to $Re_x = 62,400$ (see figure 3.10). We did not observe any spanwise vortical structures inside the boundary layer. Interestingly, however, in their earlier publication, Kyriakides *et al.* (1996) presented streamwise velocity spectra at $Re_D = 385$, which had a pronounced growth in the low-frequency content, consistent with the presence of long streamwise scales encountered in our simulations.

To investigate the connection between the cylinder wake and boundary-layer streaks, we examined the instantaneous flow field for the three Re_D cases. In figure 3.12, isosurfaces of pressure fluctuation (gray) are superimposed on top of streamwise velocity fluctuation contours inside the boundary layer for the $Re_D = 385$ and $Re_D = 3900$ cases. For the low Re_D case we also show isosurfaces of positive streamwise vorticity fluctuation (light gray) and isosurfaces of negative streamwise vorticity fluctuation (black). The pressure isosurfaces highlight large spanwise vortices behind the cylinder and the vorticity isosurfaces show the braid vortices around the spanwise rollers. Vorticity isosurfaces are omitted for the $Re_D = 3900$ case because they do not correspond to coherent structures at this higher Reynolds number, *i.e.* the braid vortices break down to fine-scale turbulence early on. The domain is repeated in the spanwise direction in order to show the boundary-layer streaks more clearly.

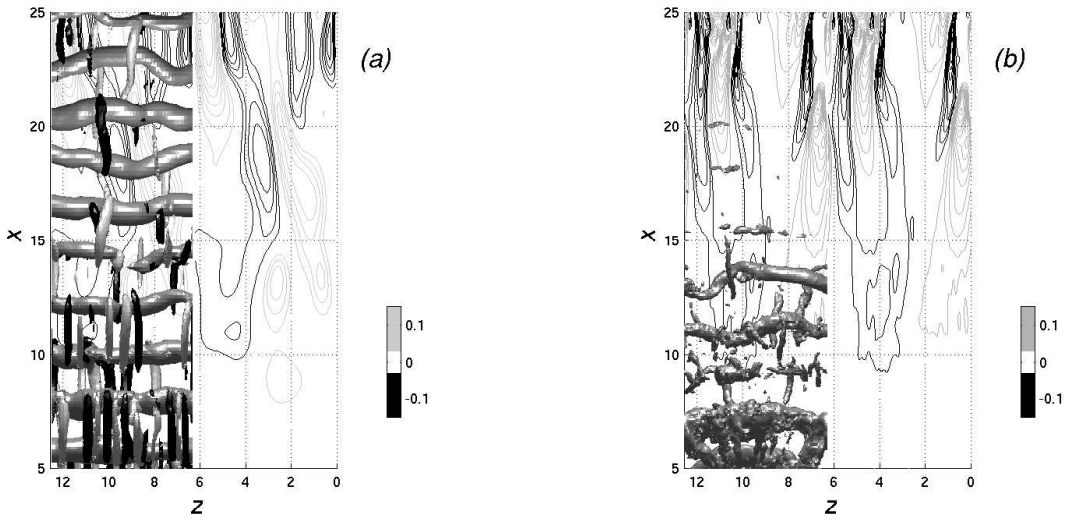

Figure 3.12: Isosurfaces of pressure (gray, p = -0.08), isosurfaces of positive (light gray, $\omega_x = 1$) and negative (black, $\omega_x = -1$) streamwise vorticity fluctuation above contours of streamwise velocity fluctuation inside the boundary layer; vorticity is shown only for the $Re_D = 385$ case. (a) $Re_D = 385$, contours are plotted at $y = 0.4$ (b) $Re_D = 3900$, contours are plotted at $y = 0.1$.

The pressure isosurfaces become wavy with downstream distance indicating the deformation of the spanwise rollers. The dominant spanwise wavelength of this deformation equals about one half of the domain size for both cases, around $3D$. This value is in agreement with the scale of the elliptic instability of the primary vortex cores, which at Reynolds numbers in the range $170 < Re_D < 240$ give rise to mode A instability of the cylinder wake (Williamson 1996). That this wavelength seems the same for two simulations separated by a factor of 10 in the Reynolds number implies a weak Reynolds number dependence for the primary roller instability. At higher Reynolds numbers, as observed in our cases, cylinder wake dynamics are dominated by mode B instability, which corresponds to the dynamics of the quasi-streamwise oriented vortices in the braid region. From the contours of u' inside the boundary layer and the spanwise correlation data presented earlier, it appears that the streaks occur on the same spanwise scale as the deformation of the rollers. They are unlikely to be induced by the braid vortices (which correspond to the mode B instability of the cylinder wake), whose spanwise length scale is smaller, approximately $1D$, for the $Re_D = 385$ case, and which have nearly degenerated into small-scale turbulence by location $x = 10$ for the $Re_D = 3900$ case. In both cases (and also for $Re_D = 1155$, not shown), well defined streaks appear at location $x \approx 15$. The fact that this location is the same at $Re_D = 385$ and $Re_D = 3900$, despite a factor of three difference in the boundary-layer δ_{99} between the two cases, indicates that for this flow configuration the location of streak inception is not very sensitive to the Reynolds number. To gain more insight into the mechanism of streak

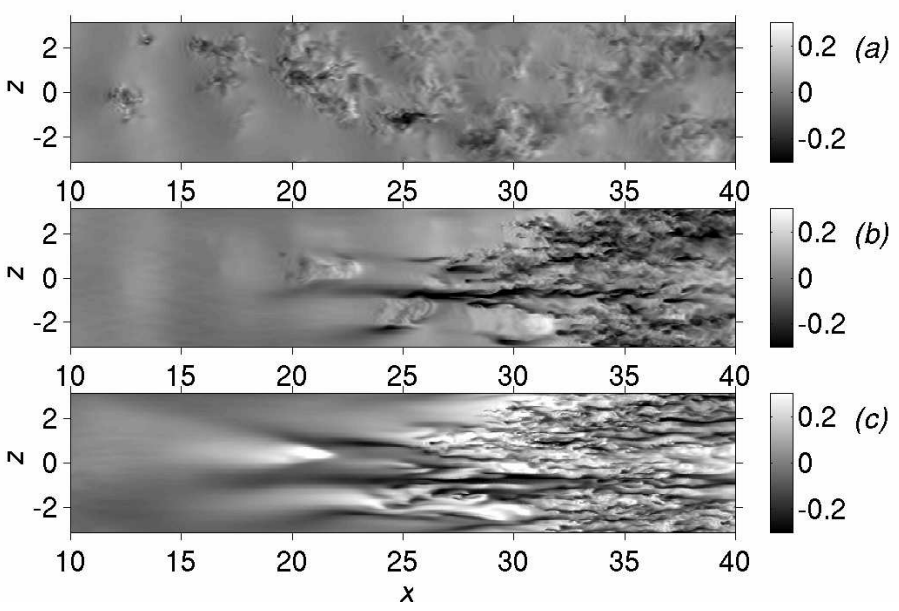

Figure 3.13: Contours of instantaneous streamwise velocity fluctuation; (a) $y = 0.1$, (b) $y = 0.3$, (c) $y = 1.0$. At $x = 10$: $Re_x = 39,000$, $\delta_{99} = 0.28$; at $x = 40$: $Re_x = 156,000$, $\delta_{99} = 0.79$, $Re_D = 3900$.

generation, we examined a time sequence of velocity fluctuations in a cross-stream plane located at $x = 10$ for the $Re_D = 385$ case. When the plane cut across a spanwise roller, the contours of the streamwise velocity fluctuation were sinusoidal (oscillatory) in the core of the vortex, consistent with the deformation of the roller in the xz-plane. Such deformation partially reorients the spanwise vorticity of the roller in the streamwise direction. The streamwise-oriented sections of the roller inject fluid into the boundary layer that gives rise to laminar velocity streaks.

While cross-stream planes proved useful for the $Re_D = 385$ case, for the $Re_D = 3900$ case they were more difficult to interpret because of finer-scale structures present in the flow. A different perspective is provided in figure 3.13, which

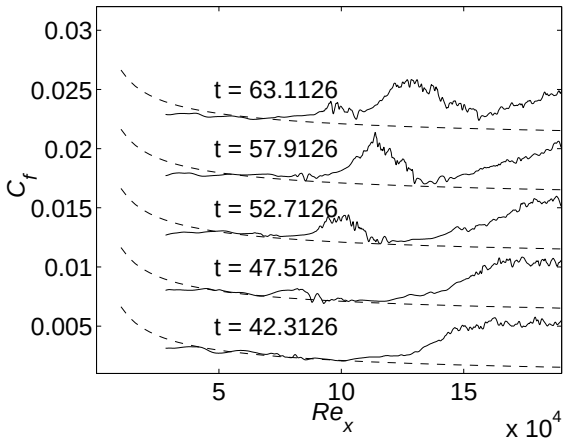

Figure 3.14: Instantaneous spanwise-averaged and time- and spanwise-averaged skin friction coefficient; —— instantaneous C_f, --- Blasius C_f; $Re_D = 3900$. The successive curves are offset by 0.005 in the vertical direction.

shows contours of the streamwise velocity fluctuation at three xz-planes, located at $y = 1$, 0.3, and 0.1, top to bottom. The boundary-layer thickness, δ_{99}, is 0.28 at $x = 10$ and 0.79 at $x = 40$. The top plane, located outside of the boundary layer, shows patches of small scale turbulence occurring at intervals of length five, close to the Strouhal wavelength of wake shedding. This is consistent with the wake ejecting fluid towards the boundary layer. The patches located at $x \simeq 20$ and $x \simeq 25$ are also visible in the middle and bottom planes, both of which are within the boundary layer at these locations. The bottom plane also shows two low-speed streaks surrounding the patch of high-speed turbulence ejected from the wake at $x \simeq 20$. Thus, it appears that at $Re_D = 3900$ the laminar velocity streaks are the direct result of turbulence ejected by the wake into the boundary layer. Unfortunately, we do not have time series of the velocity field or xz-planes at $Re_D = 3900$, which could

confirm the connection between wake turbulence and the boundary-layer streaks at $Re_D = 3900$. Instead, the above discussion is supported by two instantaneous velocity fields.

Because the cylinder Reynolds number is sufficiently high at 3900, the laminar streaks rapidly break down to turbulence. The region of breakdown is intermittent; the intermitency may be visualized from plots of skin friction at different instants in time. Figure 3.14 shows the temporal evolution of instantaneous (spanwise-averaged to remove high-frequency noise) skin friction. The intermittency is similar to the turbulent spots found in bypass transition studies, (see Jacobs & Durbin 2001; Alfredsson & Matsubara 2001). One can see high C_f regions associated with turbulence moving downstream, as the peak C_f inside the region is also increasing. Note, in particular, the curve corresponding to $t = 57.9$, which shows a turbulent region surrounded by low skin-friction values, indicating the presence of turbulence inside laminar flow. From the instantaneous skin-friction plots, we estimated the convective speeds of the front and the rear of an intermittency region to be $0.99U_\infty$ and $0.66U_\infty$, respectively. These values are higher than those reported by Henningson, Spalart & Kim (1987), who simulated the development of a "classical" arrowhead-shaped turbulent spot, and found convection velocities of $0.9U_\infty$ and $0.5U_\infty$, respectively. These differences may be due to the different types of boundary-layer disturbances in the two simulations, as was suggested by Jacobs & Durbin (2001): Henningson *et al.* (1987) introduced a disturbance near the wall, whereas in our case, the disturbance entered the boundary layer from the free-stream. Finally, it is not clear

whether, in the present case, the intermittency is due entirely to streak instability or to the impingement of wake turbulence on the boundary layer. The intermittency was not observed for the $Re_D = 1155$ case, probably because the Reynolds number was not sufficiently high. Downstream of the location of transition onset, the flow did not exhibit instantaeous laminar levels of skin friction as in the $Re_D = 3900$ case.

In summary, we have found that the interaction of a cylinder wake with a flat-plate boundary layer results in the generation of streamwise streaks that in the high Re_D cases breakdown to turbulence. The profiles of u_{rms} inside the boundary layer indicate that the streaks bear similarity to Klebanoff modes (Klebanoff 1971). A rapid initial growth in the low-frequency components of the streamwise velocity spectrum suggests that the incipient streaks are preferentially amplified inside the boundary layer. The streaks appear to be generated by the three-dimensional instability of the primary vortex in the wake. The scale of this instability is approximately the same for the three cases, which results in the same spacing between the boundary-layer streaks for the three Reynolds numbers. The proposed mechanism is an example of strong interaction, *i.e.* one in which the disturbance acting on the boundary layer is coherent. We also found that the transitional region in the $Re_D = 3900$ is intermittent and similar to that in bypass transition due to FST

As mentioned previously, Kyriakides *et al.* (1996) carried out experiments on wake induced boundary layer transition for several Reynolds numbers, including $Re_D = 385$, $Re_D = 1155$, and $Re_D = 3,500$. They observed transition in all three

cases, respectively at $x = 7.3$, 2.7, and 54.5, corresponding to $Re_x = 2,625$, for the first two cases, and 21,000 for the last. They stated that the transition scenario is the same for all three cases. Unfortunately, a meaningful comparison of our simulations with their experiments is difficult, primarily because the indicator of boundary-layer transition used in their work is only qualitative. Kyriakides *et al.* (1996) state that "the x-location where the [streamwise] velocity signal loses its sinusoidal character is considered to be the onset of transition." The velocity spectra obtained for our $Re_D = 385$ case show that the peak corresponding to the Strouhal frequency inside the boundary layer disappears by location $x = 40$. At this location the velocity signal is certainly non-sinusoidal. However, as we have shown, the flow does not transition to turbulence inside the domain. The observation that the momentum thickness Reynolds number was 105 at $Re_x = 34,650$, further suggests that it is improbable, if not impossible, to see transition at $Re_D = 385$ within the flow region considered. Furthermore, the experimental observation that, at $Re_D = 1155$, the onset of transition occurs at a distance from the leading edge smaller than the distance between the cylinder and the plate, cannot be caused by the response of the boundary layer to wake turbulence (which would imply particle trajectories that form an angle greater than 45^o to the wake centerline). Instead, it suggests that the phenomena observed in the experiment are due to the advection caused by the von Kàrmàn street and reflect the wake breakdown more than the boundary layer response to the perturbation. Thus, the loss of a sinusoidal character may not be an appropriate measure of transition. Instead, it may be an indicator of the onset of a

perturbed flow regime inside the boundary layer that may lead to transition farther downstream.

3.5.3 Onset of turbulence

The ability to predict and control the onset of transition is the ultimate goal in theoretical and applied transition studies. Although our simulations span only a decade in the Reynolds number range, we can use the present data to make a conjecture on the effect of increasing the cylinder Reynolds number on transition onset. The location of the cylinder inside the domain is another important variable, and its effects on transition should be investigated in a future study.

Figure 3.5 shows skin-friction coefficients for the three cases as a function of Re_x. The curves do not collapse under the Re_x scaling; in fact, the onset of transition in the high Reynolds number case occurs at a Re_x value that is more than two times larger than for $Re_D = 1155$. To understand this behavior, we compare in figure 3.15 contours of the spanwise vorticity in an xy-plane in the transition region for the two cases. This figure shows that the wake spreading is very similar for the two cases, *i.e.* it is a weak function of the Reynolds number. An obvious difference in the range of turbulent scales is present due to the factor of three difference in the Reynolds numbers. The boundary layer is also much thinner in the $Re_D = 3900$ case, since $\delta \sim Re^{1/2}$. Because of the weak Reynolds-number dependence of the wake spreading, the boundary layer and the wake begin to interact at approximately the

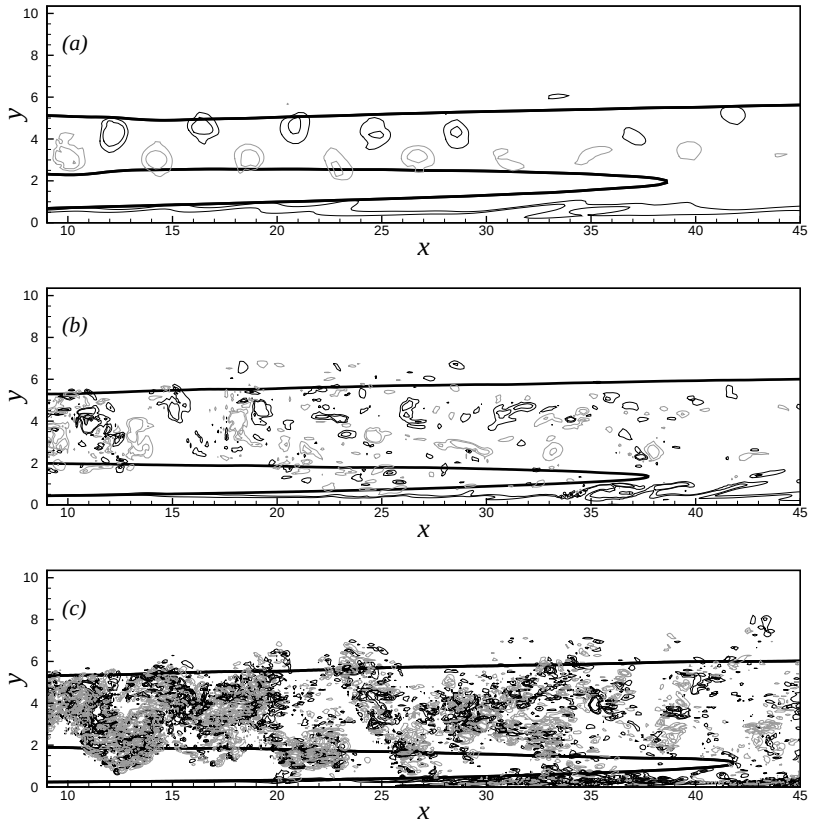

Figure 3.15: Contours of the spanwise vorticity. *(a)* $Re_D = 385$; *(b)* $Re_D = 1155$; *(c)* $Re_D = 3900$. Contour levels are ± 0.5 and ± 1; negative contours are grey. The thick lines are $U = 1$ isolines, showing the wake and boundary-layer thickness.

same distance from the leading edge for the three cases. The visualization in the figure shows wake turbulence impinging on the boundary layer around $x = 20$ for all three Reynolds numbers. However, at some instants of time, direct impingement of the wake turbulence on the boundary layer can be visually observed as far upstream as $x = 15$. The figure also shows that the mean velocity profile loses its inflection points near $x = 40$ ($x = 39$, 38, and 42, for the three Re_D cases, from lowest to highest), indicating that the location of merger between the wake and the boundary layer is relatively insensitive to the cylinder Reynolds number. However, once the boundary layer has been perturbed, the Reynolds number effect becomes important: the higher the Reynolds number the more rapid the breakdown to turbulence.

The effect of the Reynolds number on the dynamics of the wake/boundary-layer interaction is further illustrated in figures 3.16 and 3.17. Figure 3.16 shows the mean velocity and turbulent kinetic energy profiles at several x-locations for the three Re_D cases. Figure 3.17 shows TKE profiles at three x-locations, the onset of transition, the middle of the C_f rise ("halfway" through transition), and the onset of full-blown turbulence (the end of transition and the location of maximum C_f). The distance to the wall is normalized by the boundary-layer thickness, δ_{99} (which was computed on the basis of U_{edge} instead of U_∞, as explained in §4.1).

The weak dependence of wake development on the Reynolds number is evident in figure 3.16. Apart from the initial decay of TKE in the near wake, one sees relatively little difference between the profiles, despite a factor of 10 in the Reynolds numbers. We note that, due to the difference in the boundary-layer growth-rates,

the turbulence intensity at the edge of the boundary layer is different for the three cases. At the beginning of the transition region, for instance, the turbulence level at the boundary-layer edge is higher by almost a factor of two in the $Re_D = 1155$ case compared to the $Re_D = 3900$ case (figure 3.17). It is not clear whether this difference plays a significant role in accelerating transition since the wake introduces instabilities into the boundary layer as close upstream as $x = 10$ at some instances. It is possible that increased turbulence at the edge of the boundary layer accelerates the laminar breakdown. Figure 3.17 shows that the turbulent kinetic energy near the onset of transition is nearly 50% lower at $Re_D = 3900$, in comparison with the $Re_D = 1155$ case. The TKE grows much faster in the high-Re case, and the level of TKE at the end of transition is, in fact, larger than that for $Re_D = 1155$.

Thus, it would appear that wake induced boundary-layer transition in the present configuration depends both on the physical distance from the plate leading edge, x/D, and on the plate Reynolds number, Re_x. The former dependence appears as an "interaction distance," the physical streamwise distance needed for the wake disturbance to contaminate the boundary layer, while the Re_x dependence enters through the degree of boundary-layer instability, which increases with Re_x. From the above observations, we can conjecture that transition may depend on a Reynolds number based on the distance from the impingement point, x_i. If, in the present simulations, we take the impingement distance to be $x_i/D = 15$, which corresponds to the streamwise location at which laminar streaks are first clearly observed, independent of Re_D (see figure 3.12 and the accompanying discussion),

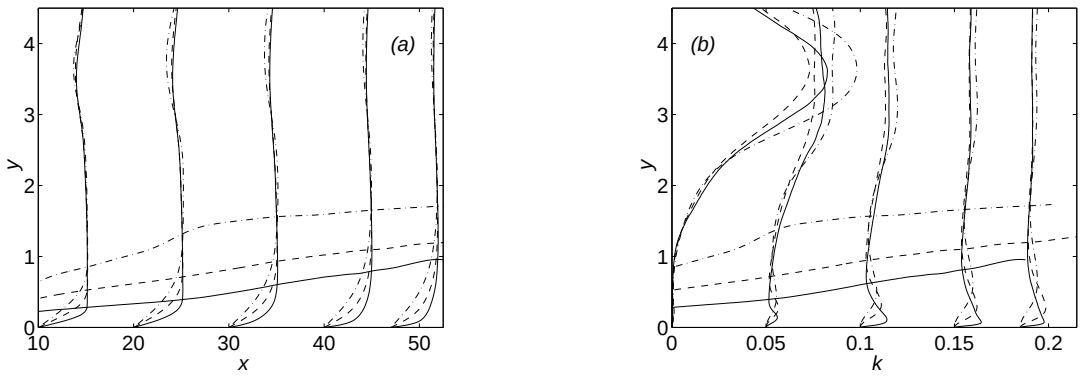

Figure 3.16: Profiles of streamwise velocity (a) and TKE (b) at locations $x = 10$, 20, 30, 40, 47 from left to right. —— $Re_D = 3900$, --- $Re_D = 1155$, —·— $Re_D = 385$; the horizontal lines represent the boundary-layer thickness for each case. In *(a)*, the velocity profile is amplified by a factor of five for clarity; in *(b)*, the TKE profiles are offset by 0.05.

then we can compute a modified Reynolds number as $Re_i = (x - x_i)U_\infty/\nu$. This formula yields $Re_i \simeq 17,500$ and $Re_i \simeq 19,500$ for the locations of transition onset at $Re_D = 1155$ and $Re_D = 3900$, respectively. In order to verify the relevance of Re_i, experiments and simulations should be carried out at higher Reynolds numbers and with varying locations of the cylinder inside the flow domain.

3.6 Conclusion

High resolution DNS and LES studies of cylinder wake induced boundary layer-transition were carried out at three Reynolds numbers, $Re_D = 385$, 1155 and 3900. In all three cases, coherent, almost two-dimensional spanwise rollers, are present di-

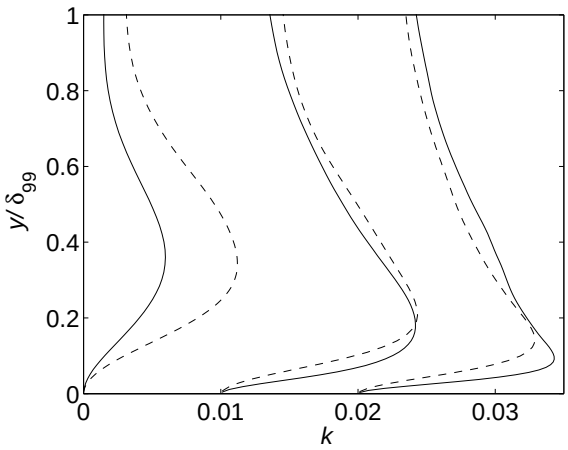

Figure 3.17: Turbulent kinetic energy profiles in the beginning, the middle, and the end of the transition region; —— $Re_D = 3900$ --- $Re_D = 1155$; from left to right, the streamwise locations of the profiles are $x = 30$, 50, 70 for the $Re_D = 1155$ case, and $x = 20$, 30, 40 for the $Re_D = 3900$ case.

rectly behind the cylinder. A short distance downstream of the cylinder, these rollers develop spanwise-periodic deformations, which cause the injection of external wake momentum into the boundary layer. The disturbances entering the boundary layer evolve into streaks of streamwise velocity, which, in the two higher Re_D cases, lead to transition to turbulence. The onset of transition occurs at relatively low Reynolds numbers, $Re_x \simeq 60,000$ for the $Re_D = 1155$ case, and $Re_x \simeq 120,000$ for the $Re_D = 3900$ case. The transition scenario is somewhat similar to bypass transition due to free-stream turbulence, in which transition onset also occurs at comparable Re_x values: profiles of u_{rms} inside the perturbed laminar boundary layer were similar to those documented by Matsubara & Alfredsson (2001), and spectra of streamwise velocity showed rapid initial growth in the low-frequency component,

consistent with observations of bypass transition due to FST Furthermore, for the $Re_D = 3900$ case, the transitional region was intermittent and bore similarity to intermittency in transition due to FST, that is caused by the formation and subsequent evolution of turbulent spots. Despite these similarities, the two transition scenarios are distinct in the nature of the external perturbation: in our case it is strongly coherent and anisotropic, whereas in transition due to FST it is approximately isotropic and has no large-scale unsteadiness. The simulations indicate that the spacing of laminar boundary-layer streaks is the same for the all three velues of Re_D, being determined by the scale of the deformation of the primary roller core, which has only a weak Reynolds number dependence. In contrast, in transition due to FST, laminar streaks are on the order of δ_{99} apart. For these reasons, the parallels between the two cases should be made with caution. We have examined mean velocity statistics, Reynolds stress profiles, and TKE budgets throughout the computational domain and concluded that, in the $Re_D = 1155$ and $Re_D = 3900$ cases, the boundary-layer turbulence is fully developed. Finally, we noted that transition in the two higher Re_D cases was observed at widely different Re_x values. This phenomenon can be explained by conjecturing that transition can occur only after a fixed, nearly Re_D-independent "interaction distance," *i.e.*, the streamwise length needed for the wake disturbance to reach the boundary layer. Once the boundary layer is contaminated, transition depends primarily on the boundary-layer Reynolds number, Re_x. Future work should include studies of transition due to different types of upstream disturbances, such as wakes behind other types of bluff bodies.

Acknowledgments

The first two authors acknowledge the financial support of the NASA Langley Research Center, under Cooperative Agreement NAG12285.

3.7 References

[1] Balaras, E. 2004 Modeling complex boundaries using an external force field on Cartesian grids in large-eddy simulations. *Comput. Fluids* **33**, 375–404.

[2] Balaras, E., Benocci, C. & Piomelli, U. 1995 Finite difference computations of high Reynolds number flows using the dynamic subgrid-scale model. *Theoret. Comput. Fluid Dyn.* **7**, 207–216.

[3] Balaras, E., Piomelli, U. & Wallace, J. M. 2001 Self-similar states in turbulent mixing layers *J. Fluid Mech.*, **446**, 1–24.

[4] Bandyopadhyay, P. R. 1987 Resonant flow in a row of small transverse cavities submerged in a turbulent boundary layer. *AIAA Paper 1987-1235.*

[5] Brandt, L., Schlatter, P. & Henningson, D. S. 2004 Transition in boundary layers subject to free-stream turbulence. *J. Fluid Mech.* **517**, 167–198.

[6] Chorin, A. J. 1968 Numerical solution of the Navier-Stokes equations. *Math. Comput.* **22**, 742–762.

[7] Fadlun, E. A., Verzicco, R., Orlandi, P. & Mohd-Yusof, J. 2000 Combined immersed-boundary finite-fifference methods for three-dimensional complex flow simulations. *J. Comput. Phys.* **161**, 35–60.

[8] Henningson, D., Spalart, P. & Kim, J. 1987 Numerical simulations of turbulent spots in plane Poisseuille and boundary-layer flow *Phys. Fluids* **30**, 2914–2917.

[9] Huai, X., Joslin, R. D., Piomelli, U. 1997 Large-eddy simulation of transition to turbulence in boundary layers. *Theoret. Comput. Fluid Dynamics* **9**, 149–163.

[10] Jacobs, G. J. & Durbin, P. A. 2001 Simulations of bypass transition. *J. Fluid Mech.* **428**, 185–212.

[11] Kim, J. & Moin, P. 1985 Application of a fractional step method to incompressible Navier-Stokes equations. *J. Comput. Phys.* **59**, 308–323.

[12] Klebanoff, P. S. 1971 Effect of freestream turbulence on the laminar boundary layer. *Bull. Amer. Phys. Soc.* **10**, 1323.

[13] Kravchenko, A. G. & Moin, P. 2000 Numerical studies of flow over a circular cylinder at $Re_D = 3900$. *Phys. Fluids* **12**, 403–417.

[14] Kusunose, K. & Cao, H. V. 1994 Prediction of transition location for a 2-D Navier-Stokes solver for multi-element airfoil configurations. *AIAA Paper 1994-2376.*

[15] Kyriakides N. K., Kastrinakis, E. G., Nychas, S. G. & Goulas, A. 1996 Boundary layer transition induced by a von Karman vortex street wake. *Proc. Inst. Mech. Eng.* **210**, 167–179.

[16] Kyriakides N. K., Kastrinakis, E. G., Nychas, S. G., & Goulas, A. 1999 A bypass wakeinduced laminar turbulent transition. *Eur J. Mech. B-Fluid* **18**, 1049–1065.

[17] Liu, X. & Rodi, W. 1991 Experiments on transitional boundary layers with wake-induced unsteadiness *J. Fluid Mech.* **231**, 229–256.

[18] Matsubara, M. & Alfredsson, H. 2001 Disturbance growth in boundary layers subjected to free-stream turbulence. *J. Fluid. Mech.* **430**, 149–168.

[19] Meneveau, C., Lund, T. S. & Cabot, W. H. 1996. A Lagrangian dynamic subgrid-scale model of turbulence. *J. Fluid Mech.* **319**, 353–385.

[20] Meredith, P. T. 1993 Viscous phenomena affecting high-lift systems and suggestions for future CFD development. *AGARD* **CP-515** 19.1–19.8.

[21] Morinishi, Y., Lund, T. S., Vasilyev, O. V. & Moin, P. 1998 Fully-conservative higher order finite difference schemes for incompressible flow. *J. Comput. Phys.* **143**, 90–124.

[22] Moser, R. D., Kim, J. & Mansour, N. N. 1999 Direct numerical simulation of turbulent channel flow up to $Re_\tau = 500$. *Phys. Fluids* **11**, 943–945.

[23] Norberg, C. 1993 Pressure forces on a circular cylinder in cross flow. *Proceedings of IUTAM Symposium on Bluff-Body Wakes, Dynamics and Instabilities,* Göttingen, Germany, September 7-11, 1992, Proc. eds. Eckelmann, H., Graham, J. M. R., Huerre, P. & Monkewitz, P. A., Springer-Verlag, Berlin, 275-278.

[24] Ong, L. & Wallace, J. 1996 The velocity field of the turbulent very near wake of a circular cylinder. *Exp. Fluids* **20**, 441–453.

[25] Orlanski, I. 1976 Simple boundary condition for unbounded hyperbolic flows. *J. Comput. Phys.* **21**, 251–269.

[26] Ovchinnikov, V. O., Piomelli, U. & Choudhari, M. M., 2004 Inflow conditions for numerical simulations of bypass transition *AIAA Paper*, **2004-0591**.

[27] Piomelli, U., Balaras, E. & Pascarelli, A. 2000 Turbulent structures in accelerating boundary layers. *J. Turbulence* **1**, (001) 1–16.

[28] Piomelli, U., Choudhari, M. M., Ovchinnikov, V. O. & Balaras, E.,2004 Numerical simulations of wake/boundary layer interactions. *AIAA Paper*, **2004-0975**

[29] Rai, M. M. & Moin, P. 1993 Direct numerical simulation of transition and turbulence in a spatially evolving boundary layer. *J. Comput. Phys.* **109**, 169–192.

[30] Roach, P. E., & Brierley, D. H. 1992 The influence of a turbulent free-stream on zero pressure gradient transitional boundary layer development part I: test cases T3A and T3B. In *Numerical Simulation of unsteady flows and transition to turbulence*, O. Pironneau, W. Rodi, I. L. Rhyming, A. M. Savill and T. V. Truong, eds. Cambridge, 319–347.

[31] Spalart, P. R. 1986 Numerical study of sink-flow boundary layers. *J. Fluid Mech.* **172**, 307–328.

[32] Squire L. C. 1989 Interactions between wakes and boundary-layers. *Prog. Aerospace Sci.* **26**, 261–288.

[33] Westin, K. J. A., Boiko, B. G. B., Klingmann, G. B., Kozlov, V. V., Alfredsson, P. H. 1994 Experiments in a boundary layer subjected to free stream turbulence. Part I. Boundary layer structure and receptivity. *J. Fluid. Mech.* **281**, 193-218.

[34] Williamson, C. H. K. 1996 Three-dimensional wake transition. *J. Fluid Mech.* **328**, 345–407.

[35] Wu, X., Jacobs, R. G., Hunt, J. C. R. & Durbin, P. A. 1999 Simulation of boundary layer transition induced by periodically passing wakes *J. Fluid Mech.* **398**, 109–153.

[36] Zhou, M. D. & Squire, L. C. 1985 The interaction of a wake with a turbulent boundary-layer. *J. Aeronaut.* **89**, 72–81.

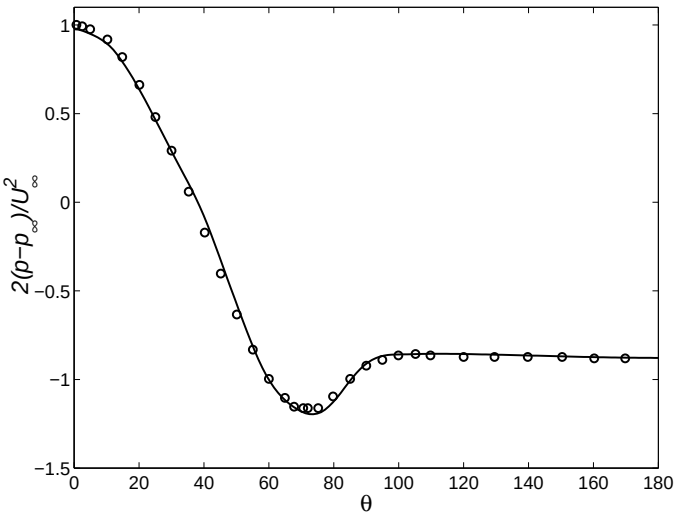

Figure 3.18: Evolution of the pressure coefficient along the cylinder surface at $Re_D = 3,900$ (validation case). The stagnation point corresponds to $\theta = 0$. ——, Immersed boundary simulation; ∘ experiments by Norberg (1993)

3.8 Addendum

In this section, we provide additional data that were not included in the article due to space limitations. Figure 3.18 presents a comparison of the pressure coefficient, $C_p = 2\left(p - p_\infty\right)/U_\infty^2$, along the cylinder surface at $Re_D = 3,900$ from our immersed boundary simulation and the experimental data of Norberg (1993). The good agreement demonstrates the ability of the immersed boundary method to accurately predict the forces that a fluid exerts on a submerged object.

In figure 3.19 we show a comparison of the skin friction coefficient (C_f) of box I of the $Re_D = 1155$ case (LES) obtained on the final mesh ($1056 \times 384 \times 128$) and on a coarser mesh ($816 \times 288 \times 96$), as described in §3. We see that the onset

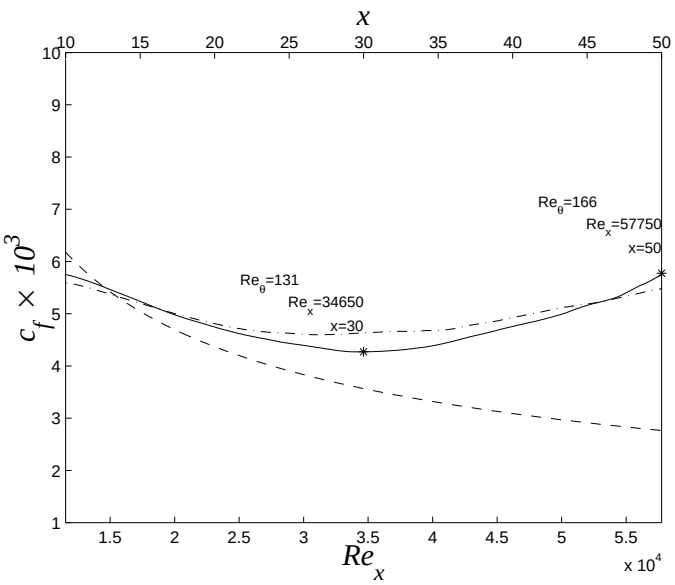

Figure 3.19: Grid resolution study. $Re_D = 1155$ box I. ——— , 816 × 288 × 128, —·— , 1056× 384 × 128, - - - , laminar C_f

of transition does not change significantly for the low-resolution case, and therefore conclude that the final mesh, in particular, resolves the transitional flow field adequately.

Next, we present the TKE budgets for cases $Re_D = 385$ and $Re_D = 3900$. The budget corresponding to the intermediate $Re_D = 1155$ case is included in the article. Figures 3.20 ($Re_D = 385$) and 3.21 ($Re_D = 3900$) complement the discussion in §4. Note, in particular, that the evolution of the $Re_D = 3900$ budget is qualitatively similar to that of the $Re_D = 1155$ case (figure 3.8). At $Re_D = 385$, the budget at the final position, ($x = 88$), is that of a perturbed-laminar boundary layer. This can be seen by noting the low levels of dissipation and diffusion in the near-wall region compared to a turbulent boundary layer. Aside from this difference, the

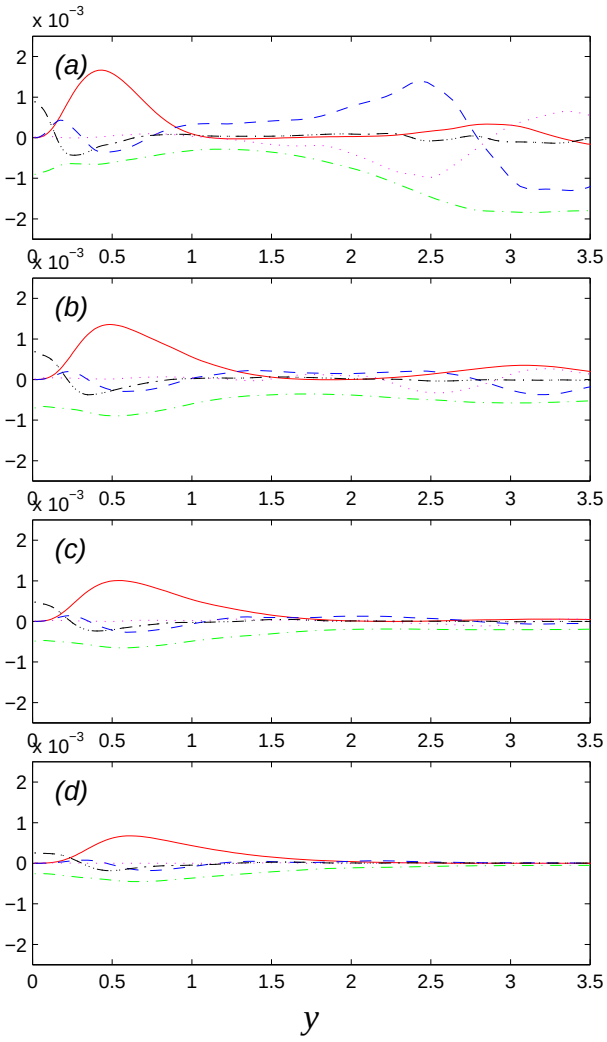

Figure 3.20: Budgets of k at various locations; $Re_D = 385$. All terms are normalized by U_∞ and D. (a) $x = 20, Re_x = 7,700, \delta_{99} \simeq 1.25$; (b) $x = 40, Re_x = 15,400, \delta_{99} \simeq 1.5$; (c) $x = 60, Re_x = 23,100, \delta_{99} \simeq 2.0$; (d) $x = 88, Re_x = 33,880, \delta_{99} \simeq 2.4$. —— production —·— dissipation, - - - turbulent transport, ····· pressure diffusion; —···— viscous diffusion.

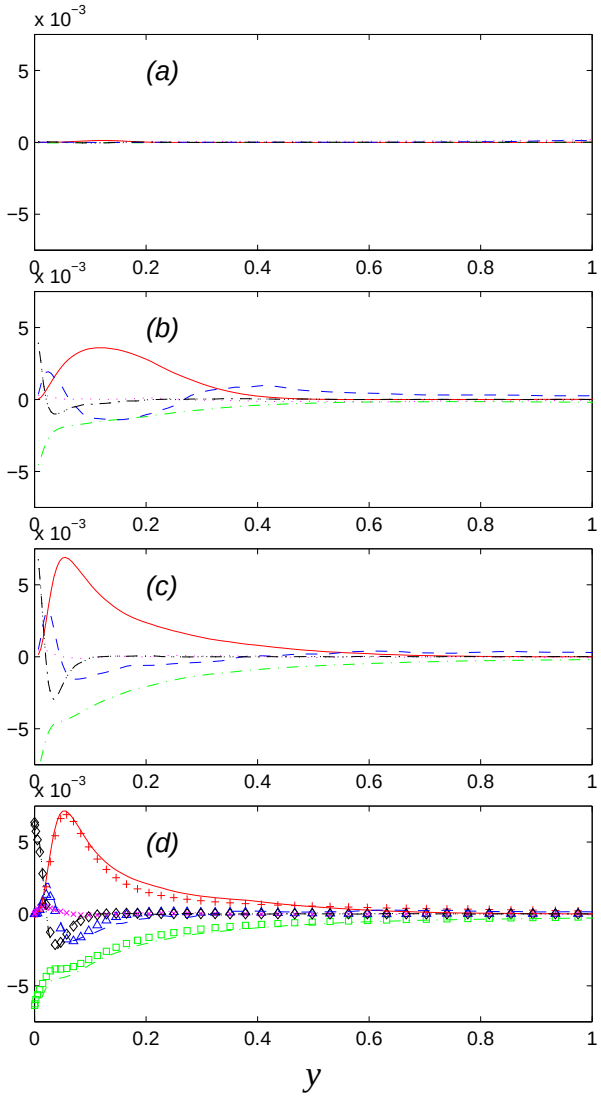

Figure 3.21: Budgets of k at various locations; $Re_D = 3900$. All terms are normalized by U_∞ and D. (a) $x = 8, Re_x = 31,200, \delta_{99} \simeq 0.25$; (b) $x = 26, Re_x = 101,400, \delta_{99} \simeq 0.5$; (c) $x = 41, Re_x = 159,900, \delta_{99} \simeq 0.82$; (d) $x = 47, Re_x = 183,300, \delta_{99} \simeq 0.96$. Symbols: channel flow DNS by Moser *et al.* (1999); lines: present simulation. +, ——— , production; □ , —·— Dissipation; △ , - - - Turbulent transport; × , ····· Pressure diffusion; ◇ , —···— Viscous diffusion.

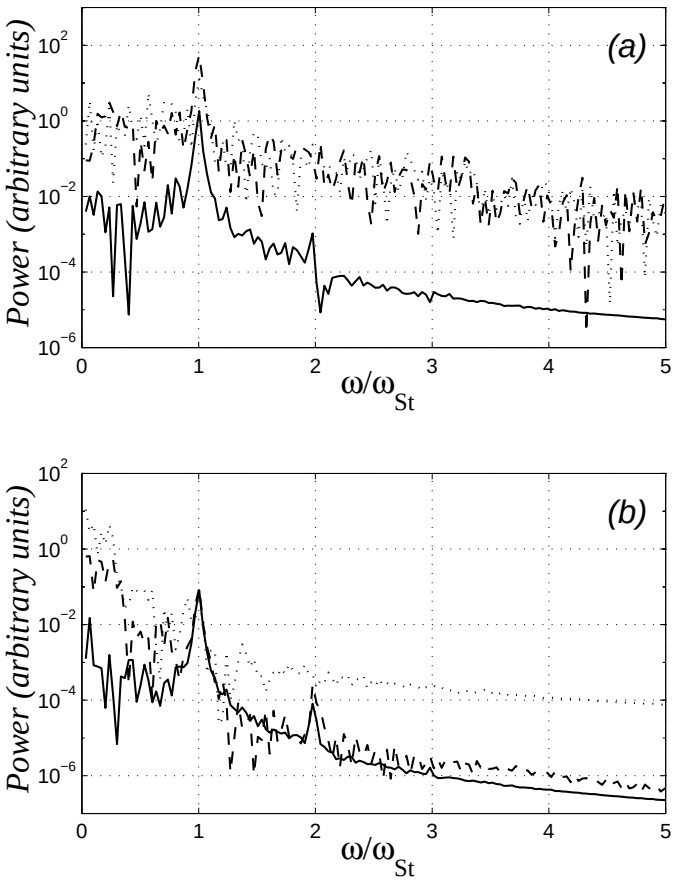

Figure 3.22: Spectra of the streamwise velocity for the $Re_D = 385$ case; (a) in the free stream ($y = 2$), (b) inside the boundary layer ($y = 0.1$); —— $x = 0$, - - - $x = 10$ ····· $x = 30$

perturbed-laminar budget looks remarkably similar to that of a near-wall turbulent flow.

In figures 3.22 and 3.23 we show frequency spectra for the $Re_D = 385$ and $Re_D = 3900$ cases, respectively. The spectra in figures 3.22a and 3.22b are plotted at locations $y = 0.1$ and $y = 2$, respectively, and show the difference between the boundary layer and the free stream. In accordance with the discussion in §4.2, we

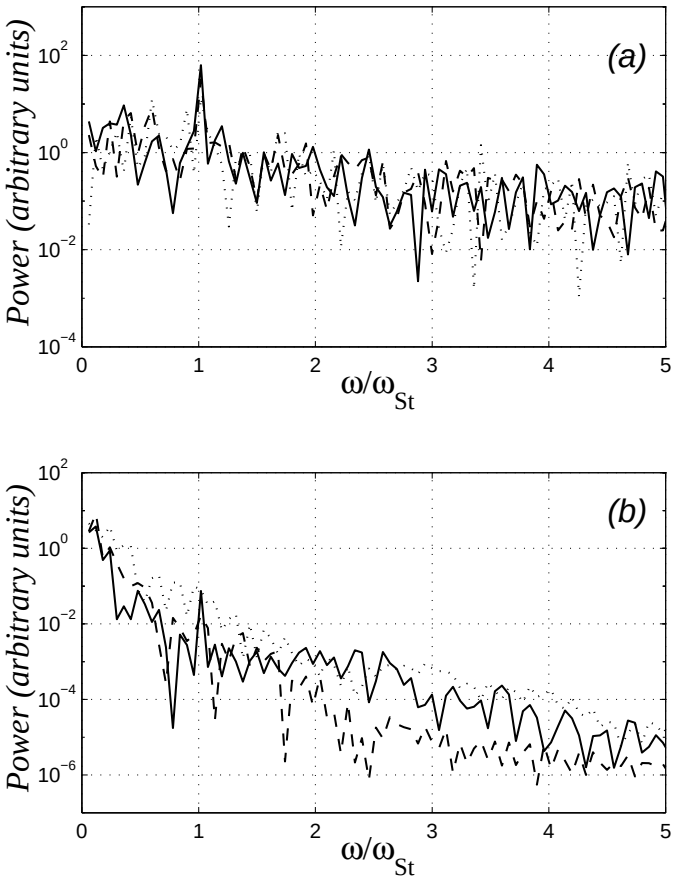

Figure 3.23: Spectra of the streamwise velocity for the $Re_D = 3900$ case; (a) in the free stream ($y = 2$), (b) inside the boundary layer ($y = 0.05$); —— $x = 0$, - - - $x = 10$ ····· $x = 30$

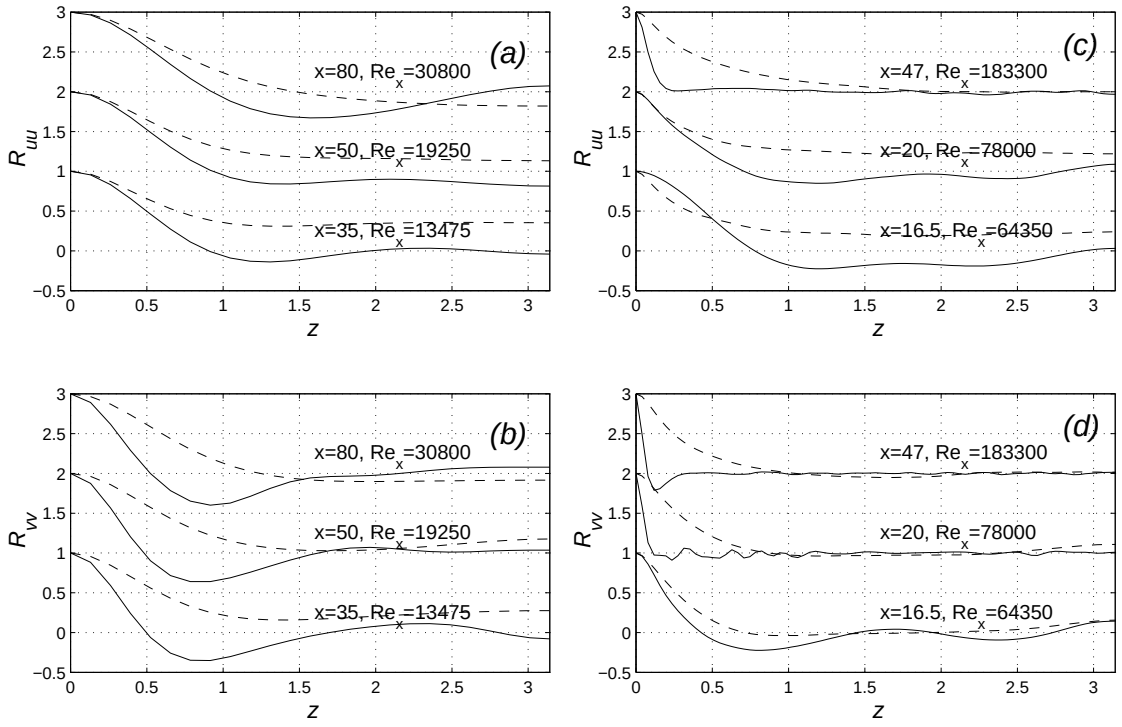

Figure 3.24: Spanwise correlation functions of the streamwise and wall-normal velocity fluctuations; (a) $Re_D = 385$, R_{uu}; (b) $Re_D = 385$, R_{vv}; (c) $Re_D = 3900$, R_{uu}; (d) $Re_D = 3900$, R_{vv}; - - - , $y = 2$; ——— , $y = 0.2$

see that preferential amplification of low-frequency components with $\omega/\omega_{St} \leq 0.5$, occurs in the boundary layer, but not in the free stream. Figures 3.23*(a)* and 3.23*(b)* show similar behavior (but less pronounced) for the $Re_D = 3900$ case.

In figure 3.24 we supplement the near-wall correlation data of figure 3.10 with that in the free stream (dashed lines). The plots corresponding to the free stream do not show a dip in the correlation functions that is present close to the wall. Thus, we see that streaks are present only inside the boundary layer. Also we note that due to the coherence of the wake, the free-stream velocities remain correlated in

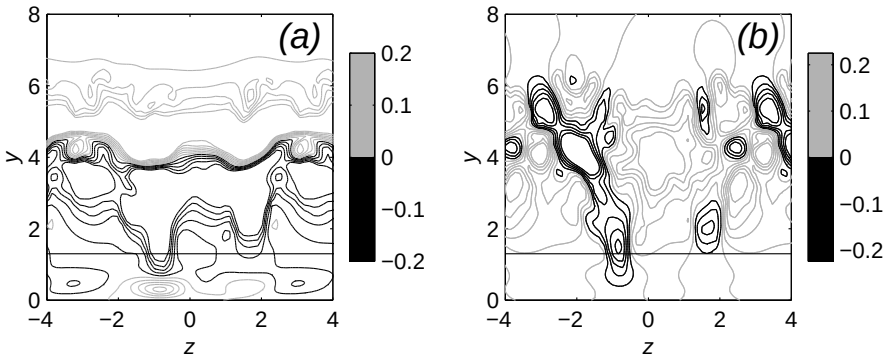

Figure 3.25: Contours of (a) streamwise and (b) wall-normal velocity fluctuations in the $y-z$ plane at $x = 10$; horizontal line denotes the boundary-layer edge. Contour levels are clustered near zero for a better view inside the boundary layer.

the spanwise direction, but, as intuitively expected, the correlation diminishes with increasing streamwise distance and flow Reynolds number.

Next, in figure 3.25*(a)* and 3.25*(b)*, we show contours of the streamwise and wall-normal velocity fluctuation for the $Re_D = 385$ case in a cross-stream $(y-z)$ plane. The plane is located at $x = 10$ and a horizontal line denotes the edge of the boundary layer. Figure 3.25*(a)* indicates that the plane cuts across a clockwise-rotating spanwise roller (if the flow is from left to right). The waviness of the contours in the center is consistent with the deformation of the roller in the $(x-z)$ plane, which partially reorients the spanwise vorticity of the roller in the streamwise direction. The streamwise-oriented sections of the roller inject fluid into the boundary layer, as shown by the two regions of negative wall-normal velocity fluctuation across the boundary layer at locations $z \simeq -0.8$ and $z \simeq 1.8$. At these two locations, the streamwise fluctuation is negative because the lower part of the wake

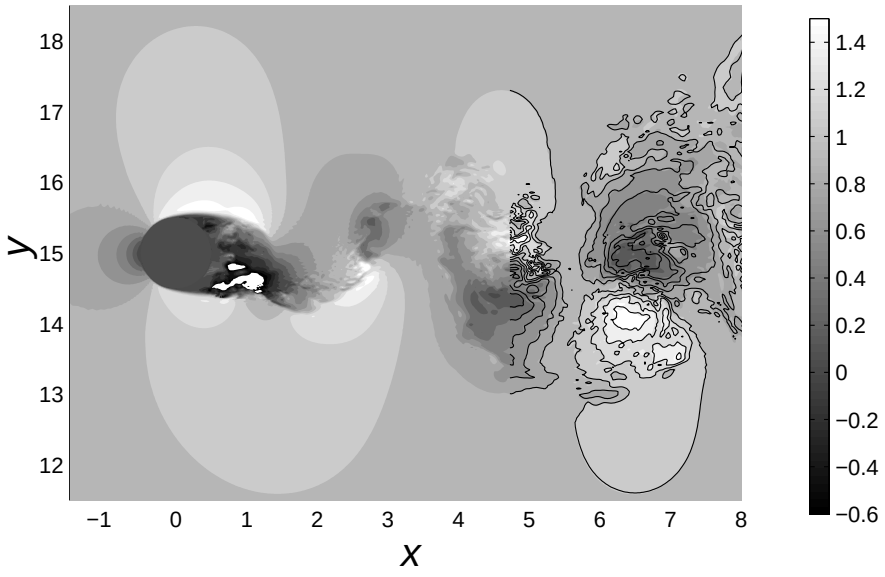

Figure 3.26: Contours of the streamwise velocity fluctuation. Filled contours – box I of auxiliary simulation; lines – box II

is moving slower than the average particle at the boundary-layer edge. In response to the injections of low-speed flow, the boundary layer appears to develop laminar velocity streaks.

In response to one referee's concern about violating the ellipticity of the NS equations by using one-way coupling between two streamwise subdomains, we performed an auxiliary simulation of flow past a circular cylinder at $Re_D = 3,900$ in two ways: with single domain and with two overlapping subdomains, as described in the third paragraph of §2.2. The simulations were run synchronously, which permitted comparisons of instantaneous quantities. Here we present a plot of u-velocity contours from the two simulations superimposed on top of each other (figure 3.26). It can be seen that the violation of ellipticity is sufficiently minor that our results

can be deemed reliable.

Preface to Chapters 4 & 5

In the next two articles, we investigate the validity of synthetic-turbulence inflow conditions for simulations of boundary-layer transition due to free-stream turbulence (FST). Because of the high cost of computation, to date, all well-resolved DNS of bypass transition have been performed on truncated domains, *i.e.* domains in which the inflow plane is at some arbitrary location downstream of the leading edge (LE). Not including the LE region in the computation raises the question of the inflow condition for the truncated domain. Here, the scientist is forced to make an educated guess about the state of boundary-layer/FST interaction at the inflow plane. The simplest solution that has been used in most simulations, is to specify the inlet velocity as a superposition of a zero-mean disturbance field (approximation to FST) and the Blasius mean velocity profile.

Chapter 4 examines several possible choices for the first component, and the effect of parameter choices that the investigator has to make. The influence of the FST length scale on the transition location is also discussed. Chapter 5 compares the results of truncated-domain simulations to those of a simulation which includes the plate leading edge.

We conclude that truncated-domain simulations, as currently implemented, do not yield reliable predictions of transition onset. The two chapters precede a thorough investigation of the transitional boundary layer in a high-amplitude FST

environment performed on a domain that contains the leading edge of the plate.

Chapter 4

Inflow conditions for numerical simulations of bypass transition[1]

4.1 Abstract

High-resolution, direct numerical simulations of boundary-layer bypass transition due to free-stream turbulence are performed and the effects of different inflow conditions and inflow noise parameters on the location of the transition onset are examined. The length scale of the free-stream noise and the extent of noise penetration into the boundary layer are found to affect strongly the transition point location, regardless of the inflow-generation method used. It is concluded that in order to assure unambiguous comparisons between simulation and experiment, future experimental data must provide information on the length scale of the free-stream turbulence, and profiles of the Reynolds stresses across the boundary layer at locations well upstream of the transition point.

[1]Originally published as

Ovchinnikov, V. O., Piomelli, U. & Choudhari, M. M., 2004 Inflow conditions for numerical simulations of bypass transition *AIAA Paper*, **2004-0591**.

4.2 Introduction

Transition prediction has its place among the most important practical problems in fluid dynamics today. Among its immediate applications are optimization of airfoil and turbine design, in which it is frequently desirable to delay transition to turbulence and avoid boundary layer separation.

The classical picture of transition in wall-bounded flows in a benign disturbance environment, the so-called 'natural transition', begins with linear stability theory. The Orr-Sommerfeld equation obtained from linear stability analysis admits solutions in the form of Tollmien-Schlichting waves (Drazin & Reid 1981), which have been observed during experiments on boundary layer transition (Kachanov, Kozlov & Levchenko, 1980). Transition due to Tollmien-Schlichting waves, however, is a slow process and occurs if the boundary layer perturbations are very small (*e.g.* less than about 0.5% of the free-stream velocity). When the levels of free stream disturbances rise above 1%, as is the case in many engineering applications, transition occurs farther upstream. This behavior has been termed "bypass transition" after the fact that the transition process seems to bypass the Tollmien-Schlichting waves completely (Morkovin 1969). The phenomenon of transient algebraic growth due to the non-normality of the linear NS operator has been implicated in bypass transition and studied theoretically and numerically (Ellingsen & Palm 1975; Butler & Farrel 1992; Andersson, Breggren & Henningson 1999).

Bypass transition due to moderate to high levels of FST in laminar bound-

ary layers with zero streamwise pressure gradient has been studied experimentally (Roach & Brierlay 1992, Matsubara & Alfredsson 2001) and numerically through LES (Voke & Yang 1995) and DNS (Jacobs & Durbin 2001, Rai & Moin 1993, Brandt, Schlatter & Henningson 2004).

It was initially surmised that a realistic simulation of bypass transition would involve only moderate computational cost. Voke and Yang (1995) performed LES simulations on a coarse mesh (with a total of 0.7 M points) and obtained reasonable agreement with experiments. In an earlier study, Rai and Moin (1993) estimated the grid resolution requirements for a satisfactory DNS to be seven times finer in the streamwise and spanwise directions (each) than those used in the LES by Voke & Yang (1995). Their numerical method had fourth-order overall spatial accuracy, but was upwind-based for convective terms and thus was not energy conserving. Due to the unavailability of computational resources, Rai and Moin (1993) were forced to use sub-optimal resolution (with a total of 1.8 M points) and yet obtained good qualitative agreement with experiments.

Recently, well-resolved simulations of bypass transition were performed by Jacobs and Durbin (2001) who relied on the detailed grid refinement studies of Wu, Jacobs, Hunt and Durbin (1999). Jacobs and Durbin (2001) confirmed the resolution requirements of Rai and Moin (1993) for their second-order code and used grids with 71 and 45 million points for simulations of transition due to 3% and 7% free-stream turbulence intensity, respectively. At this resolution, Jacobs and Durbin were able to provide valuable insights into the physics of the transition mechanism, showing,

in particular, that very fine streamwise and spanwise resolution are essential for capturing laminar streak breakdown on the path to turbulence. They also obtained good overall agreement with experiments. Properly resolved DNS simulations of bypass transition were performed by Brandt *et al.* (2004), but with the aim of studying the flow physics rather than to match any experiment.

Assuming adequate grid resolution, when performing calculations of bypass transition, the issue of generating physically realistic inflow conditions must also be addressed. In experimental studies, typically, a flat plate is immersed in a fluid stream downstream of a grid that generates homogeneous isotropic turbulence. The turbulence characteristics are measured some distance upstream and/or above the plate. In numerical calculations, on the other hand, the leading-edge of the plate is generally excluded. Inflow conditions usually consist of a Blasius laminar velocity profile, over which perturbations resembling (more or less closely) homogeneous isotropic turbulence are superimposed. While it is possible to match the turbulence free-stream intensities of an experimental study, and even the turbulence length scales, if necessary, the absence of the leading edge introduces a degree of arbitrariness. Physically, the penetration of the free-stream turbulence into the boundary layer is determined by the interaction of the leading edge with the free-stream turbulence. In numerical studies, however, it is imposed *a priori*, as the turbulence intensity is forced to go to zero as the wall is approached.

The simplest inflow condition used for bypass transition studies uses a prescribed turbulence spectrum with random phases (Rogallo 1981) to generate ap-

proximately isotropic turbulence in the free-stream region. The correct phase relationships between the modes of the noise is established downstream, hopefully close to the inlet. The advantage of this method is that it is relatively simple to implement; its greatest weakness is that the noise thus generated must be suitably attenuated inside the boundary layer such that the no-slip boundary conditions are satisfied at the solid surface. The shape of this decay function must be assigned on an *ad hoc* basis.

Alternatively, inflow can be generated through precursor simulations over a computational domain that extends farther upstream of the intended inflow location for the bypass transition calculations (Voke & Yang 1995). The precursor simulation is driven by (unphysical) random noise at the inlet, typically with free-slip boundary conditions on the bottom wall. One then estimates a streamwise location inside the upstream box at which the disturbance has become physical, and uses cross-flow planes at that location as inflow conditions for the main simulation. The advantage of this method is that one does not need to generate physical disturbances for the precursor simulation and that the precursor simulation guarantees a physical noise (away from the wall) with a well-defined length scale. A serious drawback is that one must still use an (arbitrary) cut-off function to force the disturbance to zero at the wall and that the disturbance evolving in the precursor box is not influenced by the boundary layer, and may not be physical near the wall. The increased cost of the calculation and the additional storage requirements are additional drawbacks of this technique.

Jacobs and Durbin (2001) proposed a novel inflow-generation method based on the earlier work of Grosch and Salwen (1978). In their method, an arbitrary disturbance is expressed as a superposition of Orr-Sommerfeld modes from the continuous spectrum, which have a finite L_∞ norm, but unbounded L_2 norm[2]. The eigenfunctions of this alternative basis, when computed about the Blasius profile as the base flow, have the added virtue of automatically satisfying the no-slip boundary conditions at the solid wall, thus obviating the need for arbitrary cut-off functions. Arguing that the Orr-Sommerfeld eigenfunctions behave as Fourier modes in the free-stream, the authors use a procedure similar to the one proposed by Rogallo (1981) to obtain the amplitude coefficients for each eigenfunction.

Although the inflow-generation algorithm of Jacobs and Durbin (2001) represents an improvement over the other two approaches, ambiguity still remains in the choice of the wall-normal modes used to represent the disturbance. This arbitrariness, as will be shown, may significantly affect the prediction of the inception of transition. The objective of this work is to investigate how the inflow-generation mechanisms affect the transition process. First, we will present the results of our-grid refinement study inside domains identical to those used by Jacobs and Durbin (2001) to facilitate comparisons with their data and experiments by Roach and Brier-

[2]The expansion of an arbitrary three-dimensional velocity disturbance requires the addition of wall-normal vorticity (Schmid & Henningson 2001), obtained by solving Squire's equation. However, Jacobs and Durbin (2001) argued that an adequate approximation to free stream noise can be obtained using only the Orr-Sommerfeld spectrum.

lay (Roach & Brierlay, 1992), and point out the consequences of under-resolution. In addition, we have implemented and tested the three inflow-generation mechanisms mentioned above and investigated the effects of varying the length scale of the free-stream noise and its penetration depth into the boundary layer.

In the following, we will first present the problem formulation and discuss the numerical method used and the inflow-generation techniques employed. Then, we will discuss the numerical results. Conclusions will finally be drawn, and directions for future work will be presented.

4.3 Problem formulation

In this work we use the incompressible Navier-Stokes equations to perform DNS simulations of boundary layer transition under free-stream turbulence. The equations of motion

$$\frac{\partial u_j}{\partial x_j} = 0, \tag{4.1}$$

$$\frac{\partial u_i}{\partial t} + \frac{\partial}{\partial x_j}\left(u_j u_i\right) = -\frac{1}{\rho}\frac{\partial p}{\partial x_i} + \nu \nabla^2 u_i, \tag{4.2}$$

are solved numerically using a second-order accurate finite-difference method on a staggered grid. The method fully conserves mass, momentum and kinetic energy in the discrete sense (see Morinishi, Lund, Vasyliev & Moin 1998). The coordinates x_1, x_2 and x_3 (or, interchangeably, x, y and z) refer, respectively, to the streamwise, spanwise and wall-normal directions. The velocity components in these directions are, respectively, u, v and w. All grids used are uniform in the spanwise direction

y, stretched in the streamwise and wall-normal directions to allow accurate resolution of boundary layer disturbances, particularly in the transitional region. The discretized equations are integrated in time using an explicit fractional time-step method, (Chorin 1968, Kim & Moin 1985) in which all terms are advanced in time using the Adams-Bashforth method. The Poisson equation for the pseudo-pressure is solved, and the velocity is corrected to make the field solenoidal. The code has been extensively validated for a variety of turbulent (Balaras, Benocci & Piomelli 1995, Balaras, Piomelli & Wallace 2001) and re-laminarizing (Piomelli, Balaras & Pascarelli 2000) flows.

The code was parallelized with the MPI message-passing protocol. The computational box is divided into n subdomains in the streamwise direction, and each of the n processors integrates the equations of motion in one of the subdomains. The pressure field is obtained by applying spanwise FFT to the Poisson equation. This yields a pentadiagonal matrix for each Fourier mode, which is then inverted by a cyclic reduction algorithm. Each processor is assigned a subset of the Fourier modes resulting from the application of FFT.

4.3.1 Initial and boundary conditions

Our computational domain is a rectangular box with dimensions $L_x \times L_y \times L_z = 620\delta_{99}^o \times 30\delta_{99}^o \times 40\delta_{99}^o$, where δ_{99}^o is the 99% thickness of the laminar boundary layer at the inlet. The inlet is located at $Re_\theta = 106$, ($Re_x = 6000$). At the outflow,

δ_{99} is approximately 1/4 of the wall-normal domain. All velocity components are normalized with the free-stream velocity.

The following boundary conditions were applied

1. In all of our simulations the inlet velocities are imposed by adding zero-mean perturbations to the Blasius base flow. When the noise is generated using the algorithm of Rogallo (1981) or obtained from a precursor simulation, the zero-mean perturbation velocity field is multiplied by a hyperbolic tangent cut-off function, which forces the perturbation field to approach zero at the wall.

2. At the outlet, non-reflecting boundary conditions (Orlanski 1976) were applied. Simulation results in the last 15% of the domain (where the grid was also stretched exponentially in the streamwise direction) were deemed unphysical, due to potential contamination associated with an imperfect outflow condition.

3. In the spanwise direction, y, periodic conditions were used.

4. At the free-stream, we imposed $u = 1,\ v = 0,\ w = d\delta^*/dx$, where δ^* is computed for the Blasius profile. The boundary condition on the wall-normal velocity component, w, is accurate through the onset of transition and becomes less so as transition to turbulence takes place. The effect of using an incorrect top outflow condition may result in a favorable or adverse pressure gradient, which could delay or accelerate transition, respectively. In our simulations,

however, the acceleration coefficient K ($\equiv -(\nu/U_\infty^2)\,(dU_\infty/dx)$) was of the order of 10^{-7}, which is well below the levels that are known to affect transition.

5. No-slip conditions were used on the bottom wall.

4.3.2 Free-stream disturbance generation

Complete details of the three methods can be found in the Appendix. Here we outline only the essential features. We have performed calculations using three types of inflow conditions. In the first, we use the algorithm developed by Rogallo (1981), and multiply the noise by a hyperbolic tangent cut-off function which decays to zero at the wall. In the second, we employ the algorithm of Rogallo to generate noise as input into a precursor simulation of spatially-developing homogeneous isotropic turbulence. We then use velocity data from a cross-stream plane at an appropriate streamwise location as the inlet condition for the main simulation. Note that the inflow obtained from the precursor simulation is cut-off with the same hyperbolic tangent function as in the first method, so that the planes of data used for the inflow condition have zero turbulence levels at the solid wall. The third type of inflow condition used is the one proposed by Jacobs and Durbin (2001), which modifies the Rogallo algorithm by replacing the Fourier basis with the continuous Orr-Sommerfeld basis and, therefore, requires no cut-off function near the wall. Following Jacobs & Durbin (2001), the free-stream noise amplitude imposed at the inflow location ($Re_x = 6000$), $u_0 = (\sqrt{\overline{u'u'}} + \sqrt{\overline{v'v'}} + \sqrt{\overline{w'w'}})/3$, was 7% for all

simulations; the three velocity r.m.s. values were within 10% of u_0. The overline here indicates Reynolds averaging, and the prime a fluctuation from the mean. The disturbance integral length scale,

$$L_{11} = \int_0^\infty \frac{\overline{u'(x)u'(x+r)}}{\overline{u'(x)u'(x)}} dr \tag{4.3}$$

was varied between $1.0\delta^o_{99}$ and $3.0\delta^o_{99}$. For the simulations that used the Orr-Sommerfeld eigenfunctions we also explored the effect of the range of modes used to generate the inflow disturbance.

4.4 Results

4.4.1 Grid refinement study

To gain confidence in our results we performed a grid refinement study of bypass transition due to 7% FST, using the inflow-generation algorithm of Jacobs and Durbin (2001). For the simulations in this and the remaining sections, our computational domain was a box with dimensions $L_x \times L_y \times L_z = 620\delta^o_{99} \times 30\delta^o_{99} \times 40\delta^o_{99}$, chosen to match that of Jacobs and Durbin. The disturbance integral length scale, L_{11}, was set to $3.0\delta^o_{99}$ (Jacobs and Durbin do not mention the value used in their simulations), and the wave-numbers $k_y = 2\pi n_y/L$ and $k_z = 2\pi n_z/L$ (where $L = 30\delta^o_{99}$) and the frequency $\omega = U_\infty k_x$ were chosen in the manner described in the Appendix, using 32 modes in each direction. The 3D energy spectrum of the inlet disturbance (where we have assumed $k_x = \omega/U_\infty$) is shown in the Appendix.

Mesh	$nx \times ny \times nz$	Δx^+	Δy^+	Δz^+_{min}
Coarse	$500 \times 96 \times 96$	Fig.4.1	3.0	1.0
Medium	$900 \times 180 \times 150$	Fig.4.1	2.5	0.5
Fine	$1200 \times 256 \times 180$	Fig.4.1	2.4	0.5

Table 4.1: Meshes used in the grid refinement study.

Simulation parameters are summarized in Table 4.1 and the streamwise mesh spacing is shown in Fig. 4.1, which also shows the streamwise resolution used by Jacobs and Durbin and the resolution estimate of Rai and Moin (1993)[3] ($\Delta x^+ = 12$, $\Delta y^+ = 6$). Note that up to $Re_x = 100,000$ and $Re_x = 140,000$ for the medium and the fine grids, respectively, the streamwise spacing is nearly constant. Beyond these values the stretching is mild with $\Delta x_{i+1}/\Delta x_i \leq 1.01$ for both grids.

Figure 4.2 shows the streamwise development of the skin-friction coefficient

$$C_f = \frac{\tau_w}{\frac{1}{2}\rho U_\infty^2}, \tag{4.4}$$

where τ_w is the wall shear stress. The medium and fine grids show very good agreement up to the onset of transition, which is the region of the flow in which we are most interested. At $Re_x \simeq 120,000$ the two curves depart, the medium grid giving a sharper transition to a fully turbulent regime. The reason for this departure can be understood by looking at the distribution of streamwise mesh spacing for the fine

[3]Rai & Moin (1993) used a compressible NS solver with fifth-order upwind differencing for the convective terms and fourth-order central differencing for the diffusive terms.

and medium grids (Fig. 4.1). The increased slope of the rise in skin friction correlates with a substantial increase in mesh spacing, which occurs farther downstream for the fine grid. The result that an under-resolved grid produces a premature and abrupt transition is somewhat counterintuitive, since mesh coarsening implies not resolving small-scale instabilities. By looking at the skin friction plot it can be seen that in both medium and fine grids adequate resolution is maintained in the early transitional regime. We therefore believe that the medium grid is adequate in predicting transition inception. As the latter provides an adequate metric to assess the effects of varying inflow parameters, the medium grid will be used for all remaining calculations presented in this paper.

Our results also imply that transitional flows are more sensitive to grid resolution than fully turbulent flows. Looking at near-wall streamwise velocity, Reynolds stresses and a budget for the turbulent-kinetic energy obtained on the medium grid and shown in Figs. 4.3 and 4.4, we observe the expected turbulent behavior. In particular, very good agreement with turbulent channel data of Moser, Kim and Mansour (Moser, Kim & Mansour 1999) can be seen despite the coarser streamwise resolution in the fully turbulent region.

4.4.2 Free-stream turbulence decay rate

In all of our simulations, after a short transient, free-stream turbulence intensity decayed as $(x - x_0)^{-\alpha}$, with $\alpha \in [0.7, 0.8]$. We note, however, that the virtual

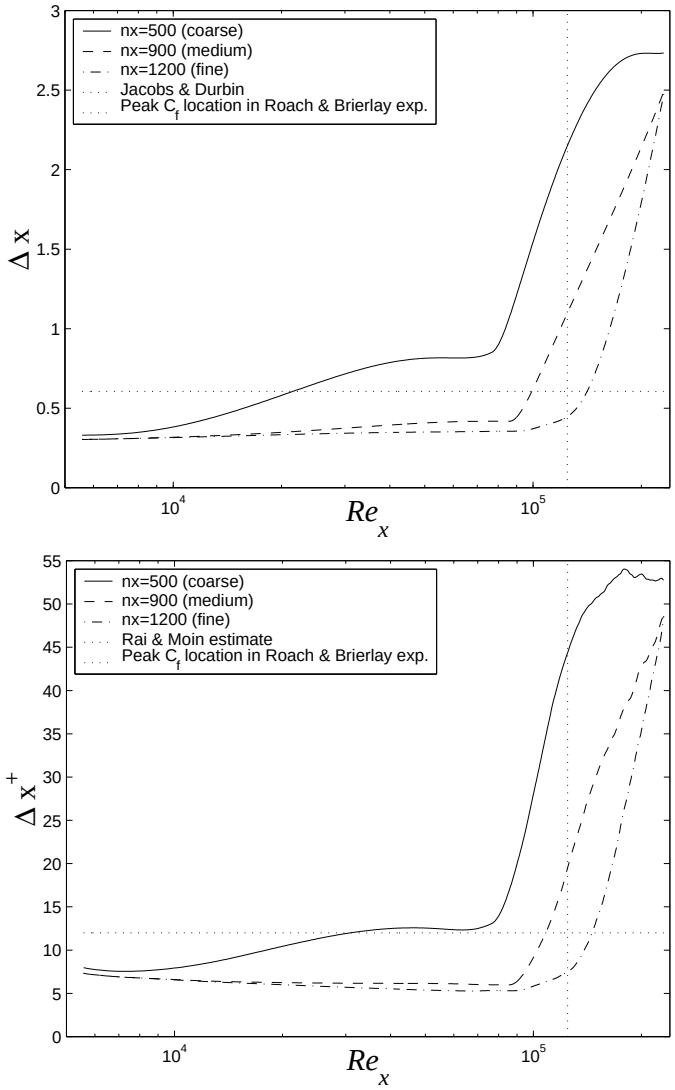

Figure 4.1: Grid-refinement study. Streamwise mesh spacing in absolute units (top) and wall units (bottom).

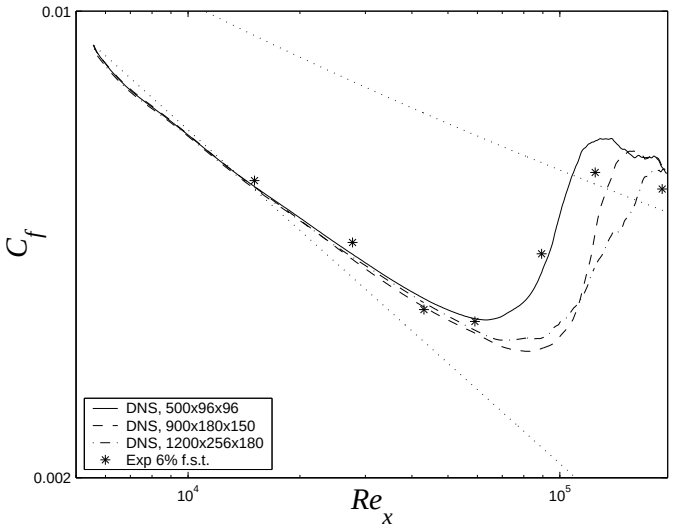

Figure 4.2: Grid-refinement study. Skin friction coefficient distribution.

origin of turbulence, x_0, is as important a parameter as the actual decay exponent. While Fig. 4.5 (and other figures) show that in the experiments by Roach and Brierlay (1992), the free-stream turbulence decayed at a significantly lower rate than that in our simulations (as was also the case in the work of Jacobs and Durbin, 2001, and Brandt and Henningson, 2004), both curves could be fit to the above decay law with nearly the same decay exponent, but with different virtual origins. As has been suggested previously (Jacobs & Durbin, 2001, Brandt *et al.* 2004), the slower decay of the experimental turbulence is most likely due to the larger length scale. For convenience, in our free-stream turbulence decay plots we also report the dissipation length scale, $L_k = \left(k^{3/2}\right) / \left(U_\infty dk/dx\right)$, computed at the inflow, where k denotes the turbulent kinetic energy.

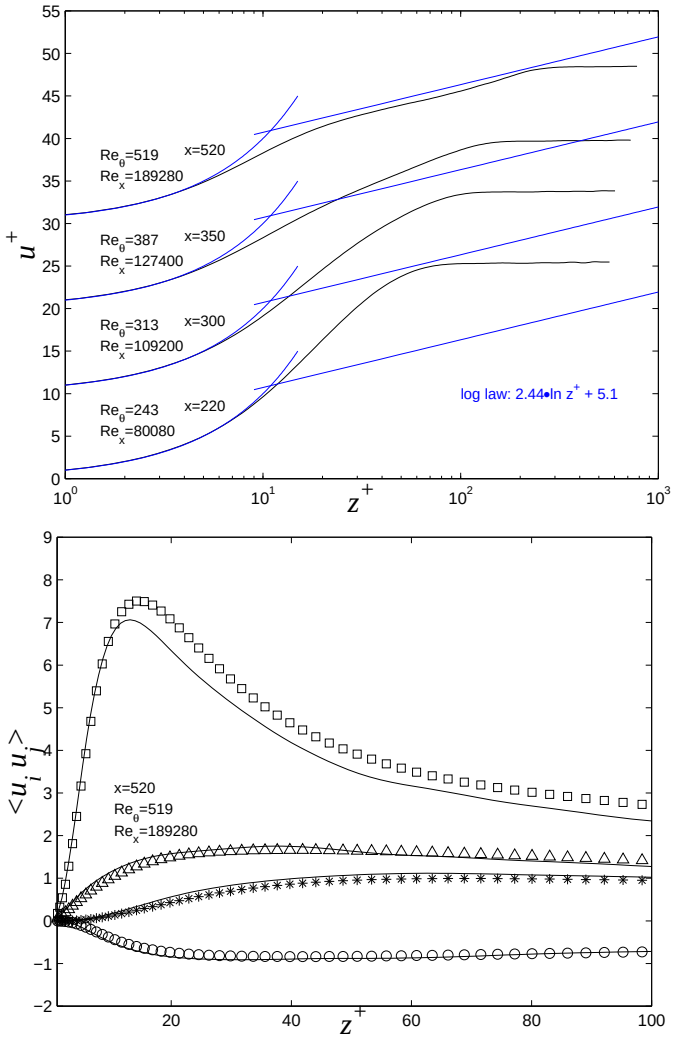

Figure 4.3: Top: near-wall streamwise velocity at variuos $x-$locations. Bottom: Reynolds stresses in the turbulent region at $x = 520$, $(Re_x = 189,280)$. The four curves correspond to $\overline{u'u'}$, $\overline{v'v'}$, $\overline{w'w'}$, and $\overline{u'w'}$, from top to bottom, and the symbols correspond to the DNS data for channel flow (Moser *et al.* 1999). Medium grid DNS.

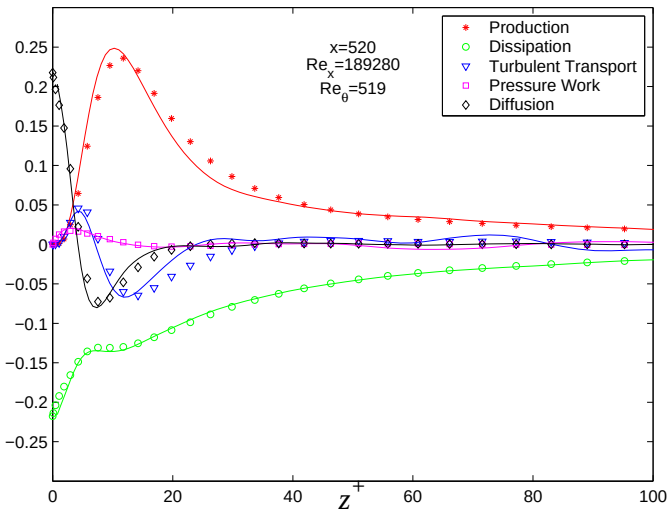

Figure 4.4: Near-wall TKE budget in the turbulent region; medium grid DNS. The symbols correspond to the DNS data for channel flow (Moser *et al.* 1999).

4.4.3 Flow structure

A detailed description of boundary layer transition via the bypass mechanism can be found in various references (Jacobs & Durbin 2001, Brandt *et al.* 2004). Here we merely identify the streaky structures and turbulent spots that are the classical features of this flow. Figure 4.6 shows the average and instantaneous skin-friction distribution, and contours of velocity and pressure in an $xz-$ and $xy-$plane, taken from the fine-grid simulation. Between $x = 200$ and 400 ($73,000 < Re_x < 146,000$) we can observe two so-called "turbulent spots" – isolated patches of irregular motion – alternating with regions of laminar-like quiescence. The spots are clearly seen in the v- and w-velocity contour plots at the bottom of the figure, and also, indirectly, in the spikes in C_f in the top plot. These spots are convected with the local mean

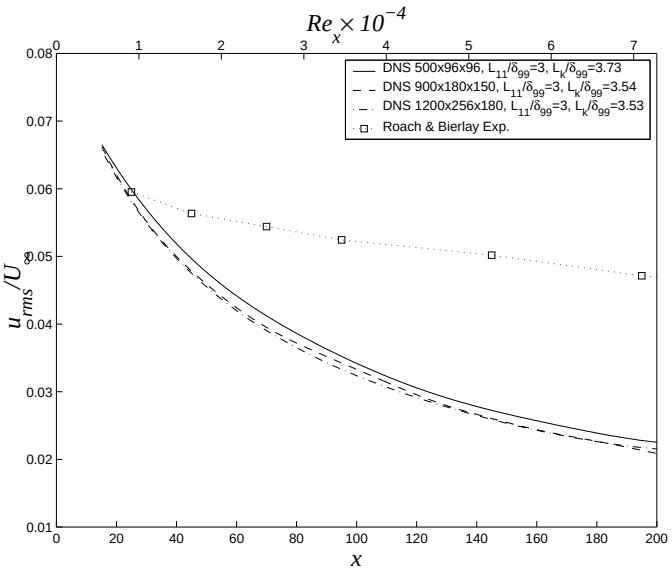

Figure 4.5: Grid refinement study: disturbance decay rate.

velocity and merge with the fully turbulent front (shown at $x = 450$, $Re_x = 150,000$ in the figure 4.6). The gradual increase in the averaged skin-friction plot is obtained by averaging over the passage of several such turbulent spots. In this context the essential feature of grid under-resolution can be illustrated: our medium and coarse grid results show the breakdown to turbulence, but do not show the quasi-laminar region at $400 \leq x \leq 450$. Apparently, the coarseness of grid destabilizes the boundary layer, eliminating the intermittency region and forcing the flow towards full-blown turbulence earlier. A possible explanation is that the under-resolution causes unphysical energy aliasing into unstable scales of motion. Improving the resolution ensures that this energy is removed by the scales of dissipation. It is for this reason that the medium-grid skin-friction plot shown in the grid-refinement section has a higher slope than the fine-grid one. As a consequence, previous simulations in

which the grid was perhaps too coarse (Voke & Yang 1995, Rai & Moin 1993) did not report seeing turbulent spots. We reiterate, however, that although our medium grid does not capture this intermittency region, it is fine enough to predict the onset of turbulence accurately. This assertion is justified by noticing that the streamwise location of the turbulent-spot generation ($x = 200$, $Re_x = 73,000$) is well upstream of the region where our medium grid becomes too coarse by the standards of Rai & Moin (1993) and Jacobs & Durbin (2001) (see Fig. 4.1) and also by the good agreement of our medium-grid and fine-grid simulations in that region.

4.4.4 Results with Rogallo (1981) disturbance

The purpose of this set of simulations is to establish the effect of the disturbance length-scale and the extent of its penetration into the boundary layer on transition location. The simulation parameters are summarized in Table 4.2. The cutoff functions used to bring the noise to zero at the wall are shown in Fig. 4.7. Note that neither cutoff function extends far into the region of significant boundary-layer mean shear, consistent with the shear-sheltering phenomenon of boundary layers, which hinders the penetration of disturbances towards the wall. Voke & Yang (1995) used a cutoff function that attenuated the free-stream turbulence to zero over the region $0.5 < z/\delta_{99} < 1.08$ at the inflow plane. In their case the disrbance was probably placed somewhat deeper inside the boundary layer than in our cutoff I case, although they did not show the profile (or give an analytical form) of the

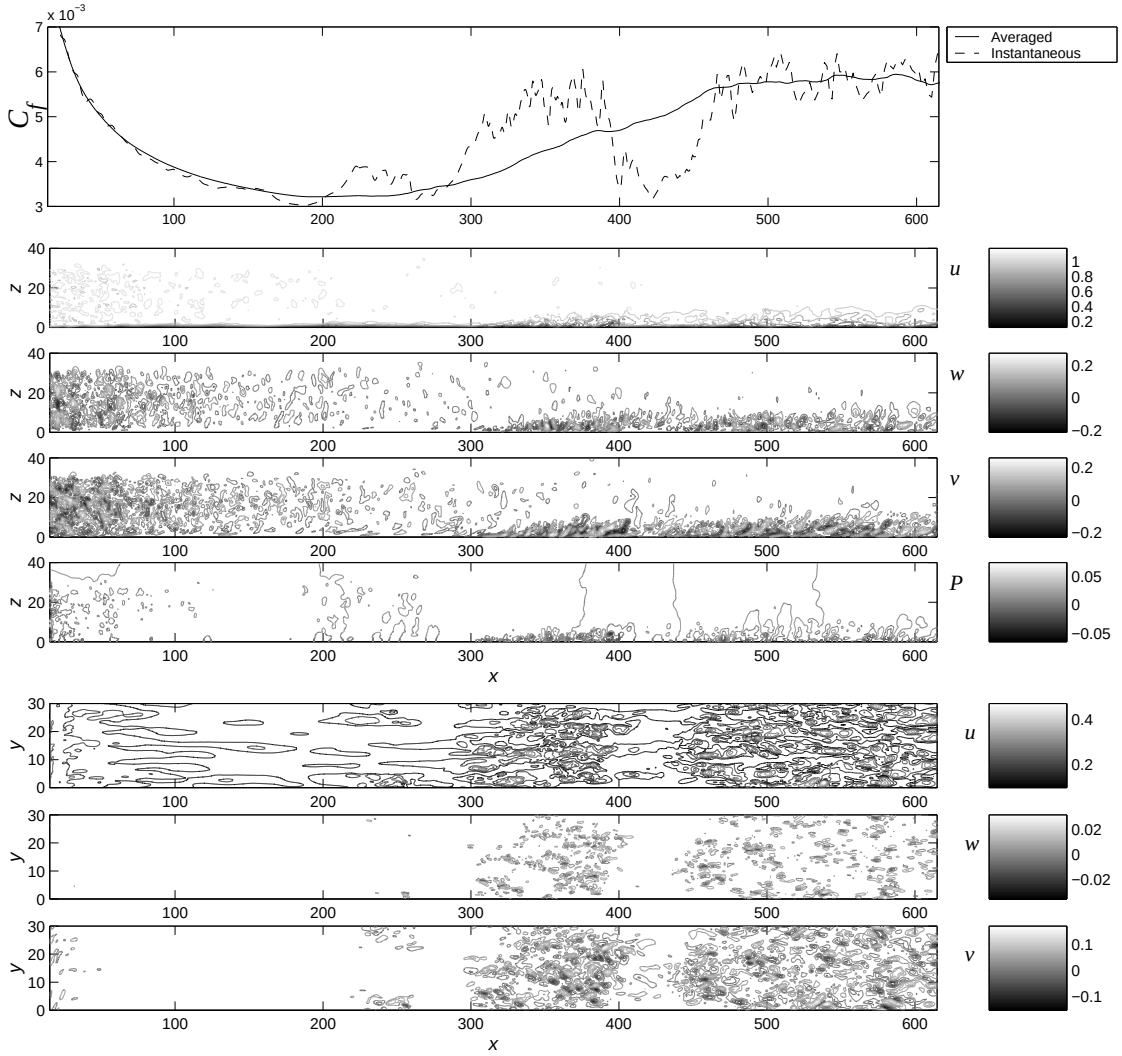

Figure 4.6: Skin friction coefficient (top); velocity and pressure contours in an $xz-$plane (middle); velocity contours in the $z/\delta_{99}^o = 0.15$ plane (bottom).

Case	$nx \times ny \times nz$	L_{11}	Modes	Cut-off
I	$900 \times 180 \times 150$	3.0	32^3	I
II	$900 \times 180 \times 150$	3.0	32^3	II
III	$900 \times 180 \times 150$	1.0	32^3	I

Table 4.2: Simulations parameters for the calculations using Rogallo noise.

attenuation function. The skin friction plots in Figs. 4.7 and 4.8 indicate that increasing noise penetration into the boundary layer and increasing the length scale of the free-stream noise causes transition to move farther upstream. It is unclear whether the latter effect is due to the lower decay rate of larger-scale turbulence (see Fig. 4.9), which increases the time interval over which the boundary layer is subjected to high-amplitude perturbations, or to the possibly increased boundary-layer sensetivity to large-scale noise. Our results are in qualitative agreement with the experiments of Jonáš, Mazur, and Uruba (2000) in which the onset of transition moves farther downstream with decreasing FST length scale.

4.4.5 Results with precursor simulation inflow

For the simulation in this section, the free-stream noise had the same length scale, wall cutoff function, and nearly the same amplitude as the first case of the previous section (see Fig. 4.7, I), but was obtained from a precursor simulation. In order to match the length scale and turbulence intensity at the main box inlet we

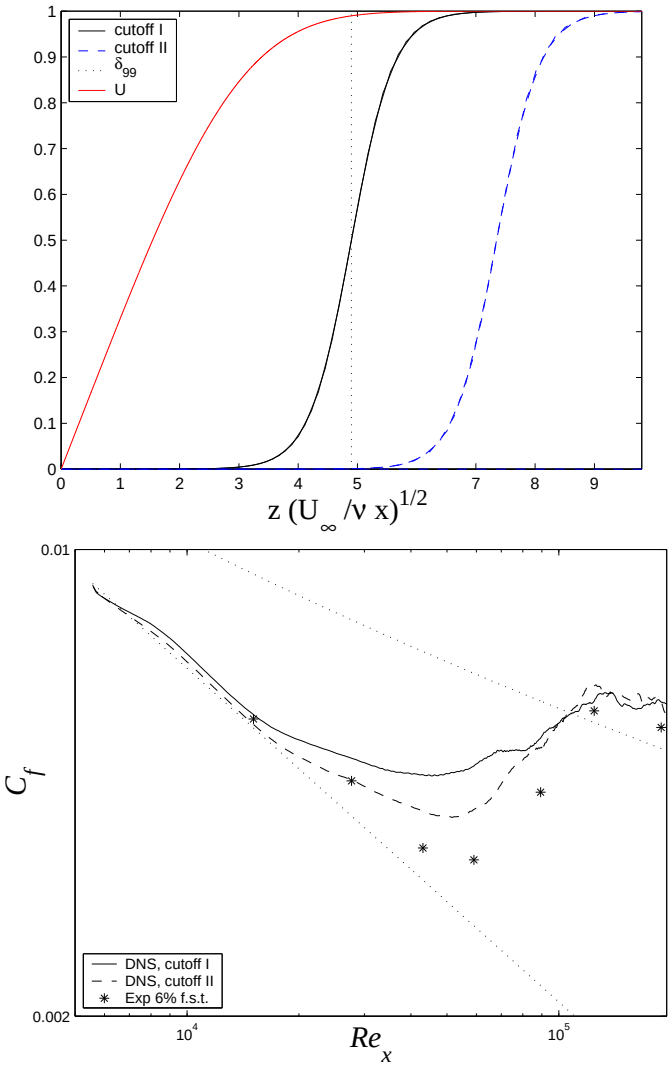

Figure 4.7: Effect of disturbance penetration-depth on transition location. Top: cutoff functions used. Bottom: skin-friction development.

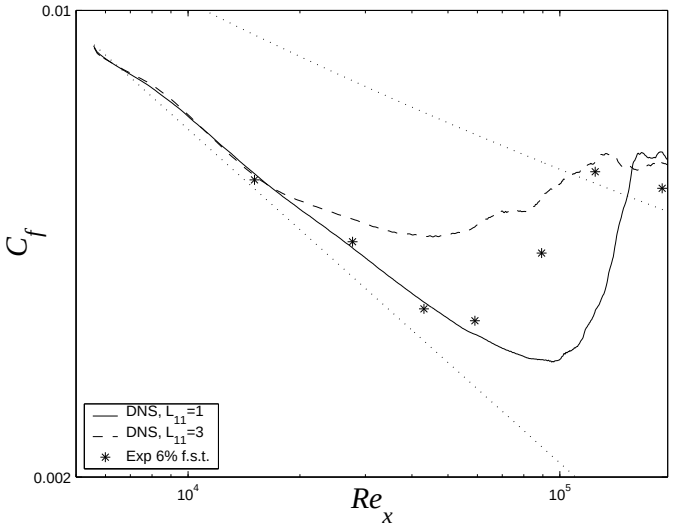

Figure 4.8: Effect of disturbance length scale on transition location; —— $L_{11} = 1.0\delta^o_{99}$, --- $L_{11} = 3.0\delta^o_{99}$.

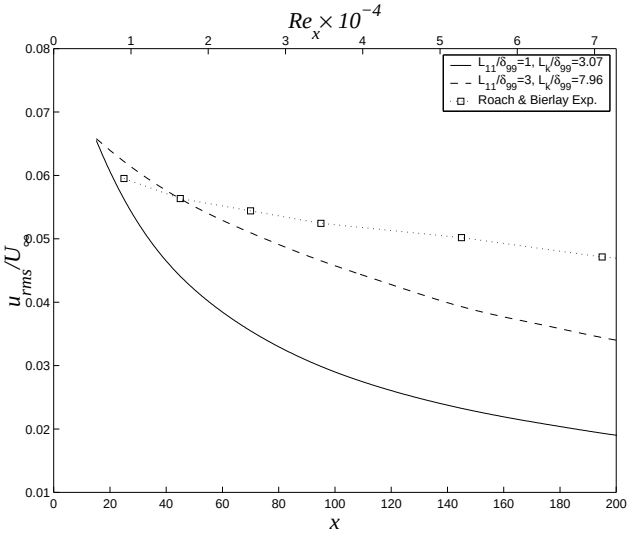

Figure 4.9: Effect of length scale on turbulence decay-rates.

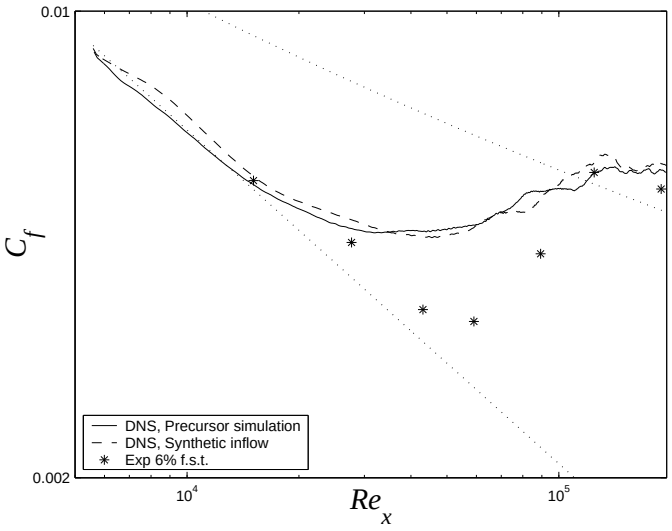

Figure 4.10: Synthetic FST vs. Precursor simulation FST; —— DNS, precursor simulation inflow, - - - DNS, Rogallo (1981) inflow.

used a lower integral length scale ($L_{11} = 2.5\delta^o_{99}$) and a higher free-stream noise amplitude ($u' = 0.1U_\infty$) for the precusor box inlet (δ^o_{99} is the boundary layer thickness at the inflow of the main simulation). At position $x = 77\delta^o_{99}$ inside the precursor box the free-stream disturbance amplitude decayed to $0.068U_\infty$, and the integral length scale, L_{11}, was approximately $3.0\delta^o_{99}$. At this position cross-stream planes were saved and used as inflow for the main simulation. Fig. 4.10 shows skin friction plots from two simulations, one using noise generated with the algorithm of Rogallo, and the other, using noise generated from a precursor simulation. The close agreement between the two curves indicates that the two methods of noise generation are effectively similar, as far as the boundary layer is concerned. Free-stream turbuence decay rates corresponding to the skin friction plots in Fig. 4.10 were nearly identical.

4.4.6 Results with Jacobs and Durbin inflow

The purpose of the simulations presented in this section was to evaluate the applicability of the disturbance generation algorithm of Jacobs and Durbin (2001) for transition prediction. As mentioned in the Section on disturbance generation and discussed in detail in the Appendix, the Jacobs and Durbin (2001) inflow-generation algorithm aims to match the von Kármán spectrum by assuming that in the free-stream the Orr-Sommerfeld modes behave as Fourier modes. Whereas the inflow produced under this assumption may still be adequate, we point out that the assumption is not valid: while the real part of an Orr-Sommerfeld mode may be normalized to have unit amplitude in the free-stream, this cannot generally be done for both the real and the imaginary parts. Thus, while the real and the imaginary part of a Fourier mode are both of unit amplitude, in the free-stream only one part of the Orr-Sommerfeld mode can be made to have this property, while the amplitude of the other part can be substantially larger or smaller (Fig. 4.11) [4]. As a consequence of this discrepancy, the energy spectrum of the generated disturbance is different from one in which true Fourier modes are used. Figure 4.12 shows the 3D energy spectrum generated using Orr-Sommerfeld and Fourier modes.

Of much greater importance is the range of wave-numbers used for the noise generation. While the exact relation $\overline{u_i' u_i'} = \int_0^\infty E(k)dk$ is valid both continuously

[4] In the solver of Jacobs & Durbin (2001), the boundedness of eigenfunctions is achieved by using the (arbitrary) boundary condition $\phi = (1, 0)$ on the top boundary, which allows for substantially different amplitudes of the real and imaginary parts.

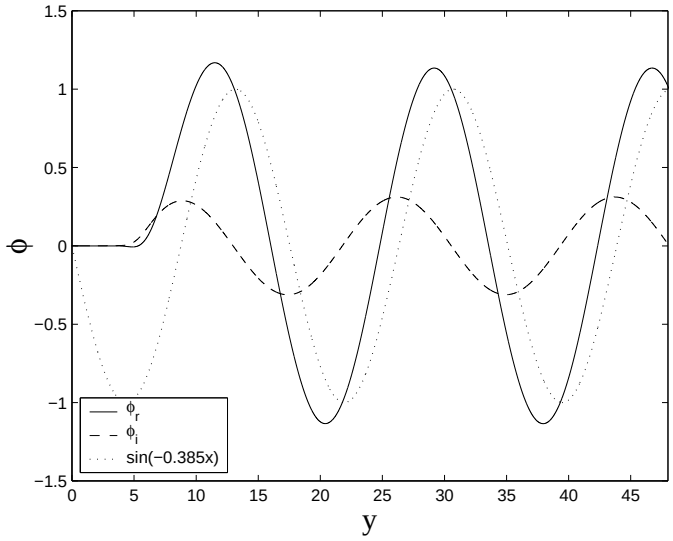

Figure 4.11: Comparison of an Orr-Sommerfeld mode with a Fourier mode.

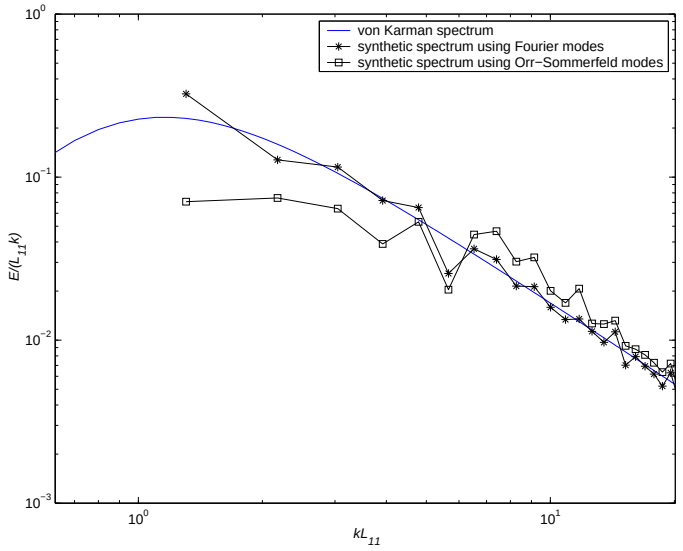

Figure 4.12: Three-dimensional spectra of disturbances generated with Fourier and Orr-Sommerfeld modes.

and discretely, the discrete integral will have no contributions from wave-numbers above a certain finite cutoff. Thus, suppose that we are generating the disturbance inside a cube of size 2π (assume $x = U \cdot t$) using 64 grid points in each direction. The maximum wave-number represented on this mesh is 32 and the generated disturbance contains no contributions from wave-numbers above this value. In order for the discrete integral to remain the same as the continuous integral (to match the experimental turbulence intensity), additional energy must be added to the resolved modes. This additional amount will, of course, decrease (or increase) as the resolution (equivalently the maximum resolved wave-number) is increased (or decreased). This argument is illustrated in Fig. 4.13. Since the extent of penetration of an Orr-Sommerfeld mode into the boundary layer increases with decreasing frequency (Fig. 4.14), using a low number of modes (with a low maximum wave-number) forces one to increase the energy of low-frequency modes to achieve a given turbulence intensity; this, in turn, increases noise penetration into the boundary layer.

It follows, then, that 7% FST with the maximum resolved wave-number k_1 will cause transition earlier than 7% FST with a maximum resolved wave-number $k_2 > k_1$, because in the former case more energy is put into the low wave-number region to compensate for the larger unresolved part and we infer from Fig. 4.14 that the disturbance penetration depth is greater in the former case than in the latter. This effect is illustrated in Fig. 4.15. The input parameters of the three simulations shown are identical except for the number of modes used for the noise generation (see Table 4.3). Interestingly, this number may also affect disturbance decay-rates

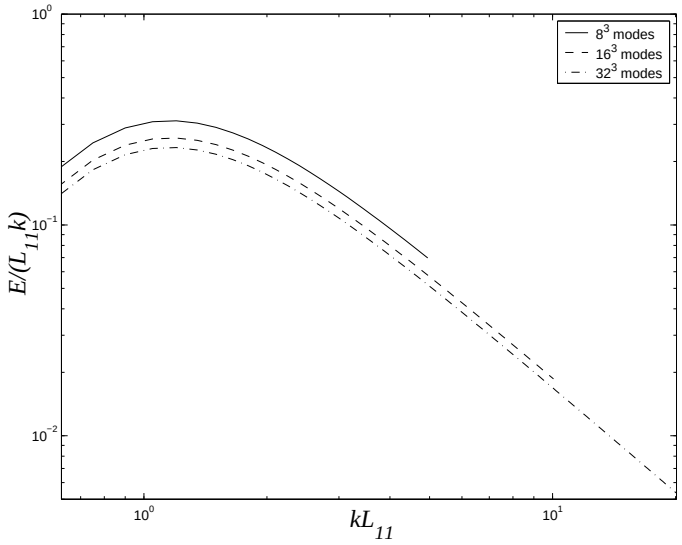

Figure 4.13: Energy spectra of a disturbance with different wave-number cutoffs, constructed to have the same turbulence intensity.

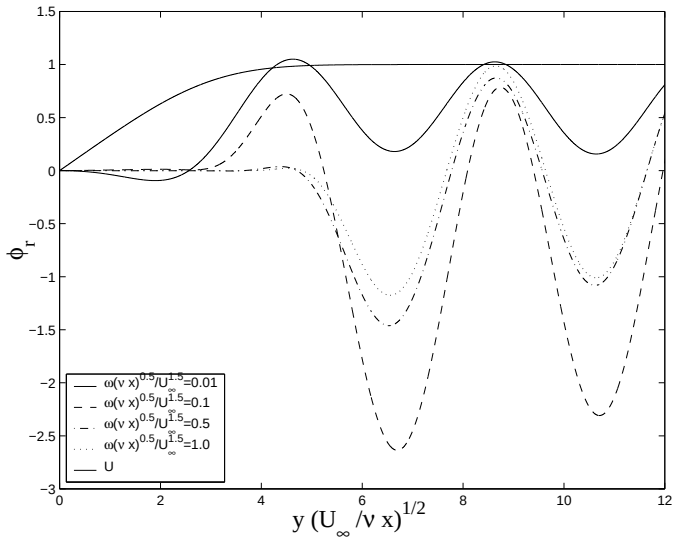

Figure 4.14: Effect of ω on the penetration depth of an Orr-Sommerfeld mode into the boundary layer ($Re = 500,\ k_y = \pi/2$).

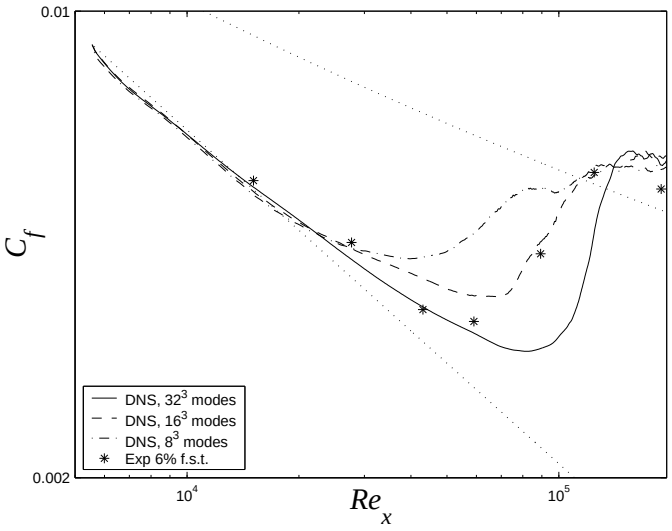

Figure 4.15: Effect of wave-number cut-off on transition location.

significantly (Fig. 4.16), but the difference between the decay rates of the 16^3 and 32^3 mode simulation does not appear to be sufficiently large to account by itself for the much larger shift in skin friction.

Case	$nx \times ny \times nz$	L_{11}	Modes
I	$900 \times 180 \times 150$	3.0	32^3
II	$900 \times 180 \times 150$	3.0	16^3
III	$900 \times 180 \times 150$	3.0	8^3
IV	$900 \times 180 \times 150$	1.0	8^3

Table 4.3: Simulations with Jacobs & Durbin (2001) inflow

As can be seen, by keeping all simulation parameters the same but changing the frequency range used to represent the disturbance, the skin friction curve can

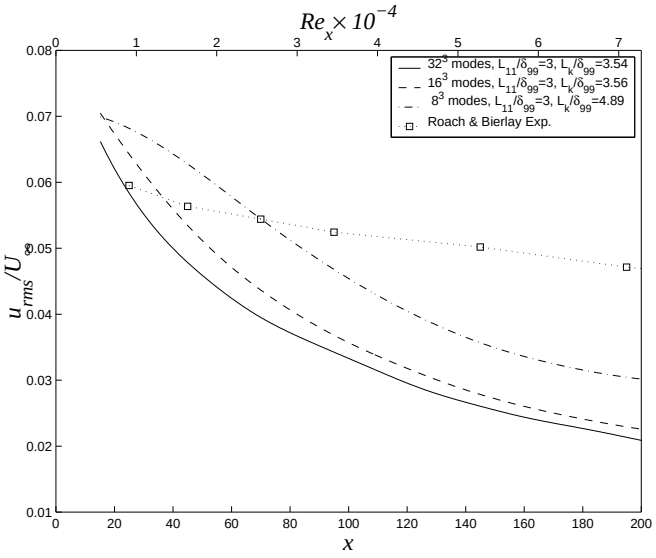

Figure 4.16: Effect of wave-number cut-off on disturbance decay rate

be shifted in either direction to obtain a match with experiments. If one is allowed to adjust the integral length scale, even greater freedom is obtained. In Figs. 4.15 and 4.17 we have obtained agreement with experiments in two separate ways: by varying the modal content in the disturbance spectrum and the length scale of the free-stream noise.

The paper by Jacobs and Durbin (2001) does not specify the number of modes used to generate their disturbance, but does mention that this number was small. Brandt *et al.* (2004) have implemented a very similar inflow-generation algorithm[5] and mention that they used 800 modes. Moreover, whereas the number of wave-number triplets $k_1,\ k_2,\ k_3$ such that $\lfloor\sqrt{k_1^2+k_2^2+k_3^2}\rfloor = k'$ grows quadratically with k', Brandt *et al.* (2004) set this value to 40. While there is little *a priori* reason

[5]Both Orr-Sommerfeld and Squire modes were used in their simulations.

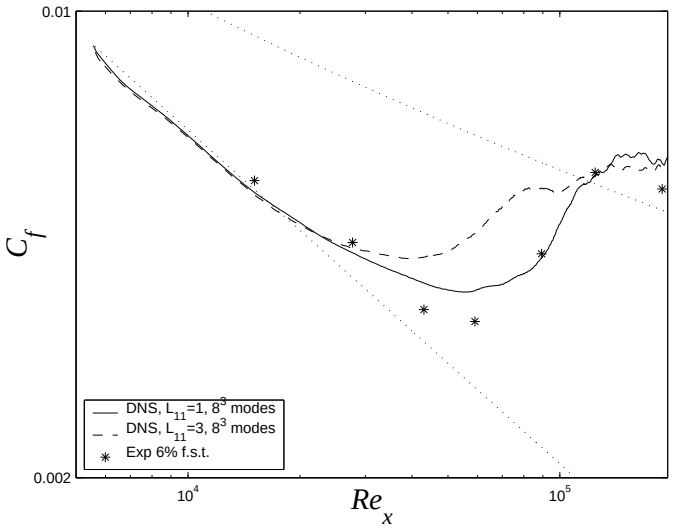

Figure 4.17: Effect of disturbance length scale on transition location.

to prefer one set of modes to another, the choice clearly has repercussions on the location of transition.

4.5 Conclusions

We have performed a grid refinement study of boundary-layer bypass transition due to 7% free-stream turbulence. In the present simulations, the inflow plane is located downstream of the leading edge, and the inlet velocity is a superposition of a Blasius base flow and a presecribed disturbance profile. Our results support the resolution estimates of Rai and Moin (1993) for simulating the transition region; the C_f predictions based on the medium-grid simulation begins to disagree with the fine-grid simulation when the local streamwise resolution falls below their estimates. We have also shown that a consequence of under-resolution is the disappearance of

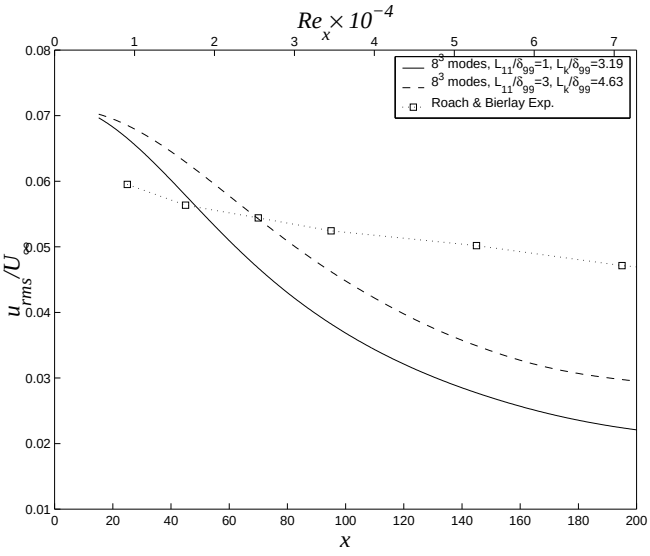

Figure 4.18: Effect of disturbance length scale on disturbance decay rate.

the intermittency region characterized by the passage of turbulent spots surrounded by quasi-laminar quiescent regions: insufficient resolution causes an earlier and more abrupt transition to turbulence.

We have demonstrated that boundary layer bypass transition is strongly dependent on the integral length scale of the noise and the extent of its penetration into the boundary layer. We also implemented the inflow-generation algorithm of Jacobs and Durbin (2001) and compared our simulation results with experiments by Roach and Brierlay (1992). By varying simulation parameters that were not specified in the experiment within a sensible range, while keeping the amplitude of the free-stream turbulence the same, we were able to move the transition point within the computational box upstream or downstream. These results indicate that, in order to specify the problem fully (1) a reliable value for the length scale of the free-

stream turbulence and (2) the extent of disturbance penetration into the boundary layer must be available from experiments. Simulations should match experimental Reynolds-stress profiles inside the boundary layer well upstream of the transition location.

Alternatively, in order to avoid the problem of specifying the near-wall behavior altogether, numerical simulations could include the boundary-layer leading edge modeled as an elliptical body to avoid velocity discontinuities. Our future work will include simulations of this type with the superelliptical leading-edge represented using the immersed boundary method (Balaras 2004). The simulation will be performed on a Cartesian coordinate system inside a multi-block domain. The multi-block approach is necessary because, in order to resolve properly the formation of the boundary layer around the leading edge, very fine wall-normal grid resolution is required, which is not necessary throughout the entire domain. Through simulations of the above type it becomes possible to follow the development of the free-stream disturbance near the boundary layer edge and to monitor the extent of its penetration into the boundary layer. Furthermore, such simulations can also enable one to make more general conclusions about the universal applicability of the inflow-condition methods proposed and used in the past, and on the effect of *ad hoc* parameters in these methods.

4.6 Appendix

This section gives a detailed description of the three methods of inflow generation used in this paper. The first method uses the algorithm by Rogallo (1981) as found in Jacobs and Durbin (2001) with Fourier modes in each of the three directions (with the disturbance multiplied by a cutoff function at the wall). The second uses the same algorithm as the first, with the noise fed into a precursor simulation box. Cross-stream planes from the precursor simulation are then used as inflow for the main simulation (with the same cutoff function). The third method again employs the Rogallo (1981) algorithm but uses the continuous Orr-Sommerfeld basis in the wall-normal direction to determine the wall-normal behavior of the inflow profile (the eigenfunctions are required to be bounded but not square-integrable, Grosch & Salwen 1978).

Rogallo (1981) algorithm

In this method, a prescribed turbulence spectrum with random phases is used to generate approximately isotropic turbulence. The first step in this method consists of the choice of the range of wave-numbers used to represent the disturbance (this range need not be the same as the range of wave-numbers supported by the actual computational mesh). We use the same range in all three dimensions, which is determined by the domain size and the number of points The domain size for the disturbance calculation matches the spanwise length of the computational domain,

but need not have the same number of grid cells.

For simplicity of the current discussion we will assume a uniform mesh with $nx = ny = nz = 64$, and a cubic domain with sides $L = 2\pi$.[6] In the following, $k_{max} = nx/2$ is the maximum resolved wave-number.

Once the wave-number range has been chosen, we loop over all possible wave-number triplets and pick only those for which $k_x^2 + k_y^2 + k_z^2 \leq k_{max}^2$, essentially so that the wave-number sphere fits inside the wave-number cube. The wave-numbers that do not fit this category are left unpopulated. Given the above constraints, the number of all possible triplets for the 64^3 mesh is approximately 34,000 (the number of possible triplets grows approximately quadratically with $|k|$). Processing such a large number of triplets at each time-step of the simulation results in a substantial increase in the cost of the calculations. Therefore, we only consider every third wave-number in each direction: we let, for instance, $k_x = \omega/U_\infty = 1,\ 2,\ 3,\ 5,\ 8,\ 11, \ldots$ etc. Including all of the lower wave-numbers prevents large symmetrical structures in the inflow, and using only every third wave-number in the higher range decreases the number of triplets to approximately 1,400 —a manageable number.

The disturbance in physical space is then generated from the wave-number

[6]Notice that in reality the x direction represents time, and that $k_x = \omega/U_\infty$, where ω is the disturbance frequency; in practice, the common choice of $U_\infty = 1$ makes x and t (or k_x and ω) interchangeable.

coefficients using:

$$u(y,z,t) = \sum_{\omega}\sum_{k_y}\sum_{k_z} \widehat{u} e^{ik_y y} e^{ik_z z} e^{-i\omega t} \tag{4.5}$$

$$v(y,z,t) = \sum_{\omega}\sum_{k_y}\sum_{k_z} \widehat{v} e^{ik_y y} e^{ik_z z} e^{-i\omega t} \tag{4.6}$$

$$w(y,z,t) = \sum_{\omega}\sum_{k_y}\sum_{k_z} \widehat{w} e^{ik_y y} e^{ik_z z} e^{-i\omega t} \tag{4.7}$$

where we have replaced $k_x x$ with $-\omega t$ using Taylor's hypothesis. When looping over all the possible wavenumber triplets, the Fourier amplitude coefficients of the velocity fluctuations are computed as follows:

$$\widehat{u} = \frac{ik_z \omega A}{\sqrt{\omega^2 + k_y^2}} + Bk_y \tag{4.8}$$

$$\widehat{v} = -i\sqrt{\omega^2 + k_y^2} A \tag{4.9}$$

$$\widehat{w} = \frac{ik_y k_z A}{\sqrt{\omega^2 + k_y^2}} - B\omega \tag{4.10}$$

where

$$A = Fe^{i\theta_1} \cos\delta \tag{4.11}$$

$$B = F\sqrt{\frac{\omega^2 + k_z^2 + k_y^2}{\omega^2 + k_y^2}} e^{i\theta_2} \sin\delta \tag{4.12}$$

$$F = \sqrt{2}\sqrt{\frac{E\left(\sqrt{\omega^2 + k_z^2 + k_y^2}\right)}{4\pi(\omega^2 + k_z^2 + k_y^2)^2}}. \tag{4.13}$$

In the above, δ, θ_1 and θ_2 are uniformly distributed, random angles, which randomize the mode phases. Multiplying the wave-number coefficients in (4.8-4.10) by their complex conjugates, averaging and substituting for A and B produces the isotropic

energy spectrum tensor:

$$\overline{\widehat{u}_i \widehat{u}_j^*} = \frac{E(|k|)}{4\pi |k|^4}(|k|^2 \delta_{ij} - k_i k_j) \tag{4.14}$$

which contracts to give,

$$\overline{\widehat{u}_i \widehat{u}_i^*} = \frac{E(|k|)}{2\pi |k|^2} \tag{4.15}$$

The von Kármán spectrum is defined as:

$$E(k) = \overline{u_0^2} \frac{L^5 k^4}{C[1 + (kL)^2]^{17/6}} \tag{4.16}$$

where

$$\overline{u_0^2} = \frac{2}{3} \int_0^\infty E(k) dk \tag{4.17}$$

$$L = 1.339 L_{11} \tag{4.18}$$

$$C = 0.6883, \tag{4.19}$$

and L_{11} has been defined in the text and $\overline{u_0^2}$ is the square of the desired FST intensity.

To perform the averaging in Eq. (4.14), we count all the wave-number triplets such that $\sqrt{\omega^2 + k_y^2 + k_z^2} = k'$ for some k' and divide the combined energies in these wave-numbers by that number. This will ensure that Eq. (4.14) holds. However, to obtain the correct spectrum, the following equality must hold in the discrete sense:

$$\sum_{\sqrt{\omega^2 + k_y^2 + k_z^2} = k'} \widehat{u}_i \widehat{u}_i^* = E(k'). \tag{4.20}$$

This implies that the Fourier amplitude coefficients must be multiplied by $\sqrt{(2\pi k'^2/n)}$ where n is the number of wave-number triplets that sum to k'^2.

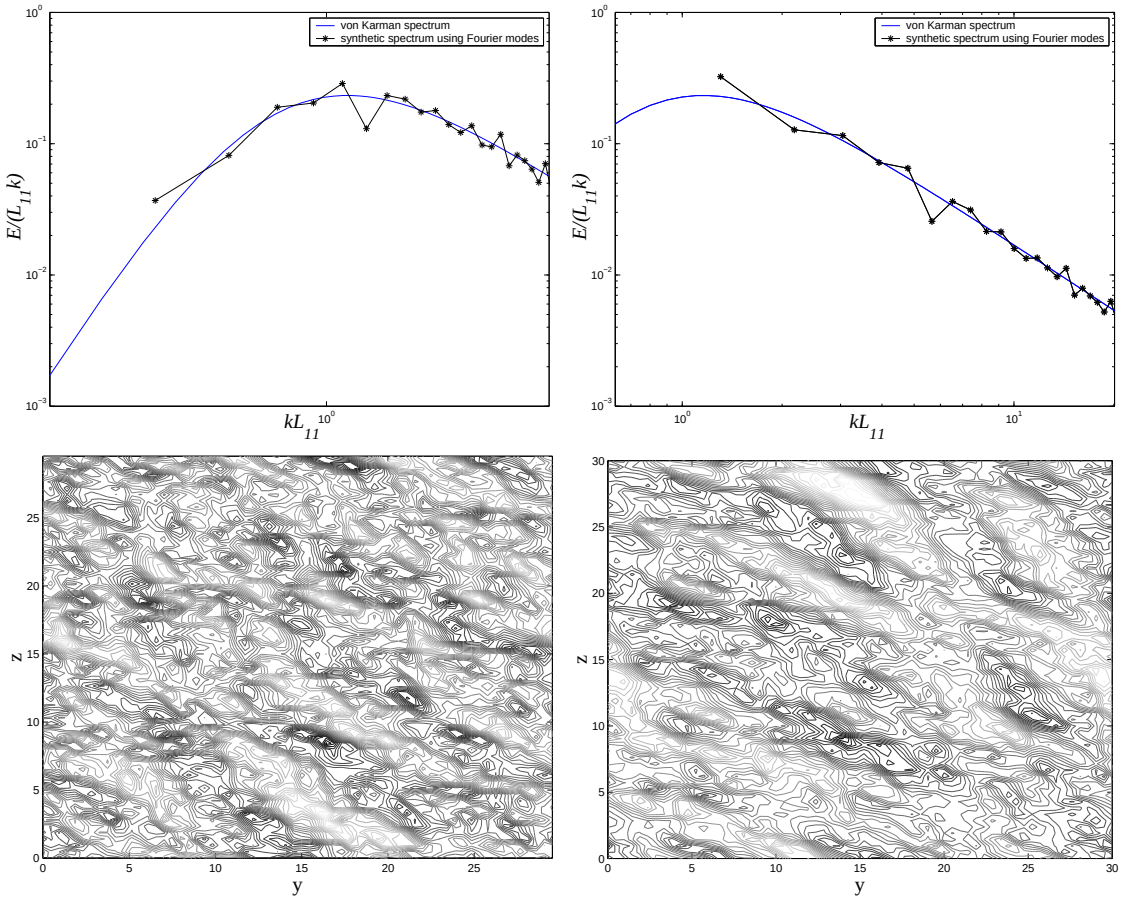

Figure 4.19: 3D disturbance spectra (top) and contours of streamwise disturbance velocity (bottom). Left column: $L_{11} = 0.7$, right column: $L_{11} = 3.0$.

The discrete spectrum is compared to the analytical expression for $E(k)$ in Fig. 6.9, which also shows the instantaneous velocity fields in real space, for two values of the integral length L_{11}.

Precursor simulation

In this method, free-stream turbulence was obtained by feeding synthetic noise generated using the algorithm of Rogallo, described above, into a precursor simu-

lation box of dimensions $100\delta^o_{99} \times 30\delta^o_{99} \times 40\delta^o_{99}$ where δ^o_{99} is the initial boundary layer thickness of the main simulation. Slip-wall boundary conditions were applied on the top and bottom walls of the precursor simulation box. Slip-wall, rather than periodic conditions were chosen in the wall-normal direction because the latter were incompatible with our pressure solver. The turbulence intensity at the inlet of the precursor box was $u_0 = 0.1U_\infty$. At position $x = 77\delta^o_{99}$ inside the precursor box, the turbulence intensity decayed to $u_0 = 0.068U_\infty$ and the disturbance integral length scale was approximately $3\delta^o_{99}$, consistent with the values imposed for the simulations with the Rogallo (1981) synthetic inflow. Therefore, at this location cross-stream planes were saved and used as inflow for the main simulation. Only the central region of the precursor cross-planes was used because the slip-wall condition of the precursor box is unphysical (e.g. the slip-wall destroys turbulence near the wall). To bring the disturbance to zero at the wall we used the same cutoff function as for the Rogallo synthetic inflow (see Fig. 4.7 cutoff I).

Jacobs and Durbin Algorithm

In the algorithm proposed by Jacobs and Durbin (1998), an arbitrary disturbance is expressed as a superposition of the continuous spectrum modes of the Orr-Sommerfeld equation. To generate the continuum eigenmodes, we use the numerical method described in Jacobs & Durbin (1998). To validate the solver we compared our results with the plots in Jacobs & Durbin (1998, 2001) with excellent

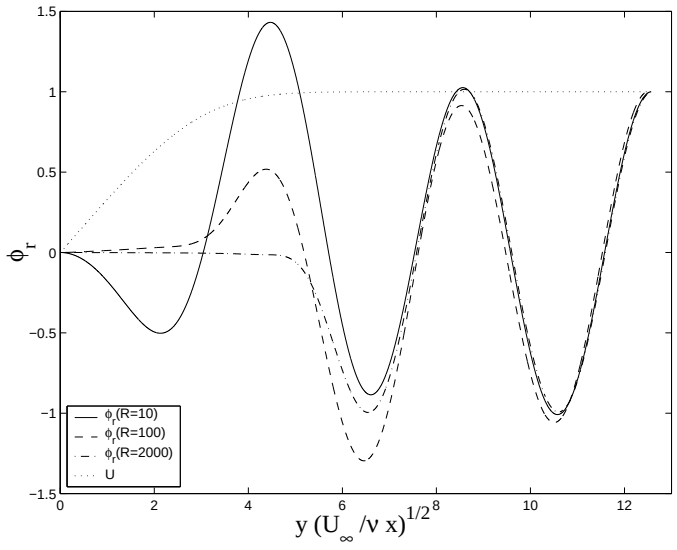

Figure 4.20: Validation of Orr-Sommerfeld solver (compare with Fig. 7 in Jacobs & Durbin (1998).

agreement (compare Fig. 4.20 with Fig. 7 in Jacobs & Durbin 1998). The procedure to synthesize the inflow disturbance from these eigenmodes is then similar to the Rogallo algorithm described above, with the following modification: In the summations (4.5-4.7) the Fourier mode $e^{ik_z z}$ is replaced by the Orr-Sommerfeld eigenmode $\phi(\omega, k_z, R; z)$ (note the explicit dependence on ω, k_z and R, the Reynolds number based on Blasius variables). The summations now read:

$$u(y,z,t) = \sum_{\omega}\sum_{k_y}\sum_{k_z} \phi'(\omega, k_z, R; z)\frac{\widehat{u}}{ik_z}e^{ik_y y}e^{-i\omega t} \tag{4.21}$$

$$v(y,z,t) = \sum_{\omega}\sum_{k_y}\sum_{k_z} \phi(\omega, k_z, R; z)\widehat{v}e^{ik_y y}e^{-i\omega t} \tag{4.22}$$

$$w(y,z,t) = \sum_{\omega}\sum_{k_y}\sum_{k_z} \phi'(\omega, k_z, R; z)\frac{\widehat{w}}{ik_z}e^{ik_y y}e^{-i\omega t} \tag{4.23}$$

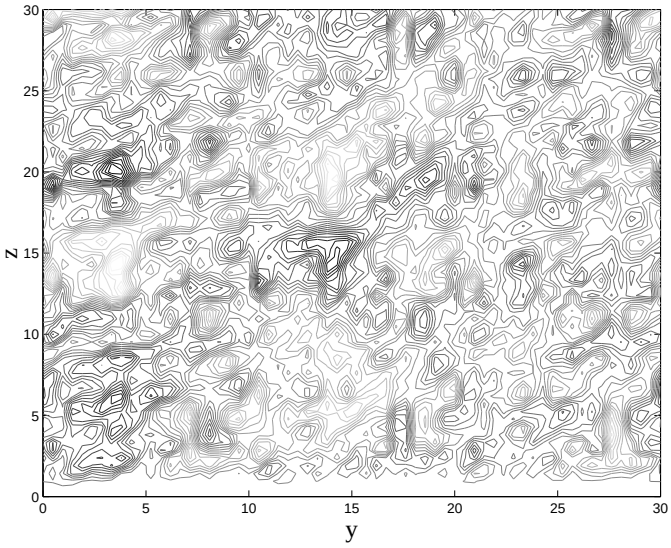

Figure 4.21: Streamwise contours of a disturbance generated using Orr-Sommerfeld modes, corresponding to the spectrum in Fig.4.12

The necessity to divide the u and w wave-number coefficients by ik_z is seen by substituting $\phi = e^{ik_z z}$ into the above expression and comparing with (4.5-4.7). We note that following Jacobs & Durbin (2001) we do not compute the eigenmodes of the Squire's equation, which are required to form a complete 3D basis.

4.7 Acknowledgments

The authors acknowledge the financial support of the NASA Langley Research Center, under Grant NAG12285.

4.8 References

[1] Andersson, P., Berggren, M. & Henningson, D.S. 1999 Optimal disturbances and bypass transition in boundary layers. *Phys. Fluids* **11** 134–150.

[2] Balaras, E. 2004 Modeling complex boundaries using an external force field on Cartesian grids in large-eddy simulations. *Comput. Fluids* **33**, 375–404.

[3] Balaras, E., Benocci, C. & Piomelli, U. 1995 Finite difference computations of high Reynolds number flows using the dynamic subgrid-scale model. *Theoret. Comput. Fluid Dyn.* **7**, 207–216.

[4] Balaras, E., Piomelli, U. & Wallace, J. M. 2001 Self-similar states in turbulent mixing layers *J. Fluid Mech.*, **446**, 1–24.

[5] Brandt, L. & Henningson, D. S. 2002 Transition of streamwise streaks in zero-pressure-gradient boundary layers. *J. Fluid Mech.* **472** 229–261.

[6] Brandt, L., Schlatter, P. & Henningson, D. S. 2004 Transition in boundary layers subject to free-stream turbulence. *J. Fluid Mech.* **517**, 167–198.

[7] Butler, K. M., Farrel, B. F. 1992 Three-dimensiona optimal perturbations in viscous shear flow. *Phys. Fluids A* **4** 1637–1650.

[8] Chorin, A. J. 1968 Numerical solution of the Navier-Stokes equations. *Math. Comput.* **22**, 742–762.

[9] Drazin, P. & Reid, W. H. 1981 *Hydrodynamic Stability*, (Cambridge University Press, Cambridge).

[10] Ellingsen, T., Palm, E. 1975 Stability of linear flow. *Phys. Fluids* **18** 487–488.

[11] Grosch C. E., Salwen, H. 1978 The continuous spectrum of the Orr-Sommerfeld equation. Part 1. The spectrum and the eigenfunctions *J. Fluid Mech.* **87**, 33–54.

[12] Jacobs, G. J., Durbin, P. A. 1998 Shear sheltering and the continuous spectrum of the Orr-Sommerfeld equation. *Phys. Fluids* **10** 2006–2011.

[13] Jacobs, R. G. 1999 Bypass transition phenomena studied by numerical simulation. PhD thesis (Report No. TF-77), Department of Mechanical Engineering, Stanford University.

[14] Jacobs, G. J. & Durbin, P. A. 2001 Simulations of bypass transition. *J. Fluid Mech.* **428**, 185–212.

[15] Jonáš, P., Mazur, O., Uruba, V. 2000 On the receptivity of the by-pass transition to the length scale of the outer stream turbulence. *Eur. J. Mech. B-Fluids* **19** 707–722.

[16] Kachanov, Y. S., Kozlov, V. V., Levchenko, V. Y. 1980 Experiments on nonlinear interaction of waves in a boundary layer. In *Laminar-Turbulent Transition* (R. Eppler and H. Fasel, eds.) (Springer, Berlin), 135–152.

[17] Kim, J. & Moin, P. 1985 Application of a fractional step method to incompressible Navier-Stokes equations. *J. Comput. Phys.* **59**, 308–323.

[18] Matsubara, M. & Alfredsson, H. 2001 Disturbance growth in boundary layers subjected to free-stream turbulence. *J. Fluid. Mech.* **430**, 149–168.

[19] Morinishi, Y., Lund, T. S., Vasilyev, O. V. & Moin, P. 1998 Fully-conservative higher order finite difference schemes for incompressible flow. *J. Comput. Phys.* **143**, 90–124.

[20] Morkovin, M. V. 1969 On the many faces of transition. In *Viscous Drag Reduction*, C.S. Wells, ed. Plenum, 1-31.

[21] Moser, R. D., Kim, J. & Mansour, N. N. 1999 Direct numerical simulation of turbulent channel flow up to $Re_\tau = 500$. *Phys. Fluids* **11**, 943–945.

[22] Orlanski, I. 1976 A Simple Boundary Condition for Unbounded Hyperbolic Flows. *J. Comput. Phys.* **21**, 251–269.

[23] Piomelli, U., Balaras, E. & Pascarelli, A. 2000 Turbulent structures in accelerating boundary layers. *J. Turbulence* **1**, (001) 1–16.

[24] Rai, M. M. & Moin, P. 1993 Direct numerical simulation of transition and turbulence in a spatially evolving boundary layer. *J. Comput. Phys.* **109**, 169–192.

[25] Roach, P. E., & Brierley, D. H. 1992 The influence of a turbulent free-stream on zero pressure gradient transitional boundary layer development part I: test cases T3A and T3B. In *Numerical Simulation of unsteady flows and transition to turbulence*, O. Pironneau, W. Rodi, I. L. Rhyming, A. M. Savill and T. V. Truong, eds. Cambridge, 319–347.

[26] Rogallo, R. S. 1981 Numerical experiments in homogeneous turbulence. *NASA Tech. Memo. 81315.*

[27] Schmid, P., Henningson, D. S. 2001 *Stability and Transition in Shear Flows* (Springer, Berlin).

[28] Voke, P., and Yang, Z. 1995 Numerical study of bypass transition. *Phys. Fluids* **7**, 2256–2264.

[29] Wu, X., Jacobs, R. G., Hunt, J. C. R. & Durbin, P. A. 1999 Simulation of boundary layer transition induced by periodically passing wakes *J. Fluid Mech.* **398**, 109–153.

Chapter 5

DNS of boundary-layer bypass transition with leading edge effects[1]

5.1 Abstract

This study investigates the accuracy of synthetic-turbulence inflow conditions to numerical simulations of boundary-layer bypass transition. To this end we have performed three direct numerical simulations (DNS) of boundary layer bypass transition. In two of the simulations, the inflow condition is imposed downstream of the leading edge and the free-stream turbulence (FST) is attenuated inside the boundary layer using two prescribed *ad hoc* attenuation profiles. In the third simulation, we included the leading edge of the flat plate inside the computational domain; thus we were able to follow the physical evolution of the FST above the flat plate. The results of the latter simulation reveal the presence of small-amplitude laminar streaks at the streamwise location corresponding to the inflow boundary of the truncated-domain simulations. Because these boundary-layer streaks are not modeled by the

[1]Originally published as

Ovchinnikov, V. O., Piomelli, U.& Choudhari, M. M., 2005 Numerical simulations of boundary layer bypass transition with leading edge effects In *Proc. 4th Int. Symp. Turbulence and Shear Flow Phenomena*, Williamsburg, Virginia, June 25-27, 2005, 425–340.

inflow specification for the truncated-domain simulations, such simulations may not be expected to provide reliable predictions of the bypass transition process. However, our simulations underline qualitative similarities between the flow fields in all three cases. Thus it is possible that, with suitable calibration, truncated-domain simulations may be a useful tool for investigating the physical mechanisms of bypass transition.

5.2 Introduction

Transition prediction has its place among the most important practical problems in fluid dynamics today. Among its applications are airfoil design and optimization of low-pressure turbine, in which it is frequently desirable to delay transition to turbulence or avoid boundary layer separation. For this reason, the recent years have witnessed extensive experimental, theoretical, and numerical work on boundary layer receptivity and transition. In a benign disturbance envorinment typical of external flight aerodynamics, transition is often initiated by the TS instability waves. In the presence of higher amplitude external disturbances, such as those encountered in turbomachinery flows, the transition bypasses the linear TS mechanism. Although the phenomenon of bypass transition has been well-studied through experiments, added insights via numerical simulations have been slow to come because of the formidable cost of computation, even at low Reynolds numbers (see Rai & Moin, 1993, Voke & Yang, 1994, Jacobs & Durbin, 2001). With the possible

exception of Rai & Moin (1993), the above studies did not account for the interaction between incoming FST and the flat plate leading edge. Because this interaction sets the initial conditions for the disturbance evolution in the region farther downstream, it is important to understand the effects of the *ad hoc* initial conditions on the boundary-layer transition process.

We have recently carried out several bypass transition simulations (Ovchinnikov *et al.* 2004) with the aim of investigating the effects of various inflow parameters on the onset of transition. In particular, we observed that boundary layer bypass transition is strongly dependent on the integral length scale of the free-stream disturbance and the extent of its penetration into the boundary layer. By varying, within a sensible range, the simulation parameters that were not specified in the reference experiment (Roach & Brierlay, 1992) we were able to move the transition onset upstream or downstream at a fixed level of FST intensity. These results indicated that in order to specify the problem fully, (i) a reliable value for the length scale of the free-stream turbulence, and (ii) the extent of disturbance penetration into the boundary layer at the inflow location of the simulation domain must be available from experiments. Simulations may also need to match experimental Reynolds stress profiles inside the boundary layer well upstream of the transition location.

Alternatively, in order to avoid the problem of specifying the near-wall behavior altogether, numerical simulations could include the boundary-layer leading edge. To investigate the difference between simulations with an artificial inflow dis-

turbance profile and those that include the leading-edge, we present a simulation with a super-elliptical leading-edge that is represented using the immersed boundary method (implemented according to Balaras, 2004). The super-ellipse is only a convenient choice of leading-edge shape that avoids velocity discontinuities associated with simulating a sharp leading edge; the effect of leading-edge geometry may be another significant factor and is not investigated here. The simulation is performed on a Cartesian coordinate system inside a multi-block domain. Through a simulation of this type, it is possible to follow the development of the free-stream disturbance near the boundary layer edge, and monitor the extent of its penetration into the boundary layer. Furthermore, it should be possible to make more general conclusions about the accuracy of the inflow-condition methods proposed in the past, and on the effect of *ad hoc* parameters in these methods. Our primary emphasis at this stage is on using statistical flow metrics to gauge the effect of various inflow treatments. Detailed investigation of transition physics is deferred to a later stage.

5.3 Problem Formulation

In this work we use the incompressible Navier-Stokes equations to perform DNS simulations of boundary layer transition under free-stream turbulence. The

equations of motion

$$\frac{\partial u_j}{\partial x_j} = 0, \tag{5.1}$$

$$\frac{\partial u_i}{\partial t} + \frac{\partial}{\partial x_j}\left(u_j u_i\right) = -\frac{1}{\rho}\frac{\partial p}{\partial x_i} + \nu \nabla^2 u_i, \tag{5.2}$$

are solved numerically using a second-order accurate finite-difference method on a staggered grid. The method fully conserves mass, momentum and kinetic energy in the discrete sense (see Morinishi *et al.*, 1998). The coordinates x, y and z refer, respectively, to the streamwise, spanwise and wall-normal directions. The velocity components in these directions are, respectively, u, v and w. All grids used are uniform in the spanwise direction y, stretched in the streamwise and wall-normal directions to allow accurate resolution of boundary layer disturbances, particularly in the transitional region. The discretized equations are integrated in time using an explicit fractional time-step method, (Chorin, 1968, Kim & Moin, 1985) in which all terms are advanced in time using the Adams-Bashforth method. The Poisson equation is solved, and the velocity is corrected to make the field solenoidal. The code has been extensively validated for a variety of turbulent (Balaras *et al.*, 1995, Balaras *et al.*, 2001) and re-laminarizing (Piomelli *et al.*, 2000) flows.

The code was parallelized with the message-passing interface (MPI). The computational box is divided into n subdomains in the streamwise direction, and each of the n processors integrates the equations of motion in one of the subdomains. The pressure field is obtained by applying spanwise FFT to the Poisson equation. This yields a pentadiagonal matrix for each Fourier mode, which is then inverted

by a cyclic reduction algorithm. Each processor is assigned a subset of the Fourier modes resulting from the application of FFT.

5.3.1 Initial and boundary conditions

Two types of simulations of boundary layer transition have been carried out. In the first type (truncated-domain), the inflow plane is located downstream of the flat-plate leading edge. In this case our computational domain is a rectangular box with dimensions $L_x \times L_y \times L_z = 620\delta^o_{98} \times 30\delta^o_{98} \times 40\delta^o_{98}$, where δ^o_{98} is the 98% thickness of the laminar boundary layer at the inlet.[2] The inlet is located at $Re_\theta \simeq 50$, ($Re_x = 5,520$, $x = 15$). At the outflow, δ_{98} is approximately 1/4 of the wall-normal domain.

In the second type (full-domain), we used the same length scale as in the first type (*i.e.* δ^o_{98}) and our computational domain consisted of two boxes with dimensions $L_x \times L_y \times L_z = 50\delta^o_{98} \times 30\delta^o_{98} \times 40\delta^o_{98}$ and $L_x \times L_y \times L_z = 720\delta^o_{98} \times 30\delta^o_{98} \times 38.7\delta^o_{98}$, respectively. The multi-block approach is necessary because, in order to resolve properly the formation of the boundary layer around the leading edge, very fine wall-normal grid resolution is required that is not necessary throughout the entire domain. In the first box, we used the immersed boundary method to represent a flat plate with a super-elliptical leading edge (see Lin *et al.*, 1992) with radius 1.3 (or, equivalently, plate half-thickness) and aspect ratio 6. In order to

[2]Taking the location of 98% of the velocity maximum removed small-amplitude fluctuations of the velocity around its free-stream mean. The ratio δ_{98}/δ_{99} was about 0.9.

validate the immersed-boundary representation of the leading-edge geometry, we simulated laminar flow around a superellipse of aspect ratio 6, at $Re = 2,400$, based on the plate half-thickness, and obtained excellent agreement with the data of Lin *et al.* (1992). To avoid excessive computational cost, only the top half of the super-ellipse was modeled, and a symmetry condition was used on the bottom boundary. The symmetry condition is not physical, since it anchors the flow stagnation point to the tip of the super-ellipse at all times. The effect of on the fluctuations in the stagnation point location on transition characteristics needs to be ascertained.[3] The flow configuration is sketched in Figure 5.1. The inflow boundary is located at $x = -20$, inside the first box, the leading edge being at $x = 0$. At location $x = 20$, corresponding to $Re_x = 7,280$, cross-stream velocity planes were saved and used as the inflow condition for the second box. At the outflow of the second box, δ_{98} was approximately 1/3 of the wall-normal domain. All streamwise distances quoted in this article are measured relative to the leading edge.

The following boundary conditions were applied:

1. In the truncated-domain simulations, the inlet velocities are imposed by adding zero-mean perturbations to the Blasius base-flow. The disturbance was generated using the modified Rogallo (1981) algorithm as implemented by Jacobs and Durbin (2001) with Fourier modes (see Ovchinnikov *et al.*, 2004, for details). The disturbance field was multiplied by an attenuation profile f, which was smoothly decreased from $f = 1$ in the free stream to $f = 0$ at the plate

[3]Simulations without the symmetry condition are described in §6.

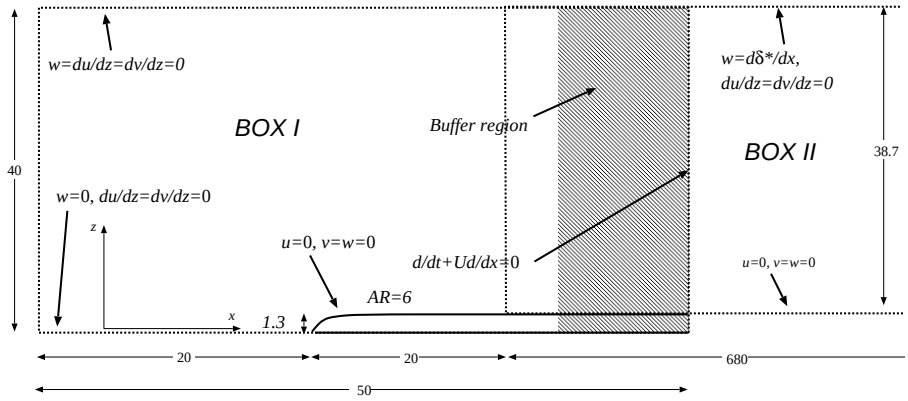

Figure 5.1: Schematic of the geometry for the full-domain simulation

surface to mimic the shear-sheltering of the boundary layer (see Jacobs & Durbin, 1998), which hampers the penetration of turbulence towards the wall. The attenuation profiles, plotted in Figure 5.3, are defined as

$$f = 1 - \frac{\tanh\left(7\left(z_0 - z\right) + 1\right)}{\tanh\left(7\right) + 1}, \tag{5.3}$$

where z_0 is the inflection point location of the attenuation profile. For Truncated I and II cases, $z_0 = 1.0$ and 1.5, respectively.

Similarly, the inflow for the first box of the full-domain simulation was obtained by adding a zero-mean field to a uniform mean velocity profile. The inflow condition for the second box was obtained by interpolating velocities from the first box onto the wall-normal grid of the second box, as mentioned above. In all cases, the initial free-stream turbulence integral length scale was $3.0\delta^o_{98}$ and the target FST intensity was 6% at $(x = 15, Re_x = 5,520)$. In all simulations, downstream of a short transient, the FST intensity decayed as a power law $(x - x_0)^{-\alpha}$ with $\alpha \approx 0.7$.

2. At the outlet, convective boundary conditions (Orlanski, 1976) were applied. Simulation results in the last 10% of the domain were discarded due the proximity of the outflow boundary condition.

3. In the spanwise direction, y, periodic conditions were used.

4. At the free-stream boundary of the truncated-domain simulations and the second (downstream) box of the full-domain simulation, we imposed $u = 1,\ v = 0,\ w = d\delta^*/dx$, where δ^* is computed for the Blasius profile. In these simulations the acceleration coefficient K, $\equiv -\left(\nu/U_\infty^2\right)\left(dU_\infty/dx\right)$, was of the order of 10^{-7}. The value of K at which a turbulent boundary layer is expected to re-laminarize is around 3.0×10^{-6} (Spalart, 1986). Since in our case K is an order of magnitude lower, we do not expect the acceleration to affect transition significantly. For the first (upstream) box of the Full-domain simulation we used a slip-wall boundary condition on the free-stream boundary. The resulting acceleration of the free-stream flow was also mild, with $K \simeq 10^{-7}$.

5. No-slip conditions were used on the bottom wall of the truncated-domain simulations, the bottom wall of the second box of the full-domain simulation, and the plate leading edge within the first box.

5.4 Results

The grid requirements for DNS of boundary-layer bypass transition can be found in various sources (Rai & Moin, 1993, Jacobs & Durbin, 2001, Ovchinnikov *et al.*, 2004). As a general rule, for a second-order accurate algorithm, the streamwise and spanwise grid spacing should be under $\Delta x^+ = 12$, $\Delta y^+ = 6$ with the same wall-normal resolution as needed for DNS of the turbulent boundary layer (*i.e.* the grid should have 7-8 cells below $y^+ = 10$ and the first node away from the wall should be below $y+ = 1$). Simulation parameters are summarized in Table 5.1 and the streamwise mesh spacing is shown in Fig. 5.2, which also shows the streamwise resolution used by Jacobs & Durbin (2001), who also used a code similar to ours.

The initial purpose of the truncated-domain simulations was to capture the region of transition onset accurately (as judged by the skin friction rise and the turbulent kinetic energy budgets), but not its final stages, or the fully-turbulent regime. While this significantly reduces computational cost, it limits the region of reliable data to the maximum of $x = 275, Re_x = 100,100$ (see Figure 5.2). Consequently, in all of the plots that follow, data from truncated simulations have been restricted to this region. Data from the full-domain simulation, in contrast, are reliable up to $x \simeq 660, Re_x \simeq 240,000$.

In subsequent figures that show streamwise evolution of various quantities, we plot a dotted vertical line at location $x = 220$, $Re_x = 80,080$ to denote the middle of skin friction rise. The skin friction coefficient, which shows a characteristic rise

Table 5.1: Summary of simulation parameters.

Case	$nx \times ny \times nz$	Δx^+	Δy^+	Δz^+_{min}
Truncated I	$900 \times 180 \times 150$	Fig.5.2	3.0	1.0
Truncated II	$900 \times 180 \times 150$	Fig.5.2	2.5	0.5
Full Upstream Box	$288 \times 192 \times 222$	Fig.5.2	2.4	0.5
Full Downstream Box	$1474 \times 192 \times 159$	Fig.5.2	2.5	0.8

in transition, is defined as

$$C_f = \frac{\tau_w}{\frac{1}{2}\rho U_\infty^2}. \tag{5.4}$$

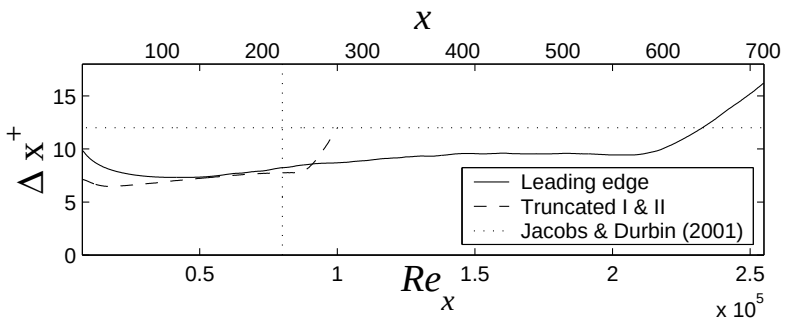

Figure 5.2: Streamwise mesh spacing in wall units

The difference between Truncated I and Truncated II cases is the choice of the attenuation profile, shown in Figure 5.3. As can be seen, in case I, turbulence is placed closer to the wall than in case II, in which the disturbance profile attenuates rapidly just inside the boundary-layer edge.

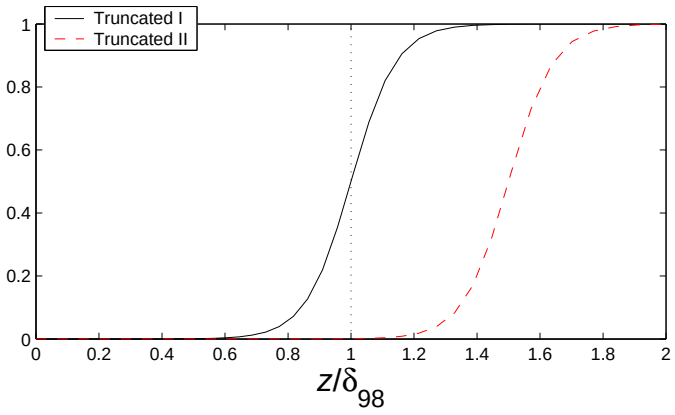

Figure 5.3: Attenuation profiles used in truncated-domain simulations.

In order to permit a direct comparison between the three simulations, the external disturbance environment must be the same. This means that the type of disturbance, its integral length scale and intensity should be identical. Since in the full-domain simulation our inflow plane was located $40\delta^o_{98}$ upstream of the truncated-domain inflow plane, [4] we were required to experiment with the intial disturbance amplitude and length scale of the Full-domain inflow in order to match the initial amplitude (6%) and decay rate of the truncated-domain simulations. The FST intensities are shown in Figure 5.4. It can be seen that the FST level in the full-domain simulation is slightly above the target value. This discrepancy, however, is small and should not cause a major shift in the onset of transition.

In addition, because the full-domain simulation inflow is located upstream of the truncated-domain simulation inflow, the boundary layer in the former (due to the FST and the leading edge geometry) could potentially evolve differently and result

[4]Recall, that $\delta^o_9 8$ is measured at the inflow location of truncated simulations

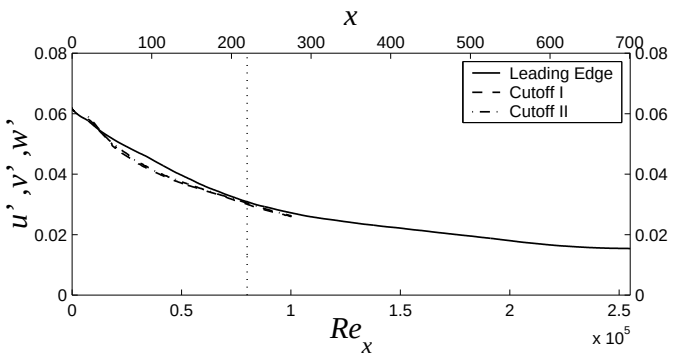

Figure 5.4: Evolution of the FST intensity.

in a different mean flow, which would complicate comparisons with the truncated simulations. To investigate this possibility, in Figure 5.5 we show the streamise evolution of the displacement and momentum thicknesses for the three simulations, which are defined as

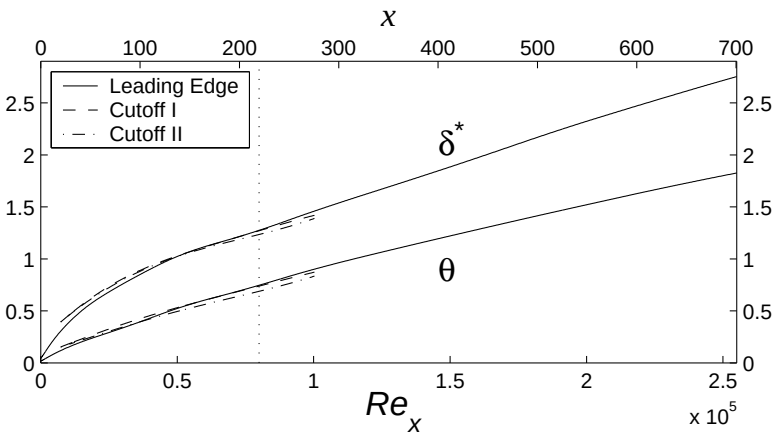

Figure 5.5: Streamwise evolution of displacement and momentum thickness.

$$\delta^* = \int_0^{y_{max}} \left(1 - \frac{\langle U \rangle}{U_\infty}\right) dy, \tag{5.5}$$

$$\theta = \int_0^{y_{max}} \frac{\langle U \rangle}{U_\infty} \left(1 - \frac{\langle U \rangle}{U_\infty}\right) dy. \tag{5.6}$$

The good agreement in these quantities ($\delta*$ and θ are within 2.5% and 5% of the average value for the three cases) indicates that the mean flows upstream of the onset of transition are very similar.

As stated before, in truncated simulations an attenuation profile is used to bring the turbulence velocities to zero at the flat plate. No generally accepted theory on the depth and shape of the penetration profile exists (although see the works by Leib *et al.* 1999 and Jacobs & Durbin 2001). To shed some light on this matter, in Figure 5.6 we show profiles of the turbulent kinetic energy (TKE), defined as $k = \langle u_i' u_i' \rangle / 2$ (a prime denoting a fluctuation from the mean), inside the boundary layer at locations $x = 25$, 75, 175, 275, ($Re_x = 9,100,\ 27,300,\ 63,700,\ 100,100$) for the three simulations (see Figure 5.3 for attenuation profiles). The first location is fully within the perturbed laminar boundary layer, the second is near the location of transition onset (judging by the skin friction rise, shown Figure 5.13) and the last, near the end of transition. The wall-normal coordinate is the Blasius similarity variable $\eta = z/\sqrt{\nu U_\infty / x}$. The laminar boundary layer edge corresponds to $\eta \simeq 4.9$. At location $x = 25$, the full-domain simulation shows nearly the same kinetic energy as the Truncated II case. The maximum TKE corresponding to the Truncated I case is twice that of the full-domain case. However, from that location on, the growth

of the TKE inside the boundary layer for the full-domain case surpasses that of the other cases, so that by location $x = 75$ the maximum boundary layer TKE for the full case is 20% larger than that of the Truncated I case. By location $x = 275$, which is at the beginning of the fully-turbulent region, all three cases show very similar TKE levels, suggesting that a turbulent equilibrium is being established. For more detail, in Figure 5.7 we show the streamwise evolution of the maximum Reynolds stresses inside the boundary layer (normalized by the friction velocity, u_τ, defined as $\sqrt{\tau_w/\rho}$). One can see the prominent growth of $\langle uu \rangle$, larger in the full domain case than in the others, which is followed by a decay towards a turbulent equilibrium in all three cases. The growth, linear-like in the region $x = 25 - 75$, is present only in the streamwise component of the Reynolds stress, which is magnified in Figure 5.8 and normalized by U_∞. From this plot one can also see that the truncated-domain simulations show an initial transient in which the streamwise stress is oscillatory. This may indicate that in the truncated simulations the inflow disturbance lacks the proper phase information inside the boundary layer and produces a lower disturbance growth-rate. The result is that in the early transitional stage the Reynolds stresses do not match the values of the full-domain simulation.

It has been shown experimentally and numerically (see, for example, Matsubara & Alfredsson, 2001, and Jacobs & Durbin, 2001) that boundary-layer interaction with moderate-amplitude FST is characterized by the appearance of low-frequency streaks of streamwise velocity[5] inside the perturbed laminar and early transitional

[5]Also known as Klebanoff (1971) modes

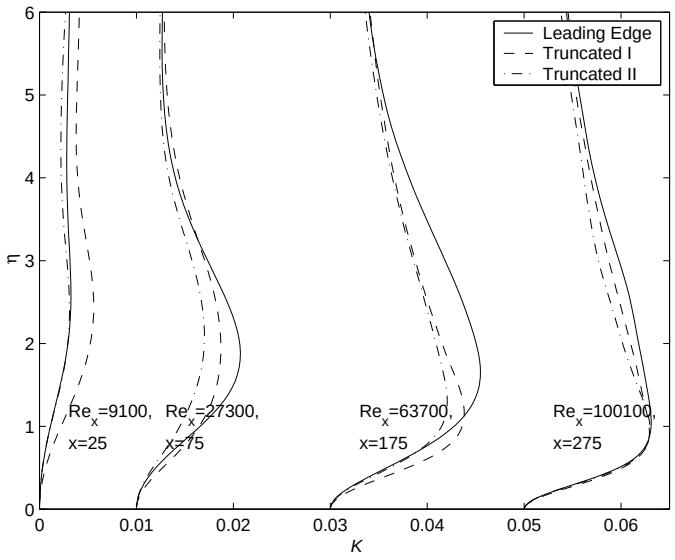

Figure 5.6: Profiles of the turbulent kinetic energy vs. η. Successive curves are offset by 0.02 on the x-axis.

boundary layer.

Jacobs & Durbin (2001) and Brandt, Schlatter & Henningson (2004) performed DNS of boundary-layer transition due to moderate levels of FST. The later group reported secondary streak instability as the cause of transition, while the former claimed that the streaks provide a receptivity path for the FST to enter the boundary layer, but are otherwise irrelevent to the transition process (*i.e.* no evidence of secondary instability was seen).

Examination of the flow field in our simulations revealed the presence of near-wall streaks in all three cases. Figure 5.9 shows contours of the streamwise velocity fluctuation in a plane parallel to the wall at $z = 0.05$, which at location $x = 15$, $Re_x = 5,500$ corresponds to 5% of the boundary layer thickness δ_{98}, and about 2%

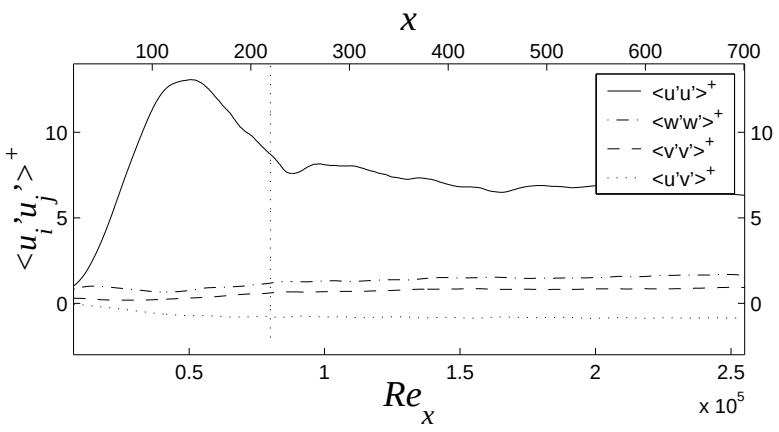

Figure 5.7: Streamwise evolution of maximum Reynolds stress levels inside the boundary layer normalized by the friction velocity u_τ.

of δ_{98} at $x = 100$, $Re_x = 36,400$. The qualitative similarity of the plots away from the inlet suggests that the transition mechanism is the same in all cases (this is further supported by the comparison between the evolution of the corresponding TKE budgets, shown in Figure 5.12 for two cases). From location $x = 15$ (where the inlet into the truncated-domain simulations is placed) to $x \approx 22$, however, only the full-domain plot shows incipient streaks. Streamwise streaks can also be inferred from spanwise correlation functions of the streamwise and wall-normal velocity fluctuation. In a streaky flow, the wall-normal velocity correlation falls below zero due to the vortical structures that must be present in order to generate the streaks. The distance to the correlation minimum can be interpreted as the size of the streak-generating vortex, or roughly one half of the average distance between a high- and a low-speed streak. Figure 5.10 shows plots of the wall-normal correlation function at two locations, $x = 120$ ($Re_x = 43,680$), just upstream of the rapid skin friction

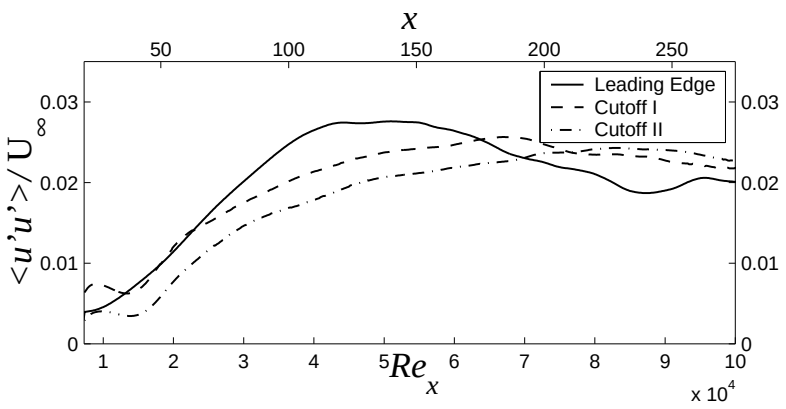

Figure 5.8: Streamwise evolution of maximum $\langle u'u' \rangle$ stress levels inside the boundary layer normalized by the free-stream velocity.

rise, and at $x = 350$ ($Re_x = 127,400$), at the onset of fully-developed turbulence. For each location, the top plot is at the edge of the boundary layer.

At location $x = 120$ (Figure 5.10 top), oscillatory behavior in the correlation curves can be observed throughout the spanwise domain, consistent with strongly-correlated laminar streaks with a dominant spacing of 3.5, ($\simeq 1.4\delta_{98}$) (at this location $\delta_{98} \simeq 2.5$). The oscillations are absent at the boundary-layer edge, indicating that the streaks are present only inside the boundary layer. At the end of transition and the onset of turbulence, the correlation function shows a single dip below zero, corresponding to one half of the average spacing between turbulent streaks of opposite sign. These streaks are closer together, separated by a distance of 2, and are different from their transitional counterparts. The boundary-layer thickness at this location is 4.5. Further characterization will determine whether the streaks in the

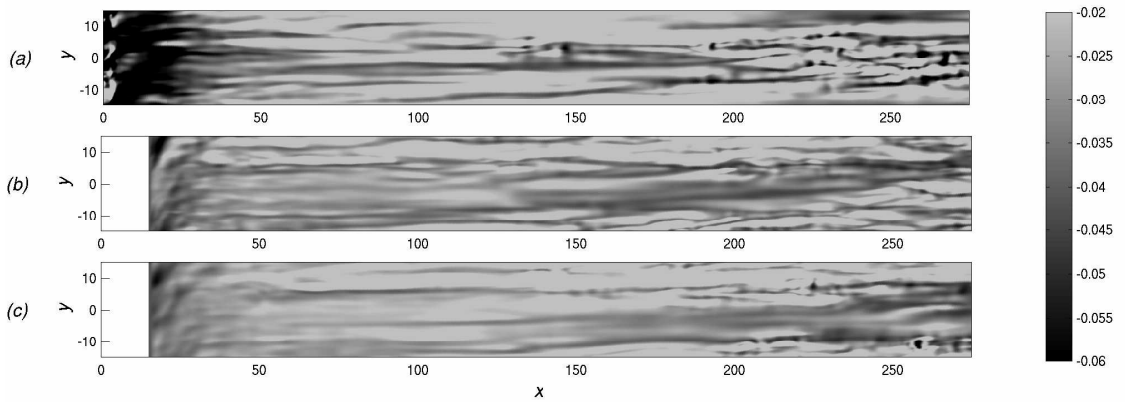

Figure 5.9: Contours of the streamwise velocity fluctuation at $z = 0.05$; (a) Full-domain, (b) Truncated I (c) Truncated II.

perturbed laminar region are Klebanoff modes. [6]

The obvious reason for the initial absence of streaks from the truncated-domain simulations is that the inlet disturbance is has been synthesized with random phases for the various Fourier modes. Distance is required for the boundary layer to generate a physical disturbance field. Examining the TKE budgets for the three cases revealed the importance of production, convection and pressure transport in this process. These terms are defined, respectively, as

$$-\frac{\partial \langle U_i \rangle}{\partial x_j}\langle u_i' u_j' \rangle, \qquad -\langle U_i \rangle \frac{\partial k}{\partial x_j}, \qquad -\frac{1}{\rho}\frac{\partial \langle p' u_i' \rangle}{\partial x_i}. \tag{5.7}$$

and are shown Figure 5.11 at location $x = 16$, for the Truncated II and the full-domain cases. The budget for the Truncated I case is qualitatively similar to the Truncated II case, with a higher amplitude for all terms. The other terms were

[6] This is done in §6.

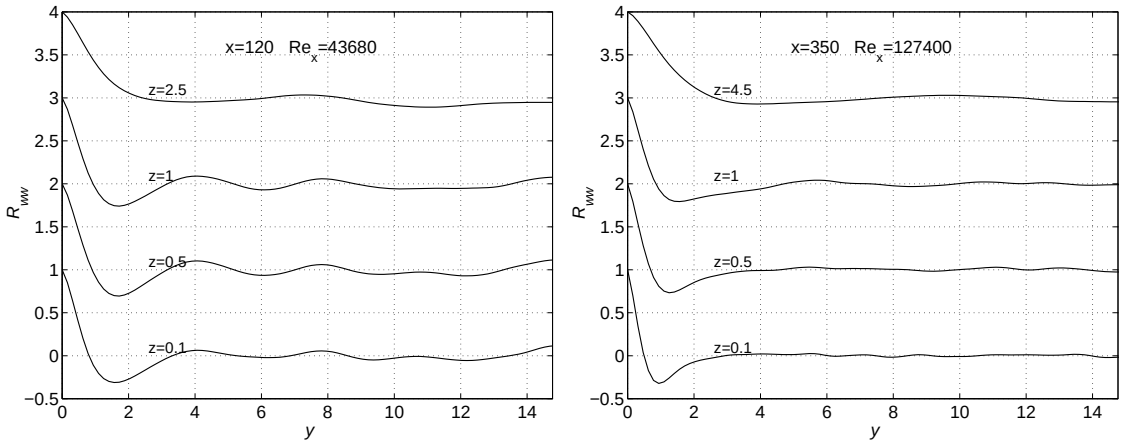

Figure 5.10: Spanwise correlation of wall-normal velocity fluctuation. left (transitional): $x = 100$, $Re_x = 36,400$; right (turbulent): $x = 300$, $Re_x = 109,200$. Successive curves are ofset by 1 in the vertical direction.

not significant in the truncated-domain simulations. The convection and pressure transport terms are most active at the inflection point of the attenuation profile (see Figure 5.3).

By location $x \simeq 30$, the convection and pressure are much smaller than the production term and from $x = 50$ on, the budgets for the two cases are very close. In figure 5.12, we plot the TKE budget terms at $x = 75$, and $x = 275$. The striking similarity between the cases indicates that despite an initial transient in the truncated simulation, the dynamics of the TKE asymptotes to the same behavior in all three cases.

In view of the discrepancies between the full- and truncated-domain simulations discussed above, it is surprising to see good agreement in the skin friction between the Truncated II case and the full-domain case that is observed in Figure

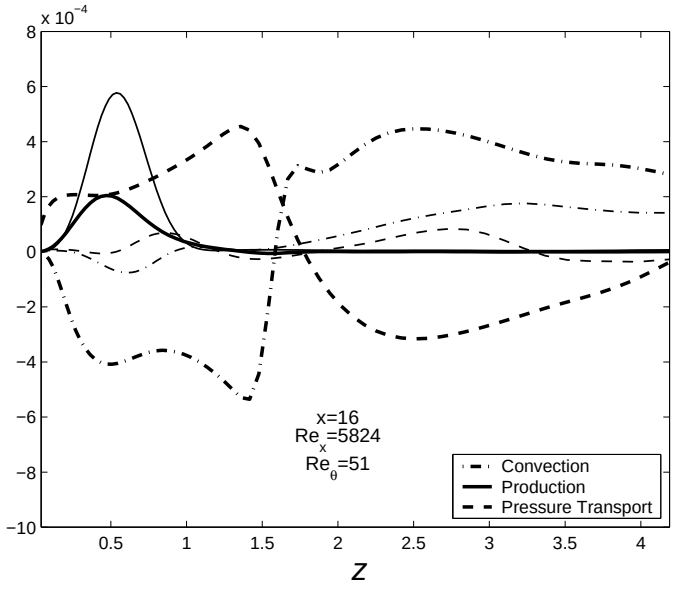

Figure 5.11: Convection, Production and Pressure Transport of TKE; thin lines: Full-domain case, thick lines: Truncated II case.

5.13. The fact that we were not able to match the FST levels in the two simulations perfectly (cf. Figure 5.4) further suggests that the agreement is likely to be coincidental. Moreover, there is no *a priori* reason to choose one attennuation profile over the other, and Figure 5.13 shows that the onset of transition is sensitive to the choice of attenuation profile. In addition, in our simulations the inlet into the truncated-domains was arbitrarily placed at $x = 15$. It is conceivable that shifting this location could significantly change the evolution of the streamwise streaks which, in turn, would shift the transition onset.

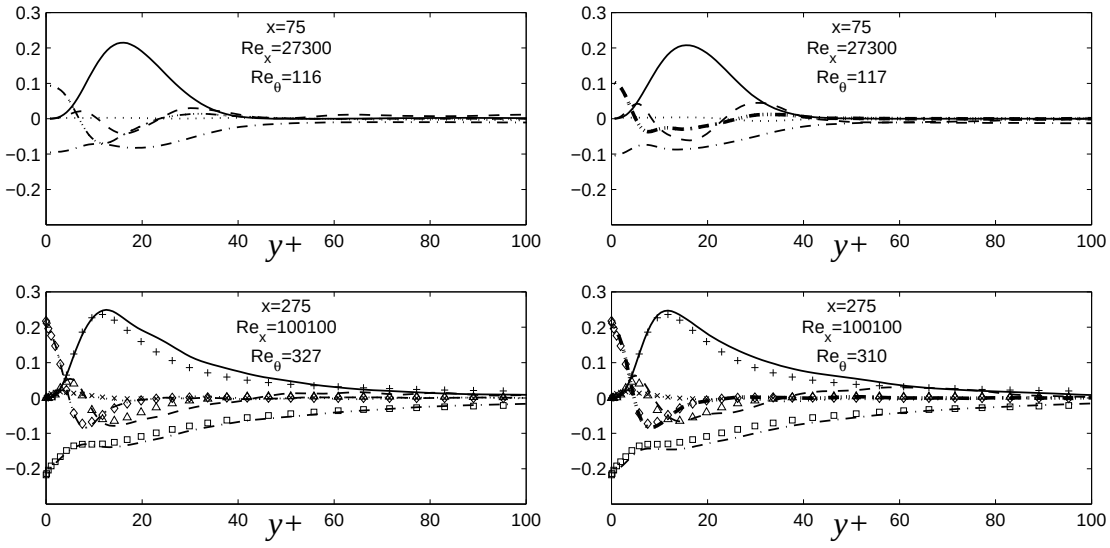

Figure 5.12: Budgets of the TKE in viscous units. Left — Leading edge; right – Truncated II; Symbols: DNS of turbulent channel flow at $Re_\tau = 395$ by Moser *et al.* 1999; lines: present simulation. +, ——— : production; □ , —·— Dissipation; △ , – – – Turbulent transport; × , ····· Pressure diffusion; ◇ , —·····— Viscous diffusion.

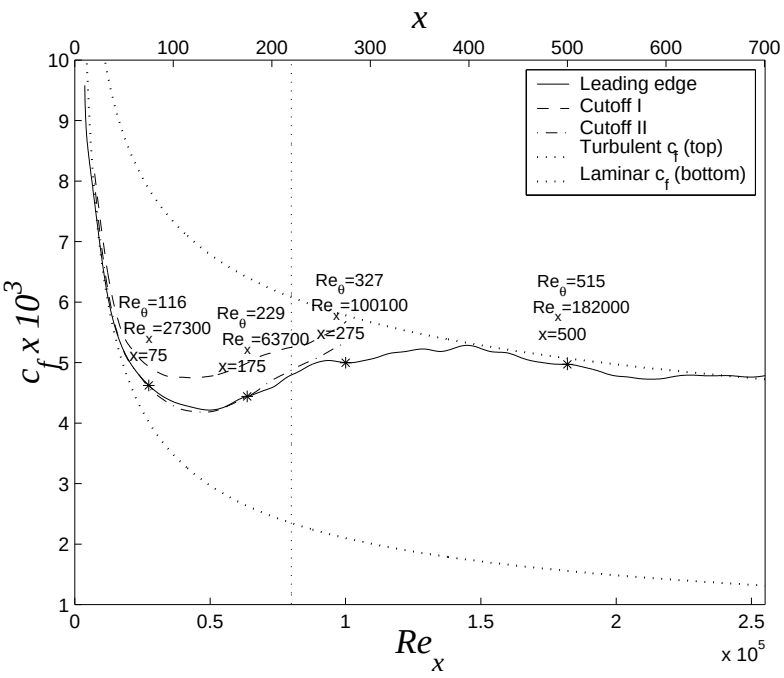

Figure 5.13: Streamwise evolution of the skin friction coefficient. The asterisks correspond to the streamwise locations indicated by the text labels.

5.5 Conclusions

In the present study we compared DNS of boundary layer bypass transition performed in a truncated domain with a simulation that includes the flat plate leading edge modeled as a super-ellipse. The results of the full-domain simulation indicate that at the streamwise location corresponding to the inflow boundary of the truncated-domain simulations, the boundary layer already contains streaks of streamwise velocity. We also noted a higher linear-like growth of $\langle u'u' \rangle$ inside the boundary layer in the full-domain simulations in the region $x \simeq 25 - 75$, which results in an overshoot of the levels found in turbulent boundary layers. The pres-

ence of streaks implies that the current inflow condition for the truncated-domain simulations is unphysical, since the streaks appear to be a necessary feature of transition (Jacobs & Durbin 2001; Brandt, Schlatter & Henningson 2004). This suggests that for accurate prediction of transition onset, truncated simulations of the type presented in this study are inadequate because they cannot ensure the correct evolution of streamwse streaks. An alternative approach to inflow specification for the truncated-domain simulations would be to use a theoretical model that acccounts for the interaction of free-stream disturbance with the wall and the upstream evolution of the disturbance signature inside the boundary layer (Choudhari, 1996, Leib *et al.*, 1999). Predictions from such models were shown to provide encouraging agreement with the measured boundary-layer data for lower levels of FST (Leib *et al.* 1999). Future investigations will show whether this approach, with proper calibration, can provide accurate inflow conditions for numerical simulations of bypass transition.

Finally, given the similarity among the low fields and TKE budgets for the three simulations described, it appears that truncated domain simulations provide a cost-effective approach if the aim is to understand the physical mechanisms underlying transtion and not to seek quantitative predictions of the transitional region.

5.6 References

[1] Balaras, E. 2004 Modeling complex boundaries using an external force field on Cartesian grids in large-eddy simulations. *Comput. Fluids* **33**, 375–404.

[2] Balaras, E., Benocci, C. & Piomelli, U. 1995 Finite difference computations of high Reynolds number flows using the dynamic subgrid-scale model. *Theoret. Comput. Fluid Dyn.* **7**, 207–216.

[3] Balaras, E., Piomelli, U. & Wallace, J. M. 2001 Self-similar states in turbulent mixing layers *J. Fluid Mech.*, **446**, 1–24.

[4] Chorin, A. J. 1968 Numerical solution of the Navier-Stokes equations. *Math. Comput.* **22**, 742–762.

[5] Choudhari, M. 1996 Boundary-layer receptivity to three-dimensional unsteady Vortical disturbances in free stream *AIAA Paper* **1996-0181**.

[6] Fadlun, E. A., Verzicco, R., Orlandi, P. & Mohd-Yusof, J. 2000 Combined immersed-boundary finite-fifference methods for three-dimensional complex flow simulations. *J. Comput. Phys.* **161**, 35–60.

[7] Jacobs, G. J., Durbin, P. A. 1998 Shear sheltering and the continuous spectrum of the Orr-Sommerfeld equation. *Phys. Fluids* **10** 2006–2011.

[8] Jacobs, G. J. & Durbin, P. A. 2001 Simulations of bypass transition. *J. Fluid Mech.* **428**, 185–212.

[9] Kim, J. & Moin, P. 1985 Application of a fractional step method to incompressible Navier-Stokes equations. *J. Comput. Phys.* **59**, 308–323.

[10] KLEBANOFF, P.S. 1971 Effects of free-stream turbulence on a laminar boundary layer. *Bull. Am. Phys. Soc.* **16**.

[11] LEIB, S. J., WUNDROW, D. W., & GOLDSTEIN, M.E. 1999 Effect of free-stream turbulence and other vortical disturbances on a laminar boundary layer *J. Fluid. Mech.* **380** 169–203.

[12] LIN, N., REED, H. L., SARIC, W.C. 1992 Effect of leading-edge geometry on boundary layer receptivity to free-stream sound. In *Instability, receptivity, and Turbulence* Hussaini, M., Kumar, A., Streett, C., eds. Springer-Verlag 421–440.

[13] MATSUBARA, M. & ALFREDSSON, H. 2001 Disturbance growth in boundary layers subjected to free-stream turbulence. *J. Fluid. Mech.* **430**, 149–168.

[14] MORINISHI, Y., LUND, T. S., VASILYEV, O. V. & MOIN, P. 1998 Fully-conservative higher order finite difference schemes for incompressible flow. *J. Comput. Phys.* **143**, 90–124.

[15] ORLANSKI, I. 1976 A Simple Boundary Condition for Unbounded Hyperbolic Flows. *J. Comput. Phys.* **21**, 251–269.

[16] OVCHINNIKOV, V. O., PIOMELLI, U. & CHOUDHARI, M. M., 2004 Inflow conditions for numerical simulations of bypass transition *AIAA Paper*, **2004-0591**.

[17] PIOMELLI, U., BALARAS, E. & PASCARELLI, A. 2000 Turbulent structures in accelerating boundary layers. *J. Turbulence* **1**, (001) 1–16.

[18] Rai, M. M. & Moin, P. 1993 Direct numerical simulation of transition and turbulence in a spatially evolving boundary layer. *J. Comput. Phys.* **109**, 169–192.

[19] Roach, P. E., & Brierley, D. H. 1992 The influence of a turbulent free-stream on zero pressure gradient transitional boundary layer development part I: test cases T3A and T3B. In *Numerical Simulation of unsteady flows and transition to turbulence*, O. Pironneau, W. Rodi, I. L. Rhyming, A. M. Savill and T. V. Truong, eds. Cambridge, 319–347.

[20] Rogallo, R. S. 1981 Numerical experiments in homogeneous turbulence. *NASA Tech. Memo. 81315.*

[21] Voke, P., and Yang, Z. 1995 Numerical study of bypass transition. *Phys. Fluids* **7**, 2256–2264.

Preface to Chapter 6

In Chapters 4 and 5, we demonstrated the sensitivity of the transition location to the FST environment. We also concluded that synthetic inflow conditions applied on truncated domains contain *ad hoc* parameters that impact the onset of transition. One obvious solution is to include the leading edge in the simulated domain, so that the FST environment develops naturally along the flat plate.

In the following article, "Numerical simulations of boundary-layer bypass transition due to high-amplitude free- stream turbulence," we perform one such simulation in an attempt to match the ERCOFTAC T3B experiment on boundary-layer transition due to 6% FST. This simulation is unique in that it is the first to compute the flow around the flat-plate leading edge, and also to match the decay and length scale of the external disturbance environment. Good agreement with experiment gives weight to our investigation of the physics.

Two additional transition simulations, performed with a smaller FST length scale, are included in our analysis. In one, only the top half of the superellipse is simulated (as in Chapter 5), and in the other, the entire superellipse. It is found that the symmetry condition inherent in the first formulation attenuates turbulence near the leading edge of the plate. The boundary layer is more receptive to the FST at the lower length scale, and thus the symmetry condition results in lower levels of disturbance inside the boundary layer. For this reason, the symmetry condition is

not permissible at low FST length scales. At much higher FST length scales (as in the T3B ERCOFTAC case), however, the boundary-layer receptivity to FST is low, and the symmetry condition is unlikely to have a significant effect.

Chapter 6

Numerical simulations of boundary-layer bypass transition due to high-amplitude free- stream turbulence[1]

6.1 Abstract

Direct numerical simulations (DNS) of bypass transition in the flat-plate boundary layer induced by high-amplitude free-stream turbulence (FST) are carried out. The computational domains employed begin upstream of the flat-plate leading edge and extend into the fully-turbulent region inside the boundary layer. In one of the simulations performed, the boundary conditions are chosen to match the ERCOFTAC benchmark case T3B. The evolution of mean velocity and Reynolds stress statistics is in good agreement with experimental data. In the other simulations, the length scale and intensity of the oncoming FST are varied to determine the effects on the onset and mechanism of transition. An examination of boundary-layer disturbance amplification suggests that the boundary-layer sensitivity to FST near the leading edge is reduced when the FST length scale is much larger than the leading edge radius and the boundary-layer thickness in the leading edge region.

[1]Submitted as Ovchinnikov, V.O., Choudhari, M.M. & Piomelli, U., Numerical simulations of boundary-layer bypass transition due to high-amplitude free-stream turbulence. *J Fluid Mech. Submitted for publication.*

We have examined the evolution of boundary-layer disturbances in the transitional region and followed the birth and growth of turbulent spots in two cases, one with a much higher FST length scale than the other. We found that elongated streamwise streaky structures were present inside the transitional regions in both cases. However, turbulent spot formation due to a streak instability was observed only in the case of lower length scale. The instability appeared to be of the varicose (symmetric) type and the resulting turbulent spot did not have an arrow-head shape. For the case with a higher length scale, turbulent spots formed upstream of the region where streaks could be detected. Two of the four spots examined had a well-defined arrowhead shape. The differences in the transition scenarios can be explained by a lower receptivity to FST at the leading edge.

6.2 Introduction

In many wall-bounded flows of engineering interest, it is desirable to delay the onset of laminar-turbulent transition. In aerospace applications, it may be advantageous to maintain laminar flow over a major portion of an airfoil to reduce drag. In turbine design, preventing/delaying transition would result in substantial increase in energy efficiency. Transition to turbulence has therefore been the focus of extensive research in the past century.

Traditionally, the study of transition in a boundary layer has been approached from the point of view of linear stability. In 1880, Lord Rayleigh derived the in-

viscid disturbance equations linearized around a mean flow. Later Orr (1907) and Sommerfeld (1908) included the effects of viscosity and, assuming a harmonic form for the disturbance, independently derived the Orr-Sommerfeld equation. The first solutions for a flat-plate boundary layer were obtained by Tollmien (1929) and Schlighting (1933) in the form of exponentially growing (TS) waves. Their existence was verified experimentally by Schubauer & Skramstad (1947). When TS wave amplitude exceeds 1% of the free-stream velocity, the perturbed boundary layer develops secondary 3D instabilities. Klebanoff, Tidstrom & Sargent (1962) observed regions of high and low disturbance velocity, "peaks and valleys," alternating in the spanwise direction. The spanwise wavelength of this pattern was the same as that of the TS wave. This transition scenario has been denoted K-type, or fundamental. The later nonlinear stages of transition are characterized by lambda vortices aligned in the flow direction. Kachanov, Kozlov & Levchenko (1977) observed a similar pattern but with the spanwise scale twice that of the TS wave. In this case, the lambda vortices had a staggered arrangement. This transition scenario is known as H-type, N-type, or subharmonic.

Because TS waves grow on a viscous time scale, they attain amplitudes that are sufficiently high for instability at Reynolds numbers on the order of 10^6. In many flows with an external disturbance environment, however, transition is observed at Reynolds numbers on the order of 10^5 and does not involve the TS mechanism. The term "bypass transition" (Morkovin, 1969) has been used to describe various transition cases in which TS waves are bypassed. The case of boundary-layer bypass

transition due to the effects of free-stream turbulence (FST), has received particular attention by experimental, theortical, and, more recently, computational scientists.

6.2.1 Experimental work on transition due to FST

Klebanoff (1971) observed that the Blasius boundary layer developes low-frequency unsteady undulations of the streamwise velocity. The amplitude of the peak response increased in proportion to the FST amplitude, and grew larger in proportion with the boundary-layer thickness. Arnal & Juillen (1978) found no evidence of TS waves in the transition process, and observed that the peak of the low-frequency disturbance energy is located in the middle of the boundary layer. Kendall (1985) observed long streamwise streaks with small spanwise scales, which he called Klebanoff modes. He also confirmed the finding of Klebanoff (1971) that the disturbance $u_{\rm rms}$ grows in proportion to the boundary-layer thickness. Westin *et al.* (1994) reported that the mean velocity profile is only slightly modified, despite boundary-layer $u_{\rm rms}$ levels of 10% of the free-stream velocity. They also confirm a linear dependence of the boundary-layer $u_{\rm rms}$ on the layer thickness. Comparing with other experiments, they note that the constant of proportionality may be variable. Matsubara & Alfredsson (2001) review several experiments performed at the Royal Institute of Technology in Stockholm (KTH). They find that the spanwise spacing of streaks increases with the FST level, and also slightly increases with the downstream distance. Towards the end of the transition zone, it is approximately

equal to the boundary-layer thickness. These authors suggested that the spanwise scale selection occurs within the boundary layer. In a later publication, however, Fransson & Alfredsson (2003) conclude that the selection process is more complex and is influenced by the FST scale, among other effects.

Matsubara & Alfredsson (2001) confirmed that the transitional boundary-layer $u_{\rm rms}$ peak is located approximately in the middle of the layer and showed that the length of streaks increases in proportion to the layer thickness. From their flow visualization studies, the authors concluded that the appearance of "turbulent spots" (Emmons, 1951) – patches of irregular fluid motion surrounded by quasi-laminar flow that appear in the last stages of transition – may be due to secondary instabilities of the streaks. Recently, Fransson, Matsubara & Alfredsson (2005) performed additional experiments using a wide range of FST intensities and length scales and made several important contributions. First, there is an initial region near the leading edge where the disturbance grows more slowly than farther downstream, *i.e.* the receptivity process requires a certain distance. Second, the disturbance energy increases in proportion to the FST energy and the flat-plate Reynolds number. Third, the transition Reynolds number is inversely proportional to the FST energy. Finally, the extent of the transition zone increases in proportion to the flat-plate Reynolds number. These findings should be confirmed in future experiments and numerical simulations. Although Fransson *et al.* (2005) vary the FST length scale in a controlled manner, they do not sort their data based on the length scale. Thus, the effect of the FST length scale is not addressed in their work. Jonáš, Mazur & Uruba

(2001) study the effect of the FST dissipation length scale on the onset of transition at the FST intensity of 3%. Based on their measurements of the intermittency, they find that the onset of transition is moved upstream with increasing length scale, and that the transition region becomes longer. Further, quantitative studies of the effect of the FST length scales are needed, especially because, together with other factors, such as leading-edge geometry, they may explain some of the discrepancies in the experiments performed to date.

6.2.2 Theoretical work

Several approaches have been taken to understand the physics of bypass transition from a theoretical point of view. Ellingsen & Palm (1975) proposed a linear mechanism for the inviscid evolution of an initial disturbance in the presence of a mean shear. Due to the non-orthogonality of the linearized incompressible Navier-Stokes (NS) operator, an initial disturbance may undergo an initial "transient" growth before exponential decay. In particular, the streamwise disturbance component may grow linearly in time, evolving into a streak (*i.e.* a streamwise elongated region of positive or negative u-velocity fluctuation). A similar mechanism due to Moffat was also referenced by Philips (1969). Landahl (1980) provided a physical explanation for this phenomenon, known as the "lift-up" effect. Pairs of counterrotating vortices are able to lift low-momentum fluid into the upper boundary-layer, producing a streak of negative velocity. Transient growth theory has been used with

some success in several wall-bounded flows. Butler & Farrel (1992) found optimal perturbations (*i.e.* those that produce the highest level of disturbance at a reference downstream location) for plane channel, Couette, and parallel boundary-layer flow. Andersson, Breggen & Henningson (1999) and Luchini (2000) used optimization techniques to find optimal disturbances for a Blasius boundary layer. The optimal initial disturbance was found to be a pair of counterrotating vortices and the downstream perturbation was a streaky structure with a spanwise scale of 1.4 times the boundary-layer thickness. Good agreement was found between the boundary-layer disturbance cross-stream profile and $u_{\rm rms}$ data of Westin *et al.* (1994). Since transient growth theory is linear, it can only describe the initial transition stages, and not its later development. A theoretical study of streak breakdown as part of a self-sustaining cycle can be found, for example, in Waleffe (1997). Andersson *et al.* (2001) used Floquet theory to investigate secondary instabilities of the optimal final disturbance from Andersson *et al.* (1999). These authors found critical streak amplitudes for the sinuous and varicose instabilities to be 26% and 37%, respectively. A different approach was used by Choudhari (1996), who used the linearized unsteady boundary layer equations (LUBLE) to examine the boundary layer response near the plate leading edge to small-amplitude convected vortical perturbations in the free stream. The forced response clearly showed gradual intensification of the streamwise velocity perturbation within the boundary layer, analogous to the measurements of Kendall (1985). A thorough analytical study by Leib, Wundrow & Goldstein (1999) showed that the FST interaction with the boundary layer doen-

stream of the LUBLE region was governed by linear boundary region equations. The results indicate the importance of the cross-stream velocity components in triggering streamwise streaks. Their predictions provide encouraging agreement with measured boundary-layer data for lower levels of FST. Bertolotti (1997) had used the parabolic stability equations (PSE) to study the response of the boundary layer away from the leading edge to vortical modes in the free stream. Although his initial profiles did not account for the upstream interaction between the free-stream disturbance and the plate leading edge, the results showed that low frequency stationary modes produce disturbance profiles that are in good agreement with the experiments.

6.2.3 Computational work

Large-Eddy Simulations (LES) and Direct Numerical Simulations (DNS) of transition in boundary layers have been slow to come due to the large computational requirements involved. Not only must the boundary layer resolution be sufficiently fine to ensure accurate disturbance evolution, but the streamwise domain size must be large enough to capture all stages of the boundary-layer development. The first DNS of boundary-layer transition due to FST in a spatial formulation was performed by Rai & Moin (1993), who used a fifth-order upwind biased finite-difference, fractional-step, compressible NS solver to model the experiments of Blair (1983). The disturbance was generated to match the von Kármán energy spectrum

with a prescribed intensity and length scale. The predicted location of transition onset showed reasonable agreement with the experimental data, but the skin friction development farther downstream was compromised because of under-resolution. Their work indicates that the resolution needed to simulate a transitional flow is as high as that for a turbulent boundary layer.

Voke & Yang (1995) used a finite volume conservative method to perform LES of boundary-layer transition, in an attempt to reproduce the experiments of Roach & Brierlay (1992). Although their simulations were severely under-resolved and the FST properties were not matched to the experiment, they were able to provide qualitative insights into the transition mechanism. The interaction of the wall-normal FST component with the mean shear was proposed to be the key mechanism for the production of Reynolds shear stress, which, together with the mean shear, drove the production of the streamwise Reynolds stress.

A properly resolved DNS of FST-induced transition was performed by Jacobs & Durbin (2001). Following Grosch & Salwen (1978), these authors expanded the FST in the eigenfunctions of the linear Orr-Sommerfeld operator to provide a somewhat realistic inflow condition without simulating flow around the leading edge. With fine, turbulent-like resolution in the entire boundary layer, they obtained very good agreement with the T3A experiment of Roach & Brierlay (1992) at 3% FST intensity. Klebanoff modes were found to be a prominent feature of their simulations, and were generated nonlinearly by the penetration of the FST into the boundary layer. The spanwise streak spacing was in agreement with the optimal results of

Andersson *et al.* (1999). No evidence of streak instability was reported in their work. Instead, low-speed streaks provide a receptivity path between the FST and the boundary layer, but are otherwise irrelevant to transition. The onset of transition was attributed to the direct penetration of the free-stream disturbance into the perturbed laminar boundary layer.

Brandt, Schlatter & Henningson (2004) performed DNS of boundary-layer transition due to FST with variable length scale and intensity. They used the disturbance generation method in Jacobs & Durbin (2001) but also included the Squire modes for the wall-normal vorticity. They found that for a given FST intensity of 4.7%, increasing the FST length scale moves the onset of transition upstream. The spanwise scale of streaks did not vary appreciably with the FST length scale. Many aspects of their simulations are in qualitative agreement with the experiments of Matsubara & Alfredsson (2001). Using flow visualizations, Brandt *et al.* (2004) conclude that streak breakdown and turbulent spot formation is caused by one of two instability modes of low speed streaks. The sinuous mode, characterized by streak oscillations in the spanwise direction, was observed more frequently than the varicose mode, which was due to streak oscillation in the wall-normal direction. The authors note that the transition mechanism due to streak instability may resemble the behaviour of streaks in turbulent boundary layers. Ovchinnikov, Piomelli & Choudhari (2004) used DNS to study the effect of inflow parameters on the onset of transition. They confirmed the finding of Brandt *et al.* (2004) on the effect of the FST length scale and also showed that by manipulating the FST spectrum one

can significantly change the location of transition onset. They also suggest that including the leading edge of the plate may be necessary for accurate transition prediction.

6.2.4 Aim of the current work

In this study we perform the first high-resolution DNS of boundary layer transition due to high-amplitude FST, in which we compute the flow around the plate leading edge, and impose a FST length scale that matches the T3B experiment of Roach & Brierlay (1992). Our hope is to approximate the experiment with sufficient fidelity, such that the simulation database can be used to examine the underlying transition physics as well as to guide the development of physics based engineering prediction methods. Two additional simulations are performed with a smaller FST length scale in order to examine the effects of length scale variation on the transition mechanism.

6.3 Problem Formulation

We use the incompressible Navier-Stokes (NS) equations to perform DNS of boundary layer transition due to FST. The equations of continuity and momentum

$$\frac{\partial u_j}{\partial x_j} = 0, \tag{6.1}$$

$$\frac{\partial u_i}{\partial t} + \frac{\partial}{\partial x_j}\left(u_j u_i\right) = -\frac{1}{\rho}\frac{\partial p}{\partial x_i} + \nu \nabla^2 u_i + f_i, \tag{6.2}$$

are discretized using a second-order accurate finite-difference method on a staggered Cartesian grid. The method fully conserves mass, momentum and kinetic energy in the discrete sense (see Morinishi *et al.*, 1998). The presence of the body forces f_i is due to the immersed-boundary method, described at the end of this section. The coordinates x, y and z refer, respectively, to the streamwise, wall-normal, and spanwise directions. The velocity components in these directions are, respectively, u, v and w. All grids used are uniform in the spanwise direction y, and stretched in the streamwise and wall-normal directions to allow accurate resolution of boundary layer disturbances, particularly in the transitional region. The equations are integrated in time using an explicit fractional time-step method (Chorin 1968, Kim & Moin 1985), in which the convective and diffusive terms are advanced in time using the second-order accurate Adams-Bashforth method. The Poisson equation for the modified pressure is solved, and the modified pressure gradient is used to make the velocity field divergence-free.

The algorithm was parallelized using the Message-passing interface (MPI). The computational box is divided into n equal subdomains in the mean flow direction and each of the n processors integrates the equations of motion in one of the subdomains. The modified pressure field is obtained by applying a spanwise Fast Fourier Transform (FFT) to the discrete Poisson equation. This yields a pentadiagonal matrix for each Fourier mode, which is then inverted by a cyclic-reduction algorithm. Each processor is assigned a subset of the Fourier modes resulting from the application of the spanwise FFT. The code has been previously validated for

a variety of turbulent (Balaras *et al.*, 1995, Balaras *et al.*, 2001), re-laminarizing (Piomelli *et al.*, 2000), and transitional (Ovchinnikov & Piomelli 2006) flows.

The governing equations were advanced in time until a statistically stationary state was reached. Flow statistics were then accumulated for a time period required for the mean flow to traverse the entire domain three times. Convergence of the statistical sample was verified by comparing the statistics obtained using only half of the sample with those obtained using the entire sample. First-order quantities differed by less than 3%, second moments by less than 6%.

6.3.1 Simulation Parameters

Three DNS were performed in the current study. The two types of geometry are illustrated in figure 6.1. In one case, we computed the flow around the entire leading edge, and in the other two we only simulated the top half of the domain and assumed that the flow was symmetric about the mid-plane of the plate.

The primary goal of the current investigation was to study the mechanism of bypass transition in a realistic environment. Thus, the configuration of the main simulation was chosen to approximate the wind tunnel experiment T3B by Roach & Brierlay (1992), conducted at the FST amplitude of 6% of the free-stream velocity (as measured near the leading edge). This simulation also served as a validation case for the other simulations.

The available experimental data includes the evolution of the FST intensity

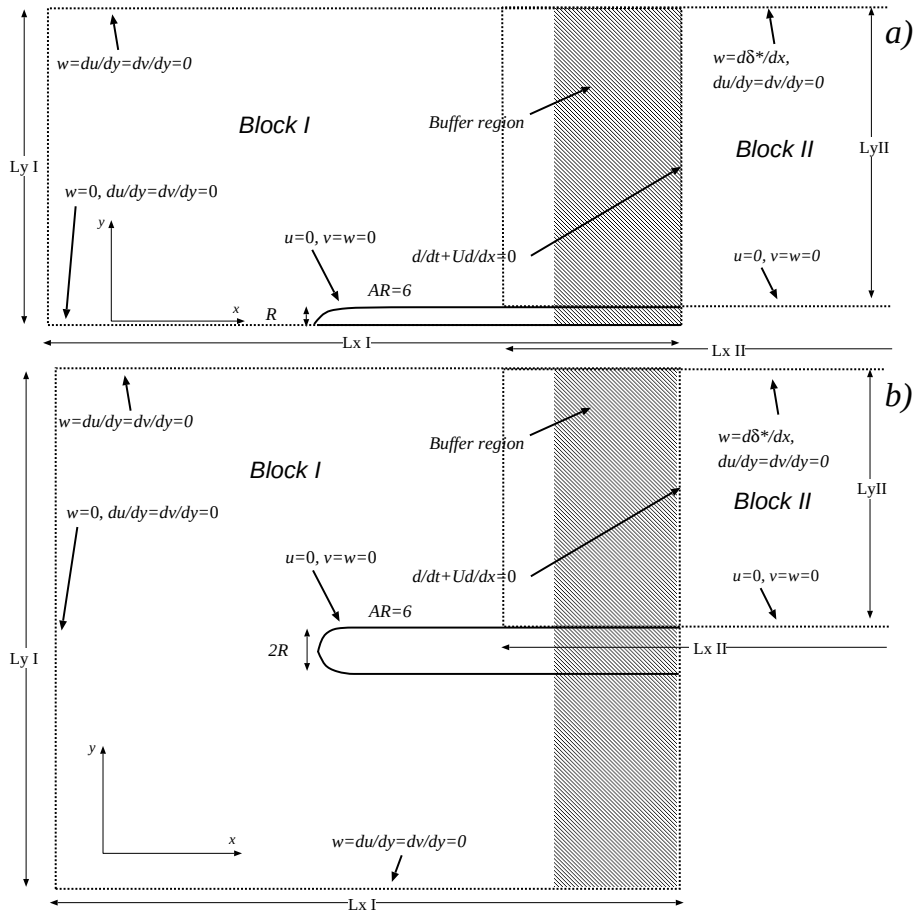

Figure 6.1: Computational configuration and boundary conditions; a) Domain with symmetry plane; b) Full domain.

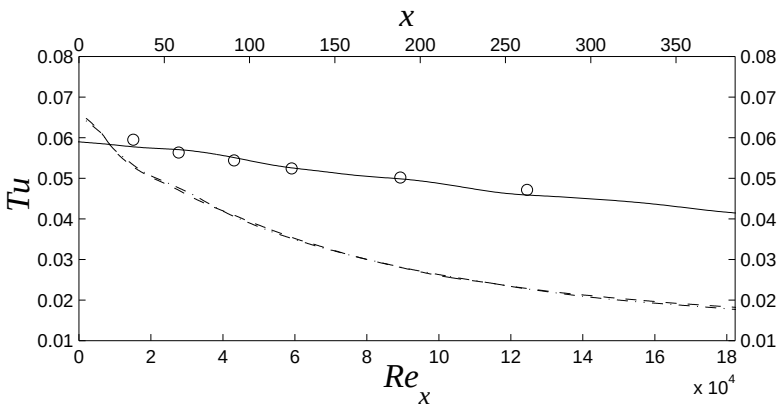

Figure 6.2: Evolution of the free-stream FST intensity. —— Case T3B; --- Case Is; —·— Case I; ∘ T3B experiment of Roach & Brierlay (1992).

with the streamwise distance, but not its integral length scale, defined as

$$L_{11} = \int_0^\infty \frac{\overline{u'(x)u'(x+r)}}{\overline{u'(x)u'(x)}} dr, \tag{6.3}$$

(where u' denotes the free-stream velocity fluctuation, and the brackets, the long-time average). The energy dissipation length scale, defined as

$$L_k = -\frac{k^{3/2}}{U_\infty dk/dx}, \tag{6.4}$$

where k denotes the turbulent kinetic energy, can be computed directly from the streamwise FST evolution. According to this definition, the smaller the turbulence decay rate, the larger the associated length scale value, consistent with the conventional (spatial) understanding of the length scale. For the T3B experimental data, assuming isotropy of the FST, we found $L_k = 25R$ at the leading edge location. To model the measured FST decay in the experiment, we chose $L_{11} = 14R$; this condition also ensures that $L_k = 25R$ as derived from the experimental data. From

this point on, we will refer to the calculation with $L_{11} = 14$ as the T3B simulation. For the other two simulations performed in this study (cases I and Is), the FST L_{11} value was set to 2.3, which is similar to the values used in other numerical investigations of FST-induced bypass transition (Jacobs & Durbin 2001; Brandt & Henningson 2004). The corresponding value for the dissipation length scale was $3R$. The evolution of the FST intensity for the experiment and simulations is shown in figure 6.2.

The leading edge of the experimental test section was asymmetrical with a circular tip of radius 0.75 mm. The Reynolds number based on the average free-stream velocity of 9.4 m/s, and the LE radius was 470. In our simulations, we used a symmetrical superellipse with an aspect ratio (AR) of 6 to model the leading edge of the plate. The geometry for the superellipse used in our study is given by:

$$\left(1 - \frac{1}{AR}\frac{x}{R}\right)^4 + \frac{y}{R}^2 = 1. \tag{6.5}$$

In all of our simulations, the Reynolds number based on the free-stream velocity and the minor half-axis of the superellipse (equivalently, the plate half-thickness, or the LE radius) was fixed at 475. Unless stated otherwise, all quantities presented in this study are normalized with the free-stream velocity (U_∞) and the LE radius (R). The above geometry was motivated by the availability of 2D numerical data for flow validation, and the assumption that this difference in geometry would not be significant because the estimated length scale of the FST was much larger than the LE radius. We note that the symmetry of the LE leads to a suction peak (see

figure 6.3) that was probably absent in the reference experiment. However, the experimental configuration cannot be reproduced exactly because the test section had a flap attached to the end, which cannot be simulated easily. Some discussion of leading-edge-geometry effects can be found in Klingmann *et al.* (1993) and Fransson (2004).

The Cartesian computational grid does not conform to the body of the superelliptical leading edge. To satisfy the no-slip boundary conditions on the superellipse surface, we employ the immersed boundary method of Fadlun, Verzicco, Orlandi & Mohd-Yusof (2000), following the implementation of Balaras (2004). In this procedure, the body forces, f_i, are non-zero only in grid-cells nearest to the cylinder surface, and are assigned in such a way that the velocity on the cylinder surface is zero to second-order accuracy. When the predicted velocity is projected onto a divergence-free field, the velocity perturbations that are introduced in the vicinity of the cylinder are small (Fadlun *et al.* 2000), so that the corrected velocity is also second-order-accurate around the plate. Finally, we note that in the case of explicit time advancement, calculating and including a force field in the momentum equations is equivalent to modifying the predicted velocities near the solid surface. The immersed boundary method, as described above, has been extensively validated in laminar and turbulent flows in the references mentioned.

To ensure that the immersed-boundary representation of the superelliptical leading edge was accurate, we performed a two-dimensional simulation of the mean flow past a superellipse with $AR = 6$, described by equation (6.5). The computa-

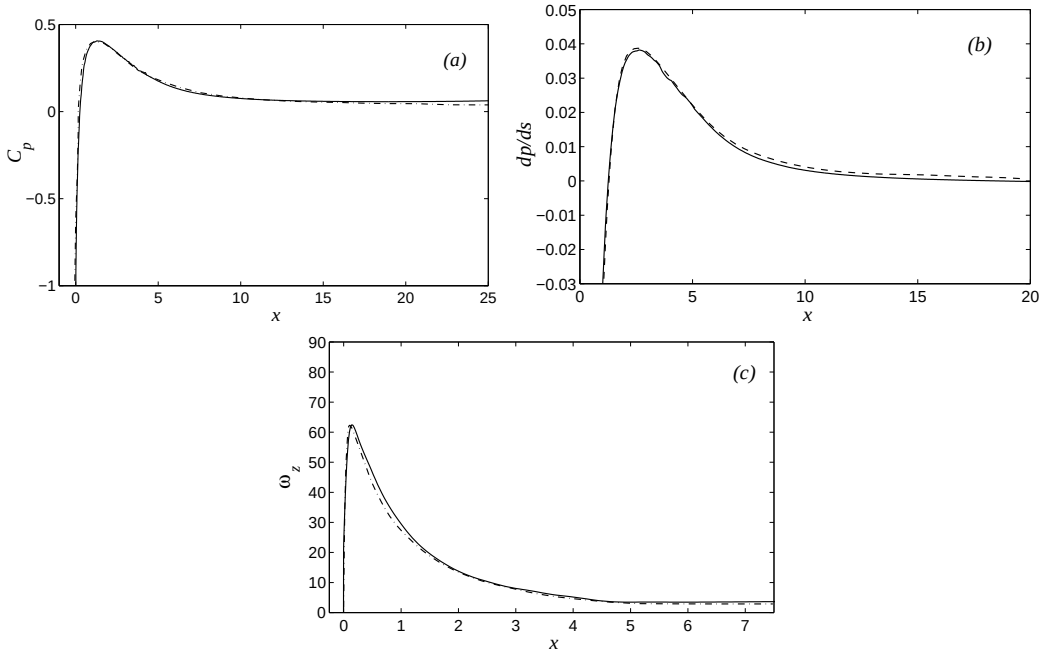

Figure 6.3: Comparison of surface properties for a 2D flow over a superellipse; (a) Pressure coefficient, C_p; (b) Pressure gradient with respect to arc length, dp/ds; (c) Wall vorticity, ω_z; —— current immersed boundary simulation, --- simulation by Collis & Lele (1996), —·— simulation by Lin (1992).

tional domain (similar to the one in figure 6.1 *(a)*) extended over 25 and 16 units in x and y directions, respectively, and was resolved with 1075 and 300 cells in the respective directions. The lengths are normalized by the ellipse minor half-axis (*i.e.* plate half-thickness), and the Reynolds number based on this length scale was $2,400$. This geometry was chosen to match the calculations of Lin (1992) and Collis & Lele (1996), who used NS solvers on curvilinear grids. Comparisons of the pressure coefficient, $C_p = 2\left(p - p_\infty\right)/\rho U_\infty^2$, along the surface of the ellipse, the pressure gradient with respect to arc length, dp/ds, and the surface vorticity, ω_z, are shown in Figure 6.3. The overall agreement is good.

The calculations performed in this study required substantial computational resources. Since the boundary-layer transition is caused by the free-stream environment, reproducing its properties to the best of ability is crucial for a proper comparison with experiments. Matching the FST intensity, length scale, and degree of isotropy, are the minimum requirements. Whereas generating nearly isotropic FST with a prescribed intensity is fairly easy, setting a large enough FST length scale may not be affordable in a computation. While the size of the smallest scales to be resolved is the same for cases I and T3B, since it depends only on the flow Reynolds number, the largest scales of the flow to be captured, which are proportional to the FST integral length scale, L_{11}, are approximately six times larger for the T3B case. Furthermore, because our simulations are spatially-developing, the streamwise domain must be large enough to capture the entire boundary-layer development, from the inception, through the transition, and into the fully-turbulent

regime. Additionally, near the leading edge of the plate, especially fine resolution is needed to ensure the accuracy of the immersed boundary method.

To decrease the overall cost of computation, each computational domain was split along the streamwise direction into two overlapping blocks. The first box contained the flat-plate superellipse, and had very fine resolution near the plate leading edge. A short distance downstream, where the boundary layer was thicker, the wall-normal resolution requirement could be relaxed. At this location, a time-sequence of planes of velocity was stored and used as the inflow condition for a second computational domain that had fewer points in the wall-normal direction, but maintained the fine streamwise resolution required to resolve the transition zone. The multi-block approach has been successfully used by researchers in the past (Huai, Joslin & Piomelli, 1997). However, strictly speaking, it violates the ellipticity of the incompressible NS equations (the pressure in the two blocks is independent). The errors due to the multi-block splitting were estimated by Ovchinnikov *et.al* (2005), who simulated boundary layer bypass transition due to a cylinder wake, and found to be insignificant. The immersed boundary representation of the superellipse was only necessary in the first block of each simulation. The second box was constructed so that its bottom boundary coincides with the surface of the plate of the upstream box.

Even with the multi-block aproach, computing the flow around the entire superelliptical body turned out to be prohibitive for the T3B case: the calculation would require more than 200 million points. This high cost was primarily due to

the need for a domain that is large enough to accomodate the FST integral scales, yet resolved finely enough to capture the smallest boundary-layer scales. Thus, we chose to make the additional approximation that the mid-plane of the plate can be represented as a plane of symmetry. The symmetry assumption halves the computational cost in the first block, reducing the overall cost to 150 million points, but, as described later, has the consequence of attenuating turbulence upstream of the plate in the vicinity of the plate mid-plane. Since the symmetry condition does not allow transpiration ($v = 0$), at the boundary $v' = 0$. This directly reduces v' levels near the symmetry plane and also indirectly inhibits the u' and w' components. This can reduce the effective amplitude of the FST interacting with the leading edge and hence may also affect the transition onset location. To estimate the errors due to the symmetry assumption, we repeated the simulation with the smaller FST length scale, $L_{11} = 2.3$ without invoking the symmetry assumption in the first block (the low FST length scale makes the full-domain simulation affordable). The two simulations with and without the symmetry condition are henceforth referred to as cases Is and I, respectively. The results of this investigation are presented in §6.4.1. The simulation parameters are summarized in Table 6.1.

6.3.2 Boundary Conditions

The following boundary conditions were applied:

1. The inlet velocities are imposed by adding a zero-mean perturbation field to

Case		L_{11}	$L_x \times L_y \times L_z$	$nx \times ny \times nz$	Largest grid size at wall $\Delta x^+ \times \Delta y^+_{wall,max} \times \Delta z^+$
I	Block I	2.3	38×62×23	288×444×192	9.5×0.6×3.5
	Block II		538×30×23	1472×160×192	12×0.7×3.6
Is	Block I	2.3	38×31×23	288×222×192	10×0.6×3.5
	Block II		538×30×23	1472×160×192	12×0.7×3.8
T3B	Block I	14	120×67×67	608×240×512	10×0.8×4.0
	Block II		330×66×67	882×170×512	10×0.8×3.5

Table 6.1: Simulation parameters.

the uniform mean flow $U = (U_\infty, 0, 0)$. The disturbance was generated using the algorithm due to Rogallo (1981) as described by Jacobs & Durbin (2001), but with Fourier modes, instead of Orr-Sommerfeld modes. The disturbance field has the model spectrum due to von Kármán, and is designed to be homogeneous, isotropic, and divergence-free to avoid large pressure fluctuations near the inflow plane. For all three cases, the FST amplitude in the vicinity of the leading edge was around 6% of U_∞; the three velocity r.m.s. values were within 10% of Tu, which was defined as $(\sqrt{\langle u'u' \rangle} + \sqrt{\langle v'v' \rangle} + \sqrt{\langle w'w' \rangle})/3$. The brackets denote Reynolds averaging, and the prime, a fluctuation from the mean. Further details on the inflow generation can be found in Ovchinnikov *et al.*(2004).

2. The interface condition between the first and second blocks was obtained by interpolating velocities from the first box onto the wall-normal grid of the second box as mentioned above. The plane from which velocity data were extracted was located at $x = 15$ for cases Is and I, and $x = 20$ for case T3B. All streamwise distances are quoted relative to the leading edge of the plate.

3. At the outlet of each computational block, a convective outflow boundary condition was applied to each velocity component (Orlanski 1976). Simulation results in the last 10-15% of each block were discarded in order to eliminate the effects of proximity to the outflow boundary.

4. In the spanwise direction, z, periodic conditions were used.

5. The no slip condition was imposed along the plate surface, whereas a symmetry condition was used upstream of the plate leading edge within the first block of cases Is and T3B.

6. Along the free-stream boundary of the first block of each simulation, we imposed slip-wall conditions, and at the free-stream boundary of the second block, we applied $\partial u/\partial y = 0,\ v = d\delta^*/dx,\ w = 0$, where δ^* is the displacement thickness computed for the Blasius velocity profile at each location. The boundary condition on the v-component provides the the correct mass flux through the top wall to account for the Blasius boundary-layer growth in the zero-pressure-gradient regime. It becomes less accurate in the transitional and turbulent boundary-layer regions, but does not result in significant free-stream acceleration.

The top (free slip) boundary condition in the first block does not allow flow normal to the boundary, causing the fluid above the boundary layer to accelerate in order to compensate for the boundary-layer growth. This approximation produces a slightly fuller velocity profile in the first computational block, but should not affect transition. The boundary layer is still fully laminar at the outflow of the first block, and in the second block, the velocity approaches the Blasius solution upstream of the transitional region. In the second block it was more important to provide outflow through the top to minimize the free-stream acceleration above the transitional region. In all three simulations, the acceleration coefficient, $\mathrm{K} = -\left(\nu/U_\infty^2\right)\left(dU_\infty/dx\right)$

was of the order of 10^{-7} for both blocks. The value of K at which a turbulent boundary layer is expected to re-laminarize is around 3.0×10^{-6} (Spalart 1986). Since the value of K in our case is an order of magnitude lower, we do not expect the acceleration to have an appreciable effect on the onset of transition.

6.3.3 Grid requirements

The computations carried out in this work required long integration times. A typical simulation required a month of clock time on an 8-processor Beowulf cluster (6000 CPU-hours). We were thus unable to perform a grid-refinement study. Ovchinnikov *et al.* (2004), however, performed calculations of bypass transition in a configuration similar to the one studied here (their calculations did not include the leading edge and were therefore much less computationally demanding). They observe that inadequate streamwise resolution in the transition region may lead to a premature and abrupt transition, probably because energy is aliased into the unstable scales due to under-predicted dissipation. They obtained grid-converged results with the grid spacings, in wall units (*i.e.*, normalized by the friction velocity u_τ and the viscosity ν) of $\Delta x^+ \simeq 7 - 12$, $\Delta y^+_{wall,max} \simeq 1$ and $\Delta z^+ \simeq 2.5 - 3$. We used similar values in our calculations, as reported in Table 6.1. Note that these spacings are typical of turbulent flow calculations, and are smaller than those used by Jacobs & Durbin (2001) and Rai & Moin (1993) in their simulations of bypass transition.

To ensure that the computational domains were sufficiently large in the spanwise direction, we computed spanwise correlations of the velocity. The u-velocity correlations are shown in figure 6.14 in §6.4.5. For the simulations with $L_{11} = 2.3$, the correlation functions approach the zero line well within the computational domain. For the T3B case, the spanwise domain size is smaller than optimal, but sufficient: an additional simulation preformed on a domain that was twice as large in the spanwise and wall-normal directions, but without the flat plate (hence without the stringent grid requirement), showed that the FST decay rate was unchanged. Therefore, we were confident that the external free-stream environment was adequately captured.

6.4 Results

We begin by examining cases I and Is to evaluate the effects of the symmetry condition on the transition mechanism and onset location. We find that at this value of the FST integral length scale, there are no qualitative differences in the transition mechanism between the two cases. The influence of the symmetry assumption is to reduce the near-wall FST intensity in the vicinity of the leading edge, producing a downstream shift in the transition onset. The essential transition physics remain the same. Examining the disturbance amplification inside the boundary-layer for case T3B, we conclude furthermore that for the choice of the larger FST length scale, the symmetry assumption should cause much smaller differences in the transtion onset.

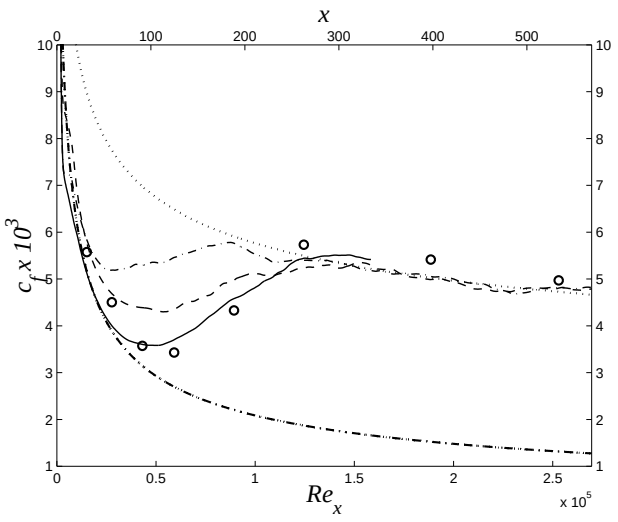

Figure 6.4: Evolution of the skin friction coeficient, C_f. —— Case T3B; --- Case Is; —·— Case I; ∘ T3B experiment of Roach & Brierlay (1992); —···— Blasius C_f; ····· Turbulent C_f.

Thus, the T3B simulation performed with a symmetry plane in the first block should capture the transition physics both qualitatively and quantitatively. We compare the transition mechanisms between cases I and T3B, and conclude the section with a visual analysis of the transitional flow fields.

6.4.1 The effect of symmetry condition

Cases I & Is were chosen to be identical except for the geometry of the first block. In case I we compute the flow around the entire superellipse and in case Is we only model the top half, using a symmetry condition at $y = 0$ upstream of the plate. The two domains were shown in figure 6.1.

Time-averaged quantities are defined as

$$F = \langle f(x,y) \rangle = \frac{1}{L_z}\frac{1}{T}\int_o^{L_z}\int_{t-T}^{t} f(x,y,z,\tau)d\tau dz. \tag{6.6}$$

The skin friction coefficient

$$C_f = \frac{\tau_w}{\rho U_\infty^2/2} \tag{6.7}$$

(where τ_w is the time-averaged wall stress), is an indicator of transition onset since it increases markedly across the laminar-turbulent shift. Its streamwise development is shown in figure 6.4.

The initial mismatch between the Blasius C_f and the simulation data is due to (i) the fact that Blasius similarity is invalid close to the leading edge, (ii) an uncertainty in the virtual origin of the boundary layer (in the figures, the start of the boundary layer, *i.e.* the location $x = 0$, is taken to be the tip of the superellipse) and (iii) the imposition of the free-slip boundary condition at the top wall of the first block of each simulation.

The C_f evolution shows that the onset of transition occurs at widely different locations, at $x = 100$, ($Re_x = 50,000$) for case Is, and at $x = 70$, ($Re_x = 35,000$) for case I. Even though the FST intensity (figure 6.2) evolves identically for the two cases, the Reynolds stress magnitudes at the boundary-layer edge are different. In figure 6.5*(a)* we plot the profiles of the TKE at several streamwise locations, and in 6.5*(b)*, profiles of the streamwise Reynolds stress, $\langle uu \rangle$, at the same locations. The short horizontal lines indicate the local boundary layer thickness, δ_{99}. Figure 6.5*(a)* shows that below $y = 5$, the TKE is lower for case Is, and at the edge of the laminar

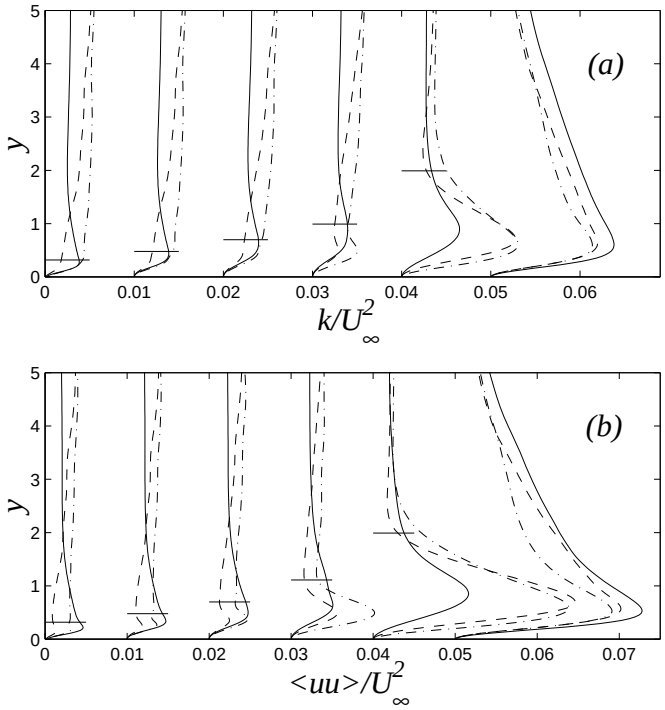

Figure 6.5: Profiles of (a) the TKE, and (b) streamwise Reynolds stress, $\langle uu \rangle$. From left to right, the plots correspond to $x = 3;\ 5;\ 10;\ 20;\ 75;\ 250;\ Re_x = 1,422;\ 2,370;\ 4,740;\ 9,480;\ 35,550;\ 118,500;$ —— Case T3B; --- Case Is; —·— Case I; The short horizontal lines indicate the local boundary-layer thickness δ_{99} On the x-axis the profiles are offset by 0.01.

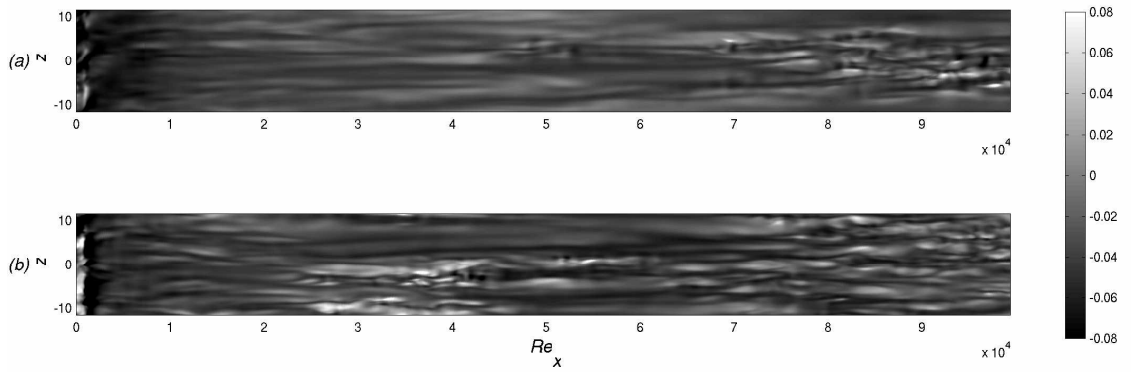

Figure 6.6: Contours of the streamwise velocity fluctuation inside the boundary layer; (a) Case Is; (b) Case I; $y = 0.04$.

boundary layer, it is about 50% of the case I value. This difference arises from the upstream development of the FST, which in case Is is inhibited by the symmetry condition at the bottom wall. The symmetry condition does not allow flow normal to the boundary, which reduces v_{rms} in the vicinity of the boundary and indirectly inhibits the other two FST intensities via the pressure strain redistribution term. Figure 6.5*(b)* shows that the boundary layer for cases Is & I is very sensitive to the free-stream level of the TKE. For $x < 30$, we see that the amplitude of the boundary-layer $\langle uu \rangle$ peak for case Is is about 50% lower than for case I.

A qualitative comparison of cases Is and I is made in figure 6.6, which shows instantaneous contours of the streamwise velocity fluctuation in the xz-plane located at $y = 0.04$ ($y/\delta^* = 0.13$ at $Re_x = 1 \times 10^4$). Only the transtional part of the flow field is shown for clarity. Higher-amplitude near-wall disturbance environment near the leading edge is evident for case I, and the corresponding boundary layer appears more disturbed throughout the domain, consistent with the more rapid transition onset

indicated in figure 6.4. Aside from the differences in the overall perturbation levels, the two flow fields are very similar. This suggests that the underlying transition mechanism is the same in both instances. The following discussion also demonstrates that this is the case.

At this FST length scale ($L_{11} = 2.3$) and range of FST intensities, transition appears to be accompanied by Klebanoff (1971) modes — long streaky structures that precede turbulent flow. These modes are responsible for the peak in $\langle uu \rangle$, located in the middle of the laminar boundary layer and growing in amplitude through the onset of transition.

A closer examination of the near-wall profiles of $u_{\rm rms}$ for cases I and Is, plotted together with the experimental data from Matsubara & Alfredsson (2001), is shown in figures 6.7*(a, c)* (the profiles corresponding to case T3B, as well as low-pass filtered disturbances in figure 6.7*(b)*, will be discussed later).

These authors performed experimental studies of FST-induced boundary-layer transition for FST intensities between 1%-6% of the free-stream velocity. They observed prominent streaks of the streamwise velocity preceding the fully-turbulent front for all experimental cases. They also showed that the wall-normal $u_{\rm rms}$ profiles show approximate self-similarity in the transition region. When the wall-normal coordinate is normalized by the boundary-layer displacement thickness, δ^*, the profiles yield a peak around 1.3, corresponding to the center of the streak (Klebanoff mode). As initially suggested by Klebanoff (1971), the expression $yd\overline{U}/dy$ provides a very good approximation to the profile shape in the near-wall region. The good agree-

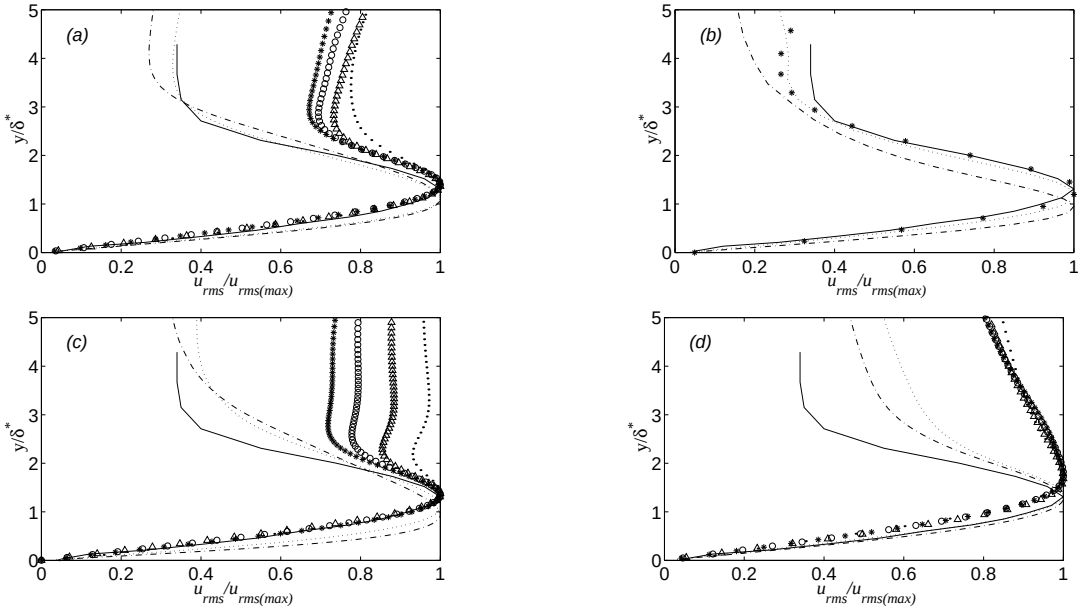

Figure 6.7: Profiles of u_{rms} across the boundary layer; δ^* is the local displacement thickness; a) Case Is; b) Case Is, low-frequency modes only (using a sharp Fourier cutoff filter); c) Case I; d) Case T3B; • $x = 4$, △ $x = 8$, ∘ $x = 12$, ∗ $x = 15$, ····· $x = 54$, —·— $x = 73$; —— self-similar profiles from Matsubara & Alfredsson (2001)

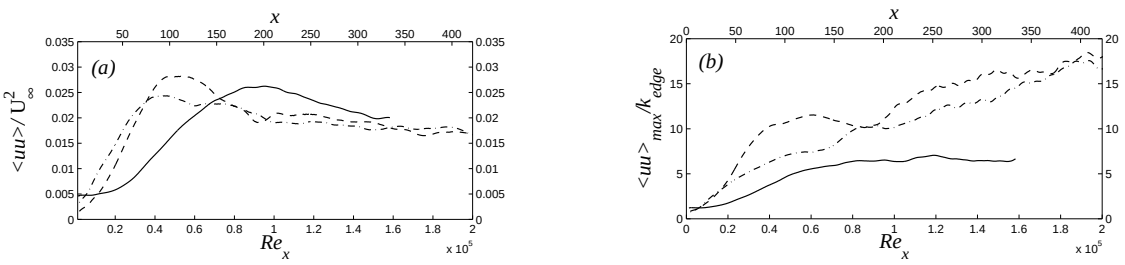

Figure 6.8: Evolution of the maximum streamwise Reynolds stress inside the boundary layer; a) normalized by U_∞; b) normalized by the TKE at the boundary-layer edge —— Case T3B, --- Case Is, —·— Case I

ment with the experimental data for cases I and Is indicates that in both instances, the transition mechanism is the same and involves the Klebanoff modes.

6.4.2 Streamwise evolution of $\langle uu \rangle$

Figures 6.8*(a, b)* show the evolution of the maximum streamwise Reynolds stress, $\langle uu \rangle$, inside the boundary layer. In 6.8*(b)*, the data are normalized using the turbulent kinetic energy at the edge of the boundary layer. The agreement between cases Is & I up to $x \simeq 30$ in figure 6.8*(b)* suggests that for the fixed FST length scale, $L_{11} = 2.3$, the initial streak amplitude is proportional to the turbulence intensity at the boundary-layer edge. Brandt *et al.* (2004) report similar behaviour in their simulations. Figure 6.8*(a)* also shows that for cases Is & I, after an initial region of slower growth, the streamwise Reynolds stress increases linearly up to locations $x = 70$ and $x = 90$, respectively. In figure 6.9*(b)*, the evolution of the disturbance energy in the low-frequency modes has the same behaviour (the low-

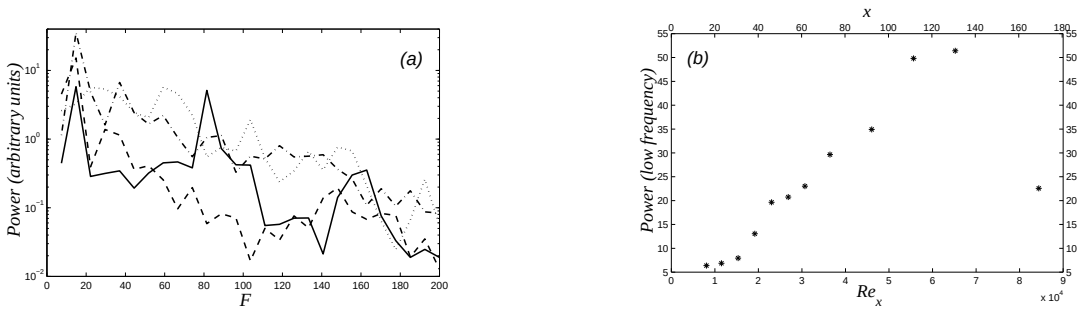

Figure 6.9: a) Spectra of the streamwise velocity inside the boundary layer for Case Is; —— $x = 16$, --- $x = 46$, —·— $x = 112$, ····· $x = 150$; b) Evolution of the power in the discrete modes $F \leq 15$ for Case Is.

frequency contribution was computed from the frequency spectrum of the streamwise velocity). These results agree with the experimental findings of Fransson *et al.* (2005), who also observed initial regions of slower growth of u_{rms} before a linear increase. They explain this phenomenon by a "receptivity distance," *i.e.* a distance needed for the adjustment of discrepant length scales in the free stream and the boundary layer. It is also likely that this receptivity distance would increase with the degree of scale mismatch, which suggests that the regions of linear disturbance growth could vary for different simulations and experiments.

In figure 6.8*(a)* there is also a region of overshoot of the turbulent levels of $\langle uu \rangle$ for $50 < x < 250$. This is a known feature of boundary-layer bypass transition (see, for example, figure 2d in Matsubara & Alfredsson 2001), and may be due to the streaks reaching supercritical amplitudes before turbulent breakdown.

To determine whether the growth of $u_{\rm rms}$ shown in figure 6.8 for cases Is & I is

localized to a particular band of frequencies, we computed spectra of the streamwise velocity at various locations within the computational domains. In figure 6.9*(a)* we show a region of the u-velocity spectrum for case Is corresponding to $F \leq 20$ at the stations x =16, 46, 112, and 150. The wall-normal location at which the spectra are calculated corresponds to the maximum boundary-layer $u_{\rm rms}$. This position is approximately in the middle of the transitional boundary-layer, but moves close to the wall at the onset of turbulence, as can be seen from figure 6.5*(b)*. The spectral power is plotted versus the nondimensional frequency $F = 10^6\omega\nu/U_\infty^2$. The figure indicates the energy in the low-frequency modes, for which $F < 20$, grows steadily up to approximately $x \simeq 120$ (as also indicated in figure 6.8). The subsequent decay of the low-freqency energy and a marked increase in high-frequency energy (not shown) are due to the breakdown to turbulence. Figure 6.9*(b)* shows the evolution of the energy in the first two discrete modes, $F \leq 15$ and figure 6.7*(b)* shows profiles of the square root of the same energy across the boundary layer. Comparison of this figure with 6.7*(a)*, in which the square root of the energy in all the modes (*i.e.* $u_{\rm rms}$) is plotted, shows that the increase in the boundary-layer u_{rms} for case Is is due to the energy growth in low frequencies.

In the above discussion we have examined several essential features of transition for cases I and Is. It is dominated by the evolution of Klebanoff modes under the influence of FST. Several characteristics of Klebanoff modes that have been found in experiments are confirmed in our simulations. We also concluded that the symmetry approximation employed in the first block of case Is does not affect

transition physics. Its effect is to delay the onset of transition through the attenuation of FST amplitudes near the leading edge. Specifically, the reasons for the more rapid onset of transition for case I are probably (i) that the higher external FST intensity creates higher-amplitude boundary-layer disturbances, which reach critical amplitudes farther upstream, and (ii) that the higher external FST intensity induces an earlier breakdown of these disturbances. The first statement is supported in figure 6.8*(b)*, and the second in*(a)*, which shows that the maximum level of $u_{\rm rms}$ is lower for case I than case Is. Evidence for a causal relationship between streak breakdown and the onset of transition for case Is will be given in §6.4.6, in which we present flow visualizations. Assuming that the above discussion also holds for the T3B case (which corresponds to a larger value of L_{11}), a possible effect of the symmetry condition on the T3B simulation results would be an analogous downstream shift in the onset of transition via the attenuation of the turbulence levels near the leading edge. However, while the change in the FST intensity near the boundary-layer edge resulted in a significant impact on the transition location in cases Is & I, the corresponding effect is likely to be weaker because of the increase in the FST length scale (six times larger compared to cases Is and I). Figures 6.5 *(a, b)* show that after an initial contamination by the FST, the maximum boundary-layer TKE and the streamwise Reynolds stress magnitudes remain constant up to location $x = 25$. In contrast, for case Is, within the region $3 < x < 25$, $\langle uu \rangle$ increases by a factor of five. A similar difference is also clear in figure 6.8 *(a)*. This observation suggests that near the leading edge, at the FST length scale of the T3B simulation,

the boundary layer is not very sensitive to the FST intensity. Downstream of the leading edge, in the x-range where turbulent spot precursors are first detected in the T3B simulation, the effective FST intensity would not be very different if the first block were performed without the symmetry assumption. Therefore, it is unlikely that the symmetry boundary condition used in block I of simulation T3B would change the location of transition onset appreciably.

Furthermore, we will observe from the flow visualization data and spanwise two-point velocity correlations that the initial path to transition in the T3B case is different from that in cases Is & I, and is unrelated to the growth of the Klebanoff modes: well-defined streaks are found downstream of $x = 75$, although small turbulent spots can be observed as close upstream as $x = 50$. This conclusion can also be anticipated from figures 6.7*(a, d)*: while there is good agreement with the experimental data of Klebanoff-mode-dominated transition for cases Is & I, for the T3B case, the u_{rms} peaks are located higher at $y/\delta^* \simeq 1.65$. This suggests that in the T3B case the boundary-layer disturbance is different from the Klebanoff modes.

6.4.3 Flow development

In this section we compare the evolution of the T3B calculation statistics across the laminar/turbulent transition region with the available experimental data. We show that the boundary layer is fully turbulent at the end of the computational domain, and discuss the development of the turbulent kintic energy (TKE) budget across

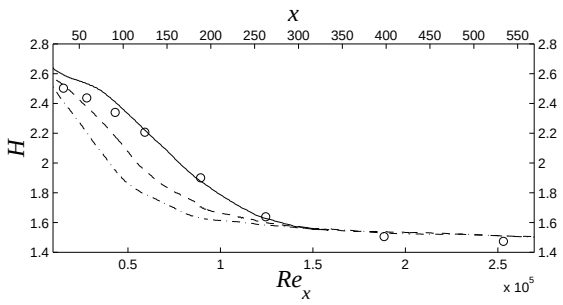

Figure 6.10: Evolution of the boundary-layer shape factor, H. —— Case T3B; --- Case I; —·— Case II; ∘ T3B experiment of Roach & Brierlay (1992).

the transitional region.

The spatial evolution of the FST turbulence intensity, Tu, and the skin friction coefficient, C_f was shown in figures 6.2 and 6.4 for the three cases. The boundary-layer shape factor, H, is shown in figure 6.10. It is defined as $H = \theta/\delta^*$, (where δ^* and θ are, respectively, the displacement and momentum thicknesses, given by

$$\delta^* = \int_0^{y_{\rm edge}} \left(1 - \frac{\langle U \rangle}{U_{\rm edge}}\right) dy; \qquad \theta = \int_0^{y_{\rm edge}} \frac{\langle U \rangle}{U_{\rm edge}} \left(1 - \frac{\langle U \rangle}{U_{\rm edge}}\right) dy), \tag{6.8}$$

and equals 2.6 in Blasius flow and around 1.4 for turbulent boundary-layer flow at low values of Re_θ. The shape factor is an inverse measure of the boundary-layer momentum, which increases in the turbulent regime. The integration in (6.8) is performed up to the edge of the boundary layer, $y_{\rm edge}$ (taken to be the location of zero mean U-velocity gradient). The effective free-stream velocity, $U_{\rm edge}$, is the mean velocity at this location.

The T3B simulation captures the onset and the progress of transition well, as indicated especially by the H and C_f curves. The approximate locations of the onset

of transition for each case (nominally defined as the x-location at which the skin friction begins to increase[2]), are $x = 100$, $x = 70$, and $x = 100$ for cases Is, I, and T3B, respectively. The corresponding Re_x values are $50,000$, $35,000$, and $50,000$. The evolution of the FST intensity for the T3B case (figure 6.2), is in agreement with the experiment. This suggests that (i) the FST length scale matches that of the experiment, and (ii) the interaction between the turbulence and the boundary layer is probably well-represented along the entire transitional boundary layer. The two conclusions suggest that the transition physics in the T3B experiment can be reliably studied through our T3B simulation.

Further comparison between the T3B simulation and experiment is shown in figures 6.11*(a–d)*. In figure 6.11 *(a)*, the velocity profiles corresponding to the simulation fall almost on top the experimental data, consistent with the good agreement in the C_f curve. Figures 6.11*(b-d)* show that the evolution of boundary-layer turbulent intensities is also captured well. The dominant component of the boundary-layer perturbation is u' and its profiles agree with the measurements at all four stations shown. The v' and w' profiles in the outer region of the boundary layer also agree well. However, noticeable disrepancies are observed in the near-wall region for the v'-component, particularly at the upstream locations. The cause of the disagreement is not fully known at present.

The domain coresponding to the T3B simulation was 40% shorter than for cases Is & I. It was larger in the spanwise direction, having 512 cells, compared with

[2]Young turbulent spots are often observed well upstream of this location

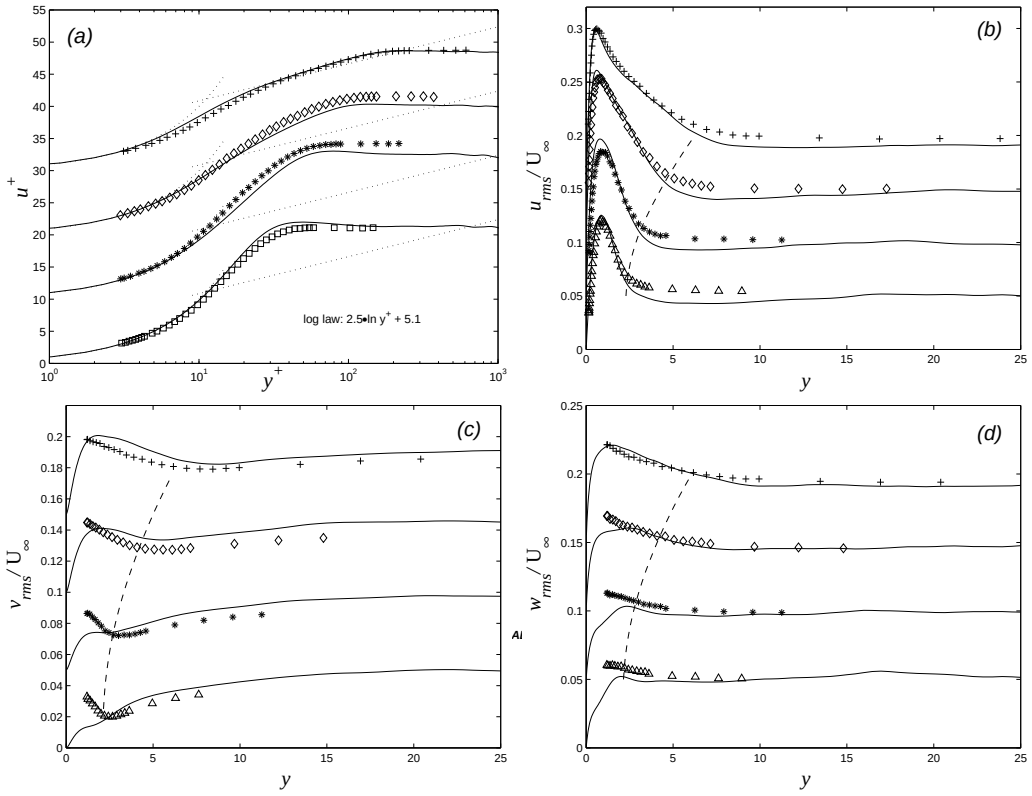

Figure 6.11: Comparison of velocity and turbulent intensities for T3B simulation *vs.* experiment. a) Mean streamwise velocity, U; b) u_{rms}; c) v_{rms}; d) w_{rms}; lines: simulation; symbols: experiment; the dashed line marks the location of the boundary-layer edge, δ_{99}; $\square$ $x = 60$, $Re_x = 28,440$; $\triangle$ $x = 93$, $Re_x = 44,082$; $*$ $x = 127$, $Re_x = 60,198$; $\diamond$ $x = 193$, $Re_x = 91,482$; $+x = 260$, $Re_x = 123,240$; in (a) successive curves are shifted in the vertical direction by 10, and in (b), (c) and (d), by 0.05.

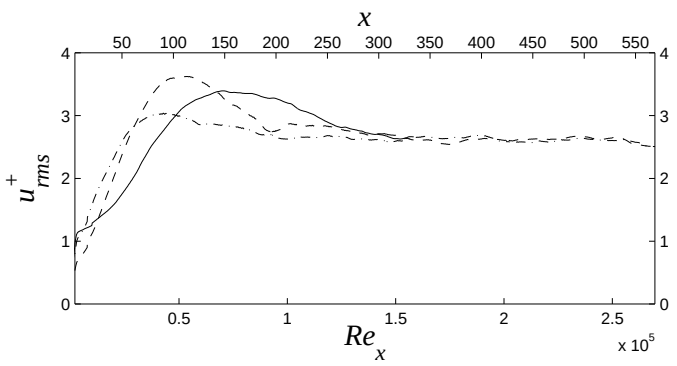

Figure 6.12: Evolution of the maximum streamwise turbulent intensity inside the boundary layer in wall units; —— Case T3B, --- Case Is, —·— Case I.

192 cells for cases Is & I, and had to be shortened to make the simulation feasible. However, as suggested by the C_f plot (figure 6.4), the boundary layer became fully turbulent within the computational domain in each simulation. The transition from the laminar velocity profile to the turbulent one occurs over a different streamwise range for each case, in correlation with the C_f plot, but in each case, the velocity fits the logarithmic law by $x = 260$, ($Re_x = 135,000$). Figure 6.12 shows the evolution of the maximum $u_{\rm rms}$ inside the boundary layer in wall units. The Reynolds stress levels converge on the same value, indicating that in each case the flow tends to the equilibrium characteristic of turbulent boundary layers.

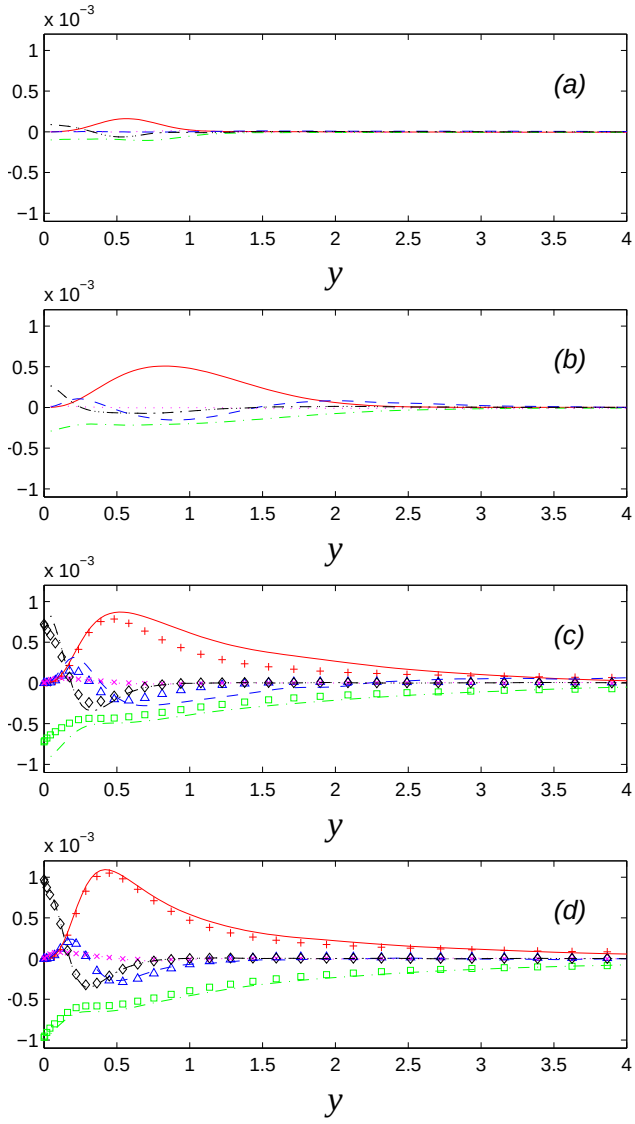

Figure 6.13: Budgets of the TKE at various locations; T3B case. All terms are normalized by U_∞ and R. (a) $x = 25, Re_x = 12,500, \delta_{99} = 1.12$; (b) $x = 100, Re_x = 50,000, \delta_{99} = 2.41$; (c) $x = 193, Re_x = 91,500, \delta_{99} = 4.36$; (d) $x = 260, Re_x = 123,250, \delta_{99} = 6.13$. Symbols: channel-flow DNS by Moser *et al.* 1999; lines: present simulation. $+$, ——: production; $\square$, —·— Dissipation; $\triangle$, - - - Turbulent transport; $\times$, ····· Pressure diffusion; $\diamond$, —···— Viscous diffusion.

6.4.4 TKE budget

Figure 6.13 shows the development of the TKE budget corresponding to the T3B case. The terms are given by

$$\frac{\partial k}{\partial t} = -\langle U_i \rangle \frac{\partial k}{\partial x_j} - \frac{\partial \langle U_i \rangle}{\partial x_j} \langle u_i' u_j' \rangle - \nu \left\langle \frac{\partial u_i'}{\partial x_j} \frac{\partial u_i'}{\partial x_j} \right\rangle - \frac{1}{\rho} \frac{\partial \langle p' u_i' \rangle}{\partial x_i} + \nu \nabla^2 k - \frac{1}{2} \frac{\partial \langle u_j' u_i' u_i' \rangle}{\partial x_j}. \tag{6.9}$$

The quantities on the right side of (6.9), which is derived from the Reynolds-Averaged Navier-Stokes (RANS) equations, are referred to, respectively, as advection, production, dissipation, pressure work, viscous diffusion, and turbulent transport. The sum of the computed terms in the budgets was very small throughout the computational domain, indicating good convergence. For example, in the fully-turbulent region, the maximum imbalance was 3% of the maximum production.

Our focus is on the T3B case but the differences from the other cases will be noted. The data are normalized by the free-stream velocity and the LE radius (both constant outer-coordinate scales), and thus are not in wall units. This choice was made in order to separate the effects of the mean flow evolution (which enters through the change in u_τ) from the evolution of the budget terms, which involve higher-order moments. The figure illustrates that the boundary layer TKE production maximum is initially near the middle of the laminar boundary layer. As the perturbed-laminar boundary grows, the peak in the production slowly moves farther away from the wall, consistent with the boundary-layer growth, up to the onset of transition at $x = 100$; beyond this location, it moves rapidly toward the wall. In

the transitional and turbulent regions, the location of the production peak approximately coincides with the location of the maximum $u_{\rm rms}$. This maximum is due primarily to low-frequency modes of the streamwise velocity, as shown in the next section. At $x = 25$, ($Re_x = 12,500$), the only active terms in the budget are the production, viscous diffusion, and viscous dissipation. The viscous terms balance each other at the wall, and together balance the production in the middle of the boundary layer. At $x = 100$, ($Re_x = 50,000$) (plot *b*), the magnitudes of the budget terms are, on the average, 40% of their turbulent values at $x = 260$, ($Re_x = 123,250$). The viscous diffusion and dissipation have increased in magnitude near the wall, and the growing production is now balanced, in addition, by the turbulent transport and the advection (not shown for clarity of the plot). By $x = 193$, ($Re_x = 91,500$), the budget is nearly that of a turbulent near-wall flow. At this and at the final location, $x = 260$, ($Re_x = 123,250$), we have also plotted the turbulent channel data of Moser *et al.* (1999) obtained at $Re_\tau = 395$ for comparison (the use of channel rather than boundary layer data for comparison is justified because the near-wall behavior of the two flows is very similar). To convert the channel data to outer coordinates, we used the local u_τ and ν from our simulation. The comparison in figure 6.13*(d)* shows that a turbulent equilibrium is fully established. An examination of the TKE budgets for cases Is & I revealed a qualitatively similar development, except that the levels of production and the corresponding balancing terms were higher in the transitional region, in correlation with higher boundary-layer $u_{\rm rms}$ levels, as discussed in the next section. The perturbed laminar stage was characterized by a linear-like growth of

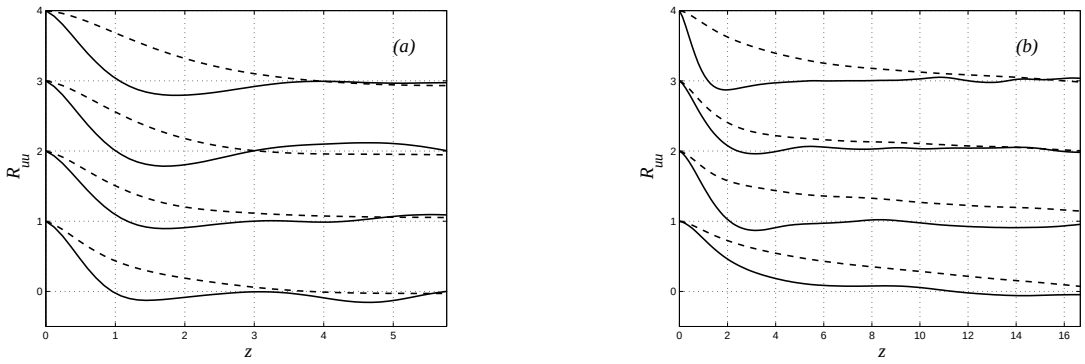

Figure 6.14: Spanwise correlation functions of the streamwise velocity fluctuations; (a) Case I, R_{uu}; (b) Case T3B, R_{uu}; —— correlation functions at the location of maximum boundary-layer u_{rms}; --- correlation functions at the boundary-layer edge; from bottom to top: $x = 38$, $Re_x = 19,000$; $x = 96$, $Re_x = 47,800$; $x = 154$, $Re_x = 76,800$; $x = 308$, $Re_x = 153,600$.

the production peak, located approximately in the middle of the boundary layer. Across the breakdown stage, the production peak moved rapidly toward the wall, accompanied by a sharp increase in the magnitudes of the dissipation, diffusion and turbulent transport. In the fully-turbulent region, the budgets collapsed with the data of Moser *et al.* (1999).

6.4.5 Two-point correlations

Two-point spanwise correlations of the velocity signal can provide information on the dominant spanwise length scale of the flow. In transitional and turbulent boundary layers, correlations of the streamwise velocity are used to estimate the average spanwise separation between adjacent low- and high-speed streaks. This

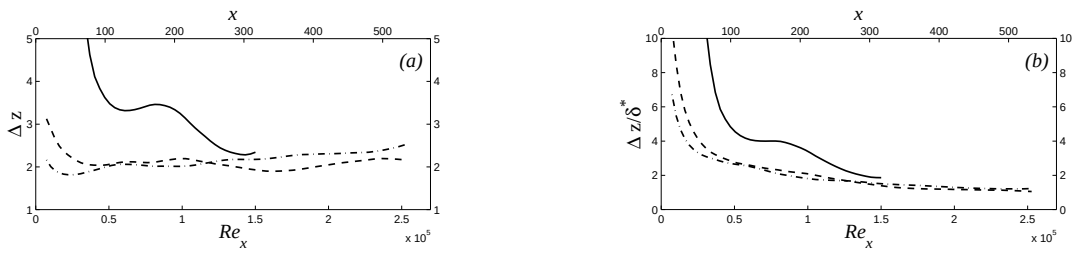

Figure 6.15: Streamwise evolution of the location of the minimum of the spanwise correlation functions of the streamwise velocity; (a) unnormalized; (b) normalized by the boundary-layer displacement thickness; the correlation functions are computed at the location of maximum boundary-layer u_{rms}; —— Case T3B; --- Case Is; —·— Case I.

distance is taken to be the distance to the first minimum of the correlation function. In figure 6.14 *(a)* and *(b)* two-point correlation functions of the streamwise velocity are shown for cases I and T3B, respectively. The corresponding plot for case Is is qualitatively similar. The dashed lines represent the correlation function at the boundary layer edge, and the solid lines, the correlation function at the location of maximum u_{rms} inside the boundary layer. The correlation function at the boundary layer edge indicates a much larger spanwise scale for case T3B, as expected. For case I, this scale clearly increases (albeit slowly) with the streamwise coordinate, but for the T3B case it appears to be almost constant. The evolution of the spanwise scale in the T3B case may be influenced by the spanwise domain size, which was smaller than optimal.

The solid curve that corresponds to $x = 96$, $(Re_x = 47,800)$ is located inside

near the onset of skin friction growth for both cases. It can be seen that the spacing between the streaks is approximately 3.4 for the T3B case, compared to about 1.8 for case I. The solid curves corresponding to $x = 308$, ($Re_x = 153,600$) show that in the fully turbulent region, the streak spacing is the same for the two cases, regardless of the differences in the upstream development, indicating a universal turbulent equilibrium. These streaks are certainly not the same as their counterparts in the transitional region. Figure 6.5*(b)* demonstrates that the location of the $\langle uu \rangle$ maximum moves close to the wall at the onset of turbulence.

Figure 6.15 *(a)* shows the streamwise evolution of the location of the minimum of the correlation function. The figure shows that for cases Is & I the transitional streak spacing of $\simeq 2$ is established by $x = 75$. For case T3B, the appearance of streaks with separation $\simeq 3.4$ is delayed to $x \simeq 100$. This was also confirmed by observing the flow field directly. Not only do the streaks appear later than for cases Is & I, but they also do not seem essential to transition. It is interesting to see that while for case T3B there is a marked shift in the streak separation distance across the laminar-turbulent transition, for cases Is & I the separation distance does not change significantly. This observation suggests that there is no universal value for streak separation in the perturbed boundary layer. Rather, it may be determined by the FST length scale. Fransson & Alfredsson (2003) performed controlled experiments of boundary-layer transition with and without distributed suction and found that the spanwise streak spacing was virtually unchanged between the two cases, despite a factor of two reduction in the boundary layer thickness for the case with suction.

They suggest that the scale selection process involves the free-stream length scales. Figure 6.15 *(a)* shows that within the transitional and turbulent regions, the streak spacing slowly increases with the downstream distance. Figure 6.15 *(b)* shows that it slowly decreases relative to the local boundary-layer displacement thickness. Both of these findings are in qualitative agreement with Matsubara & Alfredsson (2001). However, in these authors' experiments, the distance to the correlation function minimum in the transition region tends to $3\delta^*$, whereas our values for cases Is & I are closer to $2\delta^*$. For case T3B, the streak spacing is $4\delta^*$ in the transitional region. However, we will show in the next section that the streaks for this case may be due to a different phenomenon.

6.4.6 Flow visualization

Jacobs & Durbin (2001) were the first to visualize Klebanoff modes and their breakdown into turbulent spots in a spatial boundary-layer simulation. With the FST intensity set to 3%, the boundary layer developed streaks that were about $1.2\delta_{99}$ apart. Turbulent spot formation was initiated via the penetration of the FST into the outer boundary layer. The spots grew in size as they were convected downstream and merged with developed turbulence to maintain its upstream front. The authors concluded that the low-speed streak provides a path for the direct contamination of the boundary layer by the FST when the streak moves into the outer boundary layer, but is otherwise irrelevant to transition, *i.e.* no evidence of streak instability

was found. The turbulent spots resulting from this FST/boundary-layer intaraction were called 'top-down' spots because they originated from an incursion of the FST into the outer boundary-layer and spread vertically toward the wall while being convected downstream with the mean flow.

Motivated by previous work on streak instability and breakdown (Andersson *et al.* 2001, Brandt & Henningson 2002), Brandt, Schlatter, and Henningson (2004) illustrated a different mechanism. Using planar and three-dimensional images of the flow field, these authors concluded that in their simulations, the formation of turbulent spots was caused by one of two instability modes of the streamwise streak. The sinuous, or the antisymmetric mode, was observed more often than the varicose, or the symmetric mode. This could be explained by the analysis of Andersson *et al.* (2001), who found a lower critical streak amplitude for the sinuous mode. We note that neither Jacobs & Durbin (2001), nor Brandt *et al.* (2004) observed arrowhead-shaped spots, observed by Emmons (1951) (see also van Dyke 1982), and also reported by Matsubara & Alfredsson (2001). In this section we examine the evolution of boundary-layer disturbances for our cases Is and T3B. We follow the development of turbulent spots from their birth to their merger with the downstream turbulent front. We note that because of the high intensity of the background FST, it is difficult to perform a quantitative characterization of the turbulent spots, *e.g.* the location of spot origin, the spanwise spreading rate, and the speeds of the leading and trailing edges.

For case Is, two types of turbulent spots were observed. The first type is illus-

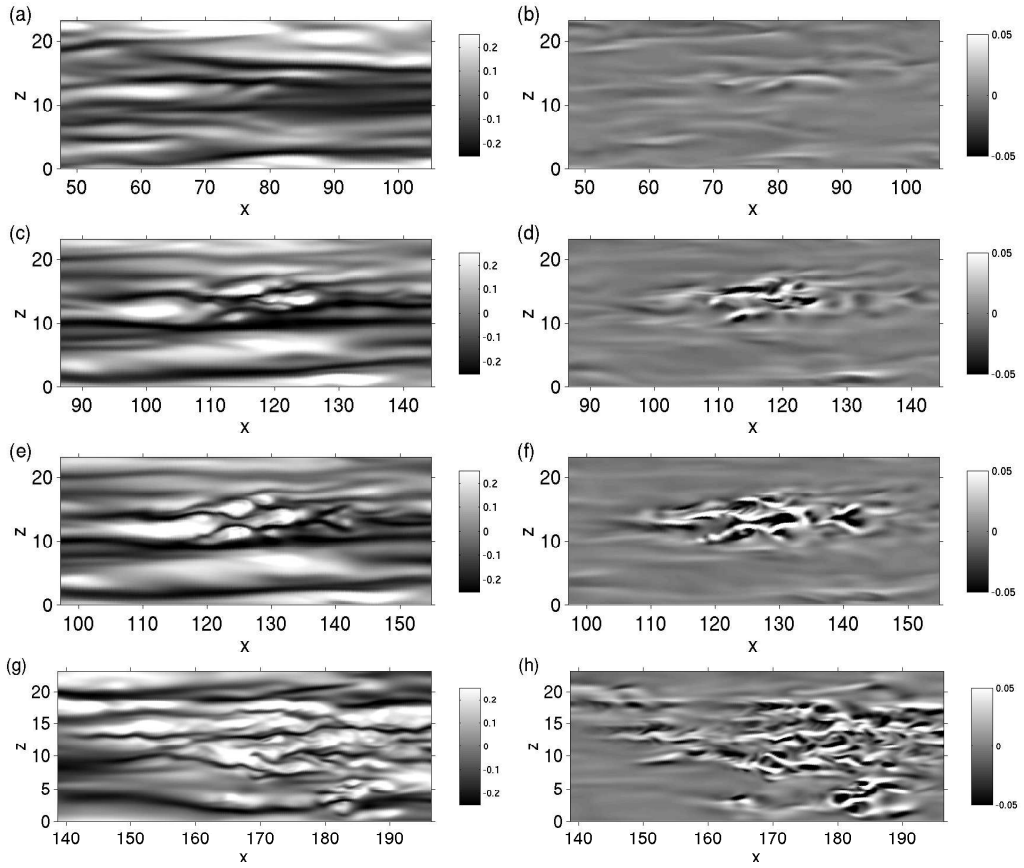

Figure 6.16: Contours of velocity fluctuations for a turbulent spot of the first type. Case Is; $y = 0.4$; a), c), e), g) streamwise velocity fluctuation; b), d), f), h) wall-normal velocity fluctuation; a), b) $t = 238$; c), d) $t = 296$; e), f) $t = 313$; g), h) $t = 391$.

trated in figure 6.16. The first column, *(a) – (g)*, shows contours of the streamwise velocity fluctuation in an xz-plane, and the second column, *(d) – (f)*, contours of the wall-normal velocity fluctuation. In this, as in all similar figures, the plane is located in the lower regions of the transitional boundary layer. The spot originates from a wiggle in a low-speed streak at position $(x, y) = (77, 13)$, $t = 238$ (figure 6.16 *(a)–(b)*), and displays prominent lateral (*i.e.* spanwise) symmetry in the u- and v-velocity components up to $x \simeq 127, t = 313$ (figure 6.16 *(e)–(f)*). The w-component is antisymmetric (not shown). It is most likely associated with the varicose instability. Its development farther downstream is disorderly, and by $x = 180$, $t = 391$ (figure 6.16 *(g)–(h)*), it has merged with the turbulent front. In its overall appearance, this spot is similar to the ones shown by Jacobs & Durbin (2001) and Brandt *et al.* (2004) in figures 9 and 11, respectively.

The second type of turbulent spot found in the case Is simulation is illustrated in figure 6.17. The origin of the spot appears to be an asymmetric streak wiggle at $(x, y) = (104, 14)$, $t = 136$ (figure 6.17 *(a)–(b)*). No definite symmetry or asymmetry, however, could be detected in the spot itself. This may be due to a higher level of background turbulence than present in the simulations of Brandt *et al.* (2004). The spanwise spreading rate of this spot is larger than that of the previous one. At $x = 142$, $t = 211$ (figure 6.17 *(e)–(f)*), fifty units downstream of the instability, it occupies two thirds of the spanwise domain. The limiting size of the spanwise domain prevents the natural growth of the spot in the spanwise direction from this point on.

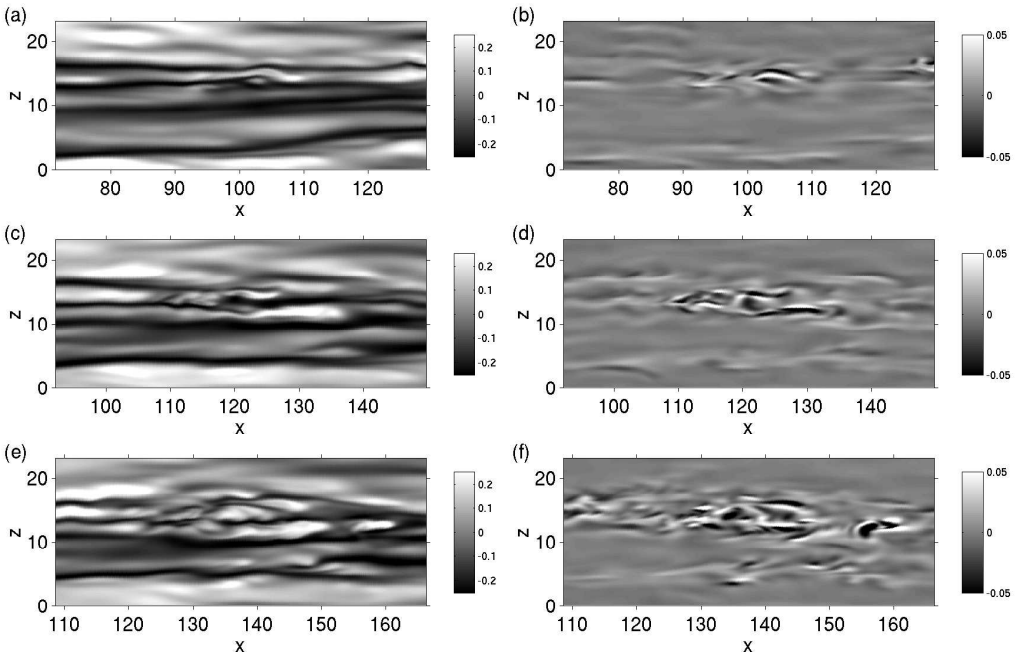

Figure 6.17: Contours of velocity fluctuations for a turbulent spot of the second type. Case Is; $y = 0.4$; a), c), e) streamwise velocity fluctuation; b), d), f) wall-normal velocity fluctuation; a), b) $t = 136$; c), d) $t = 186$; e), f) $t = 211$;

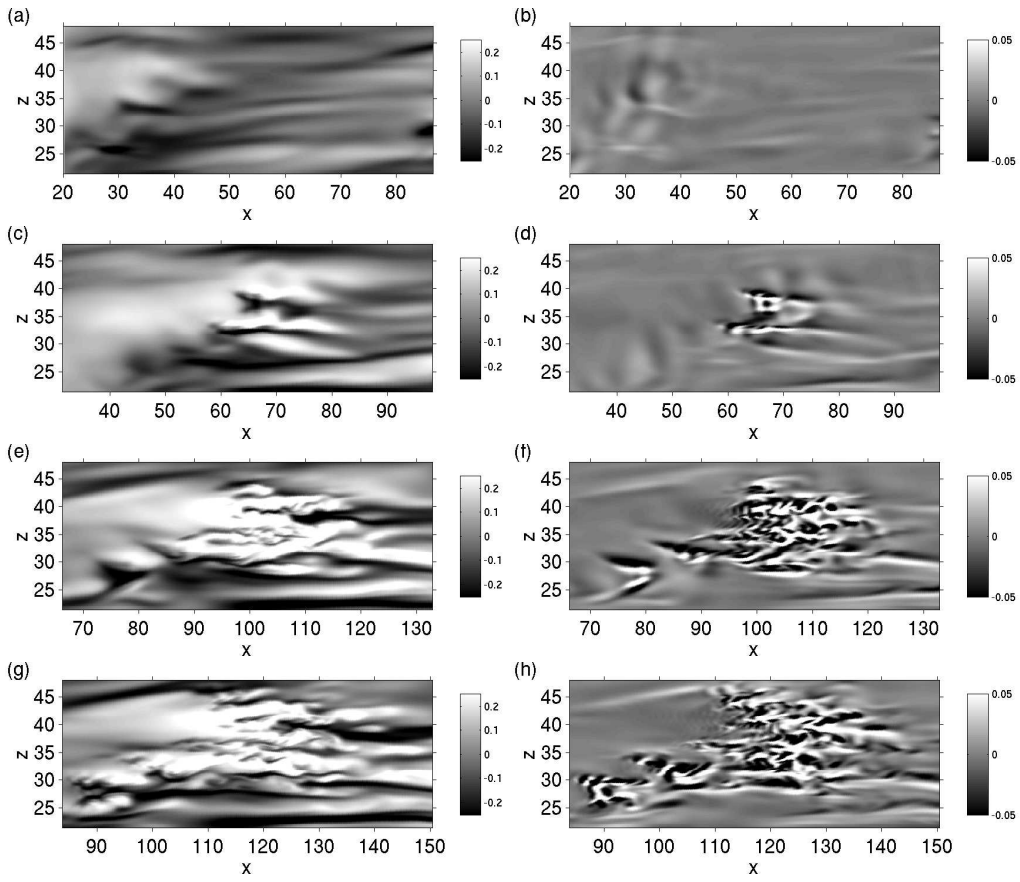

Figure 6.18: Contours of velocity fluctuations for a turbulent spot of the first type. Case T3B; $y = 0.68$; a), c), e), g) streamwise velocity fluctuation; b), d), f), h) wall-normal velocity fluctuation; a), b) $t = 189$; c), d) $t = 241$; e), f) $t = 296$; g), h) $t = 320$.

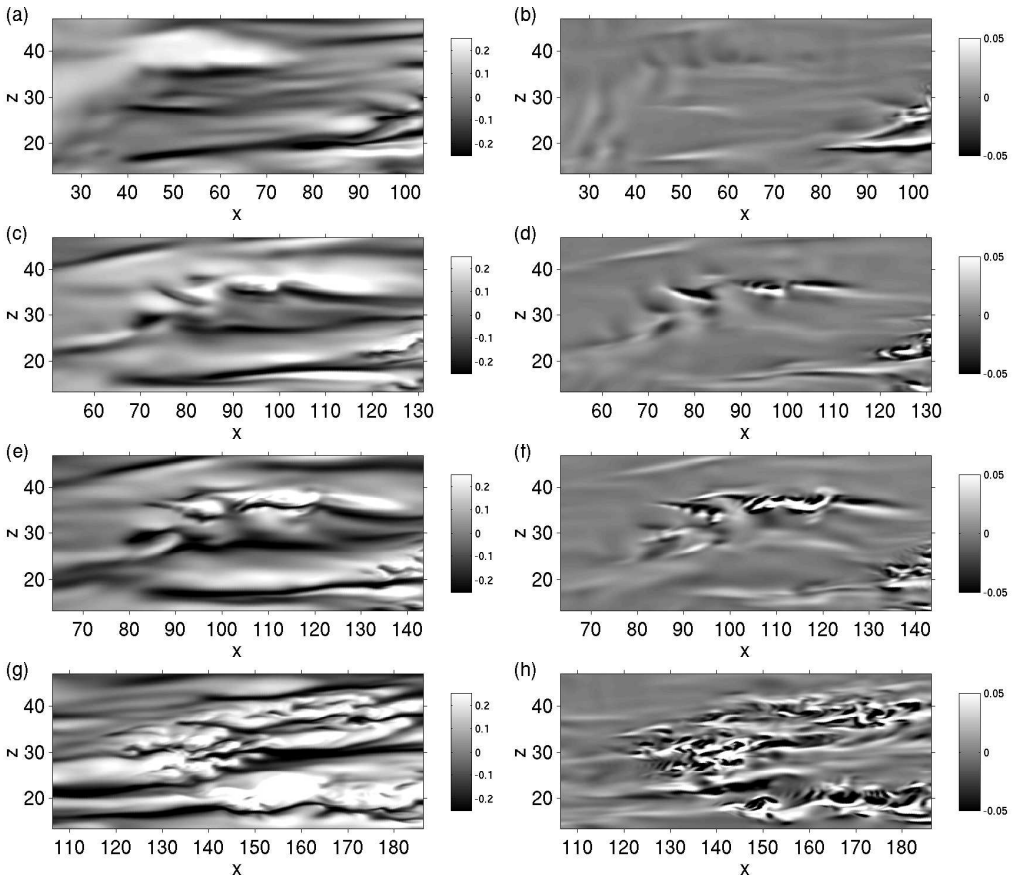

Figure 6.19: Contours of velocity fluctuations for a turbulent spot of the second type. Case T3B; $y = 0.68$; a), c), e), g) streamwise velocity fluctuation; b), d), f), h) wall-normal velocity fluctuation; a), b) $t = 82$; c), d) $t = 154$; e), f) $t = 179$; g), h) $t = 261$.

Next, we examine the evolution of turbulent spots for the T3B simulation. The agreement of the mean-flow statistics with the T3B experiment suggests that the fundamental physics of this flow are present in the simulation. Moreover, the spanwise domain of the T3B simulation is sufficiently large to permit unhindered development of the turbulent spots. Four spots were followed during the course of the simulation. Two of the spots observed have distinct arrowhead shapes, similar to the illustration in figure 4*(b)* in Matsubara & Alfredsson (2001). The other two seem to have rather arbitrary shapes. One spot from each category will be illustrated in figures 6.18 and 6.19 in the same format as used in figures 6.16 and 6.17. We found no evidence that streak instability is related to the origin of either spot. Instead, the spot precursors appear as regions of upward and downward-moving fluid, alternating in the streamwise direction, initially almost perpendicular to the direction of the flow. This is shown for the first spot in figure 6.18 *(b)* at $(x, y) = (33, 33)$, $t = 189$, and *(d)* at $(x, y) = (47, 27)$, $t = 241$, where another spot is forming close upstream of the main one, and for the second spot in figure 6.19 *(b)* at $(x, y) = (35, 30)$, $t = 82$. In the first spot, the ends of the low/high speed region are then reoriented toward the flow direction, so that the resulting perturbation has the wall-normal velocity signature of a Λ vortex. This is most clearly seen from figure 6.18 *(f)* at $(x, y) = (80, 27)$, $t = 296$ in the spot developing upstream. The reorientation of this perturbation is probably due to the the boundary-layer mean shear. When the central part of the low/high speed region is moved up by the fluctuating velocity, the velocity gradient causes it to move faster than the

ends, stretching the disturbance into a '>'-shape. This may be the origin of the arrowhead shape for many turbulent spots. For the second spot, only the top half of the low/high speed region is reoriented toward the streamwise direction, which gives it the appearance of a quasi-streamwise vortex. This is shown in figure 6.19 *(d)* at $(x, y) = (80, 33)$, $t = 154$. As a result of the asymmetry, this turbulent spot is not arrowhead-shaped.

At this point, the vortical structures develop wall-normal oscillations along their axes, which leads directly to turbulence. This is seen in figures 6.18 *(f)* at $(x, y) = (87, 32)$, $t = 296$ and 6.19 *(f)* at $(x, y) = (93, 35)$, $t = 179$. The first spot spreads upstream through its lateral edges, which preserves its arowhead shape up to the merger with the fully-turbulent region ($x \simeq 220$). Interestingly, the shape of the second spot appears to be arbitrary up to $t = 261$, at which point it has just merged with another nascent spot developing below it (seen in 6.19 *(f)* at $(x, y) = (110, 17)$, $t = 179$). The resulting larger spot has a reverse arrowhead shape (6.19 *(h)* at $(x, y) = (145, 30)$, $t = 261$).

6.5 Discussion and Conclusion

We have presented three DNS of boundary-layer transition due to 6% FST. For cases Is & I, the FST integral length scale is set to 2.3 and the two cases differ in the geometry: for case Is we use a symmetry condition along $y = 0$ in the region upstream of the plate leading edge, and for case I, the full domain is considered. The

difference in the onsets of transition is due to higher levels of FST in the vicinity of the LE for case I. This difference comes from the symmetry boundary condition, which attenuates turbulence in the immediate neighborhood of the LE of case Is. At this length scale, the boundary layer appears highly receptive to the FST and is contaminated more in case I. The boundary-layer disturbances are low-frequency modes that appear as low- and high-speed streaks of the streamwise velocity. Their energy increases approximately linearly with the streamwise distance after an initial adjustment region, and in the transitional region they have a spanwise separation of $2\delta^*$–$3\delta^*$. For case T3B, the FST length scale is 14, and the simulation is designed to match the T3B experiment, performed by Roach & Brierlay (1992). Good overall agreement with the reference experimental dataset is obtained. In this case, the boundary layer is less receptive to the FST near the leading edge because of the larger length scale difference, and the symmetry boundary condition in the first block is likely to have less impact on the evolution of the flow. In this case we did not observe perturbation growth in the vicinity of the leading edge. Streamwise streaks were visible downstream of location $x = 100$ and their spanwise spacing in the transitional region was larger compared to cases I and Is ($\simeq 4.25\delta^*$).

From our flow visualization studies we concluded that transition in case Is is in part caused by instabilities of streaks. In particular, one of the turbulent spot precursors examined shows prominent spanwise symmetry and is consistent with the varicose instability mode of the streaks. The above conclusion is also indirectly supported by the fact that in case I, which shows a more rapid transition, the initial

$\langle uu \rangle$ levels associated with the streamwise streaks are twice those of case Is. This suggests that in case I, the streaks may reach a critical breakdown amplitude closer upstream that in case Is. For the T3B case, the transition mechanism appears to be different from that in cases I and Is. We have shown that spot precursors are present as close upstream as $x = 35$, and a small turbulent spot is shown at $x \simeq 65$ in figure 6.18*(c)–(d)*. Figure 6.15 *(a)*, indicates that streaks with a well-defined spanwise separation first appear around $x \simeq 100$. Thus, they cannot be directly responsible for transition. Their appearance may be unrelated to the turbulent spots, or, alternatively, may be caused by the turbulent spots themselves, since any localized disturbance will be stretched by the boundary-layer mean shear, which will give it a streaky appearance. Rather than induce boundary-layer streaks, the FST indices streamwise 'waviness' – alternating regions of wall-normal velocity that generate spanwise vorticity. Initially perpendicular to the mean flow, these waves (vorticity) subsequently reorient themselves to become partially aligned in the streamwise direction; at this stage, appear either as symmetric hairpin vortices (two legs) or quasi-streamwise vortices (one leg). The vortices develop oscillations along their axis that lead to turbulence (*e.g.* see figure 6.19 *(f)* $(x, y) = (93, 35)$, $t = 179$). The spots that have the arrowhead shape originate from the hairpin vortices; quasi-streamwise vortices lead to spots of arbitrary shape, but may merge to form a reverse arrowhead.

Hairpin and quasi-streamwise vortices have been found in numerous previous studies of transitional boundary layers. Perry, Lim & Teh (1981) created a turbulent

spot by a short pulse of air from a small hole drilled in the floor of their windtunnel. The spot was composed of an array of 'folds' near the wall, which were similar in appearance to Λ-vortices. It had an arrowhead shape and was trailed by long streaky tails. The authors hypothesized that a tubulent spot is nothing but a staggered arrangement of a series of Λ-shaped vortices. Asai & Nishioka (1990) investigated boundary-layer transition below the linear stability critical point, caused by acoustic perturbations near the leading edge. Their smoke visualization study revealed that a hairpin-like structure was important in the transition process. Singer & Joslin (1994) and Singer (1996) performed DNS to study the evolution of a single hairpin vortex in the flat-plate boundary layer and its subsequent development into a turbulent spot. The hairpin vortex was generated by blowing at the wall and its evolution was very similar to what was described in previous studies. The spot was composed of hairpin and quasi-streamwise vortices, possessed a clear arrowhead shape and was followed by velocity streaks. In addition, the authors observed the formation of new hairpin vortices near the trailing edge of the spot.

The similarities between the spots found in our T3B simulation and those in the above studies are striking. This seems surprising, since in our case turbulent spots are generated by forcing at the boundary-layer edge and not at the wall. The similarity indicates that the turbulent spot as described in this and many previous studies is a fundamental feature of transitional boundary layers.

The essential difference between cases Is and T3B is the FST length scale. Its larger value for the T3B simulation requires the computational domain to be

much larger in order to accomodate larger eddies in the T3B simulation, and also reduces the FST decay, exposing the boundary layer to relatively higher turbulence intensities in the transitional region.

The difference in transition mechanisms between cases I and T3B can be explained by a reduced boundary-layer receptivity to the FST for case T3B, probably caused by the large difference between the FST length scale and the LE radius. For cases Is (& I) the FST length scale is comparable to the LE radius and the viscous flow scale (the Reynolds number based on the FST length scale is $Re_L = 1150$) and the FST induces streaky boundary layer disturbances, whose rapid growth is evident in figures 6.5 and 6.8. Transition is caused by a secondary instability and breakdown of streaks that have reached high amplitudes. For the T3B case, the FST length scale is six times larger than for cases Is & I ($Re_L = 6900$), and the interaction of the FST with the leading edge region does not result in growing disturbances, as was shown in figure 6.8. This is likely responsible for the delayed deviation from the laminar C_f (figure 6.4) for the T3B case. The absence of streaks unmasks another transition mechanism, whereby the FST induces a different type of disturbance, a streamwise 'waviness,' which first appears at the boundary-layer edge, and propagates towards the wall. This mechanism does not involve the vicinity of the leading edge. Unlike the streaks, which are present close to the LE (see figure 6.15), the latter type of disturbance is first detected downstream of $x \simeq 30$. The onset of transition for case T3B appears delayed and the rise in the skin friction through transition is more abrupt. The above hypothesis does not contradict the

conclusion of Brandt *et al.* (2004) and Ovchinnikov *et al.* (2004) that increasing the FST length scale accelerates transition. First, the largest FST length scale used in their simulations was approximately $3\delta_{99}$ at $Re_x \simeq 30,000$, which is comparable to the FST length scale used in our cases Is & I. Second, these authors used truncated simulations, in which the computation is started downstream of the leading edge at an arbitrarily prescribed Re_x. Therefore, their simulations do not account for the receptivity in the vicinity of the LE. The experiments of Jonáš, Mazur, & Uruba (2000), on the other hand, span the range of length scales used in the current simulations, and thus our results are in qualitative disagreement. However, the FST intensity in their experiments was fixed at 3%, compared to 6% in our simulations. It is possible that at the higher intensity, the optimal FST length scale for transition is smaller. Some support for this conjecture comes from the fact that small-scale turbulence penetrates the boundary layer more easily (Brandt *et al.* (2004), but also decays more rapidly. Thus, overall perturbation of the boundary layer is reduced compared to the case of large-scale turbulence (which decays more slowly). Increasing the FST intensity may offset the faster decay of the small-scale turbulence and make it more effective than the larger scales in inducing transition.

The present results indicate the importance of the FST length scale not only on the onset of transition, but also on the mechanism. Future numerical and experimental studies should investigate the effect of the Reynolds numbers based on the plate thickness and the FST length scale on the various aspects of boundary-layer transition. It is likely, for instance, that FST of different length scales produce

different disturbance growth rates inside the boundary layer, which could reconcile the differences in the transition onsets for experiments. The effect of the leading edge geometry should also be investigated systematically in the specific context of bypass transition.

Acknowledgments

V.O. and U.P. acknowledge the financial support of the NASA Langley Research Center under Cooperative Agreement NAG12285. Thanks are also due to Dr. Jens Fransson for sharing with us the results of flow visualizations based on wind tunnel experiments at KTH, Stockholm.

6.6 References

[1] Andersson, P., Berggren, M. & Henningson, D.S. 1999 Optimal disturbances and bypass transition in boundary layers. *Phys. Fluids* **11** 134–150.

[2] Andersson, P., Brandt, L., Bottaro, A. & Henningson, D. S. 2001 On the breakdown of boundary layer streaks. *J. Fluid Mech.* **428** 29–60.

[3] Arnal, D. & Juillen, J. C. 1978 Contribution experimentale a l'etude de la receptive d'une couche limite laminare, a la turbulence de l'ecoulement general. *ONERA Tech. No. 1/5018 AYD*

[4] Asai, M. & Nishioka, M. 1990 Development of wall turbulence in Blasius

flow. In *Laminar-Turbulent Transition* Arnal, D. & Michel, R., eds., Springer-Verlag, 215–222.

[5] Balaras, E. 2004 Modeling complex boundaries using an external force field on Cartesian grids in large-eddy simulations. *Comput. Fluids* **33**, 375–404.

[6] Balaras, E., Benocci, C. & Piomelli, U. 1995 Finite difference computations of high Reynolds number flows using the dynamic subgrid-scale model. *Theoret. Comput. Fluid Dyn.* **7**, 207–216.

[7] Balaras, E., Piomelli, U. & Wallace, J. M. 2001 Self-similar states in turbulent mixing layers *J. Fluid Mech.*, **446**, 1–24.

[8] Bertolotti, F. P. 1997 Response of the Blasius boundary layer to free-stream vorticity. *Phys. Fluids* **9** 2286–2299.

[9] Blair, M. F. 1983 Influence of free-stream turbulence on turbulent boundary-layer heat transfer and mean profile development. Part I – Experimental data. *ASME J. Heat Transf.* **105** 33–40.

[10] Brandt, L. & Henningson, D. S. 2002 Transition of streamwise streaks in zero-pressure-gradient boundary layers. *J. Fluid Mech.* **472** 229–261.

[11] Brandt, L., Schlatter, P. & Henningson, D. S. 2004 Transition in boundary layers subject to free-stream turbulence. *J. Fluid Mech.* **517**, 167–198.

[12] Butler, K. M., Farrel, B. F. 1992 Three-dimensiona optimal perturbations in viscous shear flow. *Phys. Fluids A* **4** 1637–1650.

[13] Chorin, A. J. 1968 Numerical solution of the Navier-Stokes equations. *Math. Comput.* **22**, 742–762.

[14] Collis, S. S. & Lele, S. K. 1996 A computational approach to swept leading-edge receptivity. *AIAA Paper* **96-0180**.

[15] Ellingsen, T., Palm, E. 1975 Stability of linear flow. *Phys. Fluids* **18** 487–488.

[16] Emmons, H. W. 1951 The laminar-turbulent transition in a boundary layer. *J. Aeronaut. Sci.* **18** 490–498.

[17] Fadlun, E. A., Verzicco, R., Orlandi, P. & Mohd-Yusof, J. 2000 Combined immersed-boundary finite-fifference methods for three-dimensional complex flow simulations. *J. Comput. Phys.* **161**, 35–60.

[18] Fransson, J. H. M. 2004 Leading edge design process using a commercial flow solver. *Exps. Fluids* **37** 929–932.

[19] Fransson, J. H. M., Matsubara, M. & Alfredsson, P. H. Transition induced by free-stream turbulence. *J. Fluid Mech.* **527** 1–25.

[20] Fransson, J. H. M. & Alfredsson, P. H. On the disturbance growth in an asymptotic suction boundary layer. *J. Fluid Mech.* **482** 51–90.

[21] Grosch C. E., Salwen, H. 1978 The continuous spectrum of the Orr-Sommerfeld equation. Part 1. The spectrum and the eigenfunctions *J. Fluid Mech.* **87**, 33–54.

[22] Huai, X., Joslin, R. D., Piomelli, U. 1997 Large-eddy simulation of transition to turbulence in boundary layers. *Theoret. Comput. Fluid Dynamics* **9**, 149–163.

[23] Jacobs, G. J. & Durbin, P. A. 2001 Simulations of bypass transition. *J. Fluid Mech.* **428**, 185–212.

[24] Jonáš, P., Mazur, O., Uruba, V. 2000 On the receptivity of the by-pass transition to the length scale of the outer stream turbulence. *Eur. J. Mech. B-Fluids* **19** 707–722.

[25] Kendall, J. M. 1985 Experimental study of disturbances porduced in a pretransitional laminar boundary layer by weak free stream turbulence. *AIAA Paper* **85-1695**.

[26] Kendall, J. M. 1998 Experiments on boundary-layer receptivity to free stream turbulence. *AIAA Paper* **98-0530**.

[27] Kim, J. & Moin, P. 1985 Application of a fractional step method to incompressible Navier-Stokes equations. *J. Comput. Phys.* **59**, 308–323.

[28] Klebanoff, P. S., Tidstrom, K. D. & Sargent, L. M. 1962 The three-dimensional nature of boundary-layer instability. *J. Fluid Mech.* **12** 1–34.

[29] KLEBANOFF, P. S. 1971 Effect of freestream turbulence on the laminar boundary layer. *Bull. Amer. Phys. Soc.* **10**, 1323.

[30] KLINGMANN, R. G. B., BOIKO, A. V., WESTIN, K. J., KOZLOV, V. V. & ALFREDSSON, P. H. 1993 Experiments on the stability of Tollmien-Schlighting waves. *Eur. J. Mech. B/Fluids* **12** 493–514.

[31] LANDAHL, M. T. A note on an algebraic instability of inviscid parallel shear flows. *J. Fluid Mech.* **98** 243–251.

[32] LEIB, S. J., WUNDROW, D. W., & GOLDSTEIN, M.E. 1999 Effect of free-stream turbulence and other vortical disturbances on a laminar boundary layer *J. Fluid. Mech.* **380** 169–203.

[33] LIN, N., REED, H. L., SARIC, W.C. 1992 Effect of leading-edge geometry on boundary layer receptivity to free-stream sound. In *Instability, receptivity, and Turbulence* Hussaini, M., Kumar, A., Streett, C., eds. Springer-Verlag 421–440.

[34] LUCHINI, P. 2000 Reynolds-number independent instability of the boundary layer over a flat surface. Part 2. Optimal perturbations. *J. Fluid Mech.* **404** 289–309.

[35] MATSUBARA, M. & ALFREDSSON, H. 2001 Disturbance growth in boundary layers subjected to free-stream turbulence. *J. Fluid. Mech.* **430**, 149–168.

[36] MORINISHI, Y., LUND, T. S., VASILYEV, O. V. & MOIN, P. 1998 Fully-

conservative higher order finite difference schemes for incompressible flow. *J. Comput. Phys.* **143**, 90–124.

[37] Moser, R. D., Kim, J. & Mansour, N. N. 1999 Direct numerical simulation of turbulent channel flow up to $Re_\tau = 500$. *Phys. Fluids* **11**, 943–945.

[38] Orlanski, I. 1976 A Simple Boundary Condition for Unbounded Hyperbolic Flows. *J. Comput. Phys.* **21**, 251–269.

[39] Orr W. M. F. 1907 The stability or instability of the steady motions of a perfect liquid and a viscous liquid. *Proc. R. Ir. Acad. A* **27** 9–27, 69–138.

[40] Ovchinnikov, V. O., Piomelli, U. & Choudhari, M. M., 2004 Inflow conditions for numerical simulations of bypass transition *AIAA Paper*, **2004-0591**.

[41] Ovchinnikov, V. O., Piomelli, U. & Choudhari, M. M., 2005 Numerical simulations of boundary-layer transition induced by a cylinder wake. *J. Fluid Mech. Accepted for publication*,

[42] Perry, A. E., Lim, T. T. & Teh, E. W. 1981 A visual study of turnbulent spots. *J. Fluid Mech.* **104** 387–405.

[43] Philips, O. M. 1969 Shear-flow turbulence. *Annu. Rev. Fluid Mech* **1** 245–264.

[44] Piomelli, U., Balaras, E. & Pascarelli, A. 2000 Turbulent structures in accelerating boundary layers. *J. Turbulence* **1**, (001) 1–16.

[45] Rai, M. M. & Moin, P. 1993 Direct numerical simulation of transition and turbulence in a spatially evolving boundary layer. *J. Comput. Phys.* **109**, 169–192.

[46] Rayleigh, Lord 1880 On the stability, or instability, of certain fluid motions. In *Scientific Papers of Lord Rayleigh*, Dover **1** 474–487.

[47] Roach, P. E. 1987 The generation of nearly isotropic turbulence by means of grids. *Int. J. Heat Fluid Flow* **8** 82–92.

[48] Roach, P. E., & Brierley, D. H. 1992 The influence of a turbulent free-stream on zero pressure gradient transitional boundary layer development part I: test cases T3A and T3B. In *Numerical Simulation of unsteady flows and transition to turbulence*, O. Pironneau, W. Rodi, I. L. Rhyming, A. M. Savill and T. V. Truong, eds. Cambridge, 319–347.

[49] Rogallo, R. S. 1981 Numerical experiments in homogeneous turbulence. *NASA Tech. Memo. 81315.*

[50] Schlichting, H. 1933 Zur Entstehung der Turbulenz bei der Plattenstromung. *Nachr. Ges. Wiss. G ottingen Math.-Phys. Kl.* **1933** 181–208.

[51] Schubauer, G. B. & Skramstad, H. K. 1947 Laminar boundary-layer oscillations on a flat plate *NACA Report 909*

[52] Singer, B. A. 1996 Characteristics of a young turbulent spot. *Phys. Fluids* **8** 509–521.

[53] Singer, B. A. & Joslin, R. D. 1994 Metamorphosis of a hairpin vortex into a young turbulent spot. *Phys. Fluids* **6** 3724–3736.

[54] Sommerfeld, A. 1908 Ein Beitrag zur hydrodynamischen Erklarung der turbulenten Flussigkeitsbewegung. *Atti. Congr. Int. Math., 4th, Rome* 116–124.

[55] Tollmien, W. 1929 Uber die Entstehung der Turbulenz. *Nachr. Ges. Wiss. G ottingen Math.-Phys. Kl.* **1929** 21–44.

[56] Van Dyke, M. 1982 *An Album of Fluid Motion* The Parabolic Press.

[57] van Kan, J. 1986 A second-order accurate pressure correction scheme for viscous incompressible flow. *SIAM J. Sci. Stat. Comput.* **7** 870–891.

[58] Voke, P., and Yang, Z. 1995 Numerical study of bypass transition. *Phys. Fluids* **7**, 2256–2264.

[59] Waleffe, F. 1997 On a self-sustaining process in shear flows. *Phys. Fluids* **9** 883–900.

[60] Westin, K. J. A., Boiko, B. G. B., Klingmann, G. B., Kozlov, V. V., Alfredsson, P. H. 1994 Experiments in a boundary layer subjected to free stream turbulence. Part I. Boundary layer structure and receptivity. *J. Fluid. Mech.* **281**, 193–218.

Chapter 7

Conclusion

Since each of the preceding chapters is complete with a conclusion section that summarizes the most important results presented there, in this chapter the aim is not to reiterate those summaries, but rather to present our major findings in a unified perspective.

In the current investigation we performed DNS of boundary-layer transition due to three types of free-stream disturbance, a von Kármán vortex street behind a circular cylinder, and 6% free-stream turbulence with two different values for the integral length scale. The onset of turbulence was observed at low values of the plate Reynolds number ($Re_x \simeq 10^5$), which are typical of bypass transition. The differences in the free-stream disturbance environment resulted in somewhat different transition scenarios. Nonetheless, the transitional flows had several important features in common.

In all of our simulations we observed clearly defined streaks of the streamwise velocity. In the simulations of wake/boundary-layer interactions and simulations of transition due to small-scale FST, these streaks appeared to have three universal properties. First, their corresponding near-wall u_{rms} profiles are approximately self-similar when scaled by the boundary-layer thickness[1]. Second, they are prefer-

[1] $u_{rms} \simeq y\frac{d\overline{U}}{dy}$ near the wall is a good approximation (Klebanoff 1971; Goldstein & Wundrow

entially amplified by the boundary-layer mean shear: the streamwise evolution of the frequency spectrum shows growth in the lower frequency range. In the case of FST, their initial amplitude is proportional to that of the free-stream disturbance, but the proportionality constant is probably dependent on other properties of the FST, *e.g.* length scale. Third, the energy associated with the streaks, as well as the overall streamwise Reynolds stress $\langle uu \rangle$, increases in a quasi-linear, or affine dependence on the plate Reynolds number (Re_x). The affine behavior may be caused by a short receptivity distance, across which there is no disturbance growth, as suggested by Fransson, Matsubara & Alfredsson (2005).

An essential property that does not appear to be universal is the streak separation distance in the spanwise direction. Our results from the wake/boundary-layer simulation indicate that it is dictated by the spanwise scales of the wake in the free stream. In the calculations of FST-induced boundary-layer transition by Jacobs & Durbin (2001), Brandt, Schlatter & Henningson (2004) and our cases I and Is in the previous chapter, the streak separation was close to the boundary-layer thickness δ_{99}, comparable to the value $1.4\delta_{99}$ predicted by optimal disturbance theory (Andersson *et al.* 1999). However (based on velocity correlations, flow visualization or turbulence decay rates), in all of the above simulations, the length scale of the FST was also close to this value. On the other hand, in our simulation of the T3B case (large FST length scale), streaks were not precursors of transition and were not generated by the FST directly. This observation supports the conjecture that the

1998)

FST scale has a major influence on the boundary-layer streak spacing. Moreover, Fransson & Matsubara (2003) reduced the thickness of the Blasius boundary layer by a factor of two using suction, but observed no change in the streak separation. This implies that the spacing of streaks was probably dictated by the FST environment, which was kept unchanged. Thus, in order to determine the origin of laminar streak spacing, there is clearly a need for experiments and simulations that have the FST length scale as a carefully controlled parameter.

Our observations regarding the universality of streaks are not unexpected: numerous investigators who studied the problem of bypass transition by various experimental, numerical and theoretical means, observed or predicted the generation of streamwise-elongated structures. For example, Wu *et. al* (1999) observed flow streakiness in DNS of unsteady wake/boundary-layer interaction, Berlin & Henningson (1999) demonstrated the evolution of streamwise-oriented streaks from two oblique modes of opposite angle. Elofsson & Alfredsson (1998) studied this mechanism experimentally in channel-flow transition . Bertolotti (1997) predicted the appearance of streaks using the nonlinear Parabolic Stability Equations (PSE) in response to vorticity in the free stream. Wundrow & Goldstein (1998) used the boundary-region equations to study the boundary-layer response to wall-normal vorticity, and predicted elongated streamwise structures with cross-stream near-wall u_{rms} profiles of the form $y\frac{d\overline{U}}{dy}$, as initially suggested by Klebanoff (1971).

It is also tempting to speculate that streaks of the perturbed-laminar regime may be similar to the sublayer streaks found in fully-turbulent near-wall flows.

Qualitative similarities between the two regimes have been pointed out by Brandt, Shlatter & Henningson (2004). In both cases the streaks are produced by flanking streamwise-oriented vortices, which transfer near-wall low-momentum fluid into the outer boundary layer, and outer high-momentum fluid towards the wall. Furthermore, comparing the TKE budgets in the perturbed laminar and turbulent regimes for any of our simulations demonstrates that the differences are mostly qualitative and are largely due to the lower levels of near-wall dissipation and viscous diffusion in the perturbed laminar regime. The shapes of the curves are very similar.

Thus, as the turbulent near-wall cycle may be an attractor for wall-bounded transitional flows, the laminar-streak regime may be a similar attractor for perturbed laminar flows. The turbulent self-sustaining regime has been the subject of recent theoretical and numerical investigations, *e.g.* Waleffe (1997), Jiménez & Pinelli (1999), and the possibility that the results of these analyses are also relevant to the perturbed-laminar regime is intriguing.

The appearance of flow intermitency in the form of turbulent spots in transitional wall-bounded flows is a unifying feature of many transition scenarios. These turbulent regions, surrounded by essentially laminar flow were clearly observed and photographed by Emmons (1951) (see also Van Dyke, 1982) inside a thin layer of fluid. Shaped in the form of an arrowhead, these spots spread laterally and longitudinally, preserving their shape until their merger into a fully-turbulent front. Since then, analagous turbulent spots have been seen in experiments and simulations of natural and bypass transtion and in both compressible and incompressible flows.

Matsubara & Alfredsson (2001) and Fransson, Matsubara & Alfredsson (2004) reported arrowhead-shaped turbulent spots resulting from the breakdown of a streaky flow, disturbed by FST of various amplitudes. Wu *et al.* (1999) observed turbulent spots of a reversed arrowhead shape in simulations of unsteady wake/boundary-layer interaction. Jacobs & Durbin (2001), Brandt and Schlatter & Henningson (2004) observed streaky flow contaminated with turbulent spots of arbitrary shape in FST-induced boundary layer-transition. In these simulations, as well as in our simulations of cases I & Is presented in §6, however, the spanwise extent of the domain was limited because of the computational cost. Thus, the maximum spot size was restricted and after the spot filled the entire computational domain, its shape could no longer be determined. It is possible that the shape of a turbulent spot originating in a streaky flow via an instability is initially not well defined, but tends to an arrowhead shape at later stages. The flow visualizations of Fransson, Matsubara & Alfredsson (2004) support this hypothesis: the spot formation and the initial evolution is as visually presented in Jacobs & Durbin, Brandt, Schlater & Henningson, and our case I in the previous chapter, but as the spot grows in size, an arrowhead shape becomes evident.

In experimental turbulent spot visualization studies, Perry *et al.* (1981) hypothesized that a turbulent spot is an array of Λ-shaped vortices. Spot precursors were generated by blowing through a hole in the wind tunnel wall and the resulting spot was composed of a staggered array of "folds," *i.e.* deformed vortical filaments similar to a Λ-vortex.

Krishnan & Sandham (2004) studied turbulent spots in simulations of supersonic flow at Mach numbers 2, 4 and 6. The spots were generated by a blowing strip and resulted from the breakdown of Λ and streamwise-oriented vortices. The downstream section of the spots was an arrowhead-shaped overhang caused by a particular arrangement of hairpin and streamwise vortices, and the upstream section was characterized by relatively calm flow.

Our results from the T3B simulation revealed a strikingly similar spot development, which involves Λ and streamwise- oriented vortices in the spot generation and growth. By following the evolution of spots in time, we showed the important role of Λ-shaped vortices in producing and maintaining the arrowhead shape of the spot. It is especially interesting that our T3B simulatioin results were similar to those of Krishnan & Sandham (2004) despite a fundamental difference in the disturbance origin (blowing vs. FST).

In our simulations of steady wake/boundary-layer interaction at $Re_D = 3,900$, we observed transitional intermittency that was very similar to the turbulent spots in FST-induced transition (see, for example, figure 10 in Jacobs & Durbin 2001). Unfortunately, we did not obtain enough data to follow the spots in time as was done in §6 for FST-induced transition. In this case, the spots were caused by patches of turbulent flow injected into the boundary layer by the wake in the free stream.

Despite the various possible origins of turbulent spots, as evidenced by their occurrence in natural, bypass, and wake-induced transition regimes, there is compelling evidence that turbulent spots in wall-bounded flows tend toward a universal

arrowhead shape. The preservation of shape is probably due to the orientation of the vortical structures that produce spot growth.

Based on our present work as well as on other simulations and experiments, it is apparent that while the various modes of bypass transition share prominent physical features *e.g.* streamwise streaks and turbulent spots, their connection to the transition process is not universal. Although streaky structures are present in nearly all flows undergoing bypass transition, it seems that only in certain cases turbulent spot formation is caused by a streak-related instability. Furthermore, even for FST length scales, *i.e.* in an environment in which streamwise streaks are the dominant structures, a disagreement on the origin of turbulent spots remains. Jacobs & Durbin (2001) argue that streaks provide a direct receptivity path between the FST and the boundary layer, whereas Brandt, Schlatter & Henningson (2004) report that the streaks themselves undergo instabilities, and the FST is probably important in forcing the streaks. The results of our case I simulation support the latter theory, although in a highly-disturbed free stream the two mechanisms may not be visually distinguishable.

On the other hand, as our T3B simulation shows, free-stream turbulence can interact directly with the boundary layer and this effect becomes dominant with increasing FST length scale. The turbulent spots caused by this direct interaction arise differently, although at later, more disorderly stages of evolution, they may be indistinguishable from spots originating from streak instabilities.

In the case of wake/boundary-interaction, the situation is complicated by an

additional mechanism. Aside from inducing streamwise streaks and possibly Λ-vortices, free-stream wakes are capable of injecting turbulent momentum directly into the boundary layer. The latter scenario was dominant in our wake/boundary-layer interaction simulations, and also in the simulations of unsteady interaction of Wu *et al.* (1999). In such cases, it becomes increasingly difficult to isolate the essential physics. Moreover, the dominant phenomenon may change with a small modification of the geometry or disturbance characteristics, making generalization uncertain.

In summary, in the present investigation we have observed three different mechanisms of boundary-layer bypass transition depending on the nature of the external disturbance environment. When the free-stream disturbance is composed of coherent wakes in the form of a von Kármán vortex street, boundary-layer transition is initiated by the injections of free-stream fluid from the wake into the boundary layer. The boundary layer responds by generating streamwise velocity streaks that are very similar to Klebanoff modes. At a sufficiently high Reynolds number, the wake fluid contains small scale motions that become the origin of boundary-layer intermittency, *i.e.* turbulent spots. From our data, a possible role of streak instability, however unlikely, cannot be excluded.

If the external disturbance is homogeneous and isotropic free-stream turbulence with a fairly low integral length scale (for case I in §6 the Reynolds number based on the FST integral length scale was 1150), the FST is ingested into the boundary layer in the vicinity of the leading edge, stretched by the boundary-layer

shear, and evolves as elongated streaks of streamwise velocity. In this case, the transition process appears dominated by streak instabilities. Streak breakdown results in turbulent spots that do not have the classical arrowhead shape in the early stages of development. The later stages are not available from our data, but experimental smoke visualizations indicate that the arrowhead shape is approached (Mastubara & Alfredsson 2001; Fransson, Matsubara & Alfredsson 2004).

In the case that the FST length scale is larger, as in case T3B ($Re_L = 6900$), boundary-layer transition is no longer dominated by streaks. The large-scale FST induces Λ or streamwise-oriented vortices inside the boundary layer, and the subsequent generation of turbulent spots proceeds essentially as has been described for natural transition or blowing/suction-induced turbulent spots. In this scenario, the streamwise streaks are also present, but they are most likely formed upstream of the spots, by the 'legs' of the stretched hairpin vortices, as has been suggested by Gal-ed-Hak, Blackwelder, & Riley (1981) and Perry, Lim, & Teh (1981), and are irrelevant to the transition process.

The above physical mechanisms are qualitatively distinct, and therefore will probably require different modeling strategies. Moreover, the likelihood that in some flows they may be present simultaneously will pose additional challenges for transition prediction.

7.1 References

[1] Andersson, P., Berggren, M. & Henningson, D.S. 1999 Optimal disturbances and bypass transition in boundary layers. *Phys. Fluids* **11** 134–150.

[2] Brandt, L., Schlatter, P. & Henningson, D. S. 2004 Transition in boundary layers subject to free-stream turbulence. *J. Fluid Mech.* **517**, 167–198.

[3] Elofsson, P. A. & Alfredsson, P. H. 1998 An experimental study of oblique transition in plane channel flow. *J. Fluid Mech.* **358** 177–202.

[4] Emmons, H. W. 1951 The laminar-turbulent transition in a boundary layer. *J. Aeronaut. Sci.* **18** 490–498.

[5] Fransson, J. H. M., Matsubara, M. & Alfredsson, P. H. 2004 Smoke visualization movies of bypass transition. *Private communication*

[6] Fransson, J. H. M., Matsubara, M. & Alfredsson, P. H. 2005 Transition induced by free-stream turbulence. *J. Fluid Mech.* **527** 1–25.

[7] Fransson, J. H. M. & Alfredsson, P. H. 2003 On the disturbance growth in an asymptotic suction boundary layer. *J. Fluid Mech.* **482** 51–90.

[8] Gad-el-Hak, M, Blackwelder, R. F. & Riley, J. J. 1981 On the growth of turbulent regions in laminar boundary layers. *J. Fluid Mech.* **110** 73–95.

[9] Goldstein, M. E. & Wundrow, D. W. 1998 On the environmental realizability of algebraically growing disturbances and their relation to Klebanoff modes. *Theoret. Comput. Fluid Dynamics* **10** 171–186.

[10] Jacobs, G. J. & Durbin, P. A. 2001 Simulations of bypass transition. *J. Fluid Mech.* **428**, 185–212.

[11] Jiménez, J & Pinelli, A. 1999 The autonomous cycle of near-wall turbulence. *J. Fluid Mech.* **389** 335–359.

[12] Klebanoff, P. S. 1971 Effect of freestream turbulence on the laminar boundary layer. *Bull. Amer. Phys. Soc.* **10**, 1323.

[13] Krishnan, L. & Sandham, N. D. 2004 Turbulent spots in a compressible boundary-layer flow. *IUTAM Symp. on Laminar-Turbulent Transition*

[14] Matsubara, M. & Alfredsson, H. 2001 Disturbance growth in boundary layers subjected to free-stream turbulence. *J. Fluid. Mech.* **430**, 149–168.

[15] Perry, A. E., Lim, T. T. & Teh, E. W. 1981 A visual study of turnbulent spots. *J. Fluid Mech.* **104** 387–405.

[16] Van Dyke, M. 1982 *An Album of Fluid Motion* The Parabolic Press.

[17] Waleffe, F. 1997 On a self-sustaining process in shear flows. *Phys. Fluids* **9** 883–900.

[18] Wu, X., Jacobs, R. G., Hunt, J. C. R. & Durbin, P. A. 1999 Simulation of boundary layer transition induced by periodically passing wakes *J. Fluid Mech.* **398**, 109–153.

Chapter 8

Bibliography

[1] Alfredsson, P. H. & Matsubara, M. 1996 Streaky structures in transition. In *Transitional Boundary Layers in Aeroacoustics* Henkes, R. A. W. M & Ingen, J. L. eds., 374–386.

[2] Andersson, P., Berggren, M. & Henningson, D.S. 1999 Optimal disturbances and bypass transition in boundary layers. *Phys. Fluids* **11** 134–150.

[3] Andersson, P., Brandt, L., Bottaro, A. & Henningson, D. S. 2001 On the breakdown of boundary layer streaks. *J. Fluid Mech.* **428** 29–60.

[4] Arnal, D. & Juillen, J. C. 1978 Contribution experimentale a l'etude de la receptive d'une couche limite laminare, a la turbulence de l'ecoulement general. *ONERA Tech. No. 1/5018 AYD*

[5] Asai, M. & Nishioka, M. 1990 Development of wall turbulence in Blasius flow. In *Laminar-Turbulent Transition* Arnal, D. & Michel, R., eds., Springer-Verlag, 215–222.

[6] Balaras, E. 2004 Modeling complex boundaries using an external force field on Cartesian grids in large-eddy simulations. *Comput. Fluids* **33**, 375–404.

[7] Balaras, E., Benocci, C. & Piomelli, U. 1995 Finite difference computations of high Reynolds number flows using the dynamic subgrid-scale model. *Theoret. Comput. Fluid Dyn.* **7**, 207–216.

[8] Balaras, E., Piomelli, U. & Wallace, J. M. 2001 Self-similar states in turbulent mixing layers *J. Fluid Mech.*, **446**, 1–24.

[9] Bandyopadhyay, P. R. 1987 Resonant flow in a row of small transverse cavities submerged in a turbulent boundary layer. *AIAA Paper 1987-1235.*

[10] Bario, F., Charnay, G. & Papailiou, K. D. 1982 An experiment concerning the confluence of a wake and a boundary layer. *J. Fluids Eng.* **104** 18–24.

[11] Bayly, B.J., Orszag, S. A. & Herbert, T. 1988 Instability mechanisms in shear-flow transition. *Annu. Rev. Fluid Mech* **20** 359–392.

[12] Bennet, H. W. 1953 An experimental study of boundary layer transition. *Kimberley Clark Corp. Tech. Rep.*(prepared for Off. Nav. Res.), NEENAH, Wis.

[13] Bertolotti, F. P. 1997 Response of the Blasius boundary layer to free-stream vorticity. *Phys. Fluids* **9** 2286–2299.

[14] Blair, M. F. 1983 Influence of free-stream turbulence on turbulent boundary-layer heat transfer and mean profile development. Part I – Experimental data. *ASME J. Heat Transf.* **105** 33–40.

[15] Brandt, L. & Henningson, D. S. 2002 Transition of streamwise streaks in zero-pressure-gradient boundary layers. *J. Fluid Mech.* **472** 229–261.

[16] Brandt, L., Schlatter, P. & Henningson, D. S. 2004 Transition in boundary layers subject to free-stream turbulence. *J. Fluid Mech.* **517**, 167–198.

[17] Buter, T. A.& Reed, H. L. 1994 Boundary layer receptivity to free-stream vorticity. *Phys. Fluids* **6** 3368–3379.

[18] Butler, K. M., Farrel, B. F. 1992 Three-dimensiona optimal perturbations in viscous shear flow. *Phys. Fluids A* **4** 1637–1650.

[19] Chorin, A. J. 1968 Numerical solution of the Navier-Stokes equations. *Math. Comput.* **22**, 742–762.

[20] Choudhari, M. 1996 Boundary-layer receptivity to three-dimensional unsteady Vortical disturbances in free stream *AIAA Paper* **1996-0181**.

[21] Collis, S. S. & Lele, S. K. 1996 A computational approach to swept leading-edge receptivity. *AIAA Paper* **96-0180**.

[22] Cowley, S. J., Van Dommelen, L. L., Lam, S. T. 1991 On the use of Lagrangian variables in descriptions of unsteady boundary-layer separation. *Phil. Trans. R. Soc. London Ser. A* **333** 343–78.

[23] Craik, A. D. D. 1971 Nonlinear resonant instability in boundary layers. *J. Fluid Mech.* **50** 393–413.

[24] Dietz, A. J. 1987 Boundary layer receptivity to transient convected disturbances. *AIAA Paper* **97-1962**.

[25] Doligalski, T. L., Smith C. R. & Walker, J. D. A. 1994 Vortex interactions with walls *Annu. Rev. Fluid Mech* **26** 573–616.

[26] Drazin, P. & Reid, W. H. 1981 *Hydrodynamic Stability*, (Cambridge University Press, Cambridge).

[27] Emmons, H. W. 1951 The laminar-turbulent transition in a boundary layer. *J. Aeronaut. Sci.* **18** 490–498.

[28] Ellingsen, T., Palm, E. 1975 Stability of linear flow. *Phys. Fluids* **18** 487–488.

[29] Elliott, J. W., Cowley, S. J., Smith, F. T. 1983 Breakdown of boundary layers: (i) on moving surfaces; (ii) in self-similar unsteady flows; (iii) in a fully unsteady flow. *Geophys. Astrophys. Fluid Dyn.* **25** 77–138.

[30] Elofsson, P. A. & Alfredsson, P. H. 1998 An experimental study of oblique transition in plane channel flow. *J. Fluid Mech.* **358** 177–202.

[31] Fadlun, E. A., Verzicco, R., Orlandi, P. & Mohd-Yusof, J. 2000

Combined immersed-boundary finite-fifference methods for three-dimensional complex flow simulations. *J. Comput. Phys.* **161**, 35–60.

[32] Fasel, H. 1990 Numerical simulation of instability and transition in boundary layer flows. In *Laminar-Turbulent Transition* Arnal, D. & Michel, R., eds., Springer-Verlag, 578–598

[33] Ferziger, J. H. & Peric, M. 1998 *Computational methods for fluid dynamic* (Springer Verlag, Berlin Heidelberg).

[34] Fransson, J. H. M. 2004 Leading edge design process using a commercial flow solver. *Exps. Fluids* **37** 929–932.

[35] Fransson, J. H. M., Matsubara, M. & Alfredsson, P. H. 2004 Smoke visualization movies of bypass transition. *Private communication*

[36] Fransson, J. H. M., Matsubara, M. & Alfredsson, P. H. 2005 Transition induced by free-stream turbulence. *J. Fluid Mech.* **527** 1–25.

[37] Fransson, J. H. M. & Alfredsson, P. H. 2003 On the disturbance growth in an asymptotic suction boundary layer. *J. Fluid Mech.* **482** 51–90.

[38] Gad-el-Hak, M, Blackwelder, R. F. & Riley, J. J. 1981 On the growth of turbulent regions in laminar boundary layers. *J. Fluid Mech.* **110** 73–95.

[39] Gaster, M. 1974 On the effects of boundary-layer growth on flow stability. *J. FLuid Mech.* **66** 465–80.

[40] Germano, M. 1992 Turbulence: the filtering approach. *J. Fluid Mech.* **238** 325–336.

[41] Germano, M., Piomelli, U., Moin, P. & Cabot, W. H. 1991 A dynamic subgrid-scale eddy viscosity model. *Phys. Fluids A* **3** 1760–1765.

[42] Goldstein, M. E. 1983 The evolution of Tollmien-Schlichting waves near a leading edge. *J. Fluid Mech.* **127** 59–81.

[43] Goldstein, M. E. 1985 Scattering of acoustic waves into Tollmien-Schlichting waves by small streamwise variations in surface geometry. *J. Fluid Mech.* **154** 509–529.

[44] Goldstein, M. E. & Wundrow, D. W. 1998 On the environmental realizability of algebraically growing disturbances and their relation to Klebanoff modes. *Theoret. Comput. Fluid Dynamics* **10** 171–186.

[45] Goldstein, M. E. & Hultgren, L. S. 1987 A note on the generation of Tollmien-Schlichting waves by sudden surface-curvature change. *J. Fluid Mech.* **181** 519–525.

[46] Grosch C. E., Salwen, H. 1978 The continuous spectrum of the Orr-Sommerfeld equation. Part 1. The spectrum and the eigenfunctions *J. Fluid Mech.* **87**, 33–54.

[47] Henningson, D., Spalart, P. & Kim, J. 1987 Numerical simulations of

turbulent spots in plane Poisseuille and boundary-layer flow *Phys. Fluids* **30**, 2914–2917.

[48] HERBERT, T. 1984 Analysis of the subharmonic route to transition in boundary layers. *AIAA Paper* **84-0009**.

[49] HERBERT, T. 1985 Three-dimensional phenomena in the transitional flat-plate boundary layer. *AIAA Paper* **85-0489**.

[50] HERBERT, T. 1987 On the mechanism of transition in boundary layers. *AIAA Paper* **87-1201**.

[51] HERBERT, T. 1988 Secondary instability of boundary layers. *Annu. Rev. Fluid Mech* **20** 487–526.

[52] HERBST, R. 1980 Entwicklung von Grenzschichten bei instationarer Zustromung. PhD Thesis, Technical University Darmstadt.

[53] HUAI, X., JOSLIN, R. D., PIOMELLI, U. 1997 Large-eddy simulation of transition to turbulence in boundary layers. *Theoret. Comput. Fluid Dynamics* **9**, 149–163.

[54] JACOBS, G. J., DURBIN, P. A. 1998 Shear sheltering and the continuous spectrum of the Orr-Sommerfeld equation. *Phys. Fluids* **10** 2006–2011.

[55] JACOBS, R. G. 1999 Bypass transition phenomena studied by numerical simu-

lation. PhD thesis (Report No. TF-77), Department of Mechanical Engineering, Stanford University.

[56] Jacobs, G. J. & Durbin, P. A. 2001 Simulations of bypass transition. *J. Fluid Mech.* **428**, 185–212.

[57] Jiménez, J & Pinelli, A. 1999 The autonomous cycle of near-wall turbulence. *J. Fluid Mech.* **389** 335–359.

[58] Jonáš, P., Mazur, O., Uruba, V. 2000 On the receptivity of the by-pass transition to the length scale of the outer stream turbulence. *Eur. J. Mech. B-Fluids* **19** 707–722.

[59] Kachanov, Y. S. 1984 On the resonant nature of the breakdown of a laminar boundary layer. *J. Fluid Mech.* **184** 43–74.

[60] Kachanov, Y. S. 1990 Secondary and cascade resonant instabilities of boundary layers. Wave-resonant concept of a breakdown and its substantiation. In *Laminar-Turbulent Transition* Arnal, D. & Michel, R., eds., Springer-Verlag, 65–80

[61] Kachanov, Y. 1994 Physical mechanisms of laminar-boundary-layer transition. *Annu. Rev. Fluid Mech* **26** 411–482.

[62] Kachanov, Y. S., Kozlov, V. V., Levchenko, V. Y. 1977 Nonlinear development of a wave in a boundary layer. Transl. *Fluid Dyn.* 1978 **12** 383–90.

[63] KACHANOV, Y. S., KOZLOV, V. V., LEVCHENKO, V. Y. 1980 Experiments on nonlinear interaction of waves in a boundary layer. In *Laminar-Turbulent Transition* (R. Eppler and H. Fasel, eds.) (Springer, Berlin), 135–152.

[64] KACHANOV, Y. S., KOZLOV, V. V., LEVCHENKO, V. Y., RAMAZANOV, M. P. 1985 Experimental study of K-regime breakdown of laminar boundary layer. In *Laminar-Turbulent Transition* Kozlov, V. V. ed., Springer-Verlag, 61–73.

[65] KACHANOV, Y. S., KOZLOV, V. V., LEVCHENKO, V. Y., RAMAZANOV, M. P. 1990 Transl. *Sov. J. Appl. Phys.* 1990 **4**

[66] KACHANOV Y. S. & LEVCHENKO, V. Y. 1984 The resonant interaction of disturbances at laminar-turbulent transition in a boundary layer. *J. Fluid Mech* **138** 209–247.

[67] KENDALL, J. M. 1985 Experimental study of disturbances porduced in a pre-transitional laminar boundary layer by weak free stream turbulence. *AIAA Paper* **85-1695**.

[68] KENDALL, J. M. 1990 Boundary-layer receptivity to freestream turbulence. *AIAA Paper* **90-1504**.

[69] KENDALL, J. M. 1991 Studies on laminar boundary-layer receptivity to freestream turbulence near a leading edge. *Boundary Layer Stability and Transition to Turbulence*, Technical Report FED **114**, ASME

[70] KENDALL, J. M. 1998 Experiments on boundary-layer receptivity to free stream turbulence. *AIAA Paper* **98-0530**.

[71] KIM, J. & MOIN, P. 1985 Application of a fractional step method to incompressible Navier-Stokes equations. *J. Comput. Phys.* **59**, 308–323.

[72] KLEBANOFF, P. S. 1971 Effect of freestream turbulence on the laminar boundary layer. *Bull. Amer. Phys. Soc.* **10**, 1323.

[73] KLEBANOFF, P. S., TIDSTROM, K. D. & SARGENT, L. M. 1962 The three-dimensional nature of boundary-layer instability. *J. Fluid Mech.* **12** 1–34.

[74] KLEISER, L. & ZANG, T. A. 1991 Numerical simulation of transition in wall-bounded shear flows. *Annu. Rev. Fluid Mech.* **23** 495–537.

[75] KLINGMANN, R. G. B., BOIKO, A. V., WESTIN, K. J., KOZLOV, V. V. & ALFREDSSON, P. H. 1993 Experiments on the stability of Tollmien-Schlighting waves. *Eur. J. Mech. B/Fluids* **12** 493–514.

[76] KNAPP C. F. & ROACHE, P. J. 1968 A combined visual and hot-wire anemometer investigation of boundary-layer transition. *AIAA J.* **6** 29–36.

[77] KRAVCHENKO, A. G. & MOIN, P. 2000 Numerical studies of flow over a circular cylinder at $Re_D = 3900$. *Phys. Fluids* **12**, 403–417.

[78] KRISHNAN, L. & SANDHAM, N. D. 2004 Turbulent spots in a compressible boundary-layer flow. *IUTAM Symp. on Laminar-Turbulent Transition*

[79] Kusunose, K. & Cao, H. V. 1994 Prediction of transition location for a 2-D Navier-Stokes solver for multi-element airfoil configurations. *AIAA Paper 1994-2376.*

[80] Kyriakides N. K., Kastrinakis, E. G., Nychas, S. G. & Goulas, A. 1996 Boundary layer transition induced by a von Karman vortex street wake. *Proc. Inst. Mech. Eng.* **210**, 167–179.

[81] Kyriakides N.K., Kastrinakis, E.G., Nychas, S.G., & Goulas, A. 1999a Aspects of flow structure during a cylinder-wake induced laminar/turbulent transition. *AIAA J* **37**, 1197–1205.

[82] Kyriakides N. K., Kastrinakis, E. G., Nychas, S. G., & Goulas, A. 1999 A bypass wakeinduced laminar turbulent transition. *Eur J. Mech. B-Fluid* **18**, 1049–1065.

[83] Landahl, M. T. A note on an algebraic instability of inviscid parallel shear flows. *J. Fluid Mech.* **98** 243–251.

[84] Leib, S. J., Wundrow, D. W., & Goldstein, M.E. 1999 Effect of free-stream turbulence and other vortical disturbances on a laminar boundary layer *J. Fluid. Mech.* **380** 169–203.

[85] Lin, N., Reed, H. L., Saric, W.C. 1992 Effect of leading-edge geometry on boundary layer receptivity to free-stream sound. In *Instability, Receptivity, and Turbulence* Hussaini, M., Kumar, A., Streett, C., eds. Springer-Verlag, 421–440

[86] Liu, X. & Rodi, W. 1991 Experiments on transitional boundary layers with wake-induced unsteadiness *J. Fluid Mech.* **231**, 229–256.

[87] Luchini, P. 2000 Reynolds-number independent instability of the boundary layer over a flat surface. Part 2. Optimal perturbations. *J. Fluid Mech.* **404** 289–309.

[88] Luton, A., Ragab, S. & Telionis, D. 1995 Interactions of spanwise vortices with a boundary layer. *Phys. Fluids* **7** 2757–2765.

[89] Matsubara, M. & Alfredsson, H. 2001 Disturbance growth in boundary layers subjected to free-stream turbulence. *J. Fluid. Mech.* **430**, 149–168.

[90] Mayle, R. E. The role of laminar-turbulent transition in gas turbine engines. *Trans. ASME: J. Turbomachinery* **113** 509–537.

[91] Meneveau, C., Lund, T. S. & Cabot, W. H. 1996. A Lagrangian dynamic subgrid-scale model of turbulence. *J. Fluid Mech.* **319**, 353–385.

[92] Meredith, P. T. 1993 Viscous phenomena affecting high-lift systems and suggestions for future CFD development. *AGARD* **CP-515** 19.1–19.8.

[93] Mittal R., Iaccarino, G. 2005 Immersed Boundary Methods *Annu. Rev. Fluid Mech.* **37** 239–261.

[94] Morinishi, Y., Lund, T. S., Vasilyev, O. V. & Moin, P. 1998 Fully-

conservative higher order finite difference schemes for incompressible flow. *J. Comput. Phys.* **143**, 90–124.

[95] Morkovin, M. V. 1969 On the many faces of transition. In *Viscous Drag Reduction*, C.S. Wells, ed. Plenum, 1-31.

[96] Moser, R. D., Kim, J. & Mansour, N. N. 1999 Direct numerical simulation of turbulent channel flow up to $Re_\tau = 500$. *Phys. Fluids* **11**, 943–945.

[97] Nayfeh, A. H. & Bozatli, A. N. 1979 Nonlinear wave interactions in boundary layers *AIAA Paper* **79-1456**.

[98] Norberg, C. 1993 Pressure forces on a circular cylinder in cross flow. *Proceedings of IUTAM Symposium on Bluff-Body Wakes, Dynamics and Instabilities,* Göttingen, Germany, September 7-11, 1992, Proc. eds. Eckelmann, H., Graham, J. M. R., Huerre, P. & Monkewitz, P. A., Springer-Verlag, Berlin, 275-278.

[99] Ong, L. & Wallace, J. 1996 The velocity field of the turbulent very near wake of a circular cylinder. *Exp. Fluids* **20**, 441–453.

[100] Orlanski, I. 1976 A Simple Boundary Condition for Unbounded Hyperbolic Flows. *J. Comput. Phys.* **21**, 251–269.

[101] Orr W. M. F. 1907 The stability or instability of the steady motions of a perfect liquid and a viscous liquid. *Proc. R. Ir. Acad. A* **27** 9–27, 69–138.

[102] Orszag S. A. & Patera, A. T. 1983 Secondary instability of wall-bounded shear flows. *J. Fluid Mech.* **128** 347–85.

[103] Ovchinnikov, V. O., Piomelli, U. & Choudhari, M. M., 2004 Inflow conditions for numerical simulations of bypass transition *AIAA Paper*, **2004-0591**.

[104] Ovchinnikov, V. O., Piomelli, U. & Choudhari, M. M., 2005 Numerical simulations of boundary-layer transition induced by a cylinder wake. *J. Fluid Mech. Accepted for publication.*

[105] Ovchinnikov, V. O., Piomelli, U. & Choudhari, M. M., 2005 Numerical simulations of boundary layer bypass transition with leading edge effects In *Proc. 4th Int. Symp. Turbulence and Shear Flow Phenomena*, Williamsburg, Virginia, June 25-27, 2005, 425–430.

[106] Perry, A. E., Lim, T. T. & Teh, E. W. 1981 A visual study of turnbulent spots. *J. Fluid Mech.* **104** 387–405.

[107] Pfeil, H., Herbst, R. & Schr oder, T. 1983 Investigation of laminar-turbulent transition of boundary layers disturbed by wakes. *Trans. ASME A: Engng for Power* **105** 130–137.

[108] Philips, O. M. 1969 Shear-flow turbulence. *Annu. Rev. Fluid Mech* **1** 245–264.

[109] Piomelli, U., Balaras, E. & Pascarelli, A. 2000 Turbulent structures in accelerating boundary layers. *J. Turbulence* **1**, (001) 1–16.

[110] Piomelli, U., Choudhari, M. M., Ovchinnikov, V. O. & Balaras, E.,2004 Numerical simulations of wake/boundary layer interactions. *AIAA Paper*, **2004-0975**.

[111] Rai, M. M. & Moin, P. 1993 Direct numerical simulation of transition and turbulence in a spatially evolving boundary layer. *J. Comput. Phys.* **109**, 169–192.

[112] Rayleigh, Lord 1880 On the stability, or instability, of certain fluid motions. In *Scientific Papers of Lord Rayleigh*, Dover **1** 474–487.

[113] Rist, U. 1990 Numerische Untersuchtung der r aumlichen, dreidimensionalen St orungsentwicklung beim Grenzschlichtumschlag. PhD thesis. Inst. A Mech. Univ. Stuttgart

[114] Rist U. & Fasel, H. 1991 Spatial three-dimensional numerical simulation of laminar-turbulent transition in a flat-plate boundary layer. *Boundary Layer Trasition & Control Conf.* Cambridge, UK, R. Aeronaut Soc., 25.1–25.9.

[115] Rist, U. & Fasel, H. 1995 Direct numerical simulation of controlled transition in a flat-plate boundary layer. *J. Fluid Mech.* **298** 211–248.

[116] Roach, P. E. 1987 The generation of nearly isotropic turbulence by means of grids. *Int. J. Heat Fluid Flow* **8** 82–92.

[117] Roach, P. E., & Brierley, D. H. 1992 The influence of a turbulent free-stream on zero pressure gradient transitional boundary layer development part I: test cases T3A and T3B. In *Numerical Simulation of unsteady flows and transition to turbulence*, O. Pironneau, W. Rodi, I. L. Rhyming, A. M. Savill and T. V. Truong, eds. Cambridge, 319–347.

[118] Rogallo, R. S. 1981 Numerical experiments in homogeneous turbulence. *NASA Tech. Memo. 81315.*

[119] Saric, W. S., Carter, J. D. & Reynolds, G. A. Computation and visualization of unstable-wave streaklines in a boundary layer. *Bull. Am. Phys. Soc.* **26** 1252.

[120] Saric, W.S., Reed, H. L., & Kerschen, E. J. 2002 Boundary-layer receptivity to freestream disturbances. *Annu. Rev. Fluid Mech.* **34** 291–319.

[121] Savill, A. M. & Zhou Ming De 1983 Wake/boundary layer and wake/wake interactions – smoke flow visualisation and modelling. In *Proc. Second Asian Congress of Fluid Mechanics* 743–754.

[122] Schlichting, H. 1933 Zur Entstehung der Turbulenz bei der Plattenstro-mung. *Nachr. Ges. Wiss. G ottingen Math.-Phys. Kl.* **1933** 181–208.

[123] Schmid, P., Henningson, D. S. 2001 *Stability and Transition in Shear Flows* (Springer, Berlin).

[124] Schubauer, G. B. & Skramstad, H. K. 1947 Laminar boundary-layer oscillations on a flat plate *NACA Report 909*

[125] Singer, B. A. 1996 Characteristics of a young turbulent spot. *Phys. Fluids* **8** 509–521.

[126] Singer, B. A. & Joslin, R. D. 1994 Metamorphosis of a hairpin vortex into a young turbulent spot. *Phys. Fluids* **6** 3724–3736.

[127] Sommerfeld, A. 1908 Ein Beitrag zur hydrodynamischen Erklarung der turbulenten Flussigkeitsbewegung. *Atti. Congr. Int. Math., 4th, Rome* 116–124.

[128] Spalart, P. R. & Yang, K. S. 1987 Numerical study of ribbon-induced transition in Blasius flow. *J. Fluid Mech.* **178** 345–365.

[129] Spalart, P. R. 1988 Direct simulation of a turbulent boundary layer up to $Re_\theta = 1410$. *J. Fluid Mech.* **187**, 61-98.

[130] Squire L. C. 1989 Interactions between wakes and boundary-layers. *Prog. Aerospace Sci.* **26**, 261–288.

[131] Swarztrauber,P. N. 1974 A direct method for the discrete solution of separable elliptic equations. *SIAM J. Numer. Anal.* **11** 1136–1150.

[132] Thomas, A. S. & Saric, W. S. 1981 Harmonic and subharmonic waves during boundary-layer transition. *Bull. Am. Phys. Soc.* **26** 1252.

[133] Tollmien, W. 1929 Uber die Entstehung der Turbulenz. *Nachr. Ges. Wiss. G ottingen Math.-Phys. Kl.* **1929** 21–44.

[134] Tseng, Y., Ferziger, J. H. 2003 A ghost-cell immersed boundary method for flow in complex geometry. *J. Comput. Phys.* **192** 593–623.

[135] Van Dyke, M. 1982 *An Album of Fluid Motion* The Parabolic Press.

[136] Voke, P., and Yang, Z. 1995 Numerical study of bypass transition. *Phys. Fluids* **7**, 2256–2264.

[137] Waleffe, F. 1997 On a self-sustaining process in shear flows. *Phys. Fluids* **9** 883–900.

[138] Wallace, J. M., Elckelman, H. & Brodkey, R. S. 1972 The wall region in turbulent shear flow. *J. Fluid Mech.* **54** 39–48.

[139] Westin, K. J. A., Boiko, B. G. B., Klingmann, G. B., Kozlov, V. V., Alfredsson, P. H. 1994 Experiments in a boundary layer subjected to free stream turbulence. Part I. Boundary layer structure and receptivity. *J. Fluid. Mech.* **281**, 193–218.

[140] Williamson, C. H. K. 1996 Three-dimensional wake transition. *J. Fluid Mech.* **328**, 345–407.

[141] Wu, X., Jacobs, R. G., Hunt, J. C. R. & Durbin, P. A. 1999 Sim-

ulation of boundary layer transition induced by periodically passing wakes *J. Fluid Mech.* **398**, 109–153.

[142] Zhong, S., Kittichaikarn, C., Hodson, H. P. & Ireland, P. T. 1998 Visualization of turbulent spots under the unfluence of adverse pressure gradients. In *Proc. 8th Intl. Conf. on Flow Visualization, Italy.*

[143] Zhou, M. D. & Squire, L. C. 1985 The interaction of a wake with a turbulent boundary-layer. *J. Aeronaut.* **89**, 72–81.